University of London
Imperial College London
Department of Aeronautics

# The Study of an Acoustic Resonance Anemometer

Mark William Starnes

2010

Submitted in part fulfilment of the requirements for the degree of
Doctor of Philosophy in Aeronautics of the University of London
and the Diploma of Imperial College London

# Declaration

I herewith certify that all material in this dissertation which is not my own work has been properly acknowledged.

Mark William Starnes

# Abstract

This thesis presents an investigation of the working principles of an acoustic resonance anemometer. To this end, the Navier-Stokes equations were used to generate an expression for the slowly changing, incompressible viscous flow field around and through an anemometer, and an expression for the rapidly changing, compressible inviscid convected acoustic field. The slowly changing field was simulated using a commercial computational fluid dynamics package called FLUENT. The rapidly changing, convected acoustic field was simulated using a finite element solver written for the project, capable of parallel execution using the 'Message Parsing Interface'.

Measurements performed in the '18 inch' wind-tunnel at Imperial College, London, were used to validate the simulation of the slowly changing field and provide a means to select a representative turbulence model. Measurements performed in the FloTek wind-tunnel at FT Technologies, Teddington, using a working anemometer were used to validate results generated by the finite-element solver. The finite element solver was further validated against a commercial finite element solver for acoustics in the absence of convective flow, called PAFEC.

Steady flow simulation results indicated the acoustic resonance anemometer generates a linear variation of acoustic phase with free stream velocity when operating at resonance: in agreement with measurements. The unsteady flow simulations showed fluctuations of the slowly changing unsteady flow through the duct. These were partly due to a separation region at the entrance of the acoustic duct; vortex shedding from the support pillars used to maintain the separation between the duct faces; and shedding from the anemometer body. The measurement errors caused by these fluctuations were quantified.

The findings in this project show that the simulation approach adopted is valid and that the software developed could be used for further study of acoustic resonance anemometry.

# Acknowledgements

This work was funded by FT Technologies, whose support is gratefully acknowledged. In particular I would like to thank Savvas Kapartis, for his continuous support both during my time spent at Imperial College, and afterwards.

I would like to thank my supervisor, Professor Mike Graham for his constant advice, patience and inspiration throughout this project.

Finally, I would like to thank my partner for her continuous support over the last four years.

# Contents


**1 Introduction.** **15**

1.1 Anemometry. . . . 15

1.1.1 Pressure based anemometry. . . . 16

1.1.2 Thermal anemometry . . . . 22

1.1.3 Velocity based anemometry. . . . 24

1.1.4 Acoustic anemometry . . . . 31

1.2 Numerical simulation . . . . 38

1.2.1 General approach . . . . 38

1.2.2 Solution approaches . . . . 38

1.2.3 Simulation of a convected acoustic field . . . . 39

1.2.4 Simulation of the viscous flow . . . . 42

1.3 Thesis layout . . . . 43

**2 Theory** **45**

2.1 Introduction . . . . 45

2.2 Division of the flow field. . . . 45

2.2.1 Low frequency, viscous field. . . . 45

2.2.2 Convected acoustic field . . . . 50

2.3 Numerical solution. . . . 54

2.3.1 Method overview. . . . 54

2.3.2 Method of weighted residuals. . . . 54

2.3.3 The weak form . . . . 55

2.3.4 Boundary conditions . . . . 56

**3 Measurements** **59**

3.1 Introduction . . . . 59

3.2 Equipment description . . . . 59

3.2.1 Wind-tunnel . . . . 59

3.2.2 Anemometer description . . . . 60

3.3 Surface pressure . . . . 62

3.3.1 Closed duct measurements . . . . 63

3.3.2 Open duct measurements . . . . 69

3.3.3 Unstable state . . . . 73

3.3.4 Discussion . . . . 75

3.4 Low frequency velocity field . . . . 77

3.4.1 Equipment and methodology . . . . 77

3.4.2 Hot-wire calibration . . . 78
3.4.3 Turbulence intensity and length scale. . . . 80
3.4.4 Mean velocity inside the duct . . . 82
3.4.5 Turbulence spectra . . . 84
3.5 Working anemometer measurements . . . 88
3.5.1 Amplitude results . . . 89
3.5.2 Phase results . . . 94
3.6 Conclusion . . . 99

**4 Numerical analysis of the viscous flow** **100**
4.1 Introduction . . . 100
4.2 Solution approach . . . 101
4.2.1 Solution method . . . 102
4.3 Two-dimensional simulations . . . 103
4.3.1 Test geometry . . . 104
4.3.2 Steady simulations . . . 105
4.3.3 Unsteady simulations . . . 106
4.3.4 Discussion of results from two-dimensional analysis . . . 112
4.4 Three-dimensional simulations . . . 116
4.4.1 Steady simulations . . . 119
4.4.2 Unsteady simulations . . . 130
4.5 Conclusions . . . 141

**5 Convected acoustics** **143**
5.1 Introduction . . . 143
5.2 Program description . . . 143
5.3 Code validation . . . 145
5.3.1 Three-dimensional elements . . . 145
5.3.2 Boundary condition validation . . . 146
5.3.3 Point source in an infinite baffle . . . 149
5.3.4 Concluding remarks . . . 149
5.4 Simulation domain . . . 150
5.5 Anemometer simulation . . . 156
5.5.1 Mesh and boundary conditions . . . 156
5.5.2 Low frequency velocity field interpolation . . . 158
5.5.3 Resonance hunting . . . 158
5.5.4 Steady, uniform flow . . . 160
5.5.5 Steady, non-uniform viscous flow . . . 171
5.5.6 Unsteady, non-uniform viscous flow . . . 172
5.5.7 Summation of point sources . . . 174
5.6 Performance limits . . . 180
5.7 Concluding remarks . . . 181

**6 Conclusions and Further Work** **183**

6.0.1 Research contribution . . . . . 183
6.0.2 Future work . . . . . 184

**A Appendix** **185**
A.0.3 Magnitude of acoustic velocity . . . . . 185
A.0.4 Magnitude of terms in the convected acoustic equation . . . . . 186
A.0.5 Use of the interactive convected acoustic solver . . . . . 189
A.0.6 An analysis file for the convected acoustic solver . . . . . 189

# List of Tables

2.1 Orders of magnitude for the terms of Equation 2.23. . . . . 50

3.1 Mean base pressure coefficients . . . . . 75
3.2 Hot-wire calibration data . . . . . 79
3.3 Observed frequency of first pressure amplitude peak. . . . . 93

5.1 Frequency error associated with the mesh density . . . . . 151
5.2 Effect of changing from uniform to steady, non-uniform flow, on the mean velocity in the duct. . . . . 171

A.1 Approximate magnitudes of the terms in Equation A.14 . . . . . 188
A.2 Approximate magnitudes of the terms in Equation A.14 . . . . . 189

# List of Figures


1.1 Cross section of a Venturi meter. . . . . 18
1.2 Cross section of a 'Bruhn', double Venturi meter. . . . . 19
1.3 Scattering from a moving particle. . . . . 26
1.4 Laser beam direction, observation position and observed particle velocity. . 31
1.5 Operation of a Sonic Anemometer / Thermometer. . . . . 32
1.6 The CSAT3 acoustic anemometer. . . . . 35
1.7 An acoustic resonance anemometer. . . . . 37

2.1 Shape functions at the edge of a two dimensional element. . . . . 56

3.1 Illustration of a modified anemometer used during testing. . . . . 61
3.2 $C_p$ variation at taps one and six for $Re = 33 \times 10^3$. . . . . 63
3.3 $C_p$ variation at taps one and six for $Re = 66 \times 10^3$. . . . . 64
3.4 Mean $C_p$ at taps one to six, for $Re = 33 \times 10^3$. . . . . 64
3.5 Standard deviation of $C_p$ at taps one to six for $Re = 33 \times 10^3$. . . . . 65
3.6 Standard deviation of $C_p$ at taps one to six for $Re = 33 \times 10^3$, smoothed. . 65
3.7 Mean $C_p$ at taps one to six, for $Re = 66 \times 10^3$. . . . . 66
3.8 Standard deviation of $C_p$ at taps one to six with $Re = 66 \times 10^3$. . . . . 67
3.9 $C_p$ distribution over the anemometer surface. . . . . 68
3.10 Mean $C_p$ at external taps for $Re = 33 \times 10^3$. . . . . 69
3.11 Standard deviation of $C_p$ at external taps. $Re = 33 \times 10^3$. . . . . 69
3.12 Effect on mean $C_p$ at tap six, of opening the acoustic duct. $Re = 33 \times 10^3$. 70
3.13 Effect on the $C_p$ distribution over the anemometer surface, of opening the duct. $Re = 33 \times 10^3$. . . . . 71
3.14 Time mean $C_p$ at internal taps for $Re = 33 \times 10^3$ . . . . . 71
3.15 Time mean $C_p$ at internal taps for $Re = 33 \times 10^3$. . . . . 72
3.16 Standard deviation of $C_p$ inside the duct, for $Re = 33 \times 10^3$. . . . . 72
3.17 The effect of the support pillar orientation with respect to the flow on $C_p$ inside the duct. . . . . 73
3.18 $C_p$ difference between taps eleven and twelve as the anemometer was rotated. 74
3.19 The $C_p$ difference between taps eleven and twelve may show a bistable state. 74
3.20 Circuit used with constant temperature hot-wire. . . . . 77
3.21 Best fit results compared with the source data, and the resultant errors. . . 80
3.22 Turbulence intensity values for different gain settings . . . . . 82
3.23 Comparison of the time-mean velocity ratio in the duct with the time-mean, low frequency pressure coefficient on the internal wall. . . . . 83

3.24 Turbulence intensity measurements at positions in the duct along the centre-line. . . . 83
3.25 Zero flow spectra without the wind-tunnel fan operating . . . . 85
3.26 Velocity spectra at $x = D$, outside the wake with the acoustic duct blocked. 86
3.27 Spectra inside the duct for $u_0 = 10\,ms^{-1}$ . . . . 87
3.28 Spectra inside the duct, along the centre line and in the streamwise direction for $u_0 = 20\,ms^{-1}$. . . . 87
3.29 Orientation of the anemometer with respect to the viscous flow field . . . . 89
3.30 Acoustic pressure amplitude ratios for different flow velocities for the pair, 'ac' 90
3.31 Acoustic pressure amplitude ratios for different flow velocities for the pair, 'ab' 91
3.32 Effect of flow velocity on the frequency of the first peak as a function of the zero flow resonance frequency . . . . 92
3.33 Distance travelled in unit time by a convected acoustic signal . . . . 92
3.34 Phase results for the pair, 'ac' with perpendicular external flow . . . . 94
3.35 Phase of the acoustic pressure at transducer 'b', when the duct has been excited at resonance with transducer, 'a'. . . . 95
3.36 Phase of pressure for the 'ab' pair, with flow direction parallel to the line between the transducers. . . . 96
3.37 Phase difference versus frequency, for normal and parallel transducer pair orientation, relative to the external flow. . . . 97
3.38 Phase difference at resonance for different external flow velocities for the case of the flow direction being normal, and parallel to the line joining the transducer pair . . . . 98

4.1 Reference mesh used for two-dimensional studies. . . . 104
4.2 Steady flow field solution showing asymmetry in the wake. . . . 105
4.3 $C_p$ from a steady simulation, compared with results from the literature . . . 106
4.4 Effect of doubling the distance to the downstream boundary on the base $C_p$. 107
4.5 Effect of doubling the distance to the downstream boundary, on the time-mean, unsteady $C_p$ for a circular cylinder. . . . 108
4.6 Vorticity magnitude at $t^* = 167$, with values above $1000\,s^{-1}$ saturated . . . 109
4.7 Effect on the base $C_p$ of increasing the distance to the side walls . . . . 109
4.8 Effect on the base $C_p$ of doubling the time step . . . . 110
4.9 Effect of halving the simulation time step, on the time-mean unsteady $C_p$ for a circular cylinder . . . . 111
4.10 Instantaneous $y^+$ results, late in the $dt^* = 0.01$ simulation. . . . 112
4.11 Instantaneous flow velocity magnitude near the top of the cylinder at $t^* = 120$, for $Re = 69 \times 10^3$. . . . 113
4.12 Effect of increasing the mesh density close to the cylinder on the base $C_p$ . 113
4.13 Effect of increasing the mesh density on the time-mean pressure coefficient . 114
4.14 The quarter mesh used as the basis of the three-dimensional simulations. . . 117
4.15 Aspects of the quarter mesh used for three-dimensional simulations. . . . 118

4.16 Simulated steady $C_p$ around the body without an acoustic duct, for $Re = 33 \times 10^3$. . . . 119
4.17 Measurement versus steady simulation results for the $C_p$ around the anemometer body without an acoustic duct . . . . 120
4.18 Steady $x$ velocity ratio for the quarter mesh simulation without an acoustic duct, in the plane $y = 0$ . . . . 120
4.19 Steady velocity around the anemometer without an acoustic duct. . . . . 121
4.20 Simulated steady $C_p$ around the body with the acoustic duct present. $Re = 33 \times 10^3$. . . . 122
4.21 Steady streamwise velocity results for the low frequency viscous flow field. . 124
4.22 Measurement versus steady simulation, for the $C_p$ around the body, $11.5\,mm$ above the centre plane. . . . 125
4.23 Measurement and simulation of the velocity along the duct centre line show generally good agreement . . . . 125
4.24 Steady simulation of the open acoustic duct case with support pillars. $u_0 = 10\,ms^{-1}$. . . . 127
4.25 Time-mean measurement versus steady simulation results for the $C_p$ around the body, $11.5\,mm$ above the centre plane. The acoustic duct is open . . . . 128
4.26 Measured and simulated velocity along the duct centre line . . . . 128
4.27 Velocity along the duct centre line for simulations at different free-stream velocities. . . . 129
4.28 Instantaneous, unsteady, low frequency velocity around the anemometer without an acoustic duct, at $t^* = 317$ . . . . 131
4.29 Instantaneous unsteady vorticity around the anemometer without an acoustic duct, at $t^* = 317$. . . . 132
4.30 Measurement versus steady simulation results, for the $C_p$ around the body, $11.5\,mm$ above the centre plane at $Re = 33 \times 10^3$. The anemometer acoustic duct is not present. . . . 133
4.31 Time-mean, x-velocity ratio in the $y = 0$ plane . . . . 134
4.32 Measurement versus steady simulation results for the $C_p$ around the body, $11.5\,mm$ above the centre plane. The acoustic duct is present. . . . 135
4.33 Instantaneous, unsteady, low frequency streamwise velocity ratio at $t^* = 52$, including flow through the acoustic duct. Support pillars were not included. 136
4.34 Time-mean, low frequency x-velocity ratio in the $y = 0$ plane . . . . 137
4.35 Measurement versus simulated $C_p$ around the body, $11.5\,mm$ above the centre plane. . . . 138
4.36 Time-mean, unsteady, low frequency velocity along the duct centre line, averaged over $dt^* = 5$. . . . 139
4.37 Low frequency x-velocity ratio in the $y = 0$ plane. . . . 140

5.1 Two-dimensional test mesh. . . . 145
5.2 First order, two-dimensional element validation showing good results. . . . 146
5.3 Two-dimensional, second order element validation showing good results. . . 146

5.4 First order, three-dimensional element validation showing good results. . . . 147
5.5 Finite element mesh used to test a 'quiet' boundary. . . . . 148
5.6 Convective flow is shown to change the 'quiet' boundary condition. . . . . 148
5.7 The effect of convective flow on acoustic phase. . . . . 149
5.8 Full and reduced simulation domain regions. . . . . 150
5.9 Acoustic pressure at the end of a tube. . . . . 151
5.10 A mesh used to test the effect of the distance to the 'quiet' boundary. . . . 153
5.11 The effect of changing the boundary condition terminating the domain. . . 154
5.12 The effect of changing the distance to the 'quiet' boundary. . . . . 155
5.13 The finite element mesh used for acoustic analyses. . . . . 157
5.14 Interpolated convective field results. . . . . 158
5.15 Interpolated convective field results. . . . . 159
5.16 Action of the bisection algorithm used to detect peak results. . . . . 160
5.17 Acoustic pressure distribution in the duct, no convective flow. . . . . 161
5.18 Acoustic pressure distributions with zero convective flow. . . . . 162
5.19 Acoustic pressure distribution in the duct, no convective flow. . . . . 164
5.20 Pressure magnitude distribution at the frequency marked, 'g' in Figure 5.19. 164
5.21 Measured versus simulated transfer function between transducers. . . . . 165
5.22 Acoustic phase over the duct surface, at $f = f_1$. . . . . 166
5.23 Acoustic phase along the duct surface with zero convective flow. . . . . 166
5.24 The effect of uniform flow on acoustic pressure versus frequency. . . . . 167
5.25 The effect on $f_1'$ of convective flow. . . . . 168
5.26 Acoustic pressure and phase distribution at $f_1'$ with convective flow. . . . . 168
5.27 Acoustic phase at resonance with different convective velocities. . . . . 169
5.28 The effect of observing acoustic phase at constant $f = f_1$. . . . . 170
5.29 Acoustic pressure variation with frequency and non-uniform convective flow. 171
5.30 Acoustic phase at $f_1'$ versus convective velocity. . . . . 172
5.31 Acoustic phase at $f_1'$ with an unsteady, convective flow. . . . . 173
5.32 The magnitude of phase variation at $f_1'$ with unsteady convective flow is shown to be small. . . . . 173
5.33 The effect on the acoustic pressure and phase disitribution generated with a summation of sources model, of the number of reflections. . . . . 175
5.34 Acoustic pressure and phase along the duct edge with different numbers of reflections. Zero convective flow. . . . . 175
5.35 Celerity calculation diagram. . . . . 176
5.36 Results from the direction dependent celerity algorithm. . . . . 178
5.37 Acoustic pressure and phase distibutions for different numbers of reflections. Convective flow is present. . . . . 178
5.38 Acoustic pressure and phase along the duct wall with different numbers of reflections. Convective flow is present. . . . . 179

A.1 Example .pyFE file, controlling the solution of a convected acoustic simulation. 190

# Nomenclature

| | |
|---|---|
| $[K]$ | System matrix |
| $[k]$ | Element matrix |
| $\boldsymbol{f}$ | System vector |
| $\boldsymbol{u}$ | System results vector |
| $\epsilon$ | Turbulence dissipation rate |
| $\Gamma$ | Boundary of the solution domain |
| $\gamma$ | Ratio of specific heats |
| $\lambda$ | Wavelength |
| $\mu$ | Dynamic viscosity. $\mu_{air,15°C} = 1.78 \times 10^{-5}\, kg\, m^{-1}\, s^{-1}$ |
| $\Omega$ | Solution domain |
| $\omega$ | Angular frequency $= 2\pi f$ |
| $\omega$ | Vorticity |
| $\rho$ | Density |
| $A$ | Area |
| $a$ | Hot-wire overheat ratio |
| $c$ | Celerity |
| $c'$ | Modified celerity |
| $C_p$ | Pressure coefficient $= \frac{p - p_0}{\frac{1}{2}\rho u_0^2}$ |
| $D$ | Characteristic length as a diameter |
| $e$ | Vapour pressure of water |
| $f_0$ | Frequency of greatest acoustic pressure magnitude, associated with a half wavelength resonance |
| $f_0'$ | Modified frequency of greatest acoustic pressure magnitude, dependent on flow velocity |

$f_{1\infty}$ Full wavelength resonance frequency for an infinite duct.

$f_1$ As $f_0$, but for a full wavelength resonance

$f_1'$ As $f_0'$, but for a full wavelength resonance

$f_s$ Shedding frequency

$I$ Electrical current

$k$ Turbulence kinetic energy

$k$ Wavenumber $= \omega/c$

$l$ Characteristic length

$M$ Mach number $= u/c$

$P$ Absolute pressure, nominally $101325\,Pa$

$p_s$ Static pressure

$p_t$ Total pressure

$R$ Gas constant. $R = 8.314\,472\,JK^{-1}mol^{-1}$

$r$ Electrical resistance

$R_s$ Specific gas constant. For air, $R_s = 287.056\,JK^{-1}kg^{-1}$

$Re$ Reynolds number $= \frac{\rho u D}{\mu}$

$S_t$ Strouhal number $= \frac{fL}{u}$

$t^*$ Non-dimensionalised time step $= \frac{tL}{u}$

$T_f$ Flow temperature

$T_w$ Hot-wire temperature

$u$ Velocity

$u_\tau$ Friction velocity

$V$ Voltage

$y^+$ Wall unit

TI Turbulence intensity $= \sqrt{\overline{u^2}}/u_0$

# 1 Introduction.

## 1.1 Anemometry.

From the Greek '$Ανεμος$' (Anemos), meaning 'wind'; and the Greek '$μετρο$' meaning, 'to measure': anemometry is the measurement of wind.

Wind speed measurements are required in fields of study such as aeronautics and meteorology. The measurement of general gaseous flow extends the field of application into areas such as the measurement of piped gases, and the flow through automotive exhaust systems and building ventilation systems. Anemometers commonly observed in meteorological stations include the cup anemometer, and the turbine or 'propeller' anemometer with a wind vane.

The device studied in this project uses a new method of anemometry: observation of the change occurring in a resonant acoustic duct as the flow passes through it. The approach is interesting, as unlike other anemometers currently available, the device has no moving parts; is of rugged design; does not require special treatment of the flow; and is not prohibitively expensive.

The anemometer examined during the project is a cylinder approximately five centimetres in diameter and ten centimetres long, with curved ends. The cylinder is split through its diameter to form two internal surfaces: it is between these surfaces that the measured flow passes and the acoustic resonance is established. The acoustic behaviour inside the duct is affected by convective effects.

In order to get an improved perspective of where this object fits in in the field of anemometry, it is useful to review some other anemometry methods, and consider their relative strengths and weaknesses.

The anemometry methods presented in this section fall into four categories: pressure based; velocity based; those using thermal transport; and those using acoustics. The choice of instrument for an application depends on the required performance, the operating environment and the cost.

In the following discussion a few of the options available are examined; their working principles are presented, with a discussion of their advantages and disadvantages.

### 1.1.1 Pressure based anemometry.

#### The Pitot-static tube

For an object in a subsonic flow with a diameter based Reynolds number greater than $Re \approx 2000$, reducing the flow velocity to zero results in the pressure increasing from the static value, by the dynamic value. This can be achieved using a closed end tube, with its open end pointing upstream. Subtracting the static pressure value then yields the dynamic pressure, which can be used to calculate the flow velocity. According to Duncan et al. [28], the first term from Equation 1.1 can be used with low-speed flow to this end.

$$p_t - p_s = \frac{1}{2}\rho u^2 \left(1 + \frac{M^2}{4} + \frac{(2-\gamma)M^4}{24} + \ldots\right) \tag{1.1}$$

with the total pressure, $p_t$; the static pressure, $p_s$; the density, $\rho$; the velocity, $u$; the Mach number, $M$; and the ratio of specific heats, $\gamma$. The pressure difference is related to the velocity squared so the error magnitude increases as velocity decreases if the accuracy of the pressure difference sensor is constant. Static pressure tube readings are almost independent of Reynolds number in the range, $3000 \leq Re_d \leq 53000$, according to Chue [19].

With increasing Mach number, more terms should be used to increase the accuracy. When the velocity becomes a significant fraction of the speed of sound, the compressible form of Equation 1.1 should be used (Balachandran [4]), as presented in Equation 1.2.

$$u = \sqrt{\frac{2\gamma}{\gamma - 1}\left(\frac{p_t}{\rho_t} - \frac{p_s}{\rho_s}\right)} \tag{1.2}$$

Measurements beyond Mach one are made with separate Pitot and static measurements [4], but are beyond the range of velocities of interest for this thesis.

Low Reynolds number flow results in the difference between the stagnation and total pressure no longer equalling the dynamic pressure. According to Barlow et al. [6], the pressure coefficient at stagnation for a body with a diameter based Reynolds number below $Re = 2000$ exceeds unity; compensation for this effect is possible as demonstrated by Merriam and Spaulding [72].

Duncan et al. [28] state that errors due to alignment with the flow are low as long as the alignment error is less than 5°. Barlow et al. [6] has shown that the profile of the tube can be modified to affect its sensitivity to flow direction. The Dines tube has been shown by Herschel [51] to use a separate static tube oriented normally to the Pitot tube and the nominally two-dimensional flow, and has been shown to perform well up to 20°. According to Kiel [63], the Kiel tube gives the most stable results with inclinations up to 40°.

Unsteady measurements yield root mean square rather than mean velocity values, so unsteady velocities are overestimated. This effect makes the Pitot-static tube less suitable for unsteady flow measurement. Nevertheless, an unsteady formulation is available, as

reported by Duncan et al. [28]. The RMS result, combined with the slow response of the device, make it less suitable than other methods for measurements of rapidly varying velocities.

Probe induced flow distortion can result in increased velocity in the region of the static holes. This can be balanced by a second stagnation region, caused by a bend in the pipe as used in Prandtl's design (Barlow et al. [6]).

Pitot-static tubes are used in environments with known flow directions such as wind-tunnels. They are cheap and simple, but show poor dynamic behaviour and generate a single velocity component. Their lack of moving parts results in low maintenance requirements.

### Pressure sphere

Pressure spheres sample pressure at 'pressure taps' over a spherical surface, using these pressures with a numerical model to determine flow velocity and direction. Early examples indicated by Barlow et al. [6], used few sample points and potential flow models. The number of derived velocity components were limited and significant deviation of the flow direction from the direction normal to the front of the sphere resulted in gross errors. An 'acceptance angle' was defined, describing the angle at which the errors became unacceptable. Reducing the angular separation between ports was shown to increase the acceptance angle by Wesely et al. [112], but this approach also resulted in decreased pressure differences, causing increased errors.

Increased processing power has enabled processing of the data from more ports. As a result, pressure spheres can now feature full 360° acceptance angles in one plane, as demonstrated by Dobosy et al. [27]. The spheres contain multiple pressure sensors and so tend to be quite large - tens of centimetres in diameter. This precludes them from the measurement of small scale flows. They can be used for weather monitoring, with automated 'pneumatic back-flushing' of the ports to remove rain water. As computing power increases, the number of ports and the complexity of the model can be increased, providing a means to increase accuracy and acceptance angle.

According to Barlow et al. [6], each pressure sphere is individually calibrated, and the model most often used assumes incompressible, potential flow: the flow being measured should display zero vorticity and should be of a low Mach number. Changes to the pressure tappings, results in performance changes so regular inspection of the devices are necessary. The mounting of pressure sensors close to the sphere surface extends the bandwidth of the system, enabling measurements up to $10\,Hz$ to be made by Crawford and Dobosy [22]. Pressure differences are proportional to the square of the velocity, so errors increase at low velocities. Velocities above $100\,ms^{-1}$ have been measured with an appropriate selection of transducers by Dobosy et al. [27] but the lower velocity limit is approximately one fifth the maximum velocity. The range of measurement is therefore limited. Direction errors are strongly dependent on the positions of the ports, but have been reported as low as 0.3% by Crawford and Dobosy [22] with a speed error of $\pm 0.25\,ms^{-1}$ for flows within 6° of the upstream direction.

### Venturi meter

Duncan et al. [28] used the Venturi meter to illustrate an application of Bernoulli's Theorem. As illustrated in Figure 1.1, the meter can be inserted into a pipeline. The area the flow passes through is reduced from $A_1$ to $A_2$. The flow velocity in the pinched region increases, and a pressure difference between the regions occurs: the difference in pressure, $dp = p_1 - p_2$, is used to calculate the flow velocity.

The volume passing though the meter per unit time is indicated in Equation 1.3 (from Duncan et al. [28]).

$$Q = \sqrt{\frac{2A_1^2 A_2^2 (p_1 - p_2)}{\rho(A_1^2 - A_2^2)}} \tag{1.3}$$

with the original and reduced areas, $A_1$ and $A_2$; the pressure difference, $p_1 - p_2$; and the density, $\rho$. The derivation assumes uniform, inviscid and incompressible flow approaching the meter. Like the Pitot-static tube, the result is proportional to the square root of the pressure difference, limiting low velocity accuracy. The passage of viscous fluids results in a reduced flow rate, which also varies with Reynolds number, and the pressure drop caused by the meter can be disadvantageous. The devices can be calibrated for the material being measured, but the calibration can change over time due to changing properties of the internal surfaces. The optical characteristics of the fluid are irrelevant and the devices are low cost due to the simplicity of operation.

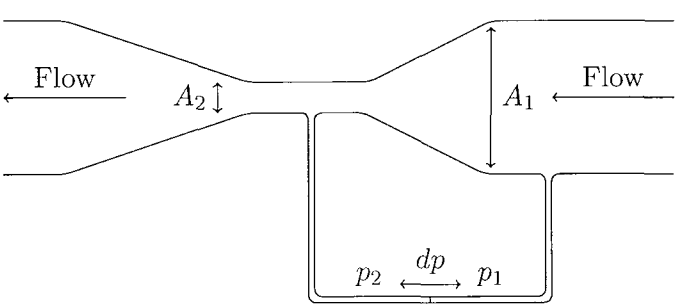



Figure 1.1: Cross section of a Venturi meter.

### Double Venturi

The double Venturi consists of a small Venturi, positioned with its outlet in the narrow region of the larger Venturi, as shown in Figure 1.2; modified from work by Stewart [100].

Stewart [100] reports that the 'Bruhn' double Venturi gives just over thirteen times the differential pressure generated by a Pitot tube, but that careful calibration of the device is required. While not stating the secondary pressure in his differential pressure claim, it appears he was referring to the static pressure. The development of a Pitot-Venturi anemometer was reported, whereby the static pressure tube was replaced with a single Venturi. Compared to the Pitot tube, six times the differential pressure increase

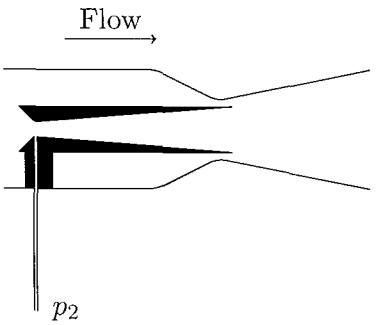



Figure 1.2: Cross section of a 'Bruhn', double Venturi meter.

was demonstrated by the Pitot-Venturi, and eleven times by the double Venturi. The sensitivity of the device was increased at the cost of increased flow disturbance and hardware complexity.

### Propeller / turbine anemometry

The term, 'propeller' is sometimes used in aeronautics to describe a rotating object with blades which is used to drive a flow; conversely, a 'turbine' is driven by the flow. In the anemometry literature, both terms are used to describe the same object: a turbine which is driven by the flow. 'Turbine' is adopted here.

Turbine meters use the lift force generated by a flow passing over an aerofoil to generate rotation. Ignoring mechanical friction, a closed form solution for the relation between flow speed and angular frequency of a turbine flow meter has been demonstrated by Duncan et al. [28] to exist, when the flow is in line with the axis of rotation.

Experimentally, the relationship is linear but does not pass through the origin: like cup-anemometers, turbine anemometers have a start-up velocity due to internal friction. Duncan et al. [28] concludes that individual unit calibration is therefore required and that the start-up velocity is likely to vary with temperature. Response parameters are similar to those of the cup anemometer: Desjardins et al. [26] specified a 'calibration distance' as the length of air column required to pass the device to cause it to rotate one radian, and demonstrated a value of $0.45\,m$. Start-up speeds of $0.06\,ms^{-1}$ were found.

Three components of velocity can be derived by orienting sets of devices at different angles to the flow, as used by the Gill anemometer detailed by Gill [43]. The steady anemometer output was shown by Hicks [52] to deviate from the cosine response to off axis flow, by an amount which varied with wind speed. This effect makes this approach less attractive. Brook [13] found the length constant varied with the direction of the flow, changing the dynamic response to off-axis flow.

The use of a vane to position the turbine axis towards the flow reduces these problems, but introduces new dynamic components to its behaviour: a minimum flow velocity requirement to position the anemometer of the order of $0.2\,ms^{-1}$ was demonstrated by Desjardins et al.

[26]. Kristensen [65] reported a complication of the dynamic response, as the turbine rotation axis continuously changed direction during unsteady flow.

Turbine anemometers are cheap but delicate due to minimum moving mass constraints. Although Tropea et al. [107] reported that they require less maintenance than cup anemometers, regular calibration is still required due to the moving parts being affected by the environment. They have similar dimensions to cup anemometers, ranging from (but not limited to) diameters of $D = 2\,cm$ as documented by Dahlberg et al. [23], to $D = 20\,cm$ (Desjardins et al. [26]).

Commercial turbine-vane products are reported by the R. M. Young Company [86] to measure velocities up to $100\,ms^{-1} \pm 0.3\,ms^{-1}$ and generate single plane direction data. Costs start from US$890 for basic models.

Commercial Gill anemometers are reported by the R. M. Young Company [89] to generate three components of velocity, but with a lower maximum velocity of $35\,ms^{-1}$. Costs are higher than the turbine-vane anemometers, currently starting at US$2500.

### Drag anemometry

Drag anemometers measure the force required to maintain the position of an object in a flow. If the variation of the drag coefficient with Reynolds number is known, restoring forces can be used to calculate the flow velocity. Most examples generate one or two-dimensional information as one end of the object is usually fixed to a mechanical ground, forming a cantilever. These systems have a mass and stiffness, and so form a second order system with a resonance: complicating high-frequency measurements, and requiring mechanical and electronic compensation. Vortex shedding from the body can occur, manifesting itself as measurement noise. This can reduce the accuracy of turbulence measurements: a comparison with hot-wire measurements by Hölling et al. [54] showed measurements of turbulence intensity using a sphere drag anemometer were close to a factor of two, too low (but still better than results from a cup-anemometer).

The method has been extended to perform measurements in low speed ($\sim cm\,s^{-1}$) flows by Pluijm et al. [84], by an appropriate selection of system parameters.

Agreement with sonic-anemometer measurements have been demonstrated to within 6% for mean velocity values up to $6\,ms^{-1}$ by Green et al. [46], and to within 2% of hot-wire measurements over a similar range by Hölling et al. [54]. The spherical drag anemometer was demonstrated to generate an output proportional to velocity squared, so decreasing velocities may show increasing error margins.

Drag anemometers can be small, cheap and can be weather resistant: Green et al. [46] detected no change in mean results when the device was exposed to precipitation. The movement of the parts is small, resulting in low maintenance. The resonant frequency places a limit on the anemometer high frequency performance, but power spectra measurements up to $80\,Hz$ have been presented by Hölling et al. [54], a frequency range exceeding that of the cup-anemometer.

### Cup anemometry

Cup anemometers feature a number of cups rotating in the same plane, around a common centre of rotation. Invented by Thomas Robinson at Armagh observatory (Bailey [3]), the differing drag force for flow incident on the front and backside of the cups results in a net torque, causing a rotation. For steady flow normal to the axis of rotation, the equilibrium cup velocity is approximately one third the flow velocity; Patterson [80] found this figure to vary between anemometers of the same type. As a result of this variation, each anemometer needs to be calibrated. Internal friction results in zero rotation occurring for low speed flows, and Dahlberg et al. [23] reported that this friction can vary slightly with temperature. The linear relation between flow rate and device output separates this device from the Pitot-static tube and pressure sphere anemometers, which show a dependence on the square of the flow rate.

According to Glo [45], the devices show response times of the order of a second, but Hristov et al. [56] reported that a degree of compensation could be applied, to improve the response times. A recent design for a cup anemometer has been reported by Solov'ev et al. [98] to generate results at up to $5\,Hz$.

Kristensen [64] reported that the devices could be characterised by a length constant, equivalent to the length of flow passing the anemometer to make it turn through one radian; and a start-up velocity. Length constants as low as $0.32\,m$ were reported by Solov'ev et al. [98], with start-up velocities of $0.2\,ms^{-1}$. Hristov et al. [56] reports that the length constant defines the smallest flow structures observable.

The difference between forces on the front and backside of each cup, while causing the cups to rotate, also cause 'overspeeding': fluctuating flow speeds are reported as higher than the mean velocity. According to Solov'ev et al. [98], this can be reduced to levels around 1%. Papadopoulos et al. [79] reported that this was of particular importance to the wind-energy industry (due to the available power being proportional to the cube of the flow rate), and to measurements made in turbulent flows.

The devices show a dependence on the velocity component parallel to the rotation axis, as reported by Dahlberg et al. [23]. Generally, small deviations from incidence normal to the rotation axis generate a cosine response. Deviations greater than 5° generate responses dependent on the anemometer design. Speed errors approaching 9% have been demonstrated for attack angles of 30°. Generally, this velocity component should be minimised.

Precipitation can cause errors roughly proportional to the rain fall rate, and inversely related to the flow speed, according to Dentler [25]. A maximum 3.5% error for $100\,mm\,hour^{-1}$ precipitation at a mean $1\,ms^{-1}$ was reported.

Papadopoulos et al. [79] reported that each device needs regular calibration due to the moving parts being affected by environmental factors such as the build up of dirt. They are cheap and operate in natural environments. Risø [88] claims that commercial products can measure velocities exceeding $70\,ms^{-1}$. Edge mounted cups of diameter $2\,cm$ have been

used, resulting in a device diameter of 11 $cm$, a height of 11 $cm$ and a mass of 100 $g$ as reported by Solov'ev et al. [98]. Current prices are reported by R. M. Young Company [90] to be of the order of $500.

### 1.1.2 Thermal anemometry

#### Hot-wire anemometry

Hot-wire anemometers use the flow to remove heat from a relatively hot, high aspect ratio wire of low thermal capacity. The lost heat is usually restored by an electrical current. Bradshaw [12] states that according to King's Law, the heat transfer coefficient for a cylinder in a flow, is related to the Reynolds number as in Equation 1.4.

$$h \propto A + BRe^{0.5} \tag{1.4}$$

with the heat transfer coefficient, $h$; constants $A$ and $B$; and the Reynolds number, $Re$. The exponent is in numerical form, as it is a result of empirical work; Bradshaw [12] reports that an exponent of 0.45 can give better results with hot-wire measurements. The heat provided by the electrical power is convected to the flow, as defined in Equation 1.5.

$$\frac{V^2}{r} \propto h(T_w - T_f) \tag{1.5}$$

with the voltage across the wire, $V$; the heated wire resistance, $r$; and the temperature of the wire and the flow, $T_w$, $T_f$. If the two equations are combined, and the wire and flow temperatures are assumed constant, Equation 1.6 can be derived.

$$V^2 = A' + B'Re^{0.5} \tag{1.6}$$

The new constants $A'$ and $B'$ vary between probes, and vary as the wire changes over time, so frequent calibrations are required. The wires are delicate as a result of the low thermal mass requirement, and are susceptible to physical and thermal stresses.

According to Tropea et al. [107], three popular versions of hot-wire equipment are in use: constant current; constant voltage; and constant temperature. The constant current method keeps the wire current, $I_W$ constant and calculates the wire resistance, $R_W$; changes in the flow velocity, $U$, affect the probe temperature, its resistance and therefore the heat provided by the electrical current. Thermal inertia effects are greater than for the other two methods, but can be compensated for with electrical filtering. The unsteady resistance component due to velocity variations is strongly dependent on the overheat ratio, $a = R_{hot}/R_{ambient} - 1$, but the contribution due to unsteady flow temperature is not.

The constant voltage method allows $I_W$ to vary, maintaining the voltage across the wire. As $U$ increases and the probe temperature drops, the decreasing probe resistance results in an increase of current; increasing the electrical power dissipated. Thermal inertia provides

less of an effect than for the constant current case, and can be compensated for during post-processing, as indicated by Tropea et al. [107]. Variation of $a$ results in a change of sensitivity to velocity perturbations that is approximately one quarter of that shown by the constant current method, but the sensitivity to flow temperature changes. High bandwidth measurements exceeding $100\,kHz$ have been demonstrated by Kegarise and Spina [62].

The constant temperature method uses a feedback loop to maintain the wire temperature, resulting in reduced thermal stresses and further reduction of thermal inertia effects. This system, however, shows a strong dependence on flow temperature.

Barlow et al. [6] has demonstrated that components of velocity can be measured, using sets of wires with different orientations to the flow. Multiple wire sets can be used to derive vorticity, and transport of vorticity.

Hot-wire anemometry is suited to highly spatially resolved measurements of rapidly fluctuating fields in a controlled environment. Wire diameters are reported by Tropea et al. [107] to be typically in the range, $0.5\,\mu m \sim 5\,\mu m$ with nominal lengths of $0.5\,mm - 2\,mm$; this results in the wires being fragile and allows the wire to respond rapidly to fluctuations in velocity. The wire changes behaviour with time and needs frequent calibration. Hot-wire anemometry was used during this project, and is discussed in more detail in Chapter 3.

### Pulsed wire anemometry

The pulsed wire anemometer is reported by Bradbury and Castro [11] to measure the time taken for a pulse of heat to travel from a heated wire to one or more sensor wires. With two sensor wires, the flow direction as well as its speed, can be determined. This is unlike the hot-wire anemometer which senses components of velocity magnitude. Also unlike the hot-wire, the measured result is not dependent on the flow temperature. Like pulsed acoustic anemometers, the measured quantity is time: since this result is inversely related to velocity, measurement uncertainty increases with velocity. Spatial resolution is similar to that of hot-wires, but according to Bradshaw [12], the temporal response is of an order worse.

Like hot-wire anemometers, the thermal mass of the wires is low, to improve temporal behaviour. As a result, pulsed wire anemometers, like hot-wires, are delicate and are used within controlled environments.

### Thermal transient anemometry

The thermal transient anemometer can be used to measure spatially averaged velocity over an area, as demonstrated by Foss et al. [34]. The device consists of a length of wire, criss-crossed over a measurement plane. The wire is heated to an initial overheat, and allowed to cool; the exponential decay of temperature with time is monitored by measurement of the electrical resistance of the wire. The temperature decay of the wire is used to calculate the mean flow rate past the mesh.

The implementation described assumes flow normal to the mesh plane. Applications include the measurement of air flow through ducts and specifically, the flow through an automotive radiator: this flow is made complex by the presence of multiple objects in the flow path. Point velocity measurements of this complex field are unlikely to represent the mean flow accurately.

A $50\,\mu m$ diameter tungsten wire (one hundred times thicker than those used in hot-wire anemometry) with a nominal sensor length to diameter ratio of 2000 was used experimentally, this ratio reportedly resulting in dominance of convection effects. Results for the resistance ratio change, $R^*$, as the wire cooled showed the expected exponential decay: the ratio defined as,

$$R^* = \frac{R_s(t) - R_{amb}}{R_s(T_H) - R_{amb}} \tag{1.7}$$

with the sensor resistance as a function of time, $R_s(t)$; the resistance at ambient temperature, $R_{amb}$; and the initial resistance when heated to temperature, $T_H$, $R_s(T_H)$. These data were used to derive the constants of a relationship between the system time constant and the product of the flow velocity and density. Observed values for the system time constant, $\tau$ varied between $\tau = 93.4\,ms$ for $u = 1.58\,ms^{-1}$ and $\tau = 47.6\,ms$ for $u = 9.21\,ms^{-1}$. The time taken to heat the wire was not specified, but these time constants would limit the measurement rate to approximately one per second. The accuracy of the calculated velocities was not reported.

Later work by Foss et al. [35], included a pre-heating measurement of resistance and application of calibration data, to calculate the ambient temperature. Each unit requires calibration, as the sensing wire properties differ between devices. Hot-wire anemometry was used to determine turbulence levels, and the authors claim the device is insensitive to turbulent fluctuations up to $TI = 20\%$.

Like the hot-wire anemometer, periodic calibration is required due to dirt build up on the wire. The thickness of the wire results in it being more rugged than the hot-wire, and less able to measure high frequencies.

### 1.1.3 Velocity based anemometry.

#### Vortex shedding flowmeter

According to Duncan et al. [28], a circular cylinder in a flow with a Reynolds number in the range, $10^2 < Re < 10^5$ sheds vortices at a frequency,

$$f_s = S_t \frac{u}{l} \tag{1.8}$$

with shedding frequency, $f_s$; Strouhal number, $S_t$; velocity, $u$; and characteristic length, $l$. In this range of Reynolds numbers, $St \approx 0.2$. Ardekani [1] has monitored the shedding frequency by observing the downstream flow with methods such as hot-wire, while Sun

et al. [101] used acoustic sensing. Barton and Saoudi [8] observed the shedding frequency using the body itself, by using a stretched fibre optic cable both as the bluff body and the sensing mechanism.

This anemometer has no moving parts, so maintenance is low if particulate build up does not occur. The flow should approach the body normally, so this method is particularly suited to the monitoring of flows within pipelines and ducts. Careful attention must be paid to the condition of the upstream flow as vortices shed by objects upstream can interfere with the measurement.

Commercial devices claim rate accuracies of $\pm 0.7\%$ for liquids and $\pm 1.0\%$ for gas and steam with operating temperatures from $-40°C$ to $400°C$. A larger measurement uncertainty of less than 6% has been reported by Sun et al. [101], and attributed to reduced frequency resolution occurring as the flow rate decreases.

### Laser-Doppler anemometry

According to Tropea et al. [107], data from the first laser Doppler anemometer measurement were published by Yeh and Cummins [115], using the heterodyne reference-beam technique with coherent detection. The method involves inspection of the Doppler shift of frequencies that occurs when a laser beam is scattered from moving particles. The frequency shift specified by vom Stein and Pfeifer [109] is slight; given by

$$f_D = \frac{2v'}{\lambda} \tag{1.9}$$

with the frequency shift, $f_D$; the particle velocity in-line with the beam, $v'$; and the beam wavelength, $\lambda$. A $10\,ms^{-1}$ object velocity detected with a $\lambda = 0.6328\mu m$ HeNe-laser generates $f_D = 32\,MHz$; a fraction of the source frequency, $4.7 \times 10^{14}\,Hz$.

The scattered beam is mixed with a fraction of the original beam, resulting in a beating frequency equal to the frequency difference between the beams. If the beam is not parallel to the direction of motion and the scattered light is observed away from the source, the frequency change of the scattered light is reported by Byrne et al. [17] to be,

$$v_D = \frac{2cos\theta}{\lambda} V cos\beta \tag{1.10}$$

with the measured frequency shift, $v_D$; the half angle between incident and observed beam, $\theta$; the light wavelength, $\lambda$; the particle velocity, $V$; and the angle between the bisector of the incident and observed beam, and the particle velocity, $\beta$. A coincident emission and observation position results in,

$$v_D = \frac{2}{\lambda} V cos\beta \tag{1.11}$$

so that the frequency shift is proportional to the component of velocity in the same direction as the beam. The use of fibre-optics to carry both the incident and scattered beam has

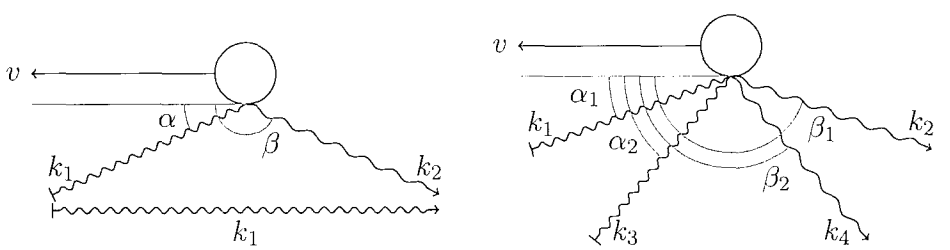
been reported by Byrne et al. [17] to generate the coincident condition mentioned above, and provides a convenient method to control the measurement position.

Byrne et al. [17] reports that reference beam measurements require manipulation of the reference beam intensity to maximise the signal to noise ratio. This can be achieved though the use of a fibre Bragg grating (FBG) with source wavelength tuning. The reflectivity of the FBG varies with wavelength, and the emission wavelength of a semiconductor laser varies with injection current; these two effects are used to control the intensity of the reference beam, in order to get the best signal to noise ratio.

vom Stein and Pfeifer [109] shows that Equations 1.9, 1.10, 1.11 are special cases of the more general,

$$f_D = \frac{v}{\lambda}\left(cos\alpha + cos\beta\right) \tag{1.12}$$

where the angles, $\alpha$ and $\beta$ are those between the direction of particle motion, and the incident beam and scattered beams, respectively. This is illustrated in Figure 1.3, from work by vom Stein and Pfeifer [109], and shows that the observed frequency shift depends not only on particle velocity, but also on observation position.




(a) Heterodyne reference beam with coherent detection.

(b) Doppler difference method.

Figure 1.3: Diagram illustrating scattering from a moving particle.

vom Stein and Pfeifer [109] extended the method of Yeh and Cummins [115] to include a second beam, coherent with the first and focussed on the same region but striking the particle at a slightly different angle, as illustrated in Figure 1.3. Observation of the two scattered beams results in a beat frequency,

$$f_D^* = |f_{D_1} - f_{D_2}| = \frac{v}{\lambda}|cos\,\alpha_1 - cos\,\alpha_2 + cos\beta_1 - cos\beta_2| \tag{1.13}$$

$$= \frac{v}{2\pi}|k_1 + k_2 - k_3 - k_4| \tag{1.14}$$

with frequency difference, $f_D$; particle velocity, $v$; wave vector, $k$; and incident and scattered angles, $\alpha$ and $\beta$. Unlike the method of Yeh and Cummins [115], the frequency difference is independent of observation angle, due to the 'reference' beam also being frequency shifted. Lebedev et al. [67] described a 'differential Doppler velocity meter' working on the same principle.

Consideration of superposition of the waves in the measurement volume, shows that a pattern of fringes are present; caused by the contributions from the two beams being alternately in, and out of phase. The phase difference between the waves can be caused by the path length to each source changing by a dissimilar amount along the direction of particle movement; as is the case illustrated in Figure 1.3(b) with $k_1 = k_3$. If the wavelengths of the source beams are identical, a static fringe pattern occurs; measurements of zero velocity and velocity sign are not possible. Changing the frequency of one of the sources results in a moving fringe pattern, enabling both measurements.

For the case of two matching wavelength beams, the fringe pattern is normal to the bisector of the beams. The fringe spacing according to Tropea et al. [107] is,

$$\delta x = \frac{\lambda_b}{2sin(\Theta/2)} \tag{1.15}$$

with the beam wavelength, $\lambda_b$; and the angle between the beams, $\Theta$. The fringe intensity and number of fringes is not constant over the measurement volume: as the beams enter and exit the measurement volume, few fringes are present; more fringes are present in the centre of the volume. This results in different numbers of fringe 'pulses' for particles crossing at different parts of the measurement volume.

Uncertainty in the Doppler frequency was considered by Rudd [91] to be due to two equivalent effects. First, that the measurements are performed with optics of finite aperture, and therefore over a range of angles. Uncertainty in the angle results in uncertainty in the frequency. The second, using the fringe model, is due to the number of fringes crossed being finite; the fewer the fringes, the larger the uncertainty.

Hanson [48] showed how further complication results from the beams being Gaussian, rather than ideal; these beams showing a Gaussian intensity distribution normal to the direction of propagation. The radius of the beam phase fronts tend to infinity at the 'beam waist', and change to being proportional to the distance from the source in the far field. If the beams intersect in the far field region, the interference pattern changes from the parallel fringes displayed by the ideal case, to fringes with a diverging distribution. Particles crossing the region on the source side, will reflect pulses at a higher frequency than those on the far side. Beam intersection before the waist reverses the effect, and intersection at the waist results in ideal behaviour. If a focussing lens is used, and the beam intersection occurs on the focal plane of the lens, the resultant broadening is claimed to equal that caused by the finite transit time. Inaccurate alignment can cause 'serious' additional broadening.

Lebedev et al. [67] described the use of a differential Doppler velocity meter, with flow seeding by polystyrene particles of diameter, $d = 0.5\,\mu m$ in water. The system reportedly measured time-mean velocities in the range $0.5\,mm \sim 50\,ms^{-1}$, and was used to measure flow velocities in a vortex chamber of $6\,cm$ diameter.

A similar apparatus was used to investigate supersonic flow by Pfeifer et al. [83], up to $v = 500\,ms^{-1}$. The intensity distribution perpendicular to the laser beams was considered

Gaussian, with ten fringes with a fringe spacing of $100\,\mu m$; the measurement length being $1\,mm$. A lens was used to contract the measurement region to $200\,\mu m$. Flow seeding was achieved with dust and tobacco smoke, considered to be of particle diameter less than $0.3\,\mu m$. The fringe spacing and the mean period of groups of oscillations were used to derive the particulate velocities. The authors claim that during measurement, a deviation from the mean of less than 1% occurred for all samples.

### Laser Transit Anemometry

Thompson [103] described a system in which the scattered signal from particles crossing two laser beams was detected; the time delay between signals and the distance between the beams was used to determine velocity. The beams were focussed to generate a position of maximum intensity along the beam length; defining the measurement position. The receiving optics rejected direct illumination and accepted scattered light, by accepting light falling into a range of scatter angles; the divergence angle of the beam defining the lower limit, and the angle of the first scattering minima defining the upper limit.

The scattering particles were naturally occurring in a wind-tunnel. Errors due to timing inaccuracy and beam position were estimated to be less than 3%; the remaining differences between velocity measured using Pitot-static equipment and the LTA were associated with the difference between the particle velocity and the flow velocity. A lower limit to measurements of $0.3\,ms^{-1}$ was estimated, the limit caused by Brownian motion and vertical motion (normal to the major velocity component) due to gravity. An upper limit was estimated as $200\,ms^{-1}$.

Tropea et al. [107] reported that turbulence intensities greater than 10% result in the path of the particle being significantly affected; the odds of a particle passing through both beams become very low. In spite of this, its high signal-to-noise ratio resulting from the highly focused beams result in its continued use; of particular relevance is its use in long-range wind speed analysis.

She and Kelly [94] reported measurements made at a distance of $500\,m$ at night, using LTA and LDA with naturally occurring aerosols, but the data occurred only once every $100 \sim 500\,s$. For success, 'photon burst correlation' analysis over time was required, as the measurement region was observed by a single device: the photon count over a given time frame was correlated with previous frames, strong correlation indicating a time difference which when used with the beam separation, can be used to derive velocity. Results show the LTA experiments generated single correlation peaks, while LDA experiments showed regular sets of peaks (as the particles pass through the fringes). The signal to noise ratios presented for the LTA measurements were approximately five times better than the LDA results, the latter using double the power.

An alternative method reported by Tropea et al. [107] used two observation devices; one for each beam. Separate 'start' and 'stop' times were recorded, as light pulses were scattered by the two beams. $dt$ versus frequency calculations can be used to generate distribution data; results were reported to show a Gaussian distribution, the peak of the plot showing

the flow velocity. If the plane the beams are in was rotated, a two-dimensional probability histogram could be generated, giving information about a second component of the flow velocity. Noise levels were increased by reflections from surfaces, flow turbulence and beam separation but low turbulence flows ($< 5\%$) were able to generate high accuracy results: measurement errors of $< 1\%$ flow magnitude and $< 0.2^o$ flow direction were claimed.

Advantages of the method include: the ability to measure remote wind speed and a reduced need to seed the flow compared to laser Doppler and particle image velocimetry methods. The method can require high-power laser equipment, however, and as a result can be expensive, and the equipment delicate.

### Particle image velocimetry

Tropea et al. [107] describes particle image velocimetry as using a laser sheet to illuminate nominally isotropically seeded particles in a flow. Pairs of images are recorded (referred to here, as frames $A$ and $B$), with a small time step between them. Each frame is split into smaller sub-domains ($A$ is split into $a_n$ and $B$ into $b_n$, where $n$ is an index), and correlation techniques are used to calculate a displacement value for each sub-domain. One method considers the distance from each particle in $a_n$ to each particle in $b_n$, the most frequently occurring distance being used as the distance for that sub-domain.

The duration of each illumination should be short enough for the moving points to appear point-like, rather than as streaks; this sets a limit on the pulse duration that is related to the velocities expected. Daichin [24] reported that the time-step and sub-domain size should be selected so that the probability of particles moving out of the sub-domain is low; that the particle count is at least exceeding ten; and so that the domain is small enough to resolve the structures of interest. Best results considering spatial resolution, error ratios and computation times were achieved when using windows sixteen pixels wide by sixteen pixels high, with a 50% overlap. This 50% overlap is reported to be the most common.

The use of a single camera results in information in the plane of the sheet being available. According to Prasad [85], through plane information can be retrieved if a second camera is used. This results in new information becoming available, including the out of plane vorticity.

Westerweel [113] reported that a velocity bias exists, resulting in the sub-domains reporting displacements approximately 0.1 pixels too small, for a square window of width 32 pixels. A compensation method was proposed to eliminate the bias.

Particle Image Velocimetry has been used with both high speed flow (for example, by Scarano [92]) and with low speed flow by Browne et al. [14]. PIV values for maximum turbulent shear stress have been observed to be lower than those from Laser Doppler Anemometry measurements by Westerweel [113]; possibly linked to the velocity bias previously mentioned.

An interesting development in PIV is the distribution of reference images generated by numerical simulation; enabling research in image processing to progress without the

researchers having access to PIV hardware, and providing absolute measures of algorithm accuracy. Both two-dimensional (Okamoto et al. [77]) and three-dimensional (Okamoto et al. [78]) data is available.

Advantages of the method include: the generation of instantaneous velocity data over a plane; measurements that do not interfere with the flow; and the availability of through plane data. The method is particularly suited to generation of data for comparison with computational fluid dynamics results, as topological detail over a plane is available. Due to the image being split into smaller regions, the analysis is amenable to parallel processing. However, the flow requires seeding, so a controlled environment is required and the hardware is expensive. Outside of the laboratory, application of PIV seems unlikely in the near future.

### Planar Doppler velocimetry / Doppler Global Velocimetry

Molecular filters are available which display absorption coefficients that depend on the wavelength of radiation passing though them. These filters display 'stop bands': ranges of wavelengths that are largely absorbed. The transition from stop band to pass band is not immediate, but occurs over a range of wavelengths. Observing monochromatic light through such a filter, can result in a fraction of the light being absorbed. Changing the wavelength of the light, can then change this fraction. If a beam of monochromatic light is passed through a moving medium containing particles capable of scattering the light, the light can be Doppler shifted, providing a change to the wavelength. Viewing the scattered light through a molecular filter can then result in the fraction of light absorbed changing, depending on the velocity of the particles; a camera can be used to record the intensity for computer processing and velocity can be calculated from the changes of intensity. Line measurements can be made by observing the transmitted intensity along the length of the beam. Alternatively, point measurements can be made by focussing the beam, or a cylindrical lens can be used to generate an illuminated plane. Fluctuations in illumination intensity over the measurement region can be compensated for by the use of a second, unfiltered camera to generate reference intensity data for each observation position.

For a point observation, the observed velocity component is that which is normal to the bisector of the beam, and the line from the camera to the observed point. This is illustrated in Figure 1.4, from Müller et al. [76].

Cameras at different positions will observe different components of the flow velocity, enabling multiple velocity components to be measured. The system is sensitive to changes in the source wavelength, but Tropea et al. [107] reported that if a laser beam is used, the beam wavelength can be adjusted through the use of an etalon. This enables the system to be tuned half way across a stop / pass band transition for maximum bandwidth, and provides a means to compensate for wavelength changes due to hardware temperature fluctuations. Further bandwidth adjustment is available though the use of molecular filters with different vapour pressures.

According to Morrison and Gaharan [74], errors using this system can be as high as

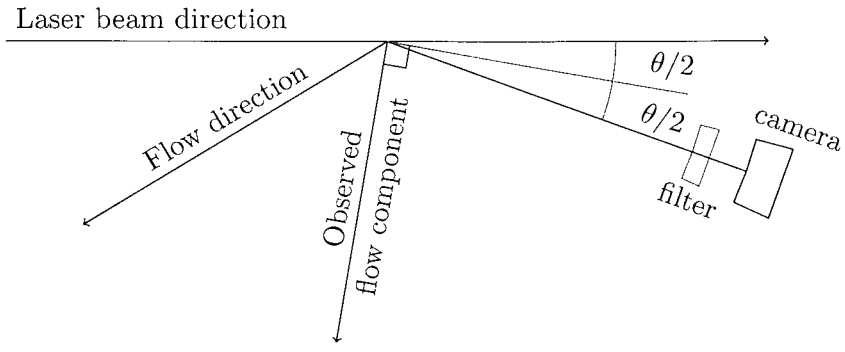



Figure 1.4: The relationship between beam direction, observation position and component of the flow velocity observed.

$u = \pm 19.9\, ms^{-1}$ for flows with large changes of velocity with position, close to boundaries for example. This is partially due to misalignment between the reference and signal cameras. Fischer et al. [30] reported that these errors can be avoided using the frequency modulation Doppler Global Velocimetry method. This approach involves modulation of the laser beam frequency with a second frequency, and comparison of the amplitudes of the fundamental oscillation and the second harmonic. Harmonics of the fundamental are present due to the non-linear change of amplitude with frequency, displayed by the filter. As the velocity of the scattering particles changes, the central frequency shifts, changing the relative amounts of fundamental and second harmonic. Spatial fluctuations of intensity (as scaled out by the reference camera) affect the fundamental and second harmonic equally and can therefore be removed, without the second camera. A measurement range of $u = \pm 240\, ms^{-1}$ was claimed, with the possibility of further extension by changing the observation angle. Uncertainties an order of magnitude lower than conventional DGV were claimed. Low speed flows of the order of $5\, ms^{-1}$ were measured to minimum standard deviations of $0.04\, ms^{-1}$. Modulation frequencies up to $f = 80\, kHz$ were used, this setting the temporal limit of the measurement according to the time taken for one modulation cycle.

The method was extended by Müller et al. [76] to measure a plane, with the use of digital photography. With four images per modulation cycle, the authors claim the second harmonic was resolvable. Camera limitations set the temporal resolution to $0.3\, s$. Measurements conducted over $180\, s$ resulted in standard deviations of $0.1\, ms^{-1}$ per pixel, and $0.02\, ms^{-1}$ when using a twenty by twenty pixel grid, when measuring the region of a rotating disk showing a velocity of $18\, ms^{-1}$.

### 1.1.4 Acoustic anemometry

#### Sonic Anemometry-Thermometry

Sonic Anemometer-Thermometers (SATs) measure the time taken for an acoustic signal to travel a known distance; the mean velocity along this path can then be calculated. According to Tropea et al. [107], two forms exist: the pulse, and the continuous wave; most commercial devices today, use the pulse method.

A continuous wave device is described by Kaimal and Businger [60], consisting of a pair of transmit/receive transducers, spatially separated. The two transmitters radiate continuously, and the radiated frequencies are not harmonically related. Under still conditions, the signals are represented as travelling directly between the units. Figure 1.5 illustrates the effect of flow on the signal path, from Kaimal and Businger [60].

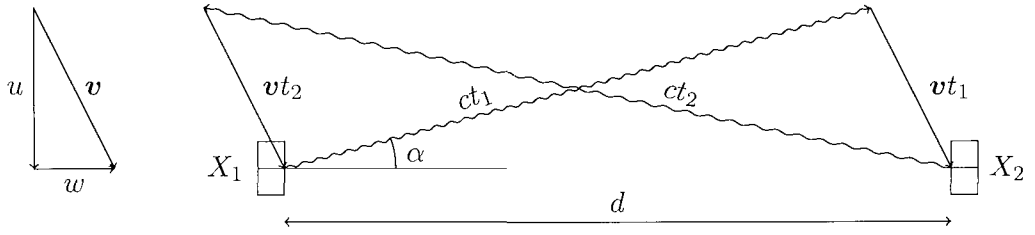



Figure 1.5: Diagram illustrating the operation of a Sonic Anemometer / Thermometer. $X_1$ and $X_2$ are transducers. The wind vector, $\boldsymbol{v}$ and its components, are shown on the far left.

The times taken for the signal to transfer, are $t_1$ and $t_2$. The distances travelled in this time are marked as products of velocity and time. It can be shown that,

$$t_1 = \frac{d}{ccos\alpha + w} \qquad t_2 = \frac{d}{ccos\alpha - w} \tag{1.16}$$

with $d$, the separation between units; $c$, the celerity; and $\alpha$, the angle of deviation caused by the flow. Considering that $sin\alpha = u/c$, and that $cos^2\alpha = 1 - sin^2\alpha$, the difference and sum of transit times can be calculated as,

$$t_2 - t_1 = \frac{2dw}{c^2 - v^2} \tag{1.17}$$

$$t_2 + t_1 = \frac{2dccos\alpha}{c^2 - v^2} \tag{1.18}$$

Equation 1.17 depends on the flow component in-line with the transducers, while Equation 1.18 does not; Equation 1.18 is used to derive the 'acoustic temperature', a value for the temperature of the medium derived from the celerity: this is discussed in more detail, shortly.

According to Coppin and Taylor [20], Tropea et al. [107], when $v \ll c$, Equation 1.17 becomes,

$$w = \frac{c^2}{2d}(t_2 - t_1) \tag{1.19}$$

yielding the flow component along the measurement direction. $c$ is calculated as,

$$c = 20.067\sqrt{T(1 + 0.32\frac{e}{p})} \tag{1.20}$$

with the absolute temperature, $T$; the vapour pressure of water, $e$; and the atmospheric pressure, $p$. Coppin and Taylor [20] reports that instruments based on this method will show drift due to changing environmental factors. Kaimal and Businger [60] separates the mean and the fluctuating variables in Equations 1.17, 1.18 and 1.20, neglects higher order terms, and derives an expression for the phase difference and sum at the two receivers: the phase difference yielding the in-line velocity component and the sum yielding the temperature.

The temperature measurement shows the largest possibility for error to be related to the humidity and velocity normal to the measurement direction. Normal velocity errors vary almost quadratically with velocity: low velocities show small errors (0.2% for $u = 1\,ms^{-1}$) but higher velocities show larger errors.

A simpler calculation is presented by Tropea et al. [107], using the time-inverses. In this case, the difference of the inverses immediately yields the in-line velocity:

$$\frac{1}{t_1} - \frac{1}{t_2} = \frac{c\,cos\alpha + w - c\,cos\alpha + w}{d} = \frac{2w}{d} \tag{1.21}$$

Furthermore, if the velocity normal to the measurement direction is known, the celerity can be solved for:

$$\left(\frac{1}{t_1} + \frac{1}{t_2}\right)^2 = \frac{4c^2}{d^2} cos^2\alpha = \frac{4c^2}{d^2}\left(1 - \frac{u^2}{c^2}\right) \tag{1.22}$$

$$c^2 = \frac{d^2}{4}\left(\frac{1}{t_1} + \frac{1}{t_2}\right)^2 + u^2 \tag{1.23}$$

Tropea et al. [107] defines the virtual temperature, $T_V = T(1 + 0.32e/p)$ and $C_T = 403m^2/s^2K$, and re-writes Equation 1.20 as,

$$\begin{aligned} C^2 &= C_T T\left(1 + 0.32\frac{e}{p}\right) \\ &= C_T T_V \end{aligned} \tag{1.24}$$

stating the virtual temperature can be calculated as,

$$T_V = \frac{d^2}{4C_T}\left(\frac{1}{t_1} + \frac{1}{t_2}\right)^2 + \frac{w^2}{403} \tag{1.25}$$

Schotanus et al. [93] uses Equations 1.26 and 1.27 to derive the acoustic temperature given by Equation 1.28:

$$\frac{1}{t_1} + \frac{1}{t_2} = \frac{2ccos\alpha}{d} \tag{1.26}$$

$$c^2 = \gamma RT(1 + 0.51q) \tag{1.27}$$

$$T_s = \frac{d^2}{4\gamma R}\left(\frac{1}{t_1} + \frac{1}{t_2}\right)^2 \tag{1.28}$$

with the specific humidity, $q$; $\gamma R = 403\,m^2 s^{-2} K^{-1}$ for air; the deviation of path, $\alpha$. This shows the relationship between celerity, temperature and humidity, and that the sum of the reciprocals of the transit times can be used to estimate temperature.

Schotanus et al. [93] showed that the temperature fluctuation, $T'$ is only measured when normal velocity and humidity fluctuations are zero: by separating the components of Equations 1.26, 1.27, 1.28 into mean and fluctuating parts, using a first order Taylor expansion, and $cos\alpha = \sqrt{1 - v_n^2/c^2}$. Equations 1.29 and 1.30 were derived, Equation 1.30 showing the dependence of $T'$ on the humidity fluctuation $q'$; and the normal velocity fluctuation, $v_n'$.

$$\bar{T}_s = \bar{T}(1 + 0.51\bar{q}) \tag{1.29}$$

$$T_s' = T' + 0.51 q' \bar{T} - \frac{2\bar{T}}{c^2} \bar{v_n} v_n' \tag{1.30}$$

Shuttleworth et al. [95] compensated for the phase change caused by the imperfect response of the transducers, and the difference in response between different transducers. The difference in the time taken for the signal to travel in the two directions was used to calculate velocity. The sum was used to determine the phase difference caused by the transducers; this result was used to adjust the phase of the transmitted signal during subsequent measurements. Comparison of measurements were made with commercial acoustic anemometers, the prototype showing increased noise in zero flow; comparable drift of wind speed; and good agreement for eddy correlation fluxes. This method appears to reduce the need for using matched transducer pairs.

Coppin and Taylor [20] reported that by replacing the separate loudspeaker / microphone objects with a single device capable of both functions, errors caused by misalignment are reduced. Furthermore, rather than inspecting phase difference, time of flight can be directly measured, and used with Equation 1.21. A prototype using this approach, with a $10\,cm$ path-length showed invariant behaviour over several months; a velocity range of $u = \pm 20 ms^{-1}$; a resolution of $\pm 0.6\,cms^{-1}$; and a maximum measurement frequency of approximately $10\,Hz$. This device used a thermistor for temperature measurement, rather than calculating the acoustic temperature.

Schotanus et al. [93] extended the use of the sonic anemometer to include measurement of heat and moisture fluxes; reporting that the temperature generated by sonic anemometers was rarely used. Temperature variance and humidity were measured with other methods and the results showed excellent agreement with those gained using a sonic anemometer. A method for calculating heat and moisture flux using the acoustic temperature was presented, with 'acceptable' results being generated.

A sonic anemometer measuring vorticity was presented by Mitsuata and Asai [73], consisting

of three, one-dimensional anemometers forming a triangle in the vertical plane: the vortex axis passing through the triangle. A path length of $l = 20\,cm$ and a frequency of $f = 100\,kHz$, resulted in a measurement rate of $400\,Hz$. Rather than using the rise of the observed signal to estimate the arrival time of the pulse, the zero crossing of the third cycle was used. Errors caused by factors resulting in a change of amplitude were therefore reduced, the increased accuracy giving a claimed minimum resolution of $0.5\,mms^{-1}$. The vorticity was calculated as,

$$\eta = \frac{C}{S} = \frac{u_1 l_1 + u_2 l_2 + u_3 l_3}{S} \tag{1.31}$$

with the vorticity, $\eta$; the circulation, $C$; the area of the triangle, $S$; the three length components, $l_i$; and the three velocity components, $u_i$. Additionally, formulas for the vertical and one of the horizontal velocities were specified. Measurements were not compared with results using other measurement methods, but the power spectra for velocity and vorticity were reported as displaying behaviour close to that expected.

Horst and Oncley [55] examined the errors caused by path averaging in commercial sonic anemometers; Figure 1.6 shows one of the test subjects. Errors in velocity spectra and sonic temperature were considered. Horizontal spectra were attenuated more than vertical; considered due to the differing projected path lengths in these directions. Most of the experiments showed little dependence on flow angle around the nominally vertical axis, due to the partial symmetry of the devices around this axis. Acoustic temperature spectra showed stronger attenuation with wavenumber than velocity spectra, but the attenuation was largely independent of angle around the vertical axis.

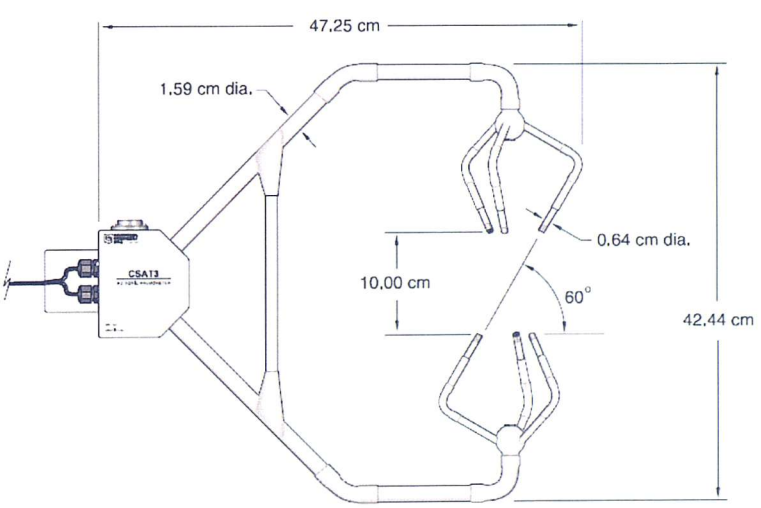



Figure 1.6: Diagram of the CSAT3 acoustic anemometer available from Campbell Scientific Incorporated. Reproduced with kind permission.

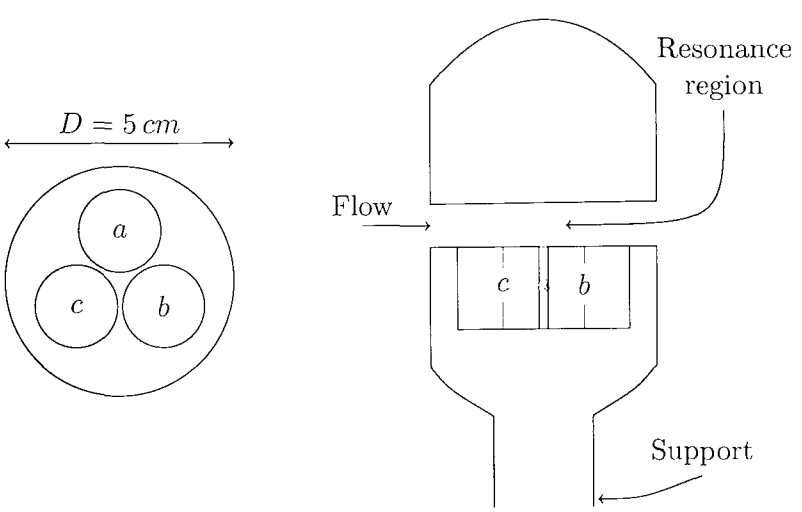
According to Gil [44], the Gill, 'Extreme Weather WindObserver' has an operating range of $0.01\,ms^{-1} \sim 75\,ms^{-1}$, a resolution of $0.01\,ms^{-1}$, an accuracy of $\pm 2\%$ at $12\,ms^{-1}$, generates velocity in a single plane, and has internal heating to reduce the chance of ice build up. It generates up to four measurements per second. Its uses include wind-turbine control,

aircraft landing systems, meteorological monitoring and structural safety. Prices for acoustic anemometers generating two-dimensional results are in the region of $1500 according to YoungUSA [90]. Devices generating three-dimensional results start at $2500. The lack of moving parts results in reduced maintenance requirements, making them popular in meteorological studies. The calculation of acoustic temperature reduces the requirement for extra temperature monitoring hardware, and allows for the calculation of thermal flux.

### Acoustic resonance anemometry

The acoustic resonance anemometer, invented by Savvas Kapartis of FT Technologies, measures the flow induced phase changes of an acoustic resonance in a duct. Referring to Figure 1.7, the acoustic wavelength is such that the duct resonance perpendicular to the flow is excited. One of the acoustic transducers is used to excite an acoustic resonance, while the phase at a different transducer is inspected. The operation of the two transducers is reversed, and the difference in phase is used to calculate the flow velocity component, in line with the transducer pair.

A third transducer on the same duct face, displaced in the direction normal to the line joining the first two, can be used to determine the flow component in a second direction. Angular resolution better than $\pm 2$ degrees, with velocities up to $100ms^{-1}$ is possible with commercial devices. Magnitude accuracy of $\pm 0.1ms^{-1}$ can be achieved, according to Kapartis [61]. The lack of moving parts and compact design results in a robust device while the acoustic resonance method reduces the errors caused by environmental factors such as changing temperature and ambient pressure by providing a continuous calibration process. Observing the phase at resonance results in an improved signal to noise ratio than would occur at other measurement frequencies, and linearises the relationship between flow velocity and phase.




(a) Top view, showing transducers $a$, $b$, $c$.

(b) Side view.

Figure 1.7: Scale diagram of an acoustic resonance anemometer.

## 1.2 Numerical simulation

The acoustic resonance anemometer operates by examining flow induced changes of the acoustic field, at resonance. Measurements of an existing device have been made during this project, but most of the work was focussed on simulation of the convected acoustic field, and of the flow in and around the anemometer. In particular, the convected acoustic field has been simulated using a finite element solver created for the project. This section introduces the principles used by the simulations, and considers some related work from the literature.

### 1.2.1 General approach

The Navier-Stokes equations are partial differential equations describing fluid behaviour. Direct solution of the equations is possible, using the Direct Numerical Simulation (DNS) approach. The method resolves the passage and development of the smallest structures in the flow, responsible for turbulent exchange. As a result, the technique is computationally expensive, and is generally limited to low Reynolds number flow studies. To use the method to simulate acoustics would involve reducing the time-steps used from those related to turbulence and the flow speed, to steps capable of resolving fractions of an acoustic oscillation. For this application, the time-steps would reduce in size by two orders of magnitude. This approach is not feasible with todays computers.

It is possible to consider the components of the Navier-Stokes equations, to consist of a slowly varying, viscous flow, and a high frequency acoustic field. Substituting these components into the Navier-Stokes equations, and applying a low pass filter results in the components linear in the acoustic variables becoming zero, while the quadratic acoustic terms become acoustic stresses. These stress terms will be extremely small compared to the low frequency components. The acoustic field, therefore, has little effect on the low-frequency field; the low-frequency field can be considered in isolation of the acoustic field. Solution of this low-frequency field is the subject of a following section.

The terms subtracted from the low-frequency field can be manipulated to generate the convected acoustic field; it cannot be considered in isolation of the low frequency component and solution of the equation requires knowledge of the convecting velocity field. This approach has been used elsewhere by Tsuji et al. [108], Peat and Rathi [81].

The low-frequency field can be solved with a computational fluid dynamics solver, and used to provide the velocities for the convected acoustic field. The convected acoustic field, described by the convected Helmholtz equation, can then be solved using a convected acoustics solver.

### 1.2.2 Solution approaches

Solution of the equations generated by the approaches outlined above, are usually performed using either the finite difference, finite element, or finite volume methods. According to

Fletcher [31], the finite difference method usually operates with the governing equation in differential form. The discretisation is regular in space, limiting its applicability for real-world simulations. This is unlike the finite volume and finite element methods, both of which can use regular or irregular grids.

The finite element method splits the simulation region into elements, and applies a trial function over each element, weighted so it matches the governing equation as well as possible. Each function has unknowns and the equations over the domain are combined in a set of simultaneous equations. Once the boundary conditions are set, the unknowns can be solved for. The use of irregular grids results in each element being transformed to a unit element; this requirement slows the solution, and storage of the system matrix is demanding on memory. As demonstrated by Zienkiewicz and Taylor [120], Gresho and Sani [47], the popularity of the finite element method for solving fluid dynamics problems is growing; partly due to increased computer capacity. As demonstrated by Peat and Rathi [81], the finite element method can be used to solve the convected acoustic equation.

The finite volume method integrates the flux passing through the surface of a control volume, to solve the governing equation in integral form: this is documented by Fletcher [31]. It is conservative, in that the fluxes passing through adjacent cell walls are matched. Irregular meshes do not require the cells to be spatially transformed, unlike the finite element method: this difference contributes to the lower computational requirement of the finite volume approach.

The commercial CFD solver, FLUENT, uses the finite volume method, and the method is described in more detail in Chapter 4.

### 1.2.3 Simulation of a convected acoustic field

The convected Helmholtz equation has been used to represent convected acoustic behaviour in automotive exhausts by Peat and Rathi [81], Tsuji et al. [108], with axisymmetric analyses. In these cases, moderate flow speeds of $M = 0.3$ were used, resulting in square Mach number terms in the convected Helmholtz equation being of similar significance to the linear Mach terms: they were therefore retained. A finite element solver was used to solve the equation in the interest region.

Transient acoustic processes in low-Mach-number shear flow have been considered by Wang and Kassoy [111], using a linearised wave equation for acoustic propagation in fully developed duct flow. The equation was solved analytically. A plane source was used across the duct cross section. The fully developed shear flow was found to diffract the planar acoustic disturbance, so that oblique waves were generated: these oblique waves were able to excite modes across the duct. The thin acoustic boundary layer was examined, and nonlinear effects and acoustic streaming were found to be negligibly small in the first few acoustic wavelengths. The work was extended by Wang and Kassoy [110] to different flow profiles, the authors finding that for slug flow parallel to the duct walls, acoustic modes normal to the flow direction were not excited.

Discrete Huygens' modelling has been used by Kagawa et al. [59] to simulate acoustic propagation through a medium displaying a propagation speed dependent on propagation direction, and for propagation speed depending on position. The former case occurs for propagation through mean flow, the latter for propagation in the ocean. The field was modelled using a network of 'acoustic tubes', connected at nodes. Impulse scattering occurs as a result of the impedance change occurring as the impulse passes from a connecting tube of a given impedance, to the node at the tube end which being connected to several tubes, has a different impedance. The authors compared their solution with that of a finite difference calculation, claiming a mesh ten times as fine was required to get the same fidelity of results.

The effect of temperature gradients as high as $100°C/mm$, on acoustics with flow has been considered by Peat and Kirby [82], again with application to automotive exhausts. This steep gradient resulted in previous analyses, which assumed isentropy, to show sound pressure errors as high as $50\,dB/m$. The analysis presented assumes flow Mach numbers up to $M = 0.3$, and acoustic frequencies from $0\,Hz$ to $2\,kHz$.

An interesting approach to modelling acoustics in flow, is to alter the boundary conditions applied to the non convected Helmholtz equation. The acoustic pressure distribution along a closed end duct, with Mach numbers up to $M = 0.3$ and excitation frequency of $f = 2\,kHz$ has been generated using this approach, by Tsuji et al. [108]. Good agreement has been demonstrated between analytical solutions, and finite element solutions of both the convected wave equation, and the non-convected wave equation with modified boundary conditions.

### Boundary conditions for the acoustic field

The finite element method has been adopted during this project, to solve the convected Helmholtz equation in, and around the region of interest: the acoustic duct. While the finite element method can handle arbitrary geometries and finite regions, special boundary conditions are required to simulate the infinite region. For time varying solutions, the boundary to the infinite region becomes particularly important when an interaction at the boundary occurs. For steady state solutions, the boundary conditions are always important. If the system matrices are not adjusted at a boundary, $\partial p/\partial n = 0$ occurs: the result is a hard, reflective surface. If the boundary is attempting to represent the interface between a finite, and an infinite region, adjustment is required.

One approach is to apply a 'quiet' boundary at the edge of the finite element region, as used by Tsuji et al. [108]. This consists of an impedance such as would be found at the boundary if the finite region were extended. Waves travelling normally to the boundary are not reflected. The boundary results in modification to the system matrices, but their sparse nature is preserved. Pressures outside the finite region are not generated.

Infinite elements, as described by Bettess [10], retain information about the infinite region and preserve the sparsity of the system matrices. The formulation involves the use of finite elements, with shape functions decaying with distance from the surface they are applied to,

the shape function extending to infinity. When used, only the surface of application and some positions a finite distance into the infinite region are specified. The decaying shape function can have an oscillatory nature, as would be expected to form in some acoustic simulations.

An alternative approach is to use a boundary element at the interface. Its use changes the system matrices from being sparse, to being dense. This increases the storage requirements but the pressure field outside the boundary element is available. This method has been used with success by Zhang et al. [118], applying the boundary element in the uniform flow region while finite elements were used to simulate behaviour in the non-uniform region. Results for the quiet boundary and boundary element terminations were found to be comparable. Tsuji et al. [108] also compared results gained using quiet boundary with those from a boundary element, and found some difference at resonance. This may have been due to their quiet boundary formulation assuming a constant speed of sound, instead of accounting for the flow speed in their calculation of impedance.

The quiet boundary formulation has been adopted in this project, as a termination approximating the infinite region is required at the ends of the acoustic duct, but the acoustic behaviour beyond the boundary is not of interest. The formulation is discussed further in Chapter 2.

### Sources of error

Solution of the convected Helmholtz equation using the finite element method, results in errors as the element edges are an approximate fit to the shape of the field. Higher order elements can represent a more complex field variation across the element length, and the size of the elements defines how much of the field variation is to be approximated across each element. Element order and size are picked, depending on the smallest wavelengths of interest. According to Gabard et al. [38], the dispersion error for a regular mesh can be defined as a measure of the wavenumber error per wavelength, and varies as

$$E_d \sim C(kh)^{2p} \tag{1.32}$$

where $E_d$ is the error; $C$ is a constant; $k$ is the wavenumber; $h$ is the internodal distance; and $p$ is the element order. The $kh$ product equals the number of radians between each node. For $kh < 1$, increasing the element order reduces the dispersion error. Increasing the resolution of the mesh reduces $h$ and therefore also reduces the dispersion error. Errors of approximately 2% per wavelength were found for upstream propagation for the first order element, with ten elements per wavelength. Increasing the flow rate increased the error. Downstream propagation showed a decreasing error as the flow speed increased, but the change was small and the error similar to the upstream case for $M = 0.3$ with the same mesh.

### 1.2.4 Simulation of the viscous flow

The Navier-Stokes equations are partial differential equations describing fluid behaviour. As mentioned above, direct solution of the equations is possible, using the Direct Numerical Simulation (DNS) approach. The method resolves the passage and development of the smallest structures in the flow, responsible for turbulent exchange. As a result, the technique is computationally expensive, and is generally limited to low Reynolds number flow studies.

The Large Eddy Simulation (LES) method models the smallest structures with a turbulence model. The physical size of the structures to be modelled in this way is set by the mesh; structures smaller than the mesh size are modelled, while those larger than the mesh are resolved. Good agreement between LES and measurement has been demonstrated for circular cylinder simulations at $Re = 3900$ Franke and Frank [36]. Accurate, high Reynolds number simulations require the energetic structures to be resolved, resulting in fine meshes and increased cost. At the Reynolds numbers of interest in this project ($Re > 33 \times 10^3$) this approach was considered too expensive.

It has been shown by Singer et al. [96] that if the flow variables in the Navier-Stokes equations are replaced with mean and fluctuating components, and a mean taken of the new expression, linear fluctuating terms average to zero: the Reynolds Average Navier-Stokes (RANS) equations result. They contain an extra term when compared with the Navier-Stokes equation: a term representing the turbulence, based on the Reynolds stresses. The turbulence is no longer resolved, so the mesh no longer needs to be fine enough to resolve the time and length scales associated with the turbulence: the mesh now resolves only boundary related structures, while the turbulence is modelled with an approximation. The result is a drastic reduction in the computing power required to perform simulations. The turbulence model used depends on several factors including the Reynolds number range of interest; the boundary conditions (defining objects in the flow); the required accuracy; the computational power available; and for the case of iterative solvers, whether a converged solution can be generated at all. At this time, more than four turbulence models are available.

The Reynolds averaged Navier-Stokes solution is steady, due to the averaging performed during formulation. An unsteady formulation (URANS), is possible in which the small scale turbulence is still modelled using the aforementioned method, but the large scale, low frequency unsteadiness (such as the vortices shed by bluff bodies) is to some extent, resolved. This is achieved by introducing a new time-scale into the previously mentioned fluctuating component: the fluctuating component is replaced with a slowly and a rapidly fluctuating component. The slowly fluctuating component is resolved, and the rapidly fluctuating component is modelled.

Results from mean URANS and RANS simulations do not always agree. In particular, simulations of circular cylinders in the diameter based, sub-critical Reynolds number range show large differences in the base pressures calculated with mean URANS data, and RANS data. This effect is demonstrated in Chapter 4, and has been demonstrated during the simulation of the unsteady flow around a square cylinder by Iaccarino et al. [57] at

$Re = 22 \times 10^3$. The time step size for URANS simulations is partly determined by the boundary conditions: simulations of the shedding from circular cylinders have used as few as 50 time steps per shedding cycle by Iaccarino et al. [57]. The size of the time-step affects which flow structures are resolved and which are modelled: studies in solution convergence with varying time-step size can therefore be necessary.

The Detached Eddy Simulation (DES) method, uses the Large Eddy Simulation approach in the regions away from walls, and uses the URANS method in the viscosity dominated regions close to the walls. It has been referred to as an LES/RANS coupling model by Fluent [33]. Accuracy of results relies partly on the turbulence model adopted by the URANS formulation, and its applicability to the simulation. The Spalart-Allmaras turbulence model is adopted by FLUENT, in the URANS region, according to Singer et al. [96]. Good agreement for pressure coefficient over a sphere has been demonstrated between measurement and simulation, for $Re \approx 1 \times 10^6$ by Squires [99]. DES simulations are reported to be between URANS and LES simulations, in terms of expense.

While data for two-dimensional circular cylinder simulations in the sub-critical Reynolds number range are available, simulations of three-dimensional circular cylinders of $l/D \approx 2$ were not found. Measurements of such an object have been made by Zdravkovich et al. [117], the results showing that flow over the ends of the cylinder was important: the observed Strouhal number was no longer constant, but varied during measurement between $S_t \approx 0.19 \sim 0.24$. The flow around the cylinder at diameter based Reynolds numbers in the sub-critical range, was found not to be steady, but to vary periodically.

While the results from Zdravkovich et al. [117] are useful for comparison with measurements and simulations of the acoustic resonant anemometer with its resonant duct blocked, no data from the literature could be found for the case of the acoustic duct being left open. For this reason, numerical experimentation was performed during this project, to establish important simulation parameters. Equally, the lack of relevant measurement data available, has prompted sets of measurements to be performed.

## 1.3 Thesis layout

The aim of this thesis was to understand the operation of an acoustic resonance anemometer. To this end, the thesis has been split into chapters, as follow:

- Chapter 2 describes the theory used to simulate the anemometer.
- Chapter 3 describes the measurements made to characterise the flow around and through an anemometer, as presents acoustic measurements made with a working device, as this information was not available from the literature.
- Chapter 4 describes simulations of the low-frequency viscous flow around a two-dimensional cylinder of width matching the tested anemometer, to establish convergence criteria. These data were then used with three-dimensional simulations, to examine the flow around, and through an anemometer. The commercial CFD code FLUENT was used during the analysis.

- Chapter 5 describes the simulation of the high frequency, convected acoustic field in the resonant acoustic duct passing through the anemometer body. The working principles of the acoustic resonance anemometer are established. The finite element solver created for the project was used for most of this work.
- Chapter 6 presents conclusions from the work, with suggestions for future research.

# 2 Theory

This chapter shows how the Navier-Stokes equations can be used to derive separate equations for the incident incompressible viscous flow about the anemometer body and the compressible inviscid linearised acoustic field which is subject to convection effects by the incident flow. The solution method for the convected acoustic field is then discussed. For brevity, the viscous flow field will be referred to as 'low frequency' component, and the inviscid acoustic field will be referred to as the 'high frequency' component.

## 2.1 Introduction

The Navier-Stokes equations in compressible and unsteady form have been expressed using tensor notation by Richards and Mead [87] as,

$$\frac{\partial \rho}{\partial t} + \frac{\partial}{\partial x_i}(\rho u_i) = 0 \tag{2.1}$$

$$\frac{\partial}{\partial t}(\rho u_i) + \frac{\partial}{\partial x_j}(\rho u_i u_j) = -\frac{\partial p}{\partial x_i} + \frac{\partial}{\partial x_j}\mu\frac{\partial u_i}{\partial x_j} \tag{2.2}$$

using the density, $\rho$; the velocity components, $u_i$; pressure, $p$; and viscosity, $\mu$. Equation 2.1 is the equation of mass transport and Equation 2.2 is the equation of linear momentum transport.

## 2.2 Division of the flow field.

The flow field can be split into a slowly varying, viscous field and an acoustic field. This approach has been used by others for example, Liow et al. [69] in determining the sound generated by flow past a rectangular cylinder. The process is described in the following sections.

### 2.2.1 Low frequency, viscous field.

The field is divided into two components. The first is associated with the incident flow and is considered to be low frequency - less than $1\,kHz$. The second is the acoustic field and is of a higher frequency, of the order of $40\,kHz$. Thus,

$$\rho = \tilde{\rho} + \rho' \qquad u = \tilde{u} + u' \qquad p = \tilde{p} + p' \tag{2.3}$$

with ˜ indicating low frequency and ′ indicating high frequency. These values can be substituted into the mass and momentum equations above. If expanded and low pass filtering is performed, the terms which are linear in the acoustic component average to zero and can be removed, while those with quadratic acoustic terms may still contribute as acoustic stresses. The process is outlined below.

**Convected conservation of mass.**

The density and velocity expansion described in Equation 2.3 can be substituted into the conservation of mass expression, Equation 2.1. The expression can be expanded and a time mean taken of long duration compared to the high frequency period but of short duration compared to the low frequency component. Components with a single high frequency component will average to zero over this time and can be neglected. Components with products of acoustic terms become very small and can also be neglected.

$$\cancel{\frac{\partial \rho'}{\partial t}} + \frac{\partial \tilde{\rho}}{\partial t} + \rho' \cancel{\frac{\partial \tilde{u}_i}{\partial x_i}} + \rho' \cancel{\frac{\partial u_i'}{\partial x_i}} + \tilde{\rho}\frac{\partial \tilde{u}_i}{\partial x_i} + \tilde{\rho}\cancel{\frac{\partial u_i'}{\partial x_i}} + u_i' \cancel{\frac{\partial \tilde{\rho}}{\partial x_i}} + u_i' \cancel{\frac{\partial \rho'}{\partial x_i}} + \tilde{u}_i \frac{\partial \tilde{\rho}}{\partial x_i} + \tilde{u}_i \cancel{\frac{\partial \rho'}{\partial x_i}} = 0 \tag{2.4}$$

The result is the 'time-mean' conservation of mass.

$$\frac{\partial \tilde{\rho}}{\partial t} + \tilde{\rho}\frac{\partial \tilde{u}_i}{\partial x_i} + \tilde{u}\frac{\partial \tilde{\rho}}{\partial x_i} = 0 \tag{2.5}$$

This result is very similar to Equation 2.1, suggesting that the slowly changing mass conservation expression can be considered separately from the high frequency, acoustic terms.

For low Mach number flow, incompressibility can be assumed. The time and space derivatives of $\tilde{\rho}$ become zero, showing that since $\tilde{\rho} \neq 0$,

$$\frac{\partial \tilde{u}_i}{\partial x_i} = 0 \tag{2.6}$$

Subtracting Equation 2.5 from the expanded form in Equation 2.4, gives the convected conservation of mass.

$$\frac{\partial \rho'}{\partial t} + \rho'\frac{\partial \tilde{u}_i}{\partial x_i} + \rho'\frac{\partial u_i'}{\partial x_i} + \tilde{\rho}\frac{\partial u_i'}{\partial x_i} + u'\frac{\partial \tilde{\rho}}{\partial x_i} + u'\frac{\partial \rho'}{\partial x_i} + \tilde{u}\frac{\partial \rho'}{\partial x_i} = 0 \tag{2.7}$$

If the acoustic quantities are small, their products will be relatively tiny and can be neglected compared to the other terms. Equation 2.7 can be linearised and re-arranged to get:

$$\frac{\partial \rho'}{\partial t} + \tilde{u_i}\frac{\partial \rho'}{\partial x_i} + \rho'\frac{\partial \tilde{u_i}}{\partial x_i} + \tilde{\rho}\frac{\partial u_i'}{\partial x_i} + u_i'\frac{\partial \tilde{\rho}}{\partial x_i} = 0 \tag{2.8}$$

The first two terms group into the convective derivative, where

$$\frac{D}{Dt} \equiv \frac{\partial}{\partial t} + \tilde{u_i}\frac{\partial}{\partial x_i} \tag{2.9}$$

to give

$$\frac{D\rho'}{Dt} + \rho'\frac{\partial \tilde{u_i}}{\partial x_i} + \tilde{\rho}\frac{\partial u_i'}{\partial x_i} + u'\frac{\partial \tilde{\rho}}{\partial x_i} = 0 \tag{2.10}$$

Assuming low Mach number flow, $\tilde{\rho}$ can be taken to be constant. Furthermore, Equation 2.6 can be used. Equation 2.10 becomes

$$\frac{D\rho'}{Dt} + \tilde{\rho}\frac{\partial u_i'}{\partial x_i} = 0 \tag{2.11}$$

Equation 2.11 looks similar to the non-convected conservation of mass expression, but it requires information about the flow velocity, due to the convective derivative.

### Convected conservation of momentum

By a similar process, the conservation of momentum expression can be transformed to the convected conservation of momentum. First, the left hand side of the conservation of momentum equation, Equation 2.2 can be simplified by expanding and substituting the conservation of mass expression (Equation 2.1) as follows.

$$\begin{aligned}
\frac{\partial}{\partial t}(\rho u_i) + \frac{\partial}{\partial x_j}(\rho u_i u_j) &= \frac{\partial \rho}{\partial t}u_i + \rho\frac{\partial u_i}{\partial t} + \frac{\partial \rho}{\partial x_j}u_i u_j + \rho\frac{\partial u_i}{\partial x_j}u_j + \rho u_i\frac{\partial u_j}{\partial x_j} \\
&= u_i\left(\frac{\partial \rho}{\partial t} + u_j\frac{\partial \rho}{\partial x_j} + \rho\frac{\partial u_j}{\partial x_j}\right) + \rho\frac{\partial u_i}{\partial t} + \rho u_j\frac{\partial u_i}{\partial x_j} \\
&= \rho\frac{\partial u_i}{\partial t} + \rho u_j\frac{\partial u_i}{\partial x_j}
\end{aligned} \tag{2.12}$$

The conservation of momentum equation (2.2) can therefore be re-written as,

$$\rho\frac{\partial u_i}{\partial t} + \rho u_j\frac{\partial u_i}{\partial x_j} = -\frac{\partial p}{\partial x_i} + \frac{\partial}{\partial x_j}\mu\frac{\partial u_i}{\partial x_j} \tag{2.13}$$

$\rho$, $u$ and $p$ can be substituted with the expansion of Equation 2.3. If low pass filtering is applied, the single acoustic entries average to zero and can be removed. Higher order acoustic products can be neglected, as they are very small.

From the left hand side of Equation 2.13:

$$\begin{aligned}
\rho\frac{\partial u_i}{\partial t}+\rho u_j\frac{\partial u_i}{\partial x_j} &= (\tilde{\rho}+\rho')\frac{\partial(\tilde{u}_i+u_i')}{\partial t}+(\tilde{\rho}+\rho')(\tilde{u}_j+u_j')\frac{\partial(\tilde{u}_i+u_i')}{\partial x_j}\\
&= \tilde{\rho}\frac{\partial\tilde{u}_i}{\partial t}+\tilde{\rho}\frac{\partial u_i'}{\partial t}+\rho'\frac{\partial\tilde{u}_i}{\partial t}+\rho'\frac{\partial u_i'}{\partial t}\\
&\quad+\tilde{\rho}\tilde{u}_j\frac{\partial\tilde{u}_i}{\partial x_j}+\tilde{\rho}\tilde{u}_j\frac{\partial u_i'}{\partial x_j}+\tilde{\rho}u_j'\frac{\partial\tilde{u}_i}{\partial x_j}+\tilde{\rho}u_j'\frac{\partial u_i'}{\partial x_j}\\
&\quad+\rho'\tilde{u}_j\frac{\partial\tilde{u}_i}{\partial x_j}+\rho'\tilde{u}_j\frac{\partial u_i'}{\partial x_j}+\rho'u_j'\frac{\partial\tilde{u}_i}{\partial x_j}+\rho'u_j'\frac{\partial u_i'}{\partial x_j}\\
&= \tilde{\rho}\frac{\partial\tilde{u}_i}{\partial t}+\rho'\frac{\partial u_i'}{\partial t}+\tilde{\rho}\tilde{u}_j\frac{\partial\tilde{u}_i}{\partial x_j}+\tilde{\rho}u_j'\frac{\partial u_i'}{\partial x_j}\\
&\quad+\rho'\tilde{u}_j\frac{\partial u_i'}{\partial x_j}+\rho'u_j'\frac{\partial\tilde{u}_i}{\partial x_j} \qquad (2.14)\\
&= \tilde{\rho}\frac{\partial\tilde{u}_i}{\partial t}+\tilde{\rho}\tilde{u}_j\frac{\partial\tilde{u}_i}{\partial x_j} \qquad (2.15)
\end{aligned}$$

The right hand side of Equation 2.13 can be considered in the same way.

$$\begin{aligned}
-\frac{\partial p}{\partial x_i}+\frac{\partial}{\partial x_j}\mu\frac{\partial u_i}{\partial x_j} &= -\frac{\partial\tilde{p}}{\partial x_i}-\frac{\partial p'}{\partial x_i}+\frac{\partial}{\partial x_j}\mu\frac{\partial\tilde{u}_i}{\partial x_j}+\frac{\partial}{\partial x_j}\mu\frac{\partial u_i'}{\partial x_j}\\
&= -\frac{\partial\tilde{p}}{\partial x_i}+\frac{\partial}{\partial x_j}\mu\frac{\partial\tilde{u}_i}{\partial x_j} \qquad (2.16)
\end{aligned}$$

showing that,

$$\tilde{\rho}\frac{\partial\tilde{u}_i}{\partial t}+\tilde{\rho}\tilde{u}_j\frac{\partial\tilde{u}_i}{\partial x_j}=-\frac{\partial\tilde{p}}{\partial x_i}+\frac{\partial}{\partial x_j}\mu\frac{\partial\tilde{u}_i}{\partial x_j} \qquad (2.17)$$

Like the conservation of mass equation treatment, this result is of a similar form to the original expression: this equation can be considered in isolation of the high frequency acoustic signals, and solved to generate the low frequency flow field. As was performed with the conservation of mass, this result can be subtracted from the original expanded expression to get the convected conservation of momentum expression.

The terms cancelled previously can be gathered and linearised with respect to acoustic fluctuations.

$$\begin{aligned}
&\tilde{\rho}\frac{\partial u_i'}{\partial t}+\rho'\frac{\partial\tilde{u}_i}{\partial t}+\tilde{\rho}\tilde{u}_j\frac{\partial u_i'}{\partial x_j}+\tilde{\rho}u_j'\frac{\partial\tilde{u}_i}{\partial x_j}\\
&+\rho'\tilde{u}_j\frac{\partial\tilde{u}_i}{\partial x_j}+\rho'u_j'\frac{\partial\tilde{u}_i}{\partial x_j}+\rho'\frac{\partial u_i'}{\partial t}+\tilde{\rho}u_j'\frac{\partial u_i'}{\partial x_j}\\
&+\rho'\tilde{u}_j\frac{\partial u_i'}{\partial x_j}+\rho'u_j'\frac{\partial\tilde{u}_i}{\partial x_j} = -\frac{\partial p'}{\partial x_i}+\frac{\partial}{\partial x_j}\mu\frac{\partial u_i'}{\partial x_j} \qquad (2.18)
\end{aligned}$$

Since the viscosity, $\mu \ll 1$, the contribution from the viscosity term is much smaller than

that of the pressure term except in the acoustic boundary layers on the walls. These terms are neglected in acoustics since the oscillatory acoustic boundary layers are very thin. The through boundary layer pressure gradient is small so that the wall pressures are approximately equal to the pressures just outside the boundary layers in the inviscid region. If it is neglected, the convected momentum expression becomes,

$$\tilde{\rho}\frac{\partial u_i'}{\partial t} + \rho'\frac{\partial \tilde{u}_i}{\partial t} + \tilde{\rho}\tilde{u}_j\frac{\partial u_i'}{\partial x_j} + \tilde{\rho}u_j'\frac{\partial \tilde{u}_i}{\partial x_j} + \rho'\tilde{u}_j\frac{\partial \tilde{u}_i}{\partial x_j} = -\frac{\partial p'}{\partial x_i} \tag{2.19}$$

Grouping into $D/Dt$ terms,

$$\begin{aligned}\tilde{\rho}\left(\frac{\partial u_i'}{\partial t} + \tilde{u}_j\frac{\partial u_i'}{\partial x_j}\right) + \rho'\left(\frac{\partial \tilde{u}_i}{\partial t} + \tilde{u}_j\frac{\partial \tilde{u}_i}{\partial x_j}\right) + \tilde{\rho}u_j'\frac{\partial \tilde{u}_i}{\partial x_j} &= \\ \tilde{\rho}\frac{Du_i'}{Dt} + \rho'\frac{D\tilde{u}_i}{Dt} + \tilde{\rho}u_j'\frac{\partial \tilde{u}_i}{\partial x_j} &= -\frac{\partial p'}{\partial x_i}\end{aligned} \tag{2.20}$$

so finally, the convected conservation of momentum equation is given by,

$$\tilde{\rho}\frac{Du_i'}{Dt} + \rho'\frac{D\tilde{u}_i}{Dt} + \tilde{\rho}u_j'\frac{\partial \tilde{u}_i}{\partial x_j} + \frac{\partial p'}{\partial x_i} = 0 \tag{2.21}$$

Equations 2.5 and 2.17 describe the incident flow which is varying slowly compared to the oscillatory components. In the present work they are solved independently from them using a commercial computational fluid dynamics solver, 'FLUENT'.

Equations 2.11 and 2.21 are used to derive the convected Helmholtz equation, below.

### Duration of the low pass filtering 'time-mean'

For the low pass filtering to remove the high frequency contribution, the 'time-mean' should act over several high frequency periods. To resolve the low frequency, it should act over a fraction of a low frequency characteristic time scale. If the measurement frequency is of the order of 40kHz and a mean over ten cycles is taken, the period is $2.5 * 10^{-4} s$. If the low frequency signal is of the order $100Hz$ with a corresponding period of $0.01\,s$, forty high frequency averages will occur over a single low frequency cycle, removing the high frequency but preserving the low frequency. This approximation becomes more difficult to justify if the difference in frequencies is reduced. The approach is similar to that used during Reynolds averaging of flows with large scale unsteadiness (so called URANS).

### 2.2.2 Convected acoustic field

Performing the convective derivative of the convected conservation of mass expression and subtracting the spatial derivative of the convected conservation of momentum expression results in,

$$\frac{D}{Dt}(2.11) - \frac{\partial}{\partial x_i}(2.21) = 0 \tag{2.22}$$

Assuming low frequency incompressible flow, the approximation described in Equation 2.6 and that $\tilde{\rho}$ is constant can be made. Furthermore, if $\frac{\partial}{\partial t}\tilde{u_i} \ll \frac{\partial}{\partial t}u_i'$ the expansion reduces to

$$\overbrace{\frac{D^2\rho'}{Dt^2}}^{1} - \overbrace{\tilde{\rho}\frac{\partial \tilde{u_k}}{\partial x_i}\frac{\partial u_i'}{\partial x_k}}^{9} - \overbrace{\frac{\partial \rho'}{\partial x_i}\frac{\partial \tilde{u_i}}{\partial t}}^{11} - \overbrace{\frac{\partial \rho'}{\partial x_i}\tilde{u_k}\frac{\partial \tilde{u_i}}{\partial x_k}}^{13} - \overbrace{\rho'\frac{\partial \tilde{u_k}}{\partial x_i}\frac{\partial \tilde{u_i}}{\partial x_k}}^{14} - \overbrace{\tilde{\rho}\frac{\partial u_j'}{\partial x_i}\frac{\partial \tilde{u_i}}{\partial x_j}}^{17} - \overbrace{\frac{\partial^2 p'}{\partial x_i \partial x_i}}^{19} \tag{2.23}$$

where repeated suffixes have been changed to $k$ to avoid confusion. This process and the origin of the numbering used to label the terms, is described in more detail in the appendix, section A.0.4.

Magnitudes of the terms involved can be estimated using characteristic length scales as calculated below. In this consideration, $l$ is the acoustic length scale and $L$ is the flow field length scale. Term numbers are referred to with the leftmost term as term number one.

| Term | Approximate magnitude | |
|---|---|---|
| 1 | $\rho'/(l/c)^2$ | $= cc\rho'/l^2$ |
| 9 | $\tilde{\rho}\tilde{u}u'/Ll$ | $= \tilde{u}u'\tilde{\rho}/(Ll)$ |
| 11 | $\rho'\tilde{u}/(lL/\tilde{u})$ | $= \tilde{u}\tilde{u}\rho'/(lL)$ |
| 13 | $\rho'\tilde{u}\tilde{u}/(lL)$ | $= \tilde{u}\tilde{u}\rho'/(lL)$ |
| 14 | $\rho'\tilde{u}\tilde{u}/(LL)$ | $= \tilde{u}\tilde{u}\rho'/(lL)$ |
| 17 | $\tilde{\rho}u'\tilde{u}/(lL)$ | $= \tilde{u}u'\tilde{\rho}/(lL)$ |
| 19 | $c^2\rho'/(ll)$ | $= cc\rho'/(ll)$ |

Table 2.1: Orders of magnitude for the terms of Equation 2.23.

Table 2.1 shows that terms 11, 13 and 14 contribute a magnitude of factor $M^2$ compared to terms 1 and 19. Terms 9 and 17 have a dependency on $u'\tilde{\rho}$ which can be shown to be of a similar magnitude to $c\rho'$ inside the anemometer duct. Terms 9 and 17 are therefore of factor $M$, compared to terms 1 and 19. In the low flow speed case, terms other than 1 and 19 contribute relatively little, and can be ignored.

This approximation results in,

$$\frac{D^2\rho'}{Dt^2} - \frac{\partial^2 p'}{\partial x_i \partial x_i} = 0 \tag{2.24}$$

Assuming the speed of sound in the flow is constant,

$$\frac{\partial p}{\partial \rho} = c^2 \tag{2.25}$$

can be used to convert the convected acoustic density to acoustic pressure. Equation 2.24 becomes,

$$\frac{1}{c^2}\frac{D^2 p'}{Dt^2} - \frac{\partial^2 p'}{\partial x_i \partial x_i} = 0 \tag{2.26}$$

**Time harmonic form for solution**

Equation 2.26 can be written in the more usual form,

$$\nabla^2 p - \frac{1}{c^2}\frac{D^2 p}{Dt^2} = 0 \tag{2.27}$$

If considered in one dimension, the $U$ component of the total derivative becomes scalar.

$$\frac{D}{Dt} \equiv \frac{\partial}{\partial t} + U_j \frac{\partial}{\partial x_j} \longrightarrow \frac{\partial}{\partial t} + U\frac{\partial}{\partial x} \tag{2.28}$$

The total derivative component of Equation 2.27 becomes,

$$\frac{D^2 p}{Dt^2} = \frac{D}{Dt}\left(\frac{\partial p}{\partial t} + U\frac{\partial p}{\partial x}\right) = \left(\frac{\partial}{\partial t} + U\frac{\partial}{\partial x}\right)\left(\frac{\partial p}{\partial t} + U\frac{\partial p}{\partial x}\right) = \frac{\partial^2 p}{\partial t^2} + 2\frac{\partial^2 p}{\partial t \partial x}U + U^2\frac{\partial^2 p}{\partial x^2} \tag{2.29}$$

Re-writing Equation 2.27 with this result yields

$$\nabla^2 p - \frac{1}{c^2}\left(\frac{\partial^2 p}{\partial t^2} + 2U\frac{\partial^2 p}{\partial t \partial x} + U^2\frac{\partial^2 p}{\partial x^2}\right) = 0 \tag{2.30}$$

Defining the Mach number, as $M = U/c$,

$$\nabla^2 p - \frac{1}{c^2}\frac{\partial^2 p}{\partial t^2} - \frac{2U}{c^2}\frac{\partial^2 p}{\partial t \partial x} - M^2\frac{\partial^2 p}{\partial x^2} = 0 \tag{2.31}$$

The Laplace operator, $\nabla^2 A = \frac{\partial^2 A}{\partial x^2} + \frac{\partial^2 A}{\partial y^2} + \frac{\partial^2 A}{\partial z^2}$, so for this one dimensional case,

$$\frac{\partial^2 p}{\partial x^2} - \frac{1}{c^2}\frac{\partial^2 p}{\partial t^2} - \frac{2U}{c^2}\frac{\partial^2 p}{\partial t \partial x} - M^2\frac{\partial^2 p}{\partial x^2} = 0 \tag{2.32}$$

rearranging to,

$$(1 - M^2)(\frac{\partial^2 p}{\partial x^2}) - \frac{1}{c^2}\frac{\partial^2 p}{\partial t^2} - \frac{2U}{c^2}\frac{\partial^2 p}{\partial t \partial x} = 0 \tag{2.33}$$

At low flow speeds, U is small, M is small and $M^2$ is very small. The $M^2$ terms can be ignored. The $\frac{U}{c^2} = \frac{M}{c}$ term cannot be ignored as the $\frac{1}{\partial t}$ term is large.

$$\frac{\partial^2 p}{\partial x^2} - \frac{1}{c^2}\frac{\partial^2 p}{\partial t^2} - \frac{2M}{c}\frac{\partial^2 p}{\partial t \partial x} = 0 \tag{2.34}$$

and the convected acoustic wave equation can be derived as,

$$\nabla^2 p - \frac{1}{c^2}\frac{\partial^2 p}{\partial t^2} - \frac{2M}{c}\frac{\partial^2 p}{\partial t \partial x} = 0 \tag{2.35}$$

If the pressure varies harmonically with time, $p = \hat{p}e^{i\omega t}$ where $\omega = 2\pi f$ is the angular frequency.

The first and second differentials of pressure with time become,

$$\frac{\partial p}{\partial t} = i\omega p \qquad \frac{\partial p^2}{\partial t^2} = -\omega^2 p \tag{2.36}$$

Using the wavenumber definition, $k = \frac{\omega}{c}$ and Equation 2.36, Equation 2.35 can be re-written as

$$\nabla^2 p - 2iMk\frac{\partial \hat{p}}{\partial x} + k^2\hat{p} = 0 \tag{2.37}$$

In the case of more than one dimension, the convected term changes from $-2iMk\frac{\partial \hat{p}}{\partial x}$ to

$$-2ikM_x\frac{\partial \hat{p}}{\partial x} - 2ikM_y\frac{\partial \hat{p}}{\partial y} - 2ikM_z\frac{\partial \hat{p}}{\partial z} \tag{2.38}$$

This is the expression solved by the finite element solver described in this report. Setting the Mach number to zero produces the acoustic wave equation,

$$\nabla^2 p + k^2\hat{p} = 0 \tag{2.39}$$

This expression is similar to that used by Tsuji et al. [108], but without the low flow velocity assumption which results in $M^2$ terms being very small. Inclusion of the $M^2$ term results in weak coupling between the slowly changing flow and the high frequency acoustic pressure gradients normal to the flow direction. An effect of excluding this small contribution is that the acoustic wave speed is not affected by the slowly changing flow velocity normal to the direction of acoustic propagation. This effect is explored in Chapter 5.

## 2.3 Numerical solution.

This section summarises the implementation of a finite element solver, to solve the previously derived form of the convected Helmholtz equation. The equation was solved with the aid of boundary conditions: both pressure and pressure gradient conditions were used. Analysis using this solver is performed in Chapter 5.

### 2.3.1 Method overview.

The finite element method was chosen as the solution method for the convected Helmholtz equation solver. It is described in many books, including those by Bang [5], Zienkiewicz and Taylor [119], Henwood and Bonet [50]. For this reason, the method is summarised in this section, with a focus on the components specific to this problem.

The weighted residuals approach was used, in which the weak form of the convected Helmholtz equation was used over small regions - 'elements', to generate a matrix defining the behaviour in that region, $[k]$. The set of matrices created were then assembled into a large, system matrix, $[K]$. The boundary conditions were used to modify the system matrix, and create the system vector, $\boldsymbol{f}$.

The matrix equation,

$$[K]\boldsymbol{u} = \boldsymbol{f} \tag{2.40}$$

is then solved, for $\boldsymbol{u}$. $\boldsymbol{u}$ contains results for the solution variable at each position, and the solution between those positions can be calculated from the surrounding values.

Elements used during development included two-dimensional, first and second order quadrilaterals; first order triangles; and three-dimensional, first order hexahedra. The body of the work was performed using the three-dimensional elements.

### 2.3.2 Method of weighted residuals.

Given a differential equation and boundary conditions, a trial function that satisfies the boundary conditions can be used. The weighted residual method substitutes the trial function into the differential equation (to calculate the residual, $R$) and integrates the product of this result with a weighting function $w$ over the domain of interest. The result is set to zero and the resulting expression, once integrated, can be solved for the coefficients in the trial function. The trial function, using the calculated coefficients is then an approximate solution of the differential equation. The following can therefore be written.

$$I = \int_{\Omega} wR = 0 \tag{2.41}$$

where $\Omega$ is the domain of interest; $w$ is the weighting function; and $R$ is the residual.

Different approaches for the weighting function are possible. The Galerkin method is used here, so the weighting functions are the same as the trial functions. The more complex the

expression being solved, the more difficult it is to find suitable trial functions. Rather than specifying a single, complex trial function valid over the whole domain, the domain can be split into sub-domains, each with its own set of trial functions. Each sub-domain is a finite element and each element has a trial function that equals zero outside the element but can be non zero within. The trial functions of adjacent elements are continuous. These trial functions are a product of internal shape functions (one for each joined position in each element) and a coefficient. The trial function over the element, is the sum of these scaled, internal shape functions.

Calculating the expression for $I$ for each element and performing the integration results in a set of simultaneous equations. Solution of these equations yields the scalar multiples for each shape function and the approximate solution for the differential equation can then be generated.

### 2.3.3 The weak form

The order of the differential equation can be reduced by using integration by parts, resulting in the 'weak' form. The reduction of order simplifies the trial solution.

Starting with the two-dimensional convected Helmholtz equation in the form

$$\nabla^2 p - 2ikM_x\frac{\partial \hat{p}}{\partial x} - 2ikM_y\frac{\partial \hat{p}}{\partial y} + k^2\hat{p} = 0 \tag{2.42}$$

It is considered throughout the region, $\Omega$, which is bounded by the surface, $\Gamma$.

Re-writing Equation 2.41, the integration of the weighted residual of the differential equation in the region $\Omega$ becomes,

$$I = \int_\Omega w\left(\frac{\partial^2\hat{p}}{\partial x^2} + \frac{\partial^2\hat{p}}{\partial y^2} - 2\imath k\left(M_x\frac{\partial\hat{p}}{\partial x} + M_y\frac{\partial\hat{p}}{\partial y}\right) + k^2\hat{p}\right)d\Omega \tag{2.43}$$

Integration by parts is used on the second derivatives to reduce the order. The result is

$$\int_\Omega -\left(\frac{\partial\hat{p}}{\partial x}\frac{\partial w}{\partial x}\right)d\Omega + \int_\Gamma \frac{\partial\hat{p}}{\partial x}wn_x d\Gamma \quad and \quad \int_\Omega -\left(\frac{\partial\hat{p}}{\partial y}\frac{\partial w}{\partial y}\right)d\Omega + \int_\Gamma \frac{\partial\hat{p}}{\partial y}wn_y d\Gamma \tag{2.44}$$

The expressions in (2.44) are summed to give a closed loop integral expression,

$$\int_\Omega -\left(\frac{\partial\hat{p}}{\partial x}\frac{\partial w}{\partial x} + \frac{\partial\hat{p}}{\partial y}\frac{\partial w}{\partial y}\right)d\Omega + \oint_\Gamma w\frac{\partial\hat{p}}{\partial n}d\Gamma \tag{2.45}$$

Substituting Equation 2.45 into Equation 2.43 and re-arranging results in,

$$\begin{aligned} I &= \int_\Omega -\left(\frac{\partial\hat{p}}{\partial x}\frac{\partial w}{\partial x} + \frac{\partial\hat{p}}{\partial y}\frac{\partial w}{\partial y}\right)d\Omega + \oint_\Gamma w\frac{\partial\hat{p}}{\partial n}d\Gamma \\ &+ \int_\Omega w\left(-2\imath k\left(M_x\frac{\partial\hat{p}}{\partial x} + M_y\frac{\partial\hat{p}}{\partial y}\right) + k^2\hat{p}\right)d\Omega \end{aligned} \tag{2.46}$$

which can be rearranged to,

$$I = \int_{\Omega} \left( -\frac{\partial \hat{p}}{\partial x}\frac{\partial w}{\partial x} - \frac{\partial \hat{p}}{\partial y}\frac{\partial w}{\partial y} - 2\imath k w \left( M_x \frac{\partial \hat{p}}{\partial x} + M_y \frac{\partial \hat{p}}{\partial y} \right) + w k^2 \hat{p} \right) d\Omega + \oint_{\Gamma} w \frac{\partial \hat{p}}{\partial n} d\Gamma \quad (2.47)$$

The first integral is used to build each element matrix, prior to addition to the system matrix. The second integral is used to define the boundary conditions, as discussed in the next section.

### 2.3.4 Boundary conditions

#### Setting the normal pressure gradient, $\partial p/\partial n$

Gradient boundary conditions are formulated by considering the line integral contribution resulting from integration by parts of the convected Helmholtz equation. If the boundary integral term of Equation 2.47 is discretised and considered as contributions from element edges instead of a boundary, Bang [5] has shown it becomes,

$$\int_{\Gamma} w \frac{\partial p}{\partial n} d\Gamma = \sum \int_{\Gamma^e} \boldsymbol{w} \frac{\partial p}{\partial n} d\Gamma \quad (2.48)$$

where $\boldsymbol{w}$ is now a vector of weighting functions in the element.

For linear elements, the flow from the element edge can be described using one-dimensional linear shape functions. From inspection of the shape function diagram below, it can be seen that for the case of a linear element with gradient applied on the edge joining two nodes at $x_i$ and $x_j$, Equation 2.49 can be derived.

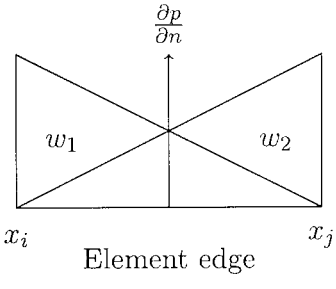



Figure 2.1: Shape functions at the edge of a two dimensional element.

$$\int_{\Gamma^e} \boldsymbol{w} \frac{\partial p}{\partial n} d\Gamma = \frac{\partial p}{\partial n} \int_{x_i}^{x_j} \begin{bmatrix} \frac{x_j - x}{x_j - x_i} \\ \frac{x - x_i}{x_j - x_i} \end{bmatrix} dx = \frac{\partial p}{\partial n} \begin{bmatrix} \int_{x_i}^{x_j} \frac{x_j - x}{x_j - x_i} dx \\ \int_{x_i}^{x_j} \frac{x - x_i}{x_j - x_i} dx \end{bmatrix} \quad (2.49)$$

with square brackets enclosing the vector. The integrals are evaluated using the result

$$\int_a^b \frac{b - x}{b - a} = \frac{1}{b - a} \int_a^b (b - x)\, dx = \frac{b - a}{2} \quad (2.50)$$

If the element length, $l = x_2 - x_1$ then

$$\int_{\Gamma^e} \boldsymbol{w} \frac{\partial p}{\partial n} d\Gamma_e = \frac{\partial p}{\partial n} \begin{bmatrix} l/2 \\ l/2 \end{bmatrix} \tag{2.51}$$

This column vector will be added to nodal locations associated with the bounding positions of $x_1$ and $x_2$. Of note is that the value added to the system vector entries is proportional to the element length.

### The infinite region

As discussed in Chapter 1, critical to the results of time steady solutions are the outer boundary conditions at all points in the simulation. Methods for representation of the infinite region include boundary elements as documented by Henshell [49]; wave envelope elements, see Astley. [2]; infinite elements, see Bettess [10]; and the 'quiet', non-reflecting boundary as described below. Comparisons between these methods were made using the commercial finite element solver, 'PAFEC' and the results that were generated were very similar. Solution time was strongly affected however, particularly in the case of the boundary element. The use of a boundary element results in the system matrices becoming densely populated and the efficient sparse solver used for the other elements is no longer applicable, as reported by Thompson [104].

Application of the impedance condition (sometimes referred to as a quiet boundary) retains the sparsity of the matrices but only appears to yield the non-reflective boundary condition to normal waves. A side effect of this is that the boundary needs to be as far from the source as possible - introducing errors with truncated simulations.

This condition was applied in the software using a convection formulation. Following an example by Henwood and Bonet [50] and work by Bang [5], the non-reflective boundary condition for the three-dimensional elements was derived. A two dimensional derivation is provided here, for brevity.

According to Henwood and Bonet [50], a convection statement using the variational form is,

$$V = \int \frac{Z}{2} (p - p_\infty)^2 ds \tag{2.52}$$

with $s$ the boundary integral of the damping path; $p$ the acoustic pressure; and $Z$ the acoustic impedance.

Using tensor notation, the acoustic pressure along the edge, is the sum of the shape functions $H_i$ and nodal pressures, $p_i$:

$$p = H_i \, p_i \tag{2.53}$$

Given the shape functions along the damped edge for the linear, two-dimensional triangle in the natural coordinate are

$$H_1(x) = x \qquad H_2(x) = 1 - x \qquad H_3(x) = 0 \tag{2.54}$$

differentiating V with respect to each shape function, re-arranging to get the result in terms of $p_i$ and evaluating the integral from 0 to 1 generates the following results:

$$\frac{dV}{dp_1} = p_1 Z \left( \int_0^1 H_1 H_1 dx \right) + p_2 Z \left( \int_0^1 H_2 H_1 dx \right) = p_1 Z \frac{1}{3} + p_2 Z \frac{1}{6} \tag{2.55}$$

$$\frac{dV}{dp_2} = p_1 Z \left( \int_0^1 H_1 H_2 dx \right) + p_2 Z \left( \int_0^2 H_2 H_2 dx \right) = p_1 Z \frac{1}{6} + p_2 Z \frac{1}{3} \tag{2.56}$$

$$\frac{dV}{dp_3} = 0 \tag{2.57}$$

Re-written in matrix form, the results are:

$$\frac{dV}{dp} = \begin{pmatrix} \frac{1}{3}Z & \frac{1}{6}Z & 0 \\ \frac{1}{6}Z & \frac{1}{3}Z & 0 \\ 0 & 0 & 0 \end{pmatrix} \begin{pmatrix} p_1 \\ p_2 \\ p_3 \end{pmatrix} \tag{2.58}$$

The square matrix is added to the system matrix according to the degree of freedom numbers associated with the nodes in question. To scale from the natural coordinate to the physical, the matrix is multiplied by the boundary length.

For a non-reflecting acoustic boundary, the impedance should be set to,

$$Z = \rho_0 c \tag{2.59}$$

so the matrix added to the system matrix for every damped edge, to provide loading equivalent to an infinite region is,

$$Zl \begin{pmatrix} \frac{1}{3} & \frac{1}{6} & 0 \\ \frac{1}{6} & \frac{1}{3} & 0 \\ 0 & 0 & 0 \end{pmatrix} \tag{2.60}$$

where $Z$ is the desired impedance and $l$ is the length of the damped edge.

# 3 Measurements

## 3.1 Introduction

Measurements can be used to validate the results of numerical calculations, and aid in the understanding of phenomena. In this case, experimental results were used not only for validation, but to select the turbulence model used during simulation of the low frequency, viscous flow field.

Three sets of measurements were performed, in order to generate data to be used during validation. The first two sets were used to evaluate the fidelity of the low frequency, viscous field simulation. First, pressures on an anemometer surface were measured by piping the pressures at the surface, to a remote pressure transducer. Second, the slowly varying velocity at points around an anemometer, and inside the acoustic duct of an anemometer were measured with hot-wire equipment.

The third measurement set was of the high frequency acoustic field. Measurements were made using a working anemometer modified to generate a transfer function between each of the transducer pairs, under different free-field velocities.

This chapter describes the experiments performed, and presents the data gained with discussion.

## 3.2 Equipment description

### 3.2.1 Wind-tunnel

Measurements were conducted in the '18-inch' wind-tunnel at Imperial College: a closed-circuit, closed-return design with a maximum flow velocity exceeding $65\,ms^{-1}$. The test section was of dimensions, $18" * 18"$, with a vent to the ambient atmosphere approximately $0.5\,m$ downstream of the measurement position. The cross sectional area of the test section was $0.209\,m^2$.

Flow velocity was controlled manually via a remote control, and measured using a Pitot-static tube $46\,cm$ upstream of the body and $7.5\,cm$ from the nearest wall. The pressure differences from the Pitot-static tube were fed to a Furness Controls, FCO510 digital micromanometer, which together with measurements of flow temperature and atmospheric pressure outside the tunnel, were used to derive the flow velocity, according to

$$u = \sqrt{\frac{p - p_s}{\frac{1}{2}\rho}} \tag{3.1}$$

with velocity, $u$; stagnation pressure, $p$; static pressure, $p_s$; and density, $\rho$. The FCO510 minimum pressure difference was $dP = 0.01\,Pa$ according to Fur [37].

Air density, $\rho$, was calculated by the device, using the ideal gas equation, Equation 3.2.

$$P = \rho R_s T_f \tag{3.2}$$

with $T_f$, the absolute temperature of the flow; $P$, the absolute pressure; and $R_s$, the specific gas constant.

The temperature was measured by a thermocouple 15 $cm$ downstream of the body. Absolute pressure was measured with a Druck PTX-1400 transducer outside the tunnel, with a typical accuracy reported by GE [40] of 0.15%. Pressure differences are accurate to 0.25%, according to Fur [37]. Temperature error data was not available.

Measurements with zero flow showed the following fluctuations: temperature, $\pm 0.005\,K$; absolute pressure, $\pm 0.5\,Pa$; and differential pressure $\pm 0.1\,Pa$.

The errors result in a best case error of $\pm 0.15\%$ for the density. The velocity error varies with velocity, low velocities being more affected by the numerical error observed in the differential pressure. The velocity error was calculated as $\pm 0.05\,ms^{-1}$, or 0.24% of the velocity; whichever was the larger.

Care was taken to ensure the tube was pointing upstream, to within $\pm 5°$. According to Duncan et al. [28] this should minimise velocity errors due to misalignment of the static ports on the tube. Due to the manual control of the fan, a warm-up period of an hour was allowed for the flow temperature to stabilise.

Values for turbulence intensity were not available, and so were derived from hot-wire measurements as described in section 3.4.3 as being 0.14%.

The speed of the tunnel fan was controlled manually, and was continually adjusted according to the velocity results calculated from the Pitot-static measurements.

### 3.2.2 Anemometer description

The device used throughout the measurements was an anemometer housing provided by FT Technologies. The device was a low aspect-ratio circular cylinder of diameter 50 $mm$, length 62 $mm$ with domed ends extending a further 13 $mm$ on the free end, and 12 $mm$ on the mounted end. The mount was a cylinder of diameter 22 $mm$ and length 68 $mm$ with its rotational axis concentric with that of the main body. The mount was extended an extra 69 $mm$ by a second rod of equal diameter, for support. The free end of the anemometer was attached to a 12.5 $mm$ diameter support rod, extending beyond the wind-tunnel wall.

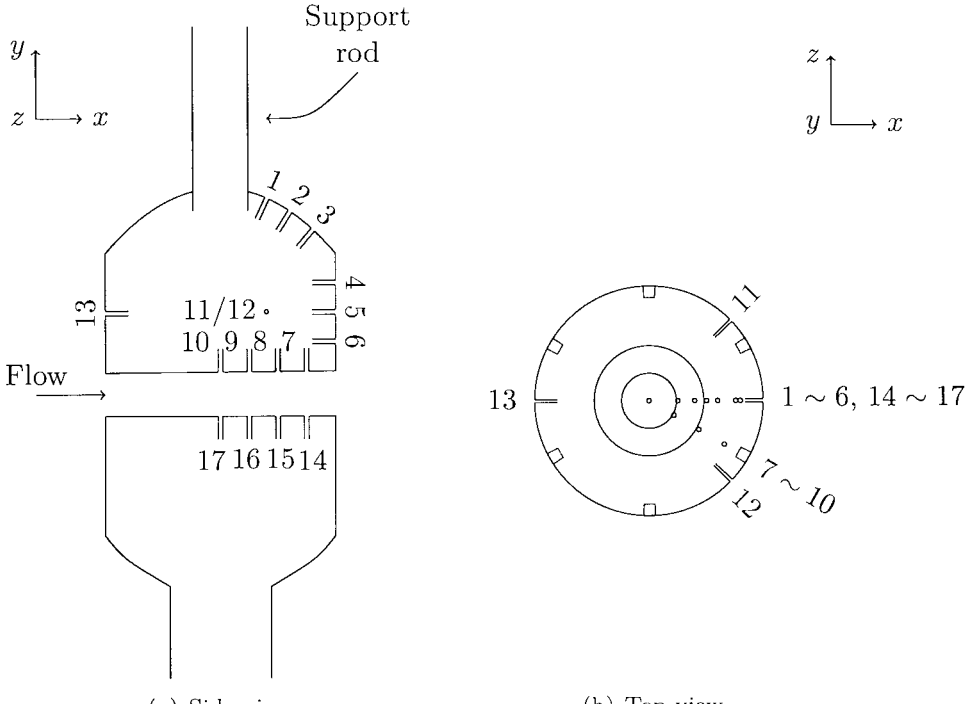
The acoustic duct splits the larger cylinder half way along its length. At the duct entrance, the separation between the major duct faces was $9.4\,mm$, increasing to $10\,mm$ just inside the duct.

The internal circuitry and transducers were removed. Pressure tappings were added to the anemometer, of inner diameter $0.7\,mm$, outer diameter $1.1\,mm$ with the tappings polished to be flush with the anemometer body. The tappings ran in a line starting on the free end dome, extending along the upper half of the major cylinder, and along the inside of the duct face. These tappings were intended to generate pressures over the anemometer surface, as it was rotated.

Three more tappings were added half way along the upper major cylinder length, at $\pm 45°$ from the line described above, and one on the opposite side. Zero pressure difference between the front two tappings was used to establish the upstream direction. The rear tapping was to measure base pressure.

Tubes connected to the pressure tappings were passed through the support rod. The opposite end of the anemometer was fixed to a stepper motor outside the tunnel, providing sub-degree positioning accuracy.

The modified anemometer is illustrated in Figure 3.1.




(a) Side view.

(b) Top view.

Figure 3.1: Positions and numbers of pressure taps on the modified anemometer. The position of the extra support rod, and pillars across the acoustic resonance region (blue) are illustrated. The coordinate system origin is considered to be at the centre of the acoustic duct.

The cross sectional area of the anemometer was estimated as $2.25 \times 10^{-3}\,m^2$ and the support poles were estimated as $6 \times 10^{-3}\,m^2$. This resulted in an estimated blockage of

3.8%. Blockage has not been accounted for in the following measurements.

## 3.3 Surface pressure

The modified anemometer was supported in the test section by fixtures in the wind-tunnel walls, providing a tight fit with the support poles. The thinner support pole was able to rotate relative to the fixture; the second pole was fixed to a stepper motor (a Standa, 8MR190-2-4247), enabling computer control of the angular position of the anemometer. The angular position was better than $\pm 0.1°$. Software was written to control the angular position, and record pressure difference results: enabling automated experiments to be performed.

Pressure measurements were originally made using a liquid filled multi-tube manometer, but at an anemometer diameter based Reynolds number of $Re = 66 \times 10^3$, the observed pressure difference between taps eleven and twelve that appeared constant over a few seconds, would change to other values with no deliberate change of experimental conditions. For this reason, extra FCO510 digital manometers were used to monitor the pressure difference between selected tap pairs, and between taps and the static pressure from the Pitot-static tube.

While easing the data gathering process, this approach resulted in the instantaneous pressure relationships between taps that were not being measured simultaneously, being lost. The data can only be used to calculate the mean and the variance of the pressure differences, and to inspect the unsteady pressure difference integrated over a second, between two taps.

The tubes transporting the pressure at the taps to the manometers were in two parts: the tubes directly connected to the taps were approximately fifty centimetres long, with an internal diameter of $1.1\,mm$. These tubes were extended by two metres, by tubes of internal diameter, $4.0\,mm$. The combined effect will be one of a resonance, limiting the high frequency response.

Output from the FC0510 manometer was via an RS232 interface, connected to a PC via the Universal Serial Bus. The `uspp` Python library from Barona [7] was used to communicate with the interface.

Position calibration was performed by rotating the device until taps eleven and twelve, as marked in Figure 3.1, gave a time-mean, zero pressure difference; measured over twenty seconds.

Unsteady pressure measurements were made at a manometer limited rate, of one per second. Angular resolution was set to two degrees, to strike a balance between acquisition time and angular resolution.

Two sets of measurements were made: A set with the acoustic duct blocked (by wrapping adhesive tape around the duct), and a set with the acoustic duct open. Blocking the duct results in a simpler system: reducing the complexity of the mesh used during simulation, and making the results easier to understand.

It is convenient at this point, to define the pressure coefficient as shown in Equation 3.3.

$$C_p = \frac{p - p_0}{\frac{1}{2}\rho u^2} \tag{3.3}$$

with the pressure coefficient, $C_p$; the total pressure, $p$; the static pressure, $p_s$; the density, $\rho$; and the velocity, $u$.

### 3.3.1 Closed duct measurements

The air density during these measurements was calculated using the ideal gas equation, Equation 3.2. The constants used were absolute pressure, $P = 102470\,Pa$; the specific gas constant for air, $R = 287.05\,J\,kg^{-1}\,K^{-1}$; and the absolute temperature, $T = 294.2\,K$. Absolute pressure and temperature were measured during the experiment. These values result in $\rho = 1.21\,kg\,m^{-3}$. Reynolds numbers were calculated using Equation 3.4.

$$Re = \frac{\rho u D}{\mu} \tag{3.4}$$

with Reynolds number, $Re$; density, $\rho = 1.21\,kg\,m^{-3}$; velocity, $u = 10\,m\,s^{-1}$; diameter, $d = 0.05\,m$; and viscosity, $\mu = 1.83 \times 10^{-5}\,Pa\,s$. These values result in $Re = 33 \times 10^3$.

The $C_p$ for taps one and six is presented in Figure 3.2, for a diameter based Reynolds number of $Re = 33 \times 10^3$. Measurements used a 2° resolution, with fifteen samples per angle; one every second. The $\theta = 80°$ point is marked as well as the angle in radians, to aid identification of the separation point of a laminar boundary layer. The plot indicates the range of $C_p$ observed at each position, and therefore gives an indication of the stability of the pressure around the body.

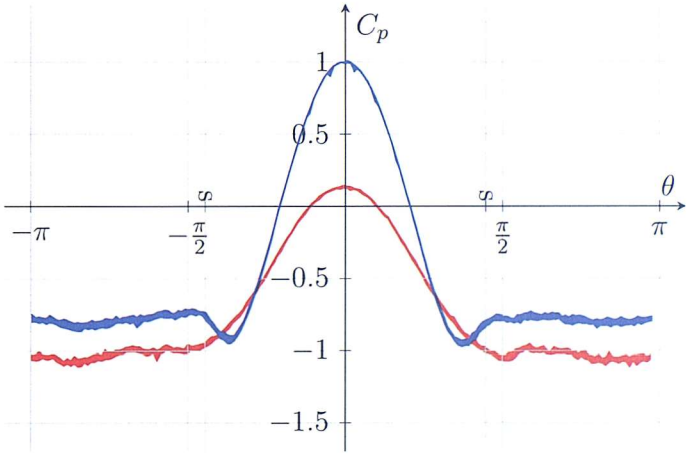



Figure 3.2: $C_p$ at taps one (red) and six (blue), for $Re = 33 \times 10^3$. 's' marks the ±80° position.

$C_p$ varies by no more than ±0.035 for tap six. Taps two, three and five generated results falling between taps one and six.

Increasing the Reynolds number to $Re = 66 \times 10^3$ generated results of similar stability, as demonstrated in Figure 3.3.

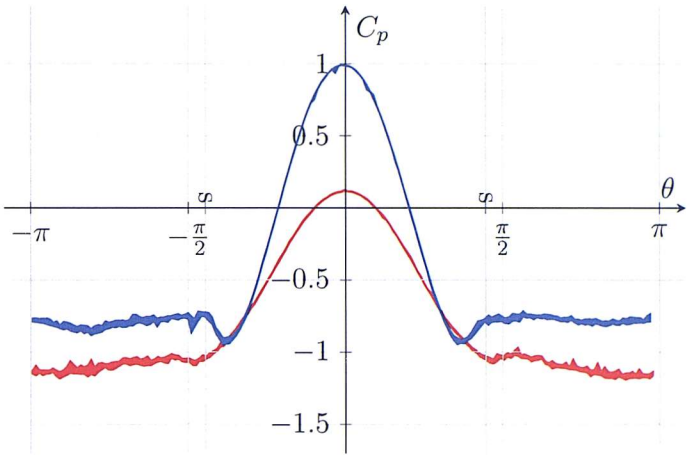



Figure 3.3: $C_p$ at taps one (red) and six (blue), for $Re = 66 \times 10^3$.

Rather than plotting the range at each position for each tap, the mean $C_p$ and standard deviation for each tap and position will be plotted. The mean $C_p$ values at $Re = 33 \times 10^3$ for taps one to six are plotted in Figure 3.4. The standard deviation of $C_p$ is plotted in Figure 3.5.

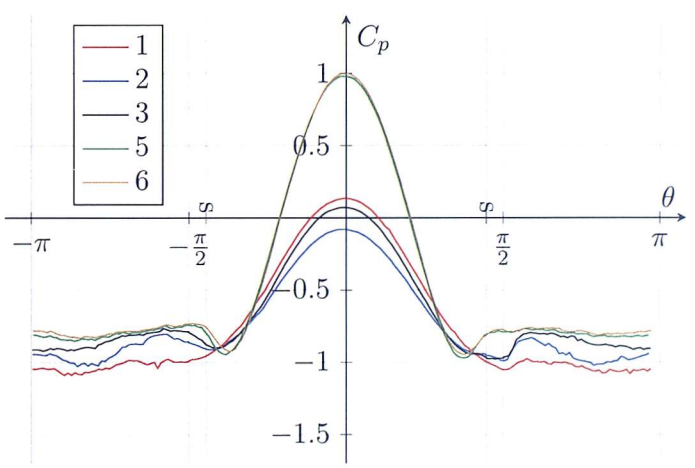



Figure 3.4: Mean $C_p$ at taps one to six, for $Re = 33 \times 10^3$.

The grassy nature of the standard deviation results is indicative of the number of samples taken, and suggests that the deviation caused by the number of samples is of a similar magnitude to the deviation caused by flow fluctuation. This pollution of results was lessened by calculating the mean standard deviation over successive positions: the effect is illustrated in Figure 3.6, as a smoothing.

Ideally, more samples would have been used, decreasing the variation of standard deviation around the body. Results at $Re = 66 \times 10^3$ are plotted in Figure 3.7 and Figure 3.8. From inspection, the change of Reynolds number has made little difference to the $C_p$ results.

The mean $C_p$ results are interpolated over the surface of the anemometer in Figure 3.9, to

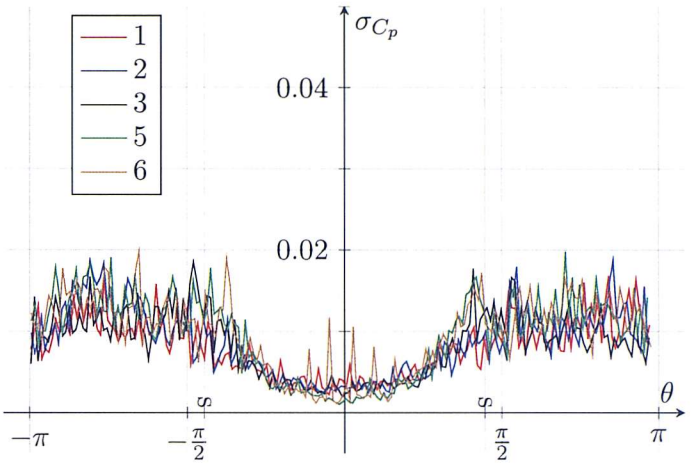



Figure 3.5: Standard deviation of the $C_p$ at taps one to six, for $Re = 33 \times 10^3$, indicating how large the $C_p$ fluctuation was over each sample. The scale limit for these closed acoustic duct measurements is constant. It is demonstrated that the fluctuation was of the order of 1% of the $C_p$ values.

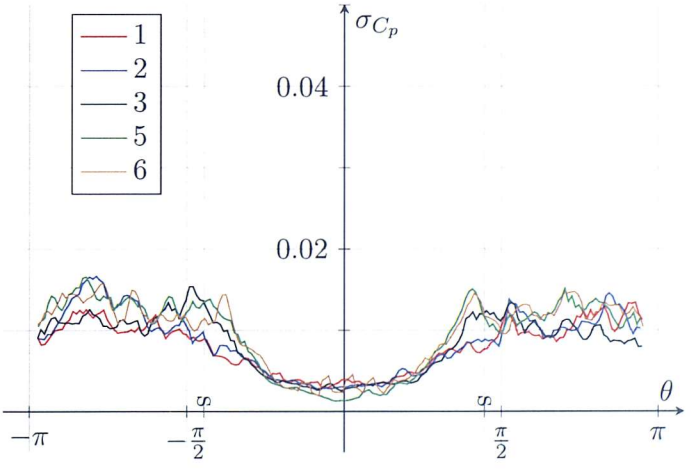



Figure 3.6: Standard deviation of the $C_p$ at taps one to six, for $Re = 33 \times 10^3$ with a five point moving average. The plateau beyond $\theta = 80°$ indicates the boundary layer may be separating near this angle.

give a feeling for the pressure distribution over the indicated part of the body.

The inflection of $C_p$ close to 80° suggests laminar boundary layer separation according to Zdravkovich [116]. Stagnation $C_p$ is close to unity when the taps are pointing upstream, for taps five and six, only. Taps one, two and three are on the domed end and do not have normals pointing upstream. They show generally lower $C_p$ values as a result.

Base $C_p$ values are summarised in Table 3.1, showing $C_{pb} = -0.78$ for both Reynolds number experiments at tap six: the tap that might be expected to show the greatest similarity to circular cylinder results. This result is similar to that found by Gerrard [41]: $C_{pb} \approx -1.0$ for $Re \approx 33 \times 10^3$, and $C_{pb} \approx -1.05$ for $Re \approx 66 \times 10^3$. The experiment by Gerrard [41] used a low free stream turbulence intensity, and a low aspect ratio ($L/D$) cylinder: similar to the object measured in this case. This can be contrasted with the $C_{pb} \approx -1.2$ extrapolated by Zdravkovich [116] for $20 \times 10^3 < Re < 100 \times 10^3$ for larger aspect ratio cylinders. It appears the three-dimensionality of the measured object is affecting $C_p$, even close to the centre of the cylinder.

The standard deviation of $C_p$ is approximately constant for $-\frac{\pi}{4} < \theta < \frac{\pi}{4}$, and then shows an increase as the angle increases to 80°. It remains approximately constant for angles greater than this. The high standard deviation after $\theta = 80°$ is likely to be a result of boundary layer separation from the body.

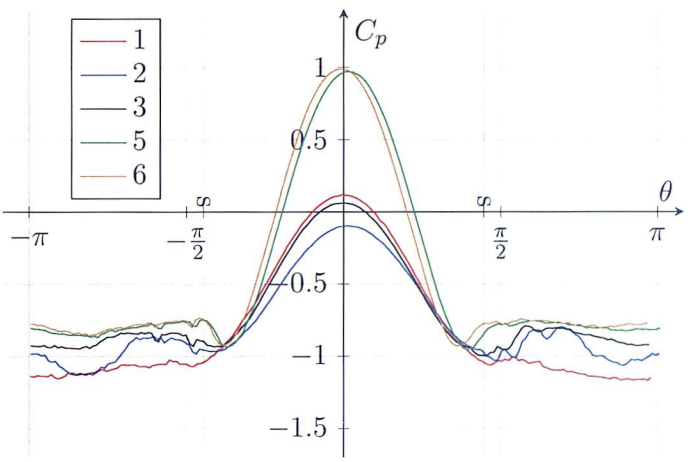



Figure 3.7: Mean $C_p$ at taps one to six, for $Re = 66 \times 10^3$.

Increasing the Reynolds number from $Re = 33 \times 10^3$ to $Re = 66 \times 10^3$ results in little change, both in the character of the mean $C_p$ and its fluctuations. Zdravkovich [116] defined the 'TrSL3' Reynolds number range as extending from approximately $20 \times 10^3 < Re < 200 \times 10^3$, encompassing these experiments; this is a part of the 'transition in wake' region, describing where the transition to turbulent behaviour occurs.

The $C_p$ distribution has been reported as largely constant in changing between these Reynolds numbers by Linke [68], in agreement with these findings. This lack of change in $C_p$ is further emphasised by the interpolation of $C_p$ over the measurement surface in Figure 3.9.

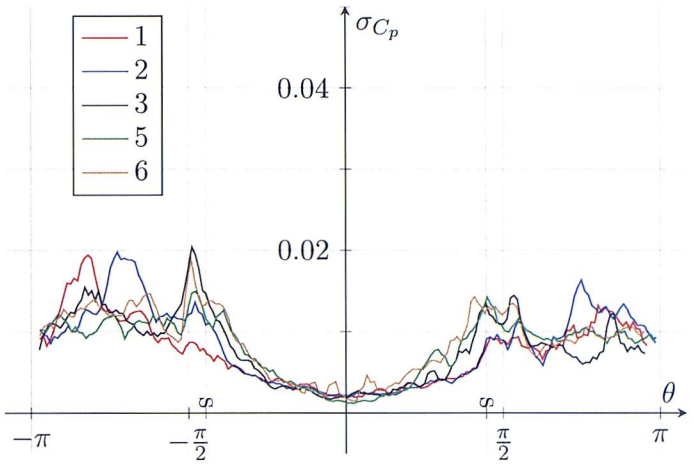
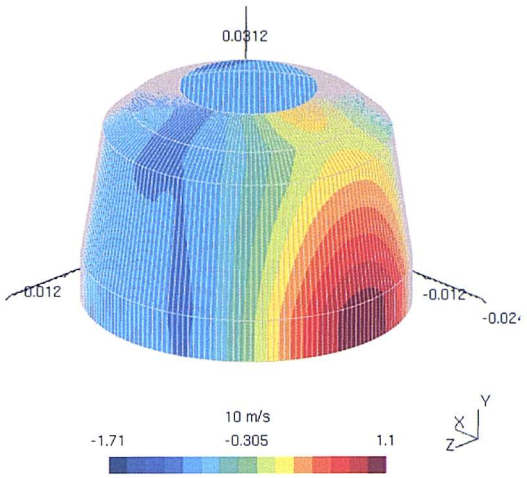
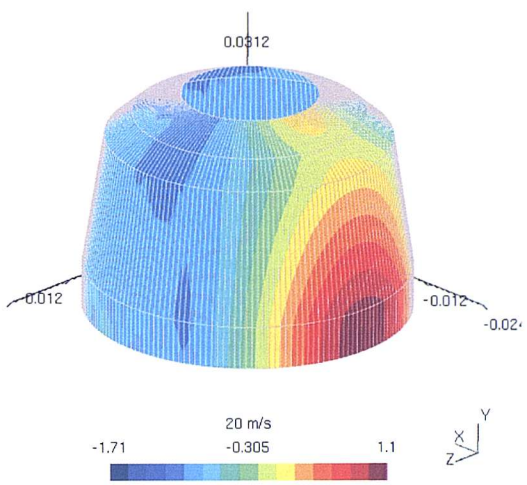



Figure 3.8: Standard deviation of the $C_p$ at taps one to six, for $Re = 66 \times 10^3$. An asymmetry in the measurement fluctuation appears to be present, in spite of efforts during the experiment to ensure symmetry.




(a) $Re = 33 \times 10^3$




(b) $Re = 66 \times 10^3$

Figure 3.9: Pressure coefficient on the surface of the axially symmetric anemometer at different Reynolds numbers. The acoustic duct is blocked. The flow is in the positive $x$ direction. There appears to be little difference between the two cases.

### 3.3.2 Open duct measurements

The $C_p$ results for taps one to six with the duct open, are illustrated in Figure 3.10 and Figure 3.11. Unlike the closed duct case, this system does not have continuous rotational symmetry, due to the six support pillars. The pressure distribution no longer represents a snapshot of the pressures resulting during a given flow direction. The data valid for this snapshot occur every 60°, as the device is rotated into its symmetry position. Nonetheless, plotting the $C_p$ for all angles is a convenient way to express the data.

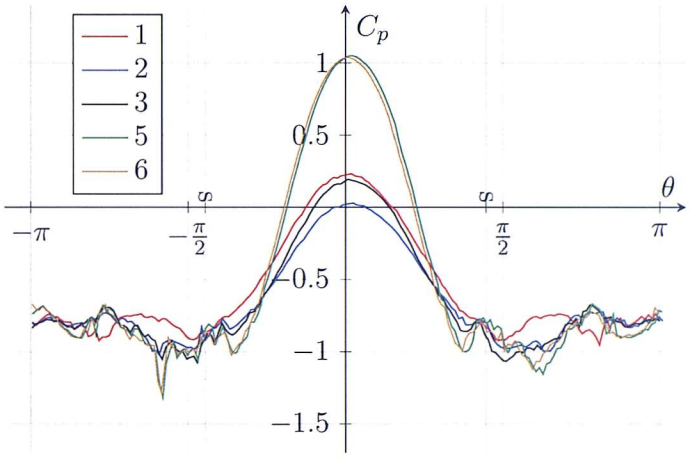



Figure 3.10: Mean $C_p$ at external taps for $Re = 33 \times 10^3$. The stagnation $C_p > 1$ may be due to measurement errors.

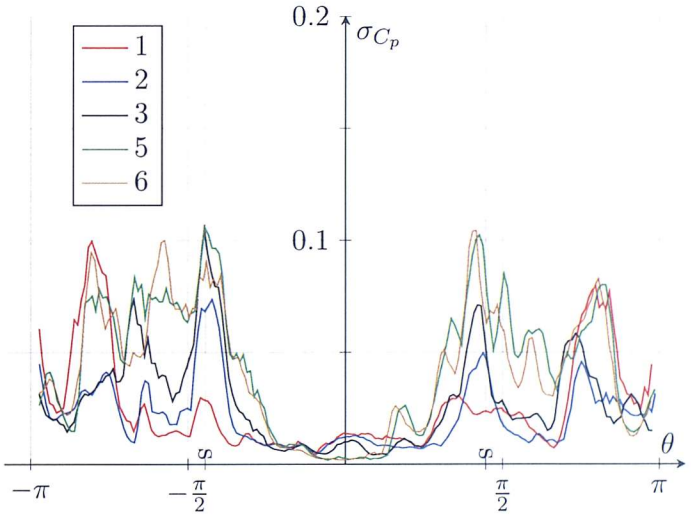



Figure 3.11: Standard deviation of $C_p$ at external taps, for $Re = 33 \times 10^3$. The y-axis range has been increased by a factor of four relative to the closed duct results.

Opening the duct has increased the fluctuations of $C_p$ at all of the outer taps. The boundary layer separation point is no longer clearly defined, and the standard deviation of all results has increased significantly. The interaction of the flow through the duct with the flow around the body appears to have increased the complexity of the system, and it is behaving

less like a circular cylinder. The comparison of $C_p$ for the open and closed duct case at tap six (the tap closest to the duct) in Figure 3.12 shows this change of behaviour clearly.

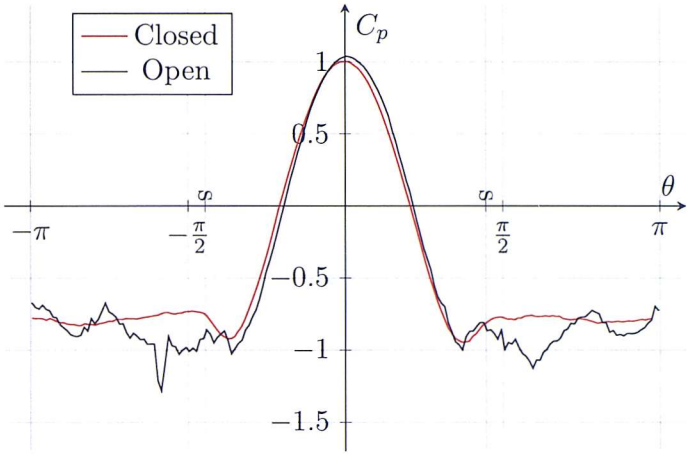
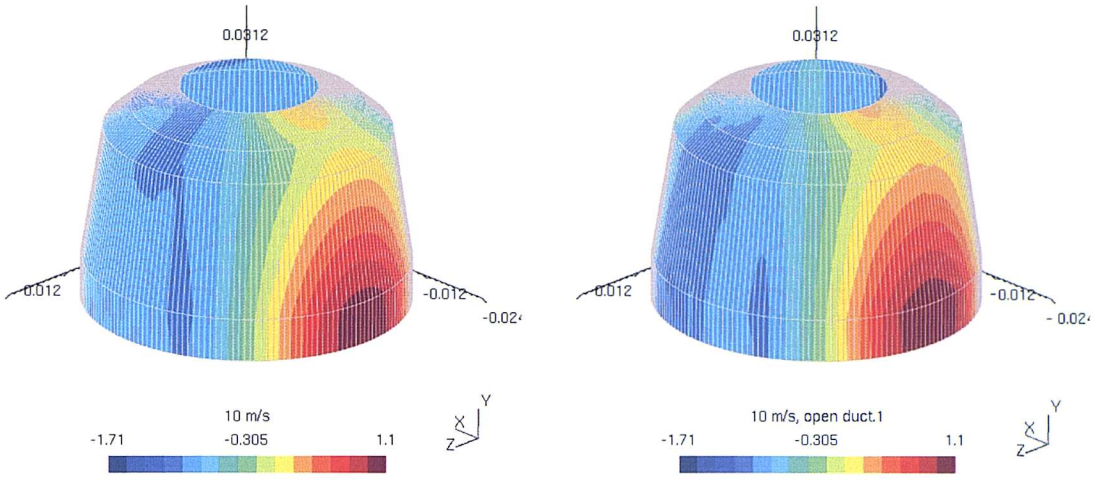



Figure 3.12: Effect on mean $C_p$ at tap six, of opening the acoustic duct at $Re = 33 \times 10^3$. The angle of boundary layer separation appears similar for the two cases, but is less clearly defined for the open duct case. The $C_p$ distribution is no longer smoothly varying after 80°.

The effect of opening the acoustic duct on the $C_p$ over the surface is presented in Figure 3.13. The distribution of pressure over the surface has changed: with $|\theta| > \frac{\pi}{2}$, $C_p$ has decreased. This is apparent from Figure 3.12, for tap six; Figure 3.13 shows the lower pressure to extend along the indicated $y$ axis.




(a) Closed acoustic duct.

(b) Open acoustic duct.

Figure 3.13: Pressure coefficient on the surface of the anemometer at $Re = 33 \times 10^3$, with the acoustic duct closed, and open. Flow is in the positive x direction. The duct is 6 $mm$ below the lowest coordinate for both images. The open duct case shows a decreased pressure region with $|\theta| > \frac{\pi}{2}$.

With the duct open, $C_p$ results inside the duct are now meaningful. Two sets of data are available, as the taps on one surface can be rotated relative to the taps on the opposing surface, as illustrated in Figure 3.1. One set of taps was rotated to be in-line with the support pillars (taps seven to ten), while the second set were aligned in between the pillars (taps fourteen to seventeen). The relative positions of the measurement taps to the support pillars is indicated in each plot.

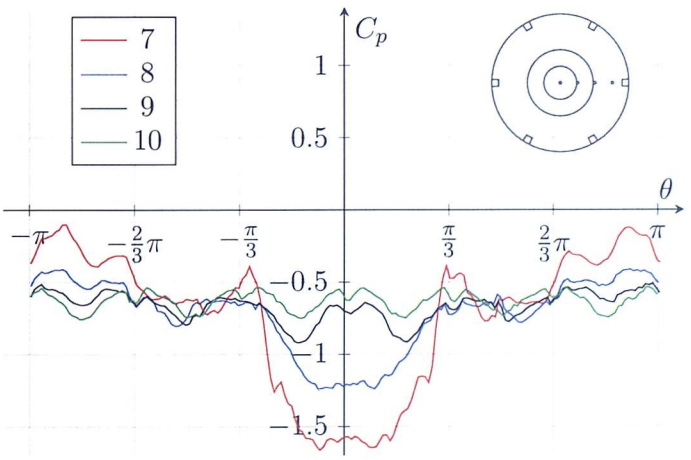



Figure 3.14: Time mean $C_p$ at internal taps for $Re = 33 \times 10^3$. The pressure taps are aligned between a support pillar pair, as indicated.

Taps ten and seventeen were opposite each other. Comparison of the results in Figure 3.14 and Figure 3.15 shows a slight difference between these two taps, possibly due to an asymmetry in the flow across the plane parallel to the major duct faces. This may be the

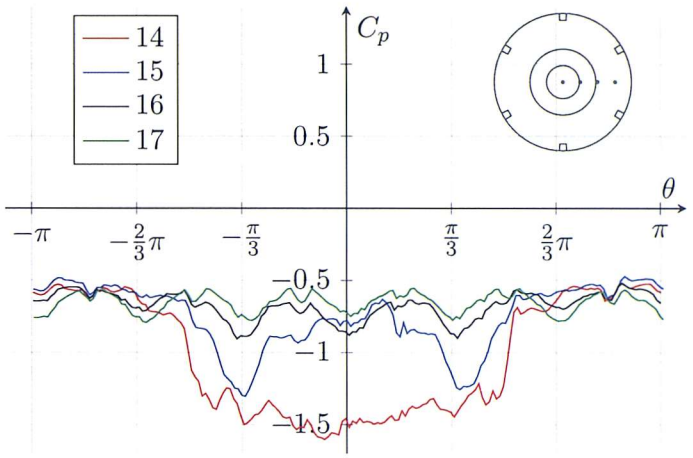



Figure 3.15: Time mean $C_p$ at internal taps for $Re = 33 \times 10^3$. The pressure taps are between the support pillars, as indicated.

case, as the support rods on opposite sides of the anemometer differ in radius.

The shadow cast downstream by the support pillars is illustrated in the result for tap fifteen, by a drop in $C_p$ close to $\theta = \pi/3$. The dip is not as deep at $2\pi/3$, as the tap has moved further downstream from the pillar causing the shadow, and the wake has been mixed into the flow.

$C_p$ for taps seven and fourteen, show large negative values when pointing upstream, due to the motion of the fluid as it passes over the lip and into the duct: it is possible that the boundary layer separates close to the entrance of the duct, passing over these two taps before re-attaching close to taps nine and sixteen. Taps nine and sixteen show $C_p$ largely constant with rotation, apart from the cyclical change due to them moving in and out of shadows from the support pillars.

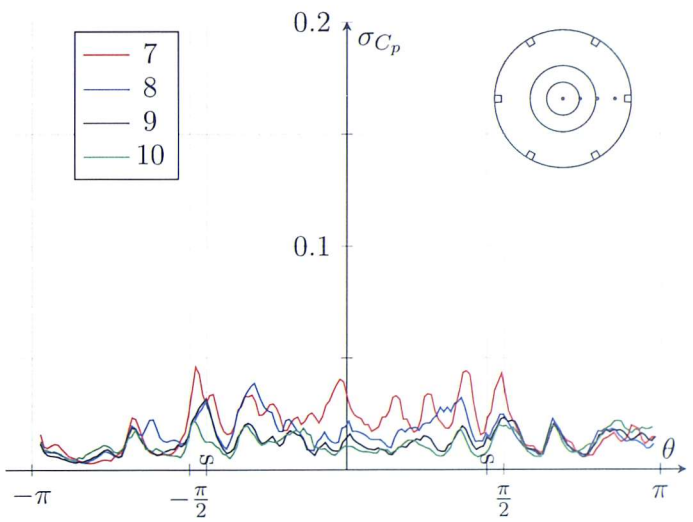
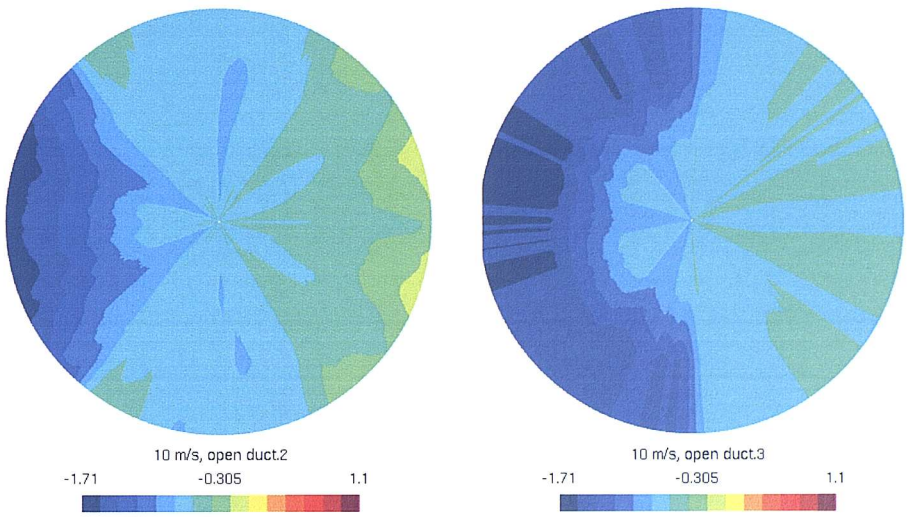



Figure 3.16: Standard deviation of $C_p$ inside the duct, for $Re = 33 \times 10^3$. The relative orientation of the taps and the acoustic duct support pillars is indicated.

Comparison of Figure 3.11 and Figure 3.16 shows that the standard deviation of $C_p$ inside the duct is less than that outside, for $Re = 33 \times 10^3$: indicating the instabilities in the external field have a reduced influence inside the duct, and that the instabilities occurring inside the duct result in smaller, low frequency fluctuations than those outside.

As the taps rotate to the downstream side of the anemometer, the deviation lessens: the turbulence appears to decrease as the flow passes through the duct. A regularity to the deviation with angle is apparent, related to the support pillar shadows.

The $C_p$ over the duct surfaces is plotted in Figure 3.17. No wakes are visible from the pillars, as the pillars are rotating around the body as the measurement angle changes. The in-line case shows a lower $C_p$ value over a narrow region pointing upstream. The out of line case shows the $C_p$ value to be less negative, but to be spread over a wider region.




(a) Support pillars in-line with taps.

(b) Support pillars not aligned with the taps.

Figure 3.17: Comparison of the pressure coefficient on the duct surface for $Re = 33 \times 10^3$: with and without the support pillars in line with the pressure taps. Flow is nominally from left to right.

### 3.3.3 Unstable state

Original measurements made with a multi-tube liquid filled manometer showed different stable states were possible with the same measurement conditions. These states would last a few seconds, then change with no deliberate change to the experiment.

Comparison of the $C_p$ difference between taps eleven and twelve shows the effect clearly: Figure 3.18 shows the difference at $Re = 33 \times 10^3$, Figure 3.19 the difference at $Re = 82 \times 10^3$.

Varying the Reynolds number is shown to change the effect: below $Re = 66 \times 10^3$, the pressure coefficient showed large irregular changes: the mean pressure field was changing. Above $Re = 66 \times 10^3$, it appeared that $C_p$ had preferred, discrete values, and

the fluctuations were smaller. In particular, $Re = 82 \times 10^3$ showed a preferred state which changed with rotation, as indicated in Figure 3.19.

No attempt has been made to simulate this effect, due to the long solution times involved (as described in Chapter 4), but lower Reynolds number simulations show vortices are shed by the support pillars in the duct. This meta-stable behaviour may be due to an interaction of the vortices shed by leading edge support pillars, with the field downstream from them and possibly outside of the duct.

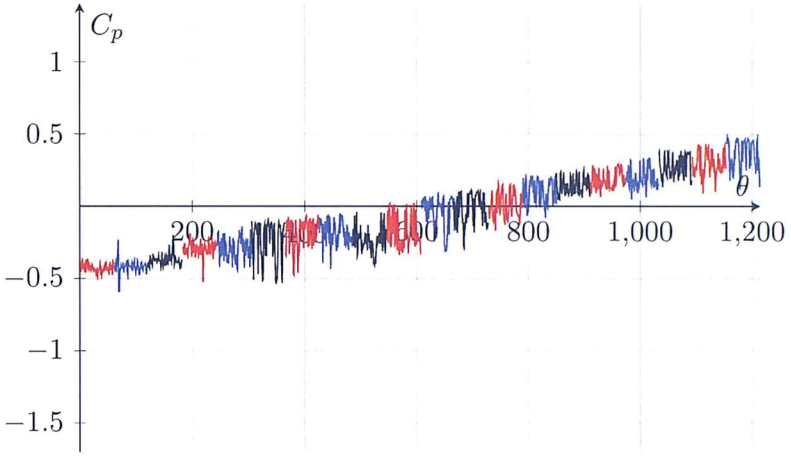



Figure 3.18: $C_p$ difference between taps eleven and twelve, as the open duct anemometer was rotated in one degree increments. Measurement rate was one per second, with sixty seconds per position. Each colour segment represents sixty samples. Samples appear to be evenly distributed about the mean for each position. $Re = 33 \times 10^3$.

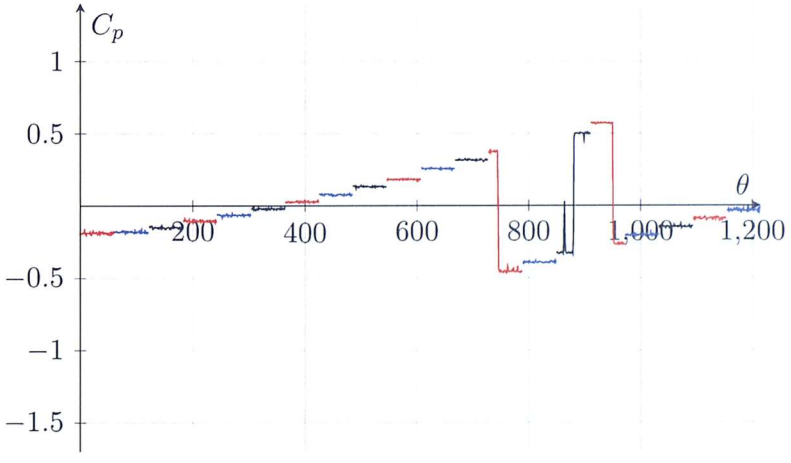



Figure 3.19: $C_p$ difference between taps eleven and twelve, as the open duct anemometer was rotated in one degree increments. The measurement rate was one per second, with sixty seconds per position. A bi-stable state is illustrated in the $700\,s \sim 1000\,s$ region, unlike the lower Reynolds number case. $Re = 83 \times 10^3$.

| Tap | Duct closed $Re = 33 \times 10^3$ | Duct closed $Re = 66 \times 10^3$ | Duct open $Re = 33 \times 10^3$ |
|---|---|---|---|
| 1 | $-1.04$ | $-1.14$ | $-7.97 \times 10^{-1}$ |
| 2 | $-9.43 \times 10^{-1}$ | $-9.83 \times 10^{-1}$ | $-8.04 \times 10^{-1}$ |
| 3 | $-9.12 \times 10^{-1}$ | $-9.28 \times 10^{-1}$ | $-8.36 \times 10^{-1}$ |
| 5 | $-8.09 \times 10^{-1}$ | $-8.05 \times 10^{-1}$ | $-7.39 \times 10^{-1}$ |
| 6 | $-7.79 \times 10^{-1}$ | $-7.77 \times 10^{-1}$ | $-6.72 \times 10^{-1}$ |

Table 3.1: Mean base pressure coefficients. Tap number four was fouled.

### 3.3.4 Discussion

Results for the time-mean pressure coefficient, $C_p$ on the surface of an anemometer, and on the walls of the acoustic duct have been presented. The $C_p$ was not steady, but fluctuated around a mean value: the fluctuation has been expressed by calculating the standard deviation of each sample set: $\sigma_{C_p}$. $C_p$ fluctuations could be due to imperfect experimentation (a lose edge, for example); vortices being shed; or turbulence.

The measurements were performed by piping the tapped pressure through approximately two metres of tubing with an internal diameter of $8\,mm$. The effect of this approach would be that of a low-pass filter, in frequency. Measurements were made once every second, for at least fifteen seconds for each case. This low pass filter may have affected the magnitude of $\sigma_{C_p}$: in particular fluctuations due to turbulence may have been suppressed more than those due to shedding, as the frequencies involved with turbulence would be higher. Inspection of the frequency content downstream of the body in a later section of this thesis indicates that the closed acoustic duct had a clearer peak in spectral content than the open duct case. Yet, the $\sigma_{C_p}$ values for the closed acoustic duct were five times lower than those for the open acoustic duct case, implying the increase in $C_p$ variation was caused by a low frequency effect that was not due to shedding, nor small scale turbulence; and that the magnitude of these low frequency fluctuations were much larger than those due to shedding.

The simpler case of the blocked acoustic duct suggested the time-mean $C_p$ was symmetric about the stagnation point for $Re = 33 \times 10^3$ and $Re = 66 \times 10^3$. $\sigma_{C_p}$ showed the $Re = 66 \times 10^3$ case was less stable on one side than the other. The reason for this is unknown. $\sigma_{C_p}$ was of the order of 1% of the mean $C_p$. The $C_p$ varied slowly and smoothly as the angle changed.

Opening the acoustic duct allowed the flow to pass through it, and decreased the stability of the $C_p$ around the anemometer by an approximate factor of five. This indicates the flow through the duct may have been acting to destabilise the pressure around the body. The previously smooth $C_p$ distribution around the body showed rapid, non-smooth changes with position. This, together with the increased $\sigma_{C_p}$ implies an increase of sample duration could have been advantageous as rapid changes of the time-mean $C_p$ with position seem physically unlikely.

$C_p$ results inside the acoustic duct showed a clear influence from the six support pillars

around the duct periphery. The central tap in the duct showed a periodic variation in $C_p$ and $\sigma_{C_p}$, as the angle between the support pillars and the approaching flow was changed. The tap close to the duct edge showed a clear variation of $C_p$ and $\sigma_{C_p}$ with angular position: when positioned towards the upstream half of the duct, both values were larger than when it was positioned in the downstream half. This indicates the pressure on the duct walls at the entrance, is fluctuating more than at the exit. This might be expected if the boundary layer is separating near the entrance, reducing the pressure stability in this region.

A metastable state has been indicated by examining the pressure difference between two taps located at different angular positions around the body, outside the acoustic duct, and at the same position along the axis of rotation. This effect was not apparent until the Reynolds number was increased beyond $Re = 66 \times 10^3$, and the acoustic duct was open. The change of relative pressure may imply the flow close to the duct has preferred directions, not necessarily in the same direction as the external flow, and dependent on the free field velocity.

## 3.4 Low frequency velocity field

Hot-wire anemometry was used to measure the slowly changing velocity inside the duct passing through the anemometer body, as the blockage effects from a hot-wire are minimal. The hot-wire method can be used to measure velocity fluctuations showing frequency components into the $kHz$ range, so the unsteady component of the slowly varying velocity field will be resolved using this method.

The principle of hot-wire operation has been described in a previous chapter. These measurements used the constant temperature approach (CTA): the resistance of the hot-wire probe is kept constant by examining the voltage across it, and comparing it to the voltage across a reference, 'overheat' resistor. A circuit diagram illustrating its operation is presented in Figure 3.4.

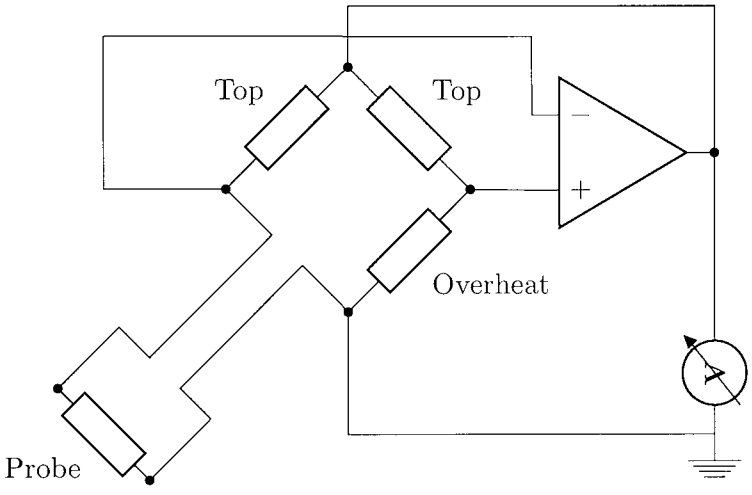



Figure 3.20: Circuit used with constant temperature hot-wire. Modified from Dantec Dynamics [29].

It is convenient at this point to define the Strouhal number,

$$S_t = \frac{fL}{u} \tag{3.5}$$

with the shedding frequency, $f$; the characteristic length (in this case the cylinder diameter), $L$; and the flow velocity, $u$.

### 3.4.1 Equipment and methodology

The hot-wire, support, cables and software were part of the Dantec Dynamics CTA kit consisting of:

- Constant temperature hot-wire: type 55P11. Calibrated as $R_{T=20\,^oC} = 3.34\,\Omega$ with a TCR $\alpha_{20} = 0.36\%/C$. $l = 1.25\,mm$, $d = 5\,\mu m$.
- Straight support, type 55H21

- Hot-wire lead, $R_L = 0.5\,\Omega$
- Four metre hot-wire cable, type A1863.
- Hot-wire power supply and signal conditioner.

The voltage output from the hot-wire signal conditioner, was digitised with a National Instruments USB-6229: a 16 bit DAC with a maximum sample rate of $250\,kS/s$, this rate decreasing with the number of sampling channels used. A second signal conditioner was used to manipulate the voltage provided by the Dantec equipment, prior to sampling. A PC was used to record the digital information. Its maximum sample frequency was observed to be $40\,kHz$. $20\,kHz$ sample rates were used during these experiments. A manual traverse was used to position the hot-wire.

The temperature of the hot-wire was maintained at the recommended $235.7°\,C$, by setting a resistor value in the hot-wire power supply unit. The resistance of the wire can be calculated using Equation 3.6.

$$R = R_{tot} + \alpha_{20} R_{20} \left(T_s - T_0\right) \tag{3.6}$$

with the resistance, $R$; the sum of the connection resistances, $R_{tot}$; the calibration value at $20°\,C$, $R_{20}$; the temperature of the sensor, $T_s$; and the temperature the wire was calibrated at, $T_0$.

The voltage output from the hot-wire hardware had a constant voltage component due to the measurement circuit, a slowly varying component dependent on the steady flow being measured, and a varying component related to the fluctuations in the flow. To maximise the accuracy achievable with the 16-bit analogue to digital converter, a second signal conditioner was coupled to the hot-wire electronics, and used to subtract the constant voltage observed under zero flow conditions. Gain was then applied to the resulting voltage. Through trial and error, the gain was set to avoid clipping the acquired voltage over the range of tunnel velocities in use.

The temperature of the measured flow affects the amount of heat removed from the constant temperature hot-wire. This effect was compensated for, using Equation 3.7 from Dynamics [29].

$$E_c = \left(\frac{T_w - T_0}{T_w - T_a}\right)^{0.5} E_a \tag{3.7}$$

with $E_c$, the compensated voltage; $T_w$, the wire temperature; $T_0$, the temperature the wire was calibrated at; $T_a$, the flow temperature; and $E_a$, the observed voltage.

### 3.4.2 Hot-wire calibration

Regular calibration of hot-wire equipment is required, as the wire properties change slowly with time; calibration was performed every day, before taking other measurements. The relationship between the temperature compensated voltage from the hot-wire equipment

and the steady flow velocity was established, by generating a line of best fit between the two quantities. Flow velocity was measured using a Pitot-static arrangement as described previously. Flow temperatures were logged for each point, to enable compensation for the ambient temperature. A fifth order polynomial was required to minimise errors caused by the best fit process. The line of best fit follows the form of Equation 3.8.

$$U = c_0 + c_1 E_c + c_2 E_c^2 + c_3 E_c^3 + ... \tag{3.8}$$

where $E_c$ is the temperature corrected voltage and the variables $c_0$ to $c_n$ are the coefficients of best fit.

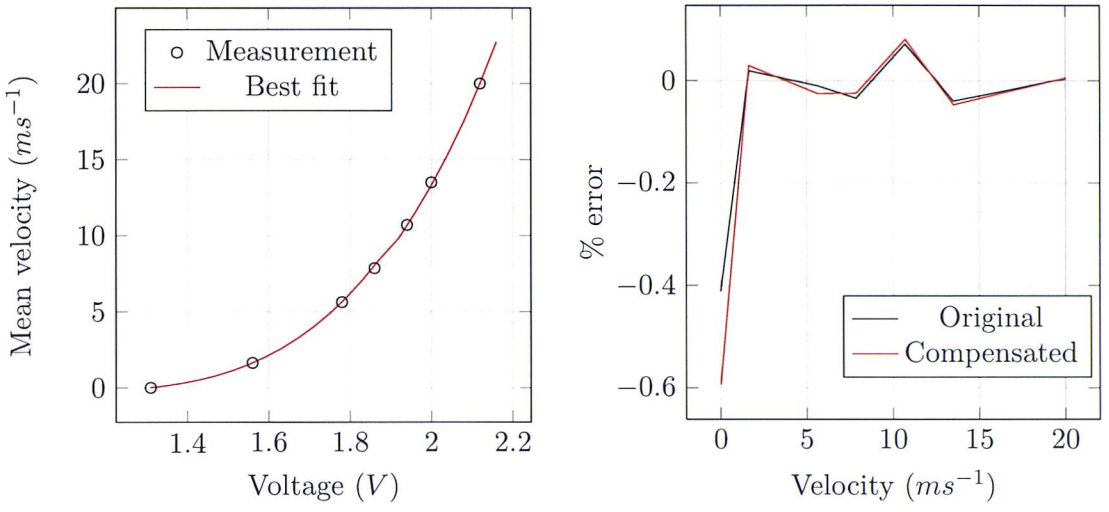
Table 3.2 shows the observed results for one such calibration. The errors in low velocity results calculated from Pitot-static tubes are inversely proportional to velocity squared (as discussed previously), so low flow speeds will result in larger errors. A fifth order polynomial generated the best-fit results indicated in Figure 3.21, using the constants:

`c = [-3.26309706, 3.4559529, 8.31110048, -14.31766057, 5.65433246].`

| | | | | % Error | |
|---|---|---|---|---|---|
| $u\,(ms^{-1})$ | $T\,(°C)$ | $P\,(kPa)$ | $\overline{V}\,(V)$ | Original | With TC |
| 20.00 | 23.16 | 102.72 | 2.117 | 0.011 | 0.014 |
| 13.53 | 23.05 | 102.72 | 2.001 | -0.064 | -0.077 |
| 10.74 | 22.97 | 102.71 | 1.938 | 0.072 | 0.078 |
| 7.86 | 22.88 | 102.71 | 1.860 | -0.006 | 0.007 |
| 5.63 | 22.81 | 102.70 | 1.784 | -0.02 | -0.0025 |
| 1.64 | 22.71 | 102.70 | 1.564 | 0.02 | 0.003 |
| 0.00 | 22.48 | 102.70 | 1.310 | -0.41 | -0.59 |

Table 3.2: Calibration data. Large percentile errors at low velocities amount to relatively small velocity errors. TC stands for, 'temperature compensation'.

The blockage was calculated using hot-wire velocity measurements upstream, and velocity measurements at the same streamwise position as the anemometer, but outside the wake. Blockage was calculated as a ratio of velocities, as $B = u0/u1$, with the upstream velocity, $u0 = 10.02\,ms^{-1}$; and the velocity at the same streamwise position as the anemometer, $u1 = 10.44\,ms^{-1}$. Blockage was therefore 4.2%, and the frontal area of the anemometer, $0.209\,m^2 \times 0.042 = 8.78 \times 10^{-3}\,m^2$. This result can be compared with the estimated figure of 3.8%, from Section 3.2.2. Since the hot-wire calibration was performed using velocities from Pitot-static tube data, in the best case, the measurement error will match that of these velocities: Section 3.2.1 shows the error to be the larger of $\pm 0.05\,ms^{-1}$, and $\pm 0.024\,ms^{-1}$ for $u = 10\,ms^{-1}$. The velocity error is therefore $\pm 0.5\%$, with a corresponding blockage error of $\pm 1\%$: the hot-wire derived blockage of $4.2\% \pm 1\%$ matching that estimated from inspection of dimensions.




(a) Measurements and best fit line.

(b) Difference between best fit and measurement, as a percentage of the measurement value.

Figure 3.21: Best fit results compared with the source data, and the resultant errors.

### 3.4.3 Turbulence intensity and length scale.

A turbulence intensity figure is required during the flow simulation, in order to seed turbulence. According to Fluent [33] the behaviour of the simulation should be relatively insensitive to the turbulence intensity level specified at the inlet, as long as it is physically realistic. This is due to it being used to generate values for the turbulence kinetic energy and dissipation. Nonetheless, it is a figure of interest, and as such it is included.

The tunnel turbulence intensity was measured at the front of the test section, close to the Pitot-static tube, in the centre of the flow. The extra signal conditioner providing extra gain and voltage offset was essential, to offset the constant voltage component, and to increase the gain to the point where the quantisation error, and electronic noise contributed minimally to the turbulence figure.

If the slowly changing flow velocity is defined using the average and fluctuating components as,

$$U = \bar{U} + u \tag{3.9}$$

then the relative (turbulence) intensity can be defined according to Hinze [53] as,

$$\frac{\sqrt{\bar{u^2}}}{\bar{U}} \tag{3.10}$$

Output from the hot-wire circuitry was recorded on two channels, both of them were direct coupled. The first used unity gain, the second used a voltage offset, and variable gain. The first channel was used to measure the mean velocity, the second to measure the varying component. The second channel was necessary as the 16 bit resolution of the AD converter

was not great enough to resolve the turbulence intensity in this tunnel.

The lowest turbulence intensity the unity gain case can measure is determined by the velocity causing the smallest detectable voltage change of the mean velocity. The 16 bit device, with a maximum range of $\pm 10\,V$ gives

$$dV_{min} = \frac{20\,V}{2^{16}} = 0.305\,mV \tag{3.11}$$

A $10\,ms^{-1}$ flow caused a mean voltage reading of $1.9291\,V$. Using the calibration coefficients, the smallest detectable voltage change implies a velocity change of $0.1189\,ms^{-1}$. The lowest turbulence intensity attainable is therefore,

$$TI_{min,\,16\,bit} = 100\% * \frac{0.1189\,ms^{-1}}{10\,ms^{-1}} = 1.19\% \tag{3.12}$$

Using the second channel with DC coupling, voltage offset and extra gain provides an increase of resolution. The extra circuity involved in channel two generated extra noise, however. This noise is not differentiated from the turbulence signal and so contributes to the turbulence intensity calculated. By measuring at different gains and plotting the calculated turbulence intensity, the lowest value gives a figure which will be closest to the true turbulence figure.

The final figure should include an error, determined by the fluctuation that could be occurring undetected by the last bit of the A/D converter. Equation 3.11 is re-written, accounting for the extra gain as,

$$dV_{min} = \frac{20\,V}{2^{16} * 500} = 0.61\mu\,V \tag{3.13}$$

The velocity change associated with this voltage, at $10\,ms^{-1}$ is $2.36 \times 10^{-5}\,ms^{-1}$. The turbulence intensity bit error is therefore,

$$TI_{Bit\,error} = 100\% * \frac{2.36 \times 10^{-5}\,ms^{-1}}{10\,ms^{-1}} = 2.36 \times 10^{-4}\% \tag{3.14}$$

As shown in Figure 3.22, the lowest value is 0.14%, with a gain of 50. Increasing the gain further, resulted in an increase of observed turbulence intensity, possibly due to increased noise contribution from the amplifier. This value of 0.14% is similar to other closed return tunnel figures, for example Manshadi et al. [71] finding 0.1%.

The turbulence length scales required for the low frequency, viscous flow simulation are related to the size of the large eddies in the upstream flow according to Fluent [33]. The length scales were approximated from the size of the cells in the honeycomb filter upstream of the test section. The observed cell diameter was $0.8\,cm$.

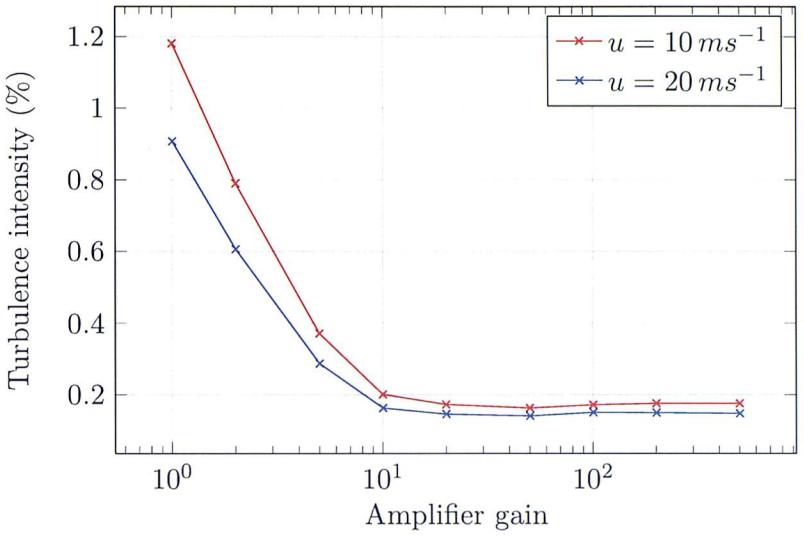



Figure 3.22: Turbulence intensity values for different gain settings. Low gain settings increased the smallest turbulence intensity figure possible, as the analogue to digital converter resolution limits are met. High gain settings result in increased noise contribution from the amplifier and other undesirable sources; increasing the observed turbulence intensity. The turbulence intensity in the free stream must be lower than the lowest point on this plot, and is therefore less than 0.14% at $20\,ms^{-1}$.

### 3.4.4 Mean velocity inside the duct

The hot-wire was positioned at the exit of the duct, with the wire in line with the anemometer axis of rotation. The wire was moved into the duct using a manual traverse: a few attempts were made to best estimate the traverse position resulting in the wire moving along the centre of the duct.

The maximum extension available was three centimetres, so the traverse had to be manually repositioned to get the full five centimetre displacement required to cross the duct. While the position display on the traverse gave an estimated extension accuracy of $\pm 0.5\,mm$, small rotational changes in the base of the traverse resulted in large movements normal to the flow, in the plane of the duct. The accuracy in this direction is estimated as $\pm 4\,mm$. The position of the wire relative to the duct major faces was easily inspected: this positional error is estimated as $\pm 0.5\,mm$.

Measurements of one minute duration were made, and averaged, to generate the data presented in Figure 3.23

The turbulence intensity results at the same positions are presented in Figure 3.24

Moving downstream from the entrance of the acoustic duct, to its exit, the time mean velocity ratio shows an initial rise, followed by a gradual reduction until the probe is close to the exit. The initial rise may be due to the flow pinching at the entrance, as it runs over the upper and lower lips of the acoustic duct. The gradual decrease may then be due to the flow moving away from the centre-line, flowing towards the sides of the anemometer.

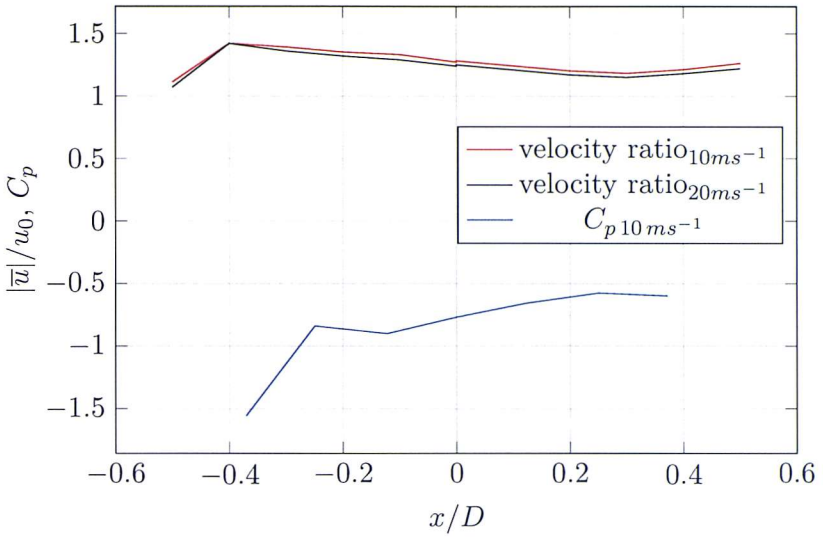
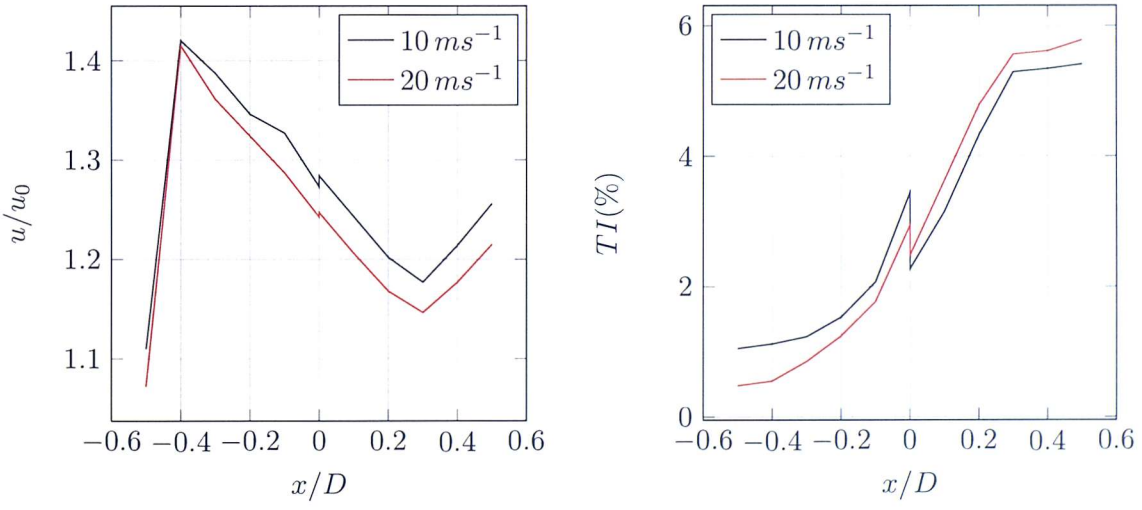



Figure 3.23: Comparison of the time-mean velocity ratio in the duct with the time-mean, low frequency pressure coefficient on the internal wall. Flow was from left to right.




(a) Velocity ratio

(b) Turbulence intensity

Figure 3.24: Turbulence intensity measurements at positions in the duct along the centre-line. These ratios show a change mid-way along the duct, as the traverse was manually repositioned. Flow was from left to right.

The rise as the probe exits the duct is unexplained: it may be due to reduced interaction of the hot-wire support with the flow.

The turbulence intensity increased as the probe moved backwards through the duct, until the probe was close to the exit. A probe at the front of the duct would be exposed to the relatively steady flow from the flow region upstream of the anemometer, and would get more exposure to eddies shed by the support pillars and the front lips as it moved downstream: this could be related to the observed increase in turbulence intensity. The decreasing time-mean velocity magnitude occurring as the probe moved downstream would cause a corresponding increase in turbulence intensity. The steadying of turbulence intensity level as the probe approaches the duct exit may be partly due to the increasing time-mean velocity magnitude in the same region.

The variation in pressure coefficient in the duct behaved differently, showing large fluctuations at the entrance, with a reduction towards the centre and the exit. Boundary layer separation at the entrance would cause pressure fluctuations in this region, while the hot-wire measurement, conducted on the centre plane of the duct, would show less variation due to this effect. Moving downstream would show increasing turbulence in the centre-plane, as vortices shed by the support pillars spread into the centre region, while the boundary layer, possibly reattaching to the acoustic duct wall, would result in increased pressure stability, relative to the separated region.

### 3.4.5 Turbulence spectra

The unsteady signal from the hot-wire can be transformed into the frequency domain by performing a Fourier transformation on the sampled data. The sample rate dictates the frequency resolution, and the sample duration sets the lowest frequencies attainable. Taking a sample that is longer than required, results in averaging over different parts of the sample being possible. According to Bruun [16], these measurements have a standard deviation equal to the spectral value. Averaging can be used to reduce the standard deviation. Spectral results here, have been generated with a time window of a length determined by the frequency of interest. The time window becomes shorter for higher frequencies, resulting in more averages and a reduction of uncertainty proportional to $1/\sqrt{n}$, where $n$ is the number of averages. The window is considered, 'adaptive'.

Power is present in the hot-wire signal at all frequencies according to Bruel & Kjaer [15]. Fourier transformed results were squared to calculate the engineering power, and divided by the size of the frequency bin to calculate the power spectrum density.

Due to the finite time-window used, the original data needed to be shaped to reduce the spectral leakage occurring in the transformed data. The shaping results in a smooth amplitude change from no data being present before the sample, to data being present, and back again to zero amplitude at the end of the sample. Numerical experimentation with synthesised data suggested the Kaiser window generated excellent spectral leakage behaviour, and a Kaiser parameter of 0.8 was selected.

The spectra recorded with zero flow is presented in Figure 3.25. The level is orders of magnitude below the levels recorded when flow is present. The non-zero result is due to limitations of the system: quantisation error, system noise and electrical pickup would all contribute to this noise floor. The electrical contamination is likely to increase when the wind-tunnel fan is operating.

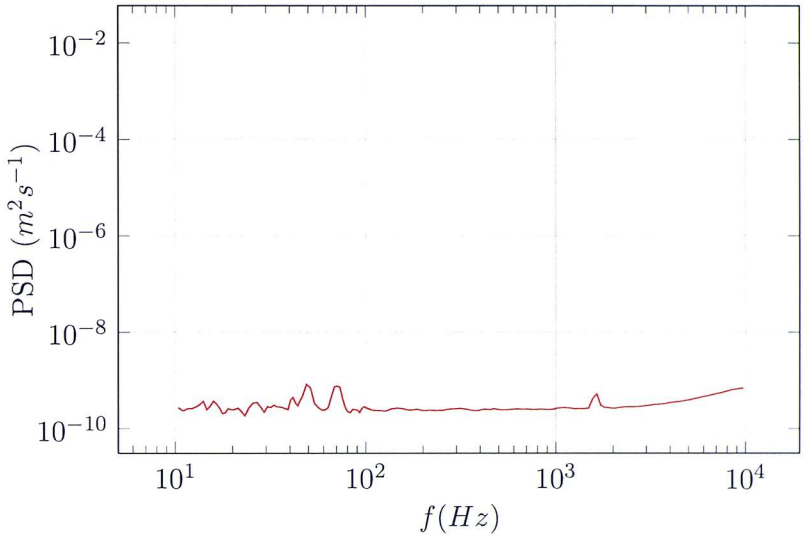



Figure 3.25: Zero flow spectra without the wind-tunnel fan operating. The effect of the 'adaptive' window is to generate a smoother response at higher frequencies.

The variation of spectra one diameter downstream from the cylinder centre with varying position normal to the flow and cylinder axis of rotation, was examined with the acoustic duct blocked. Results at a position one diameter off the centre line are plotted in Figure 3.26 for $Re = 33 \times 10^3$, and $Re = 66 \times 10^3$. Referring to Figure 3.1, this position corresponds to coordinates, $x = D$, $y = D$, $z = 0$.

Peaks at $f = 43\,Hz \pm 1.2\,Hz$ and $f = 83\,Hz \pm 1.2\,Hz$ were demonstrated for the two cases. This corresponded to a Strouhal number of $St = 0.21$.

These results can be compared with those of Zdravkovich et al. [117], in which measurements around varied aspect ratio circular cylinders were made. The Strouhal number for $L/D \approx 2$ varied between $St \approx 0.19 \sim 0.24$, and it was commented that the concept of Strouhal number appears to breakdown when three-dimensional flow (as a result of the aspect ratio) dominates. The flow around this body is significantly three-dimensional in nature, as illustrated in a following chapter.

The frequency content inside the acoustic duct is of particular interest, as the flow in this region convects the acoustic field. The probe was positioned as detailed above. The spectra are plotted in Figure 3.27, for a free-stream $10\,ms^{-1}$ flow. The upstream (negative coordinate) spectra show no emphasis of specific frequencies, showing a drop in PSD from $10\,Hz$ to $1\,kHz$, then remaining constant. Moving into the duct, downstream, the gradient of the reduction from $10\,Hz$ decreases, showing a turning close to $200\,Hz$. PSD drops again, beyond $1\,kHz$. Moving further into the duct, this effect increases, the turning

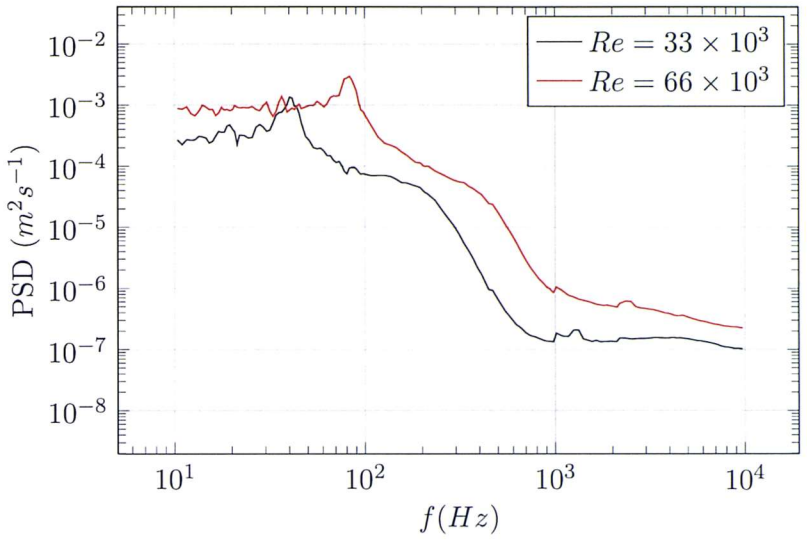



Figure 3.26: Velocity spectra at a position one diameter downstream and outside the wake, for different Reynolds numbers. The acoustic duct was blocked during these measurements.

point near $1\,kHz$ becoming clearly visible. This high frequency content may be related to vortices being shed from the support pillars. Moving further downstream, the $200\,Hz$ level increases to match the $1\,kHz$ level until at the exit of the duct, the PSD below $1\,kHz$ is approximately constant, with a reduction above; possibly due to the vortices shed by the leading support pillars dissipating as they pass through the duct. This effect is discussed further in the numerical analysis chapter, including visualisation of these vortices.

The effect of increasing the free-stream velocity to $20\,ms^{-1}$ is illustrated in Figure 3.28. The PSD level has lifted slightly, due to the increase of velocity. The trends are similar to those of the $10\,ms^{-1}$ case, but the turning point previously close to $1\,kHz$ has moved towards $2\,kHz$.

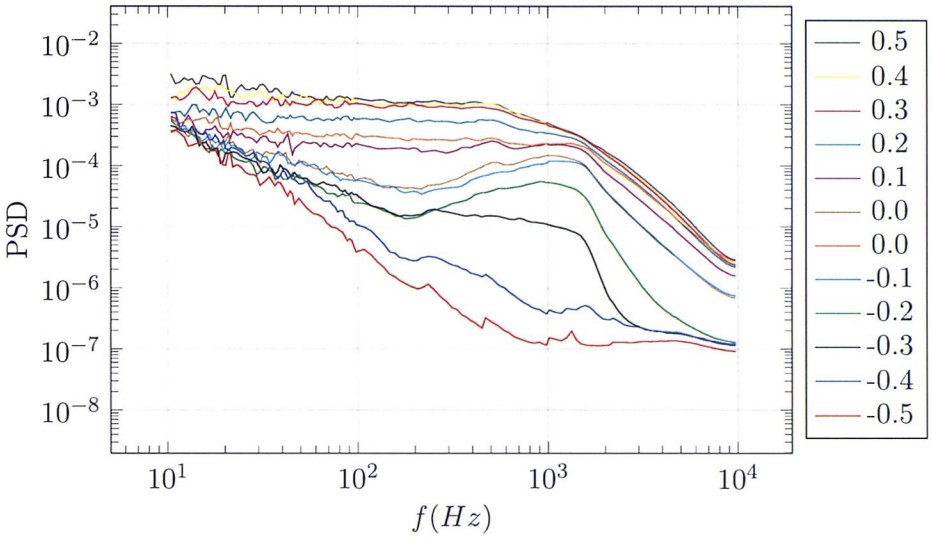



Figure 3.27: Spectra inside the duct, along the centre line and in the streamwise direction. The legend indicates the position as a multiple of the duct diameter with $-0.5$ indicating the leading edge of the duct and 0.5 indicating the trailing edge. $u = 10\,ms^{-1}$

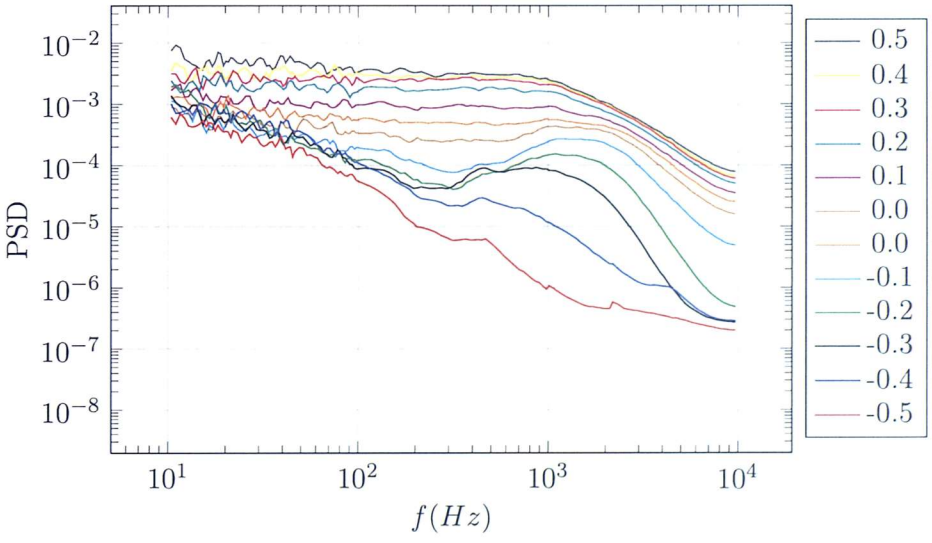



Figure 3.28: Spectra inside the duct, along the centre line and in the streamwise direction. The legend shows the position as a multiple of the duct diameter. $u = 20\,ms^{-1}$.

## 3.5 Working anemometer measurements

Measurements were made in a Flotek 1440 wind tunnel, as described by GDJ [39]. The test section was measured as $0.36\,m \times 0.36\,m \times 0.90\,m$. The anemometer duct was positioned at its centre. Pitot-static pressure was sampled $0.3\,m$ upstream of the anemometer, $0.1\,m$ from the closest wall. Temperature measurements were made $0.07\,m$ upstream from the Pitot-static tube. According to the cross-sectional area of the anemometer calculated previously, the blockage in this case is $100\% \times 8.78 \times 10^{-3}\,m^2/(0.130\,m^2) = 6.7\%$.

The tunnel was of an open-return design, with a $0.6\,m$ diameter, $11\,kW$ turbine approximately $2\,m$ downstream of the test-section. Upstream of the test-section, the tunnel flared over a distance of $0.9\,m$ to a square section of side $1.07\,m$. The tunnel entrance was packed with $0.06\,m$ long tubes of $6\,mm$ diameter, protected by a layer of gauze on the outer face. Maximum test section velocities exceeding $u = 60\,ms^{-1}$ were observed. The turbulence intensity was reported by GDJ [39] as $< 0.2\%$.

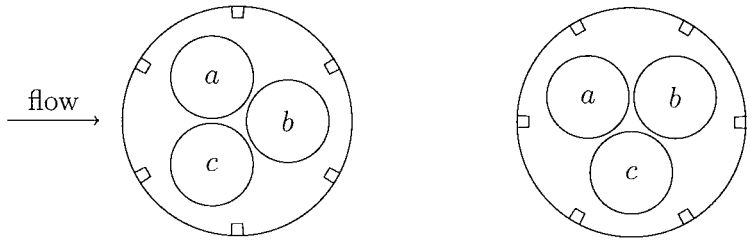
Pitot-static pressure differences were measured using the same hardware as described above but the flow velocity was computer controlled, using the output from the digital manometer: no warm up time was required. The flow temperature and static pressure outside the tunnel was measured by the micromanometer; the air density was then calculated and used with the Pitot-static results, to calculate flow velocity. Observations of the calculated velocity showed fluctuations of $\pm 1.5\,ms^{-1}$ at $u = 40\,ms^{-1}$.

The anemometer was supported in the flow with a single support rod. A computer controlled stepper motor was used to orient the anemometer for two sets of measurements as illustrated in Figure 3.29.

A working anemometer was used to measure the transfer functions between transducer pairs under different flow velocities: in this case, the transfer function was the amplitude and phase of the signal observed at a second transducer when the system was excited by the first transducer. The excitation was performed over a range of frequencies. The results will therefore include effects from (but not limited to) the transducers themselves; the electronics; conduction via the acoustic domain; conduction via the connecting structure; and coupling between electronic components.

Two sets of measurements were made, to investigate the effect of the support pillars and to obtain measurements parallel and normal to the free field velocity direction. The two orientations are illustrated in Figure 3.29. For each measurement, a frequency sweep was performed for all transducer pair combinations. An initial excitation time of $3.5 \times 10^{-3}\,s$ was used, and measurements were made during the next $3.5 \times 10^{-3}\,s$; with the excitation continuing. Each time window corresponded to approximately 120 cycles at an estimated, zero flow resonance frequency of $f = c/\lambda = 344\,ms^{-1}/0.01\,m = 34.4\,kHz$. The anemometer operated with a full acoustic wavelength across the duct.

One set of phase measurements was made, and used to generate two sets of results. The measurements were made by observing the phase at the passive transducer relative to the phase of the electrical excitation used at the active transducer: these raw results formed the




(a) Case 1 (b) Case 2

Figure 3.29: Orientation of the anemometer with respect to the low frequency viscous flow direction, for the two experiments. The support pillars used to maintain the separation between the walls of the acoustic duct, are marked in blue.

first results set. The second set was calculated by inspecting the difference in phase results for the transducer pair in question. For example, transducer, 'a' was used to excite the system and the phase at transducer, 'b' was observed. The function of the two transducers was then reversed and the measurement repeated. The difference in phase between the two measurements was used to form the second results set. This differencing approach removes any phase change that is caused by the electronics, as the same phase change is present for both measurements.

### 3.5.1 Amplitude results

As illustrated in Figure 3.29, case one features the anemometer rotated to position the front two support pillars at $\pm 30°$, with zero degrees pointing upstream. The amplitude transfer functions for a few velocities, with the pair $ac$ and $ca$ are presented in Figure 3.30. The flow velocity is normal to the line between the active transducers, for this case.

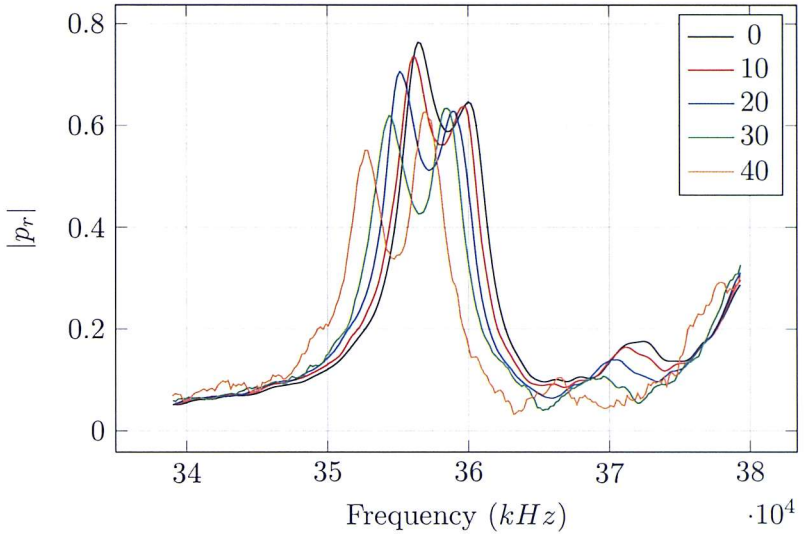
Frequency points number 216, and a five point moving average has been used to smooth the responses.

Results are sampled linearly in frequency, with a resolution of $19\,Hz$. Zero flow shows two major peaks at frequencies: $f_0 = 35643\,Hz \pm 19\,Hz$ and $f_1 = 35962, Hz \pm 19\,Hz$. These frequencies are the same for both $\overrightarrow{ac}$ and $\overrightarrow{ca}$ operation: as might be expected given the symmetry of the system.

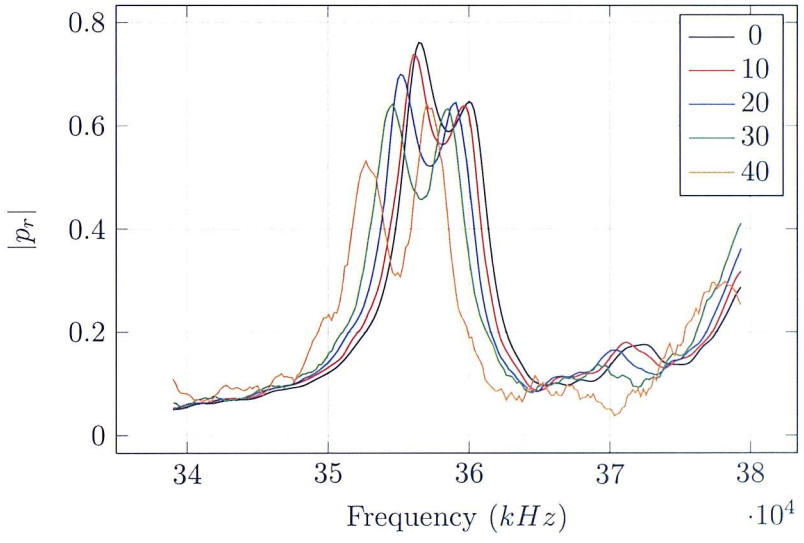
Amplitude results for case two are presented in Figure 3.31, for the pair 'ab'. This shows the effect of the acoustic propagation direction being parallel to the external flow.

As shown in Chapter 5, the first peak is associated with a resonance between the major faces of the duct. This is the frequency of interest. Increasing the flow velocity changes this frequency, as plotted in Figure 3.32.

The acoustic celerity of an acoustic wave travelling in the $z$ direction of Figure 3.1 can be calculated simply, if the flow is assumed to be travelling in the $x$ direction on the same diagram.

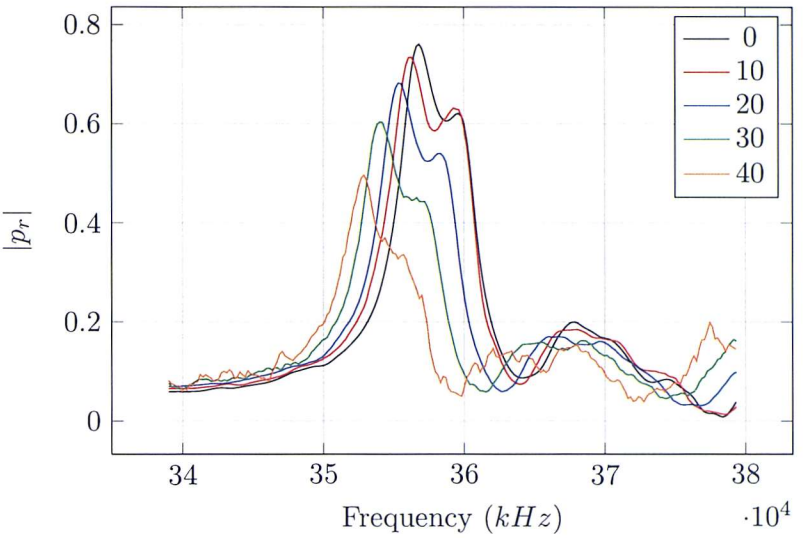



(a) 'ac' operation.

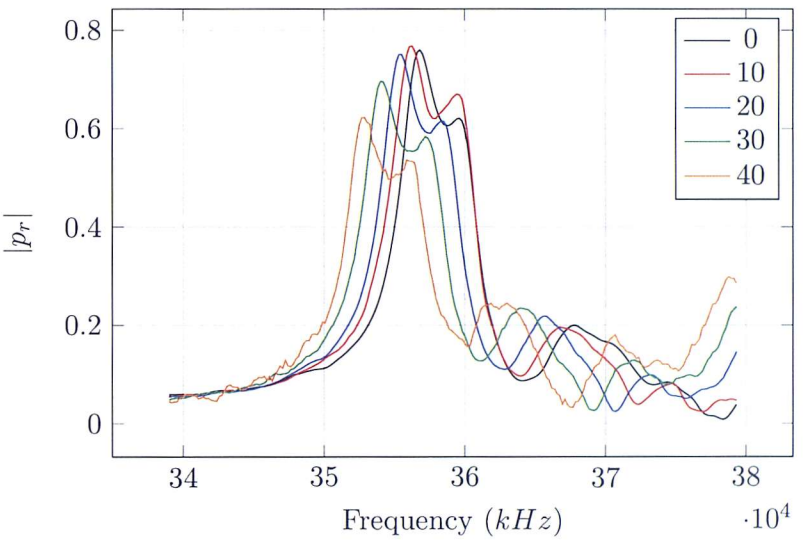



(b) 'ca' operation.

Figure 3.30: Pressure amplitude ratio for different velocities (indicated in $ms^{-1}$) for the transducer pair 'ac', case 1. A five point moving average has been used. The external flow is perpendicular to the direction of acoustic propagation.




(a) 'ab' operation.




(b) 'ba' operation.

Figure 3.31: Pressure amplitude ratio for different velocities (indicated in $ms^{-1}$) for the transducer pair 'ab', case 2. A five point moving average has been used. The external flow is parallel with the direction of acoustic propagation.

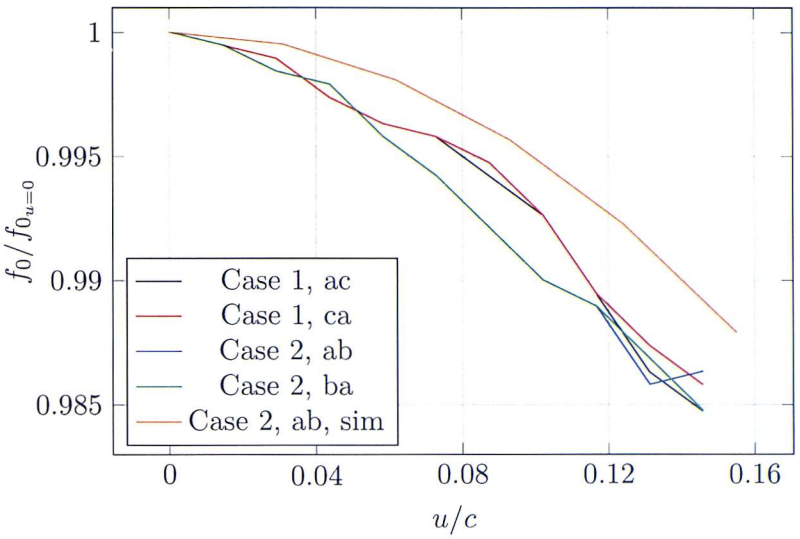



Figure 3.32: Effect of flow velocity on the frequency of the first peak as a function of the zero flow resonance frequency. Case 1 uses flow normal to the line joining the transducer pair. Case 2 uses flow travelling along the line joining the two transducers. The 'sim' value is the frequency ratio calculated using the distance triangle illustrated in Figure 3.33.

To travel in the $z$ direction in the static observation frame, the acoustic wave must travel partly in the $z$ direction, and partly against the flow: the flow continuously convects the signal in its direction, modifying the signal path observed in the static frame. The distance travelled by the signal in unit time is indicated in Figure 3.33: the signal travels from point $A$, to point $B$ and is convected by the flow, to point $C$. This process is similar to that documented in Chapter 1, to examine the behaviour of acoustic anemometers.

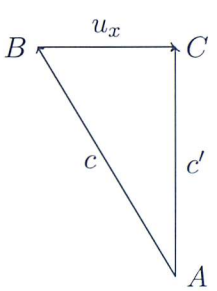



Figure 3.33: Distance travelled in unit time by a convected acoustic signal. In the frame moving with the signal, it moves from 'A' to 'B'. In the static observation frame, it moves from 'A' to 'C'. The signal moves with with celerity, $c$, in the moving frame. The flow velocity is $u_x$. The signal appears to move with celerity, $c'$ in the static frame.

The modified celerity, $c'$ can be calculated as,

$$c' = \sqrt{c^2 - u_x^2} \tag{3.15}$$

This equation was used to calculate the change of resonance frequency indicated in Figure 3.32 as 'Case 2, ab, sim', including velocity scaling for the estimated blockage of 6.7%. The difference between these calculated results and the observed results may imply a difference between the free stream velocity, and the velocity through the acoustic duct.

Table 3.3 lists the frequencies of the amplitude peak. It is shown that for the same pair, the resonance frequency remains constant, whichever transducer is active. For different pairs, this frequency can change slightly.

| | Case 1 | | Case 2 | |
|---|---|---|---|---|
| $u$ | $ac$ | $ca$ | $ab$ | $ba$ |
| 0 | 35643.8 | 35643.8 | 35681.25 | 35681.25 |
| 10 | 35606.2 | 35606.2 | 35625. | 35625. |
| 20 | 35512.5 | 35512.5 | 35531.25 | 35531.25 |
| 30 | 35437.5 | 35456.2 | 35400. | 35400. |
| 40 | 35268.8 | 35268.8 | 35287.5 | 35287.5 |

Table 3.3: Observed frequency of first pressure amplitude peak.

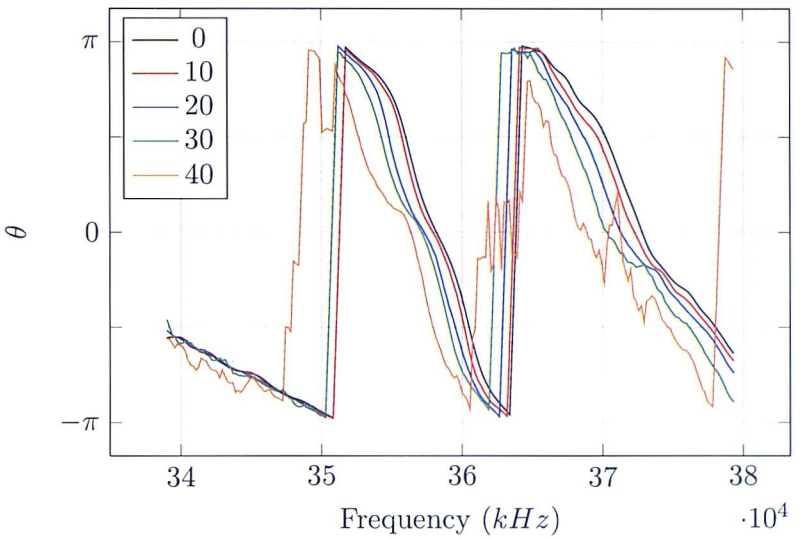
The peak occurs close to $f = 35.6\,kHz$ for zero flow: slightly different from the frequency corresponding a wavelength equal to the separation between the plates, calculated in Equation 3.16.

$$f = \frac{c}{\lambda} = \frac{\sqrt{\gamma RT}}{d} \tag{3.16}$$

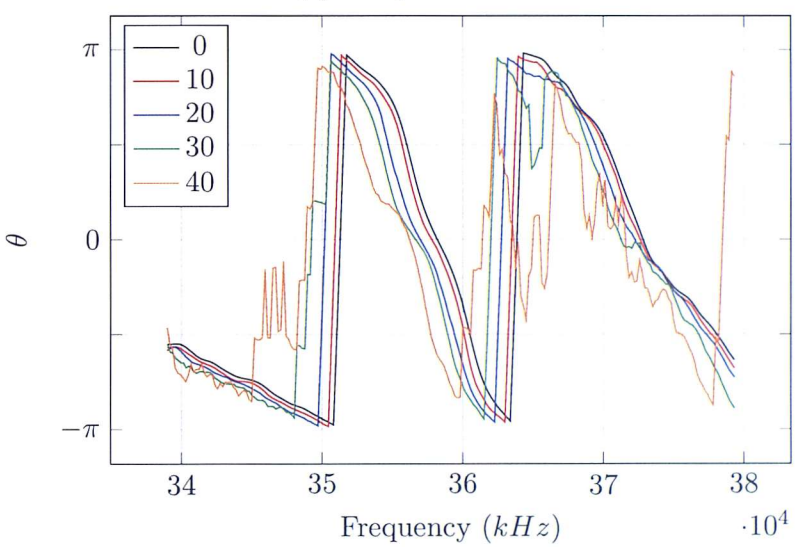
with frequency, $f$; celerity, $c$; wavelength, $\lambda$; $\gamma$, the ratio of specific heats; $R$, the gas constant; and $T$, the temperature. Using $\gamma = 1.4$, $R = 287.06\,J\,kg^{-1}\,K^{-1}$, $T = 273.14 + 21\,K$, and $d = 0.01\,m$, $f = 34381\,Hz$. This is lower than the observed frequency, possibly expected due to end effects at the duct exits causing deviation from infinite duct behaviour.

### 3.5.2 Phase results

The effect of the flow velocity on the phase difference between transducer pairs normal to the flow is shown in Figure 3.34.




(a) 'ac' operation.




(b) 'ca' operation.

Figure 3.34: Phase of pressure for the 'ac' pair, with external flow direction normal to the line joining the transducers, for flow velocity magnitudes as indicated. Reversing the pair direction does not generate identical results, possibly due to rotational position error, or an unexpected flow asymmetry.

It is shown that there is little difference in the phase observed when the operation of the transducer pair is reversed, although the results are not identical.

With reference to Figure 3.29, 'case 1', the phase observed by transducer 'b' when the duct has been excited at resonance with transducer, 'a' is plotted in Figure 3.35. This result is of particular interest as it is the result generated by simulation later in this thesis.

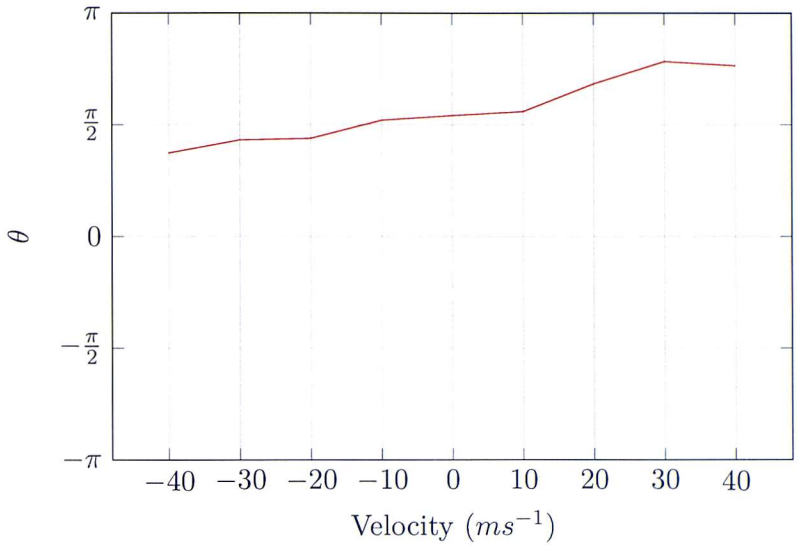
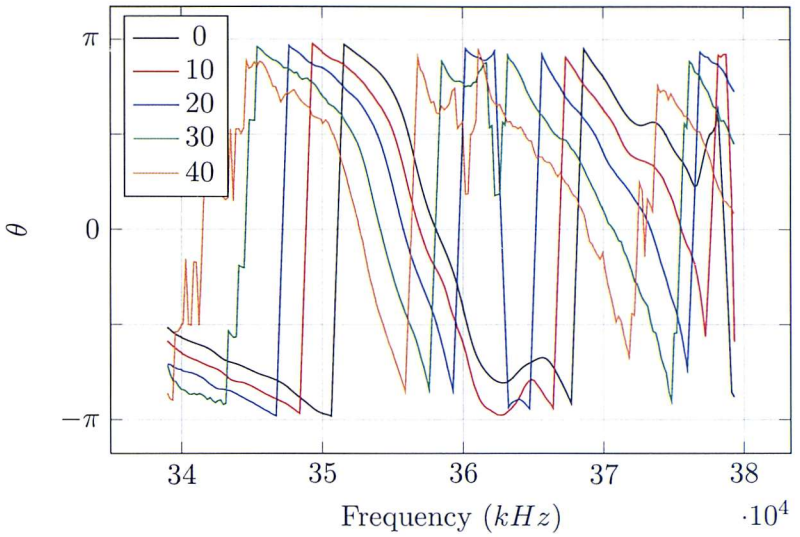



Figure 3.35: Phase of the acoustic pressure at transducer 'b', when the duct has been excited at resonance with transducer, 'a'. Least squares analysis shows the gradient is $1.7 \times 10^{-2}/(ms^{-1})$.

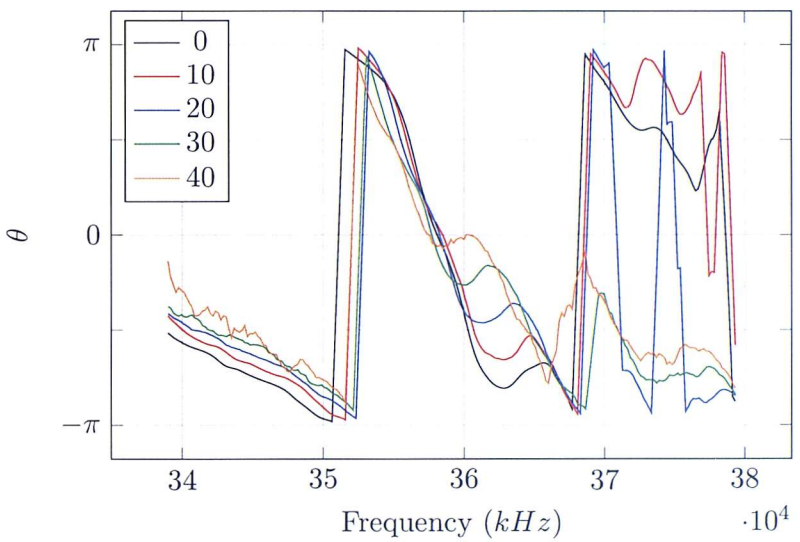
Rotating the anemometer to the 'case two' position resulted in the flow being in-line with a pair of transducers. Figure 3.36 shows that in this case, the direction of acoustic propagation relative to the flow made a large difference to the observed phase.

The phase difference between transducer pairs for case one, pair 'ac' and case two, pair 'ab' is plotted in Figure 3.37. This plot shows the reduction of noise occurring when measurement is made at resonance.

Finally, the phase difference at the frequency of the first amplitude peak for the cases of the line between the transducers being perpendicular to the free stream flow, and then normal to the free stream flow is presented in Figure 3.38. This plot indicates the phase may be changing linearly with flow velocity.

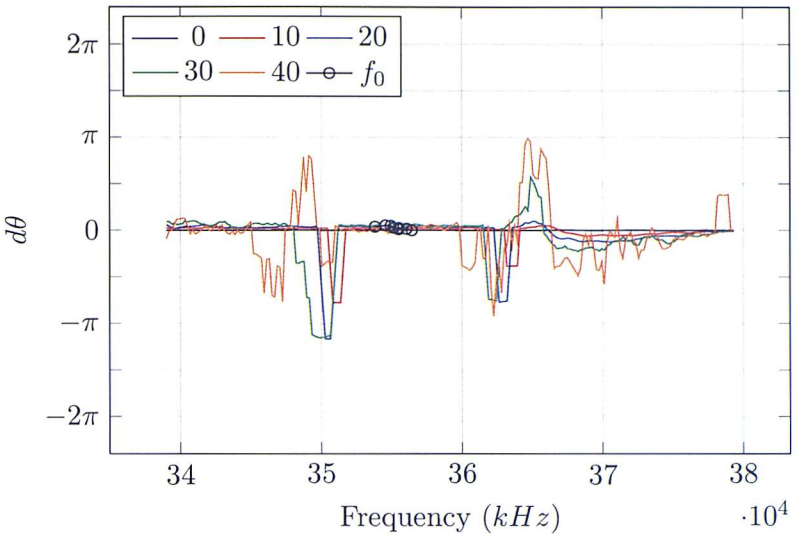



(a) 'ab' operation.

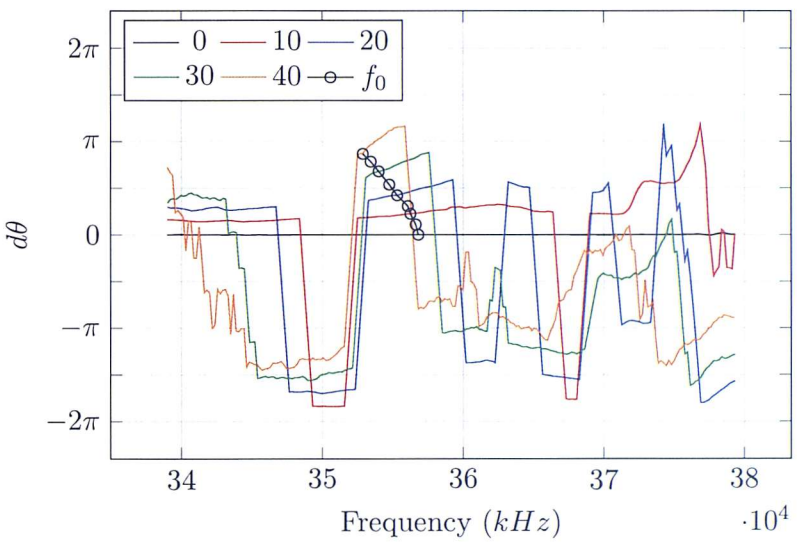



(b) 'ba' operation.

Figure 3.36: Phase of pressure for the 'ab' pair, with flow direction parallel to the line between the transducers. Velocity magnitude is indicated.




(a) Case 1, 'ac': The line between the transducers is normal to the external flow direction.




(b) Case 2, 'ab': The line between the transducers is parallel with the external flow direction.

Figure 3.37: Phase difference versus frequency, for normal and parallel transducer pair orientation, relative to the external flow. The frequency used for phase measurement during operation is indicated.

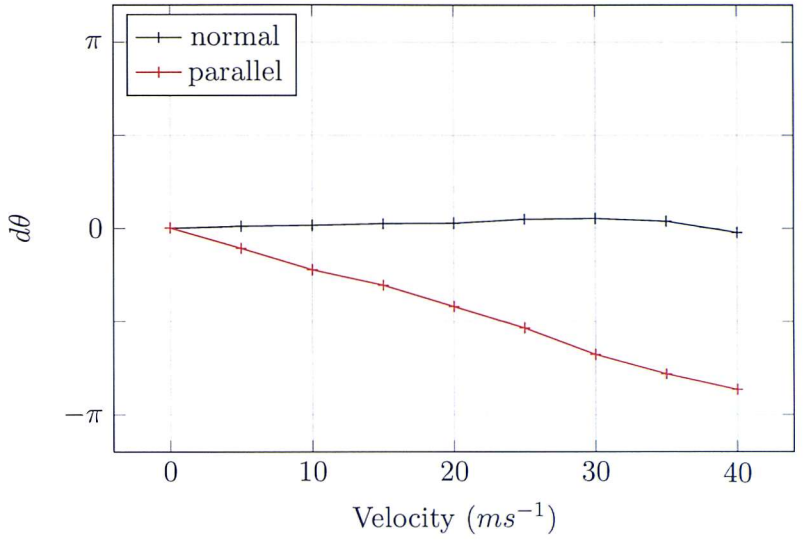



Figure 3.38: Phase difference at resonance for different external flow velocities for the case of the flow direction being normal, and parallel to the line joining the transducer pair. Little phase difference occurred when the transducer pair was normal to the flow, while a close to linear relationship between phase difference and flow velocity was suggested for the pair oriented parallel with the flow. Linear regression shows a gradient of $-6.94 \times 10^{-2}/(ms^{-1})$.

## 3.6 Conclusion

This chapter has presented the results from several sets of measurements, including:

- Turbulence intensity figures for a closed return wind-tunnel.
- The mean and fluctuating components of the pressure distribution over the surface of an acoustic resonance anemometer with its acoustic duct blocked: the object measured being equivalent to a short aspect ratio circular cylinder.
- Turbulence spectra measured outside the wake of the same object.
- The mean and fluctuating components of the pressure distribution over the surface of an acoustic resonance anemometer with its acoustic duct open to the flow: this surface extended into the duct.
- Time mean velocity values inside the acoustic duct of the same object.
- Turbulence spectra inside the acoustic duct.
- Measurements of the effect of flow velocity on the amplitude and phase of the acoustic pressure inside the duct of a functioning acoustic resonance anemometer.

These results add to the understanding of the behaviour of the flow around and through the anemometer, and to its method of operation. They will also be used in the rest of this thesis to provide experimental verification of simulation data.

The pressure coefficient results presented in this chapter show that there is little change in the pressure coefficient over the anemometer surface, in changing the external flow velocity from $10\,ms^{-1}$ to $20\,ms^{-1}$. This could be expected, as the Reynolds number for the body has changed from $33 \times 10^3$ to $66 \times 10^3$; these values falling into the sub-critical Reynolds number range. This range extends from $300 < Re < 200 \times 10^3$, so this behaviour may be stable over a wide range of velocities. However, the turbulence spectra in the acoustic duct did not show a constant behaviour with this change to the external velocity field: an increase of energy at higher frequencies was observed.

Pressure coefficient values inside the acoustic duct show a regularity with angle to the flow, possibly a result of interaction of the flow with the support pillars. The pillars may also increase the turbulence levels inside the duct. These results suggest that accurate simulations of the behaviour inside the duct, should include the effect of the pillars.

Measurements using a working anemometer showed that with increasing velocity magnitude, the acoustic pressure maxima showed decreasing frequency and magnitude. The frequency change was similar to that calculated by considering the acoustic signal to rotate into the flow and then be blown back downstream to the source position. This process is explored in more detail in Chapter 5.

# 4 Numerical analysis of the viscous flow

This chapter describes the process adopted for simulating the viscous flow field around the anemometer and through the acoustic duct. Simulation results are tested for sensitivity to simulation parameters, and compared with measurements where applicable.

## 4.1 Introduction

The low frequency, viscous flow field can be described with the Navier-Stokes equations, as discussed in Chapter 2. Direct numerical simulation (DNS) of the equations is possible, but the cost of solving for Reynolds number flows with $Re > 1000$ is prohibitively expensive. Reynolds averaging provides a means to reduce the simulation cost and is the approach adopted here.

FLUENT [33] was used to solve the Reynolds averaged Navier-Stokes (RANS) equations, simulating the low frequency, viscous flow field. FLUENT is a commercial, finite volume code which can use either the pressure correction method to solve the segregated RANS equations, or it can solve the coupled RANS equations simultaneously. FLUENT is licenced by Fluent Inc. [33]. A range of turbulence models were available to model the turbulence viscosity term required to close the RANS equations, and a range of solution methods are available to solve the chosen model. Both unsteady and steady, three and two-dimensional simulations were possible.

Three-dimensional, unsteady simulations of the anemometer were performed but in spite of the use of the RANS equations, the solution cost was still high: over a month of solution time was required to generate the unsteady field developing over a few shedding cycles of the anemometer, using the multi-core computers available during the project. For this reason, simulations using further approximations were used to establish simulation parameters such as the best turbulence model and required mesh refinement.

Two further approximations were used: reduction of the computational domain by assuming symmetries, and the removal of time variation. The computational domain size was reduced in steps: from the full, three-dimensional simulation; to a half mesh, preventing flow through the cut plane; to a quarter mesh, further extending the flow restraints; and finally to a two-dimensional mesh with no flow through the simulation plane. Each reduction reduced the simulation cost, and applied more constraints to the flow. The steady simulation removed the unsteadiness of the flow: removing shedding from the object altogether, the shedding being modelled in the mean flow. Most domain reduction steps were only possible for steady ('time-mean') solutions, a notable exception being the two-dimensional case.

The cost benefits of reducing the dimensionality of the problem were not fully realised, because of the iterative nature of the solver: the progressive departure from the three-dimensional, unsteady simulation resulted in a greater difficulty to achieve convergence of the solution. This offset has been discussed by Gresho and Sani [47] as an argument for the use of non-iterative solution methods in solving flow problems. Furthermore, numerical experiments examining the effect of the time-step size, showed that convergence became slower with larger time-steps, resulting in smaller than expected benefits in cost, as the time-step was increased.

In spite of the increased convergence difficulty, information was still gained from the use of the simpler cases, as detailed below.

## 4.2 Solution approach

The solution variables in the Navier-Stokes equations can be considered as consisting of mean and fluctuating components. Replacing the original terms with these paired terms and performing a 'time-mean' results in the Reynolds averaged Navier-Stokes equations:

$$\frac{\partial \rho}{\partial t} + \frac{\partial}{\partial x_i}(\rho u_i) = 0 \tag{4.1}$$

$$\frac{\partial}{\partial t}(\rho u_i) + \frac{\partial}{\partial x_j}(\rho u_i u_j) = -\frac{\partial p}{\partial x_i} + \frac{\partial}{\partial x_j}\left[\mu\left(\frac{\partial u_i}{\partial x_j} + \frac{\partial u_j}{\partial x_i} - \frac{2}{3}\delta_{ij}\frac{\partial u_l}{\partial x_l}\right)\right] + \frac{\partial}{\partial_{x_j}}(-\rho\overline{u_i' u_j'}) \tag{4.2}$$

where $\delta_{ij}$ is the Kronecker delta, equalling one if $i = j$. $l$ has been used as a subscript instead of $k$, as $k$ is about to be used for the turbulence kinetic energy. $\mu$ is the viscosity.

This process is discussed by Fluent [33], and in more detail by Fletcher [32]. Both equations now contain only mean variables, apart from the last term of Equation 4.2, which contains fluctuating variables: this is the term modelling turbulence.

The Boussinesq hypothesis can be used to eliminate these fluctuating terms, by relating them to the mean velocity gradients:

$$-\rho\overline{u_i' u_j'} = \mu_t\left(\frac{\partial u_i}{\partial x_j} + \frac{\partial u_j}{\partial x_i}\right) - \frac{2}{3}\left(\rho k + \mu_t\frac{\partial u_i}{\partial x_i}\right)\delta_{ij} \tag{4.3}$$

with $\mu_t$, the turbulent viscosity; and $k$, the turbulence kinetic energy. How these new parameters are calculated depends on the turbulence model adopted. $\mu_t$ is assumed to be isotropic, and scalar.

Numerical experiments during this project that used this approximation generated late boundary layer separation for a two-dimensional circular cylinder. For this reason, the Reynolds stress model (RSM) was adopted for most of the simulation of the low frequency, viscous flow.

The Reynolds Stress Model (RSM) as described by Launder et al. [66] does not assume isotropy for the turbulence viscosity. According to Fluent [33] the transport of the Reynolds stresses can be written as:

$$\frac{\partial}{\partial t}(\rho\overline{u_i'u_j'}) + \frac{\partial}{\partial x_k}(\rho u_k\overline{u_i'u_j'}) = -\frac{\partial}{\partial x_k}\left[\rho\overline{u_i'u_j'u_k'} + \overline{p(\delta_{kj}u_i' + \delta_{ik}u_j')}\right] + \frac{\partial}{\partial x_k}\left[\mu\frac{\partial}{\partial x_k}(\overline{u_i'u_j'})\right] - \rho\left(\overline{u_i'u_k'}\frac{\partial u_j}{\partial x_k} + \overline{u_j'u_k'}\frac{\partial u_i}{\partial x_k}\right) + \overline{p\left(\frac{\partial u_i'}{\partial x_j} + \frac{\partial u_j'}{\partial x_i}\right)} - 2\mu\overline{\frac{\partial u_i'}{\partial x_k}\frac{\partial u_j'}{\partial x_k}} - 2\rho\Omega_k(\overline{u_j'u_m'}\epsilon_{ikm} + \overline{u_i'u_m'}\epsilon_{jkm}) \quad (4.4)$$

also written as,

$$\frac{\partial}{\partial t}(\rho\overline{u_i'u_j'}) + C_{ij} = D_{T,ij} + D_{L,ij} - P_{ij} + \phi_{ij} - \epsilon_{ij} - F_{ij} \quad (4.5)$$

where the respective terms represent: the local time derivative; convection; turbulent diffusion; molecular diffusion; stress production; pressure strain; dissipation; and production by system rotation. $\Omega$ is the mean rate of rotation; $\epsilon$ is the turbulence dissipation rate.

Empiricism is still required to close the equations in the turbulent diffusion, pressure strain and dissipation terms, and they all depend on the turbulent viscosity, $\mu_t$:

$$\mu_t = 0.09\rho\frac{k^2}{\epsilon} \quad (4.6)$$

The empirical values were left to defaults during this project. While empiricism is still used by the RSM model, a comparison of Equation 4.3 with Equation 4.5 suggests empirical values will have a smaller influence. According to Fluent [33], the RSM model accounts for flow rotation effects with more rigour than the Boussinesq hypothesis models, and so it might be expected that simulations attempting to show these phenomena would generate more accurate results with this model.

### 4.2.1 Solution method

The RANS equations for continuity and momentum were solved numerically by FLUENT, a finite volume method solver. This approach uses a discretised form of the equations, balancing the integration of the mass flux through all faces of a given volume with the contribution from source terms inside the volume. The solution is calculated at the centre of each discretised volume, but the surface flux terms require flux values: these are extrapolated from cells upstream from the cell in question: in this case first-order 'upwinding' was used, setting the face flux value equal to the cell-centre value in the upstream cell.

The RANS equations were solved by FLUENT, using its coupled solution approach where possible. This resulted in faster convergence than the segregated approach. The coupled

solver solves the continuity and momentum equations simultaneously for all of the current fluid properties, and then solves the turbulence modelling equations using the new results from the continuity and momentum calculations. The fluid properties are updated, and the process is repeated, until the required convergence criteria are met.

The coupled approach is in contrast with the alternative, segregated approach, which solves the flow variables one at a time: for example, the $u$ velocity over the domain could be solved for using the x-momentum equation with the pressure and face mass fluxes; then the pressure could be solved for, using a different equation. This approach requires a pressure-correction step during each solution iteration, to ensure the continuity equation is locally satisfied. This approach decreased the observed solution convergence rate but less memory was required. Like the coupled approach, the turbulence equations were solved after the fluid properties were updated during each iteration, and the iterative process continued until convergence requirements were met.

The first solution iteration required the simulation domain to be initialised with a starting value: simulations in this chapter used the upstream boundary value as this first guess. The upstream boundary value was set to the measured free stream velocity, with turbulence values as discussed in Chapter 3.

Implicit linearisation was used to compute the values in each cell, using known and unknown values from the neighbouring cells. Each unknown appears more than once in the system equations, and the equations are solved simultaneously. Combined with the coupled solution, implicit linearisation is demanding on memory, as each cell has an equation for each of the coupled variables (pressure, velocity components etc.), and all of the equations in all of the cells are solved simultaneously.

## 4.3 Two-dimensional simulations

There is no previously published data on the flow around the anemometer shape studied here. Since it is circular in cross-section, simulations of circular cylinders have been used to test the flow simulations, as the pressure coefficient around the cylinder is sensitive to model quantities such as mesh refinement, and the turbulence model adopted. The flow field due to uniform flow around a circular cylinder for $Re > 150$ is three-dimensional however, so the agreement between two-dimensional simulations and measurements from circular cylinders can be limited unless measures are taken to reduce variations in the measured flow along the cylinder span. Two-dimensional simulations are appealing, as the cost is much lower than that of simulating in three-dimensions.

It is possible to asses the effects of simulation parameters using two-dimensional simulations, but with an emphasis on detection of solution convergence rather than absolute agreement between measurement and simulation. Three-dimensional simulations are required for the simulation of bluff-body flows around structures showing symmetry, such as circular cylinders. Travin et al. [106] reported that two-dimensional simulations generate too large a drag coefficient. Experiments by Szepessy [102] have shown that for a cylinder of length

ratio $l/D = 10$, pressure correlation between points separated along the cylinder length with separation greater than $D$ oscillate over time. The oscillation period was a factor of ten to twenty times lower than the Strouhal period. Two-dimensional simulations would not resolve this information.

This section presents results gained from numerical experiments with a two-dimensional mesh, using incompressible flow. Incompressibility has been assumed, as the Mach numbers tested are less that $M = 0.2$. This velocity range is below the $M = 0.3$ considered as the limit by Peat and Kirby [82] for the incompressible assumption.

It is convenient to define some quantities here. $t^*$ is a non-dimensionalised time-step, expressing a distance moved as a fraction of a cylinder diameter. $t^* = tu/d$, with the time, $t$; the flow velocity, $u$; and the cylinder diameter, $d$.

### 4.3.1 Test geometry

A parameterised mesh was created in 'Gambit', the mesh generator provided with the FLUENT solver. The mesh consisted of several regions around a circle, these regions moving out towards walls on two faces, an entrance and an exit on the other two faces. Figure 4.1 illustrates the 'reference' mesh used in this section. The region was created to approximate the measurement conditions of the wind-tunnel test section. Using $D$ as the cylinder diameter, the distance to the upstream boundary was $4.56D$; the distance to the downstream boundary, $9.14D$; the 'width' was $4.56D$.

Vertical symmetry was not exploited. The mesh was structured in the regions close to the cylinder, and unstructured in the remaining regions.

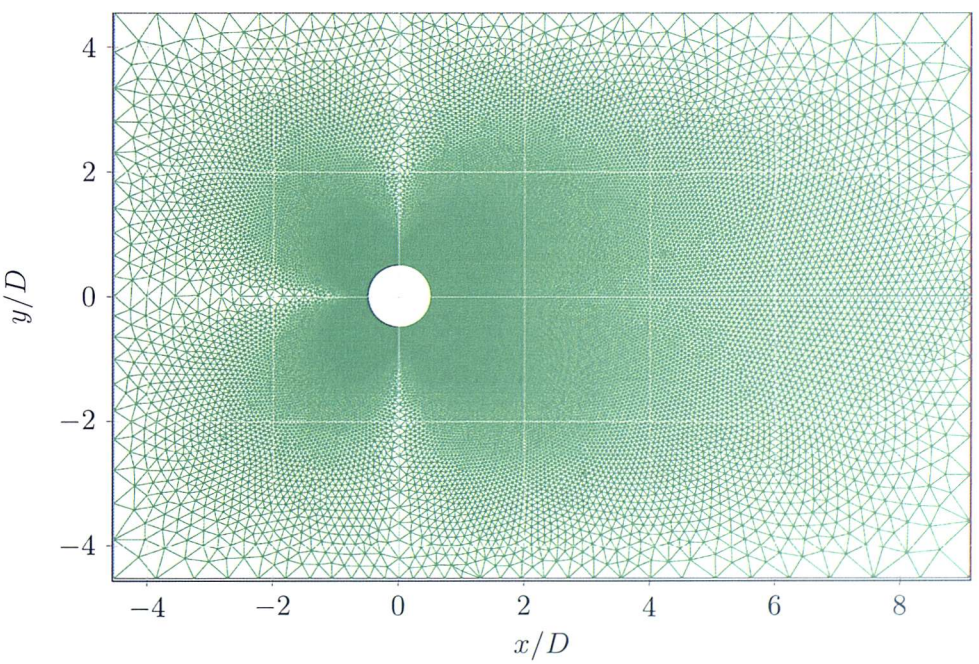



Figure 4.1: Reference mesh used for two-dimensional studies.

The refinement of the mesh next to the cylinder wall affects whether the velocity profile near the wall can be resolved. The profile near the wall can be modelled using 'law of the wall' approximations, rather than resolving the velocity profile fully. This can result in larger cells being usable in this region, but adds another approximation to the simulation. Inspection of the pressure around the cylinder surface, and the velocities close to it provide a means to assess the fidelity of the simulation, but the comparison is between measurement and a summation of the approximations made in the modelling process. Sensitivity studies provide a means to assess the effect of a single simulation variable, such as mesh density.

### 4.3.2 Steady simulations

The RANS equations can be solved assuming a stable flow solution exists. This approach can be significantly faster than the solution of the URANS equations, as a single solution is generated: in contrast with the URANS solutions which must generate a solution for each time step. When applied to flows which are clearly unsteady, such as a bluff body shedding vortices, the unsteadiness will not be resolved.

The reference mesh was used, as illustrated in Figure 4.11. Best efforts were made to achieve convergence, but as illustrated in Figure 4.2, the field downstream from the body does not show symmetry, and clear solution convergence was not demonstrated. This could be a result of poor problem convergence, or could indicate that a bistable solution exists.

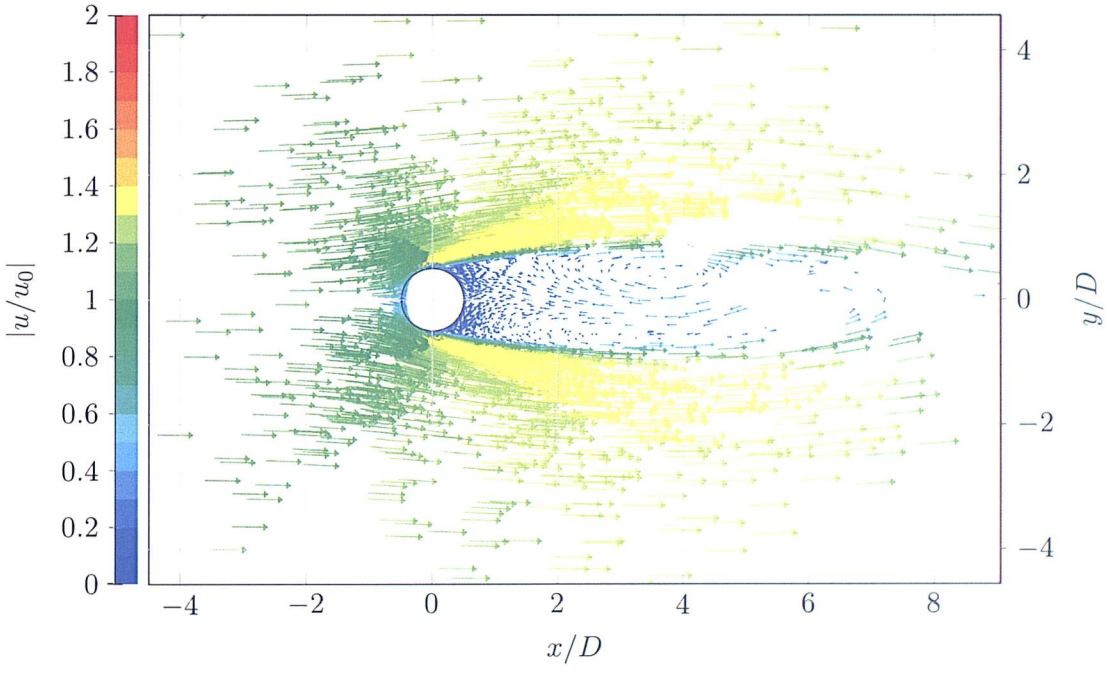



Figure 4.2: Steady flow field solution, with vectors showing steady velocity magnitude and direction. An asymmetry in the flow is present, implying difficulty in solution convergence.

The solution has generated two stretched, counter rotating regions downstream of the body. The $C_p$ around the body is plotted in Figure 4.3, showing results close to those

measured by Cantwell and Coles [18], while significantly different from those generated by URANS simulation results published by Travin et al. [106]. This was unexpected as the measurements by Cantwell were of a three-dimensional cylinder which would have been displaying a three-dimensional wake, while the two-dimensional simulation does not generate effects occurring through the plane of the mesh. The flow appears quite different from the unsteady flow around circular cylinders in the literature, but may be representative of the mean behaviour.

The simulated base pressure is less negative than that of the measurements, in agreement with the presence of the long pair of vortices downstream. An increased negative pressure value would result in a shorter separation region, as demonstrated by the URANS simulations to follow.

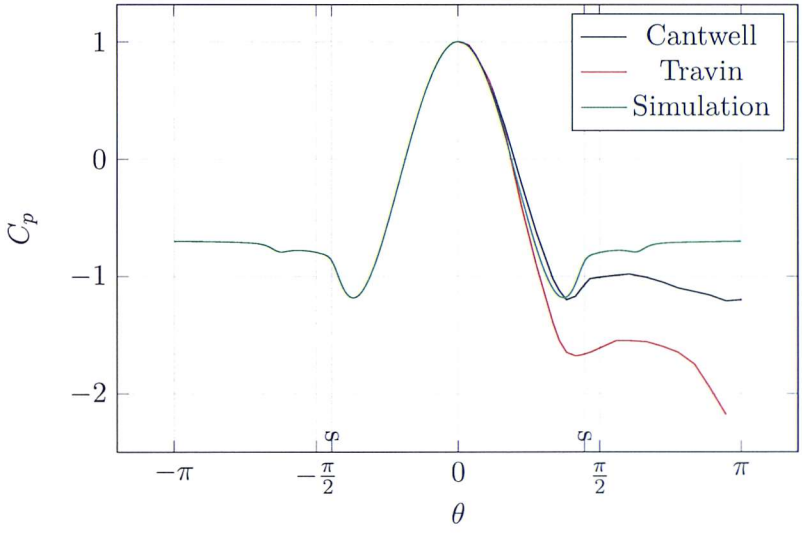



Figure 4.3: $C_p$ from a steady simulation, compared with results from the literature. 'Cantwell' shows measured data for a cylinder at $Re = 60 \times 10^3$. 'Travin' shows two-dimensional URANS data at $Re = 50 \times 10^3$. The 's' axis label marks the 80° position, the point of separation of a laminar boundary layer from a cylinder.

The steady simulation was used to determine the effect of changing the turbulence model used. The Spalart-Allmaras, k-$\epsilon$ and k-$\omega$ models all generated late separation of the boundary layer, unless the region adjacent to the cylinder was manually set to laminar. These results prompted the use of the Reynolds Stress Model for further work.

### 4.3.3 Unsteady simulations

The unsteady simulations were used to determine how close to convergence the reference mesh was. Both unsteady and time-mean results were used.

### Domain length

The effect of extending the distance to the downstream exit was tested. This is of interest as numerical experiments in the literature feature distances to the downstream exit that are larger than those used in this project, but cost prohibited further extension of the domain. For example, Singh and Mittal [97] used a total length of $38D$, while Travin et al. [106] used $15D$. It has been postulated by Zdravkovich [116] from experimental results, that a distance of $40\,D$ is required for eddy dissipation. Too short a domain will affect development of the flow field in the interest region and may cause the simulation to converge more slowly than expected.

Results from a steady solution were used to set the initial values. The flow velocity values at the shorter exit case were copied downstream for the extended case.

Figure 4.4 shows the time-shifted, unsteady $C_p$ at the rear of the cylinder, for the reference and doubled distance to exit cases. This position was chosen, as the flow velocity field is most complex at the rear of the cylinder: this is likely to be the region most sensitive to changes in the simulation.

The flow input velocity was set to $u = 20.83\,ms^{-1}$, $Re = 50 \times 10^3$ to match the values published in the literature. The turbulence intensity was set to 0.14% following measurements with a turbulence length scale of $0.01\,m$. These values are used to 'seed' the turbulence computation, and Fluent [33] states the solution should be relatively insensitive to these values. The RSM, low-Reynolds number turbulence model with a was used, with a time step of $dt = 2.5 \times 10^{-5}$, equivalent to $t^* = 0.01$.

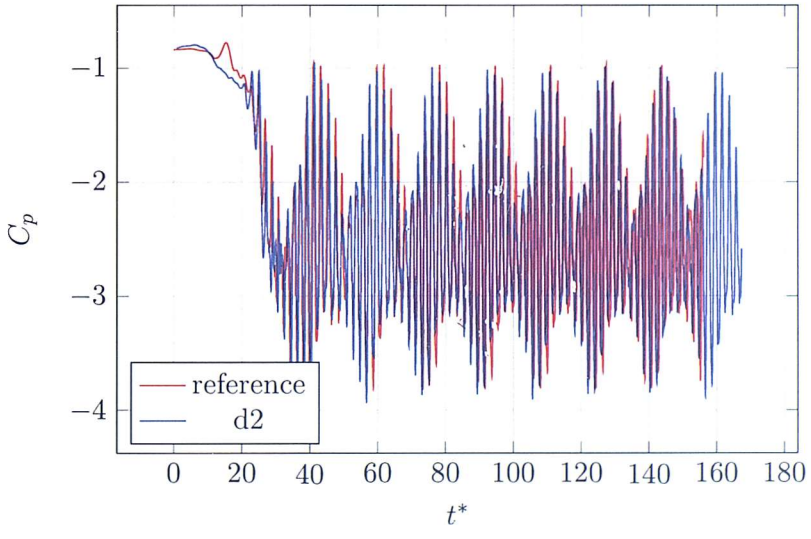



Figure 4.4: Effect of doubling the distance to the downstream boundary on the base $C_p$. A time shift of $dt^* = 2.9$ has been used to align the results. Doubling the distance has increased the shedding frequency, The difference is approximately half a cycle after 50 cycles: A 1% change. It appears that the truncated boundary makes little difference to the shedding frequency.

Figure 4.4 shows a 1% change in shedding frequency over fifty cycles: a small change. The

time-mean $C_p$ for this case is shown in Figure 4.5, and compared with circular cylinder measurements and simulation results from the literature.

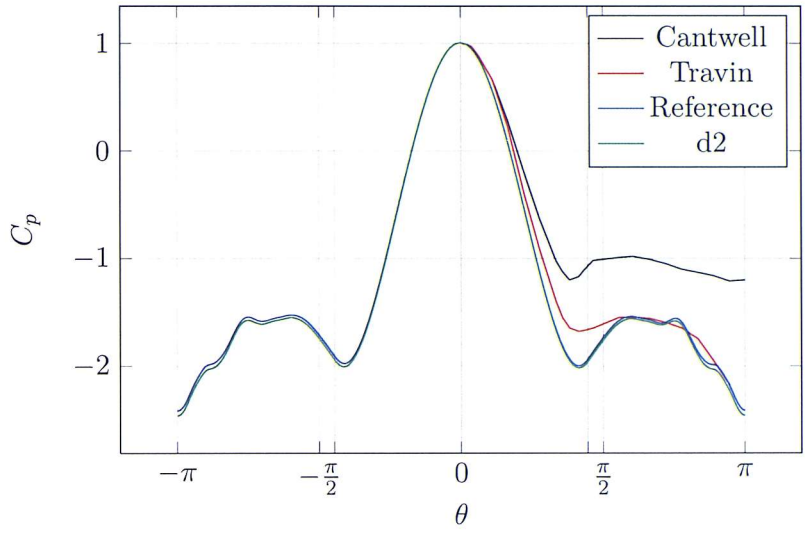



Figure 4.5: Effect of doubling the distance to the downstream boundary, on the time-mean, unsteady $C_p$ for a circular cylinder. 'Cantwell' shows measured data for a cylinder at $Re = 60 \times 10^3$; 'Travin' shows two-dimensional URANS data at $Re = 50 \times 10^3$. Extending the domain has decreased the simulated base $C_p$ slightly.

Comparison with two-dimensional URANS simulation results published by Travin et al. [106] shows good agreement between the time-mean pressure coefficient and the simulation results presented here, although the pressure coefficient just ahead of separation shows a more negative result for these simulations.

The vorticity magnitude is plotted in Figure 4.6. It is noted that the exit for the shorter domain case was at $x/D \approx 9.1$. It is demonstrated that the vorticity magnitude of the vortices leaving the domain for the extended case is lower than those of the truncated case. The contribution of errors from this source will therefore be lower for the extended domain case.

### Domain width

Previous $C_p$ plots have shown the oscillation associated with vortex shedding to be modulated by a lower frequency effect. The $y$ dimension indicated on Figure 4.1 was increased by a factor of 1.5, and a simulation performed using a time-step of $dt^* = 0.01$. The effect on the base $C_p$ is shown in Figure 4.7. It is shown that the width of the test section is related to this modulation. From inspection of results from $t^* = 85 \sim 135$, the modulating signal appears to have decreased in frequency by an approximate factor of $3/2.5 = 1.2$.

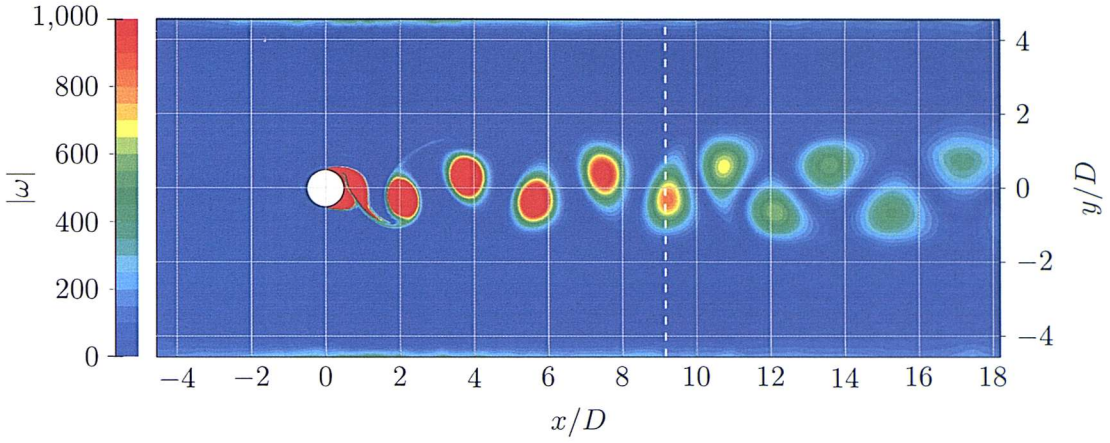



Figure 4.6: Vorticity magnitude at $t^* = 167$, with values above $1000\,s^{-1}$ saturated. The position of the reference mesh exit is marked with a dashed line. $St \approx 0.3$ from inspection.

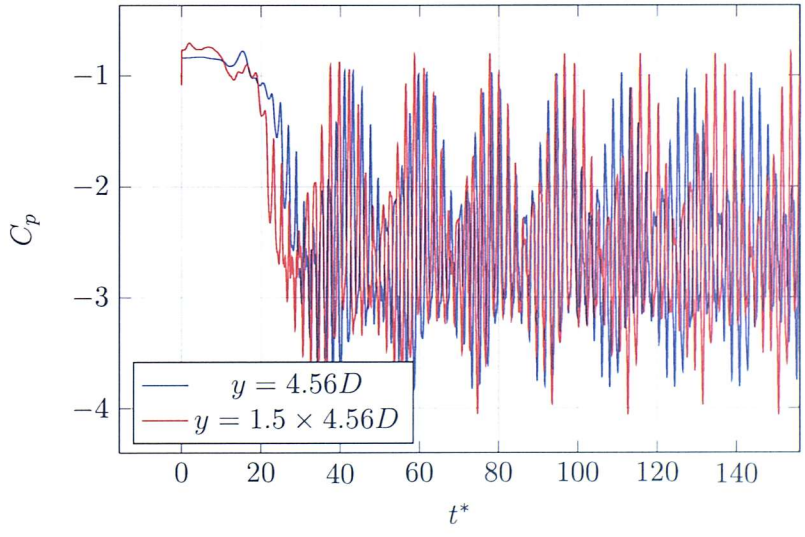



Figure 4.7: Effect on the base $C_p$ of increasing the distance to the side walls by a factor of 1.5. The modulation frequency has decreased.

### Time step

The size of time-step will affect the accuracy and the temporal detail. While it is clear that changes occurring over a step smaller than that used will not be resolved, the effect of the cumulative errors are less clear. Large time steps also slow solution convergence, offsetting the expected cost reduction implied. For the limiting case (steady RANS), three-dimensional simulations of the anemometer would not converge to spatially symmetric solutions unless symmetry planes were exploited.

Time-steps used in the literature include $t^* = 0.035 \sim 0.05$, Travin et al. [106] for URANS and $t^* = 0.0026$ for LES by Franke and Frank [36]. Cox [21] specified 300 time-steps per shedding cycle, while Iaccarino [58] used 50. Time steps of $t^* = 0.01$ and $t^* = 0.02$ were tested here. If the Strouhal number is $S_t = 0.2$, these are equivalent to 500 and 250 steps per cycle, respectively. The effect of making this change is shown in Figure 4.8 to be significant for the base $C_p$.

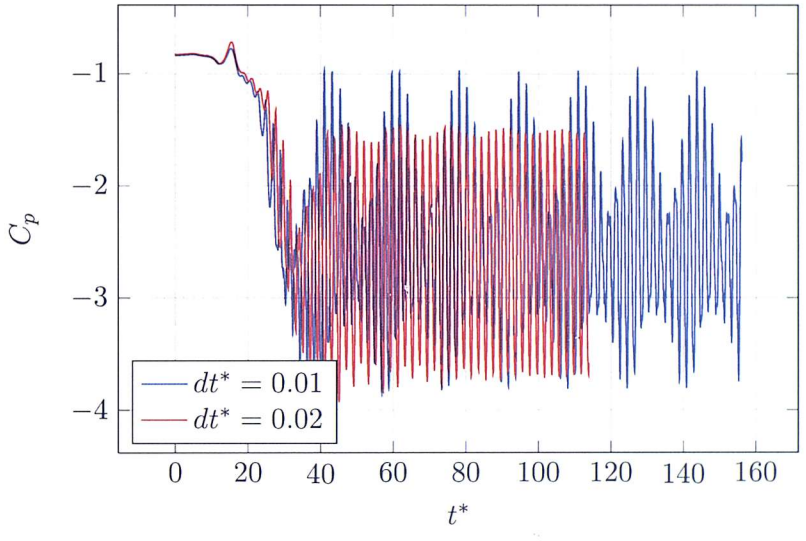



Figure 4.8: Effect on the base $C_p$ of doubling the time step. Detail appears to have been lost with the larger time step.

It is clear that detail has been lost in using the $t^* = 0.02$ time step. The frequency change is small; the change is approximately half a cycle, over the forty cycles plotted. This is close to 1%. The time-mean $C_p$ is plotted in Figure 4.9, and it shows a small (less than 0.1) change. While not converged, these time steps are smaller than those used by some in the literature. The use of smaller time-steps while possible for two-dimensional simulations, become expensive for three-dimensional cases. It is accepted that there is some error present due to the size of time steps used.

### Mesh density

At least two regions of interest existed in considering the mesh density: the near wall region, controlling the way quantities near the wall are calculated; and the region away from the wall, convecting vortices downstream.

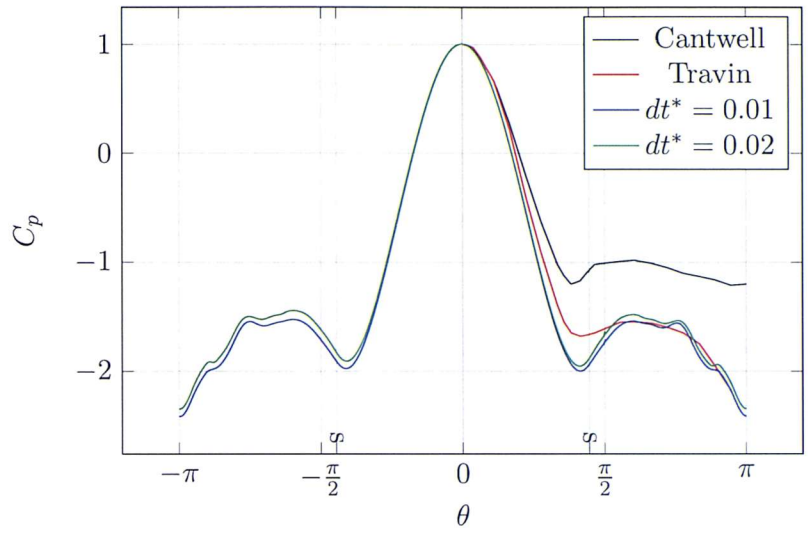



Figure 4.9: Effect of halving the simulation time step, on the time-mean unsteady $C_p$ for a circular cylinder. The smaller step resulted in a slight pressure decrease.

The thickness of the cells next to the cylinder walls control whether FLUENT adopts a 'law of the wall' approach in simulating the behaviour in this region. If the cells are relatively thick, the flow velocity profile is modelled using semi-empirical wall functions. Conversely, if the cells are thin enough, the velocity profile is resolved. According to FLUENT [33] the change occurs when the 'wall unit', $y^* > 11.225$. $y^* \approx y^+$, where,

$$y^+ = \frac{\rho u_\tau y}{\mu} \tag{4.7}$$

with the density, $\rho$; $u_\tau$, the friction velocity; the distance to the wall from the cell centroid, $y$; and the dynamic viscosity, $\mu$. Since the position of the cell centroid is used in calculating $y^+$, an ordered mesh of quadrangles or hexahedra is preferred when modelling close to boundaries.

Away from boundaries, the size of the cells limits how closely the solution can approach the smooth solution of the RANS equations. The accuracy with which structures in the fluid, and structures acting as boundaries can be represented is also set by the cell size. High cell counts result in expensive simulations, so the mesh should not be finer than it needs to be.

Attempts to use coarse meshes and wall functions with the RSM turbulence model resulted in poor performance: separation occurred at a larger angle than expected. For this reason, a fine mesh was used close to the body. The $y^+$ values around the cylinder at a moment during the $dt^* = 0.01$ case above are plotted in Figure 4.10. The figure shows low values of $y^+$, showing the velocity through the boundary layer was resolved.

The mesh close to the cylinder is presented in Figure 4.11, which shows the instantaneous flow velocity magnitude. The ordered mesh region has more than twenty cells through its thickness, resulting in more than ten elements being present across the region of high

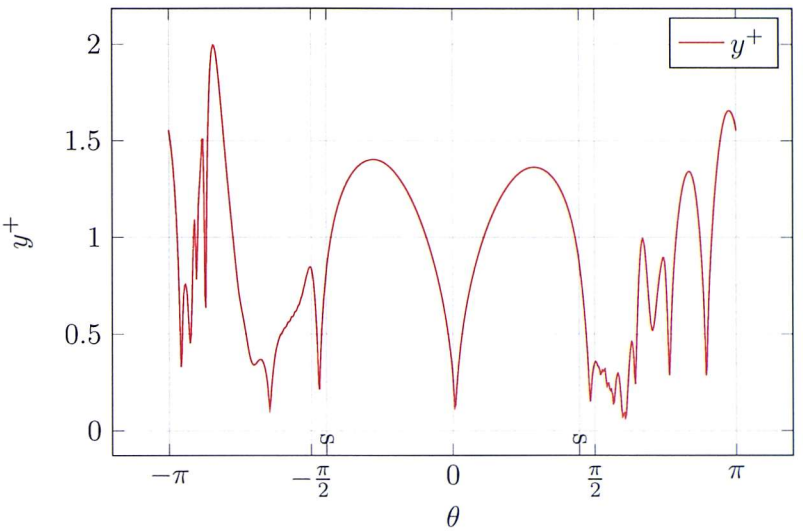



Figure 4.10: Instantaneous $y^+$ results, late in the $dt^* = 0.01$ simulation. These $y^+$ values resulted in the near wall velocity being resolved.

velocity gradient normal to the surface. The low velocity region leaving the top of the cylinder appears to be affected by the cell thickness, as the cells rotate around the cylinder. The innermost cell is $1.6 \times 10^{-5}\, m$ thick, $0.0003D$. This is almost six times the thickness used by Cox [21] for studies with similar Reynolds numbers.

The cell count was increased in two experiments; one testing the cells close to the cylinder and one testing the entire mesh. The effect on the unsteady base pressure of increasing the cell count close to the cylinder by a factor of four is indicated in Figure 4.12. The effect was to remove the regularity in the fluctuation of base pressure coefficient. A similar effect was demonstrated when the entire mesh was refined.

The effect on the time-mean $C_p$ of increasing the cell count for the two cases is presented in Figure 4.13. On one side of the cylinder, the two refined cases are nearly indistinguishable, indicating that refining the cells close to the cylinder made some difference, while the cells further away made little difference.

An asymmetry is present for the case with all cells refined, possibly indicating an instability in the simulation that required more time to fully develop.

In changing to the refined meshes, both cases show improved agreement with the results of Travin et al. [106] close to the separation region, and worse agreement in the base region.

### 4.3.4 Discussion of results from two-dimensional analysis

Two-dimensional simulations of a circular cylinder have been used to examine the effect of simulation parameters on flow results. A reference mesh matching the dimensions of the wind-tunnel test section was created.

Steady RANS results using the Reynolds Stress Model for turbulence generated results comparable to measurements of three-dimensional circular cylinders by Cantwell and

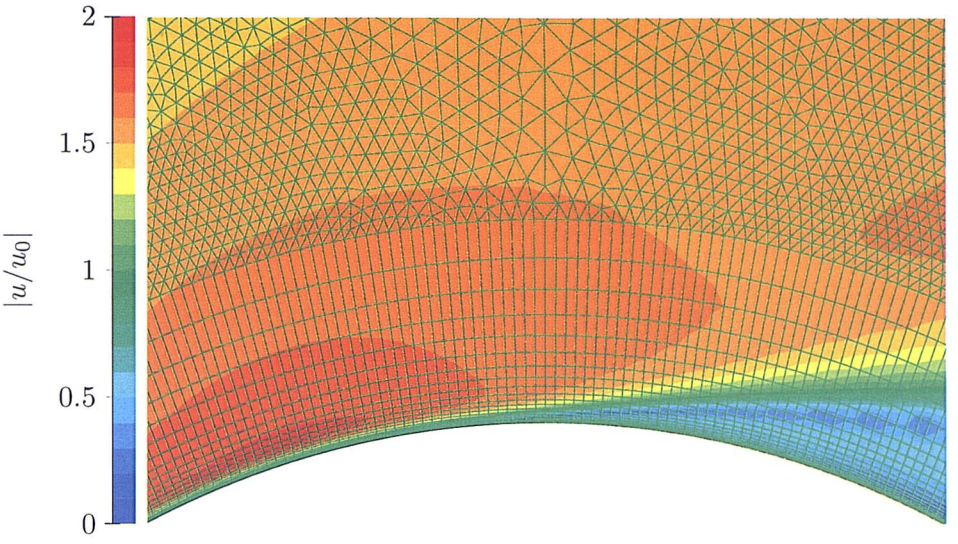



Figure 4.11: Instantaneous flow velocity magnitude near the top of the cylinder, at $t^* = 120$, for $Re = 69 \times 10^3$. The graduated mesh to resolve velocities in the boundary layer is illustrated. Cell count through the thickness of the high flow velocity gradient region on the upstream face is ten. Close inspection shows the low flow velocity trail leaving the upper region of the cylinder, may be affected by the increasing cell thickness downstream.

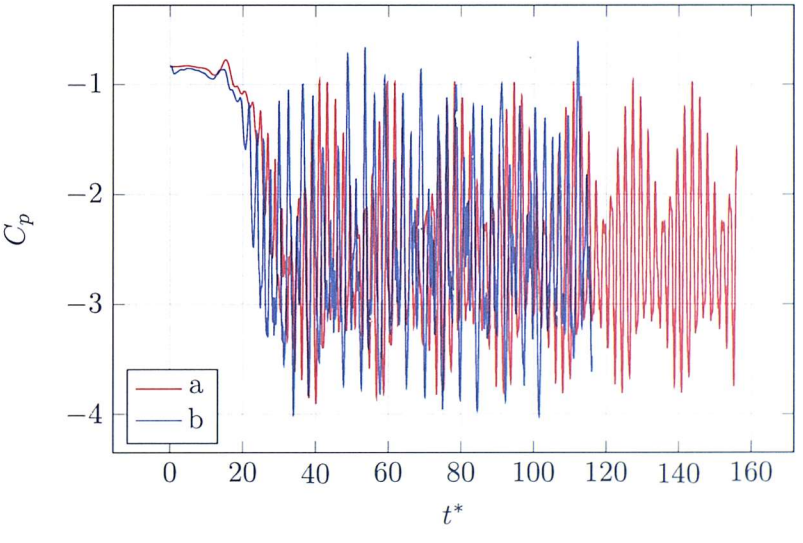



Figure 4.12: Effect of increasing the mesh density close to the cylinder on the base $C_p$. 'a' indicates results from the reference mesh. 'b' indicates results from the refined mesh. The low frequency modulation is no longer apparent. For $t^* = 40 \sim 114$, the shedding frequency has decreased by 12%.

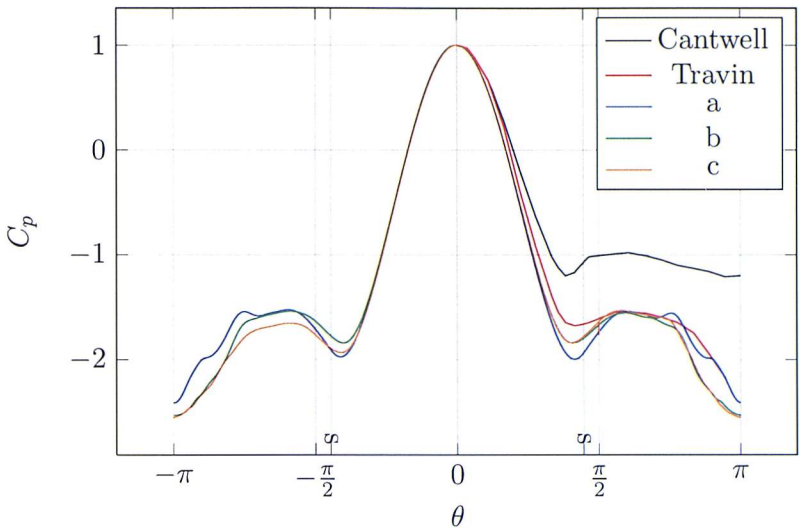



Figure 4.13: Effect of increasing the mesh density on the time-mean pressure coefficient for two cases: 'b' in the region close to the cylinder and 'c' throughout the entire mesh. 'a' indicates the reference mesh.

Coles [18]: this was unexpected, as the two-dimensional mesh does not reproduce three-dimensional effects along the span of the cylinder. The importance of these missing effects was commented on by Travin et al. [106], stating that there was no doubt that three-dimensional simulations were necessary for 'two-dimensional' bluff-body flows. The experiments by Szepessy [102] confirm the effect, showing that for a cylinder of length ratio, $l/D = 10$, pressure correlation between points separated along the cylinder length oscillate over time with a period approximately 1/10 that of the Strouhal period.

Separation was in the same region for the steady simulation and the measurements from the literature, but the simulated base pressure coefficient was of a lower magnitude than the measurement. The non-physical extended vortex pair downstream of the simulated body is related to this effect. A more negative base pressure would result in a shorter vortex pair. The RSM turbulence model generated separation close to 80°, as expected for the 'transition in wake' regime, described by Zdravkovich [116] for circular cylinders in the $Re = 50 \times 10^3$ region. Simpler turbulence models also showed this behaviour, if the region close to the cylinder was forced to behave laminarly. Best results occurred when the mesh resolved the flow velocity profile to the cylinder, rather than using wall functions.

Unsteady simulations were used to examine the effect of the mesh refinement, the simulation domain dimensions, and the size of time-step used. The unsteady base pressure coefficient was used as a measure of change, as it appeared to be a most sensitive parameter to changes in the simulation. The time-mean pressure coefficient was used for comparison with results from the literature.

The reference case showed time-mean results similar to the simulation results published by Travin et al. [106] for separation position and general character. The pressure coefficient just ahead of separation and at the cylinder base was shown to affected slightly by mesh refinement in the region close to the cylinder, in spite of the flow velocity being resolved

rather than modelled using the 'law of the wall' approach. Whether this was related to cell thickness, cell length (around the cylinder), or both parameters is unknown.

The unsteady base pressure coefficient showed an oscillation associated with shedding, and the amplitude of the oscillation was modulated by a low frequency effect. Extending the reference mesh had little effect on the shedding frequency and mean $C_p$, in spite of vortices travelling through the exit boundary. Increasing the distance to the side walls reduced the modulation frequency. The time step used was comparable to examples from the literature, and loss of detail in the unsteady base $C_p$ was demonstrated when it was increased. This had little effect on the time-mean $C_p$, however.

Travin et al. [106] used a domain reaching 15 diameters around their cylinder, and mentioned that there appeared to be no specific requirement for distance to the boundary other than the ability to demonstrate that a doubling of domain size should cause no appreciable change to the results. The domain simulated in this thesis is significantly shorter, but increasing the streamwise distance to the exit boundary was shown to make little difference. The relatively small dimension normal to the flow has been shown to affect the periodicity of the unsteady base pressure coefficient, but this dimension is preserved as it matches the dimension of the test section used to gain data during this project.

Increasing the mesh density close to the cylinder was shown to change the time-mean $C_p$ slightly, and largely removed the low frequency modulation of the base $C_p$. The effect is small however, for a significant increase in the number of cells in the mesh.

The longest numerical experiments in this section ran to $t^* \approx 150$, and appeared to be showing repetitive behaviour after $t^* \approx 50$, as shown in Figure 4.8. Travin et al. [106] reference results ranging from $t^* = 24 \sim 280$ for DES simulations of flow around a circular cylinder, showing a similar modulation of the shedding behaviour. Unlike the results generated here, Travin et al. [106] reported that the regular modulation disappeared after $t^* \approx 100$, this result suggesting a minimum duration for numerical experiments. Simulations of this duration are expensive however, even more so for three-dimensional problems.

This work suggests that the meshes used needed to be finer, and that the time-steps used needed to be reduced. This is in spite of the time-steps and mesh densities used being similar to those in the literature, and the generally good agreement between the time-mean results calculated, and those from the literature. Further refinement was not possible, due to time constraints. The turbulence model adopted has resulted in the boundary layer separating from the cylinder close to 80°, as expected for laminar separation: this was without forcing a laminar region around the cylinder. The results generated were considered good enough for the mesh to be applied to the three-dimensional simulation.

## 4.4 Three-dimensional simulations

Three-dimensional simulations of the anemometer are required, as effects occurring through the thickness of a two-dimensional simulation are lost and may be of some importance to the device behaviour.

Following the two-dimensional cylinder work, a three-dimensional mesh was constructed for the anemometer body. The three-dimensional simulation is expensive: the number of cells in the quarter mesh numbered $1.7 \times 10^6$. The full mesh numbered $6.8 \times 10^6$.

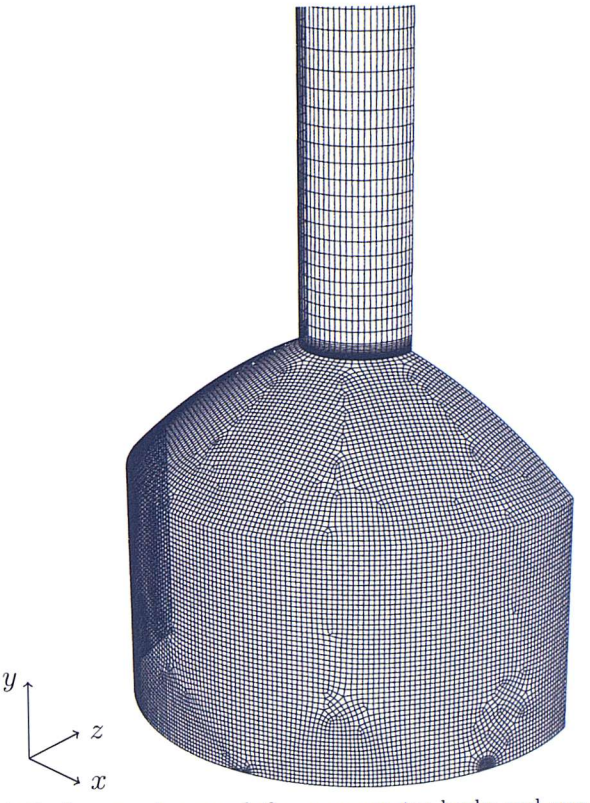
To reduce the solution cost, the region around the support rod described in Figure 3.1 and Figure 4.14 was meshed with progressively larger cells, moving away from the anemometer. Experiments showed large cells in the duct could not support vortex shedding from the support pillars indicated in Figure 4.14, so the cells in the duct became necessarily small. The acoustic duct contains two boundary layer regions, one on each major surface: this region contributed significantly to the cell count. In order to minimise the cell count, hexahedra were used where possible, particularly in the boundary layer region around the body. The region outside the layer around the anemometer used tetrahedra as a purely hexahedral mesh proved difficult to implement. Parts of the mesh are illustrated in Figure 4.14.

These simulations used the incident turbulence intensity figure calculated previously, of $TI = 0.14\,\%$. The Reynolds stress turbulence model was used, as determined necessary during the two-dimensional cylinder simulations.

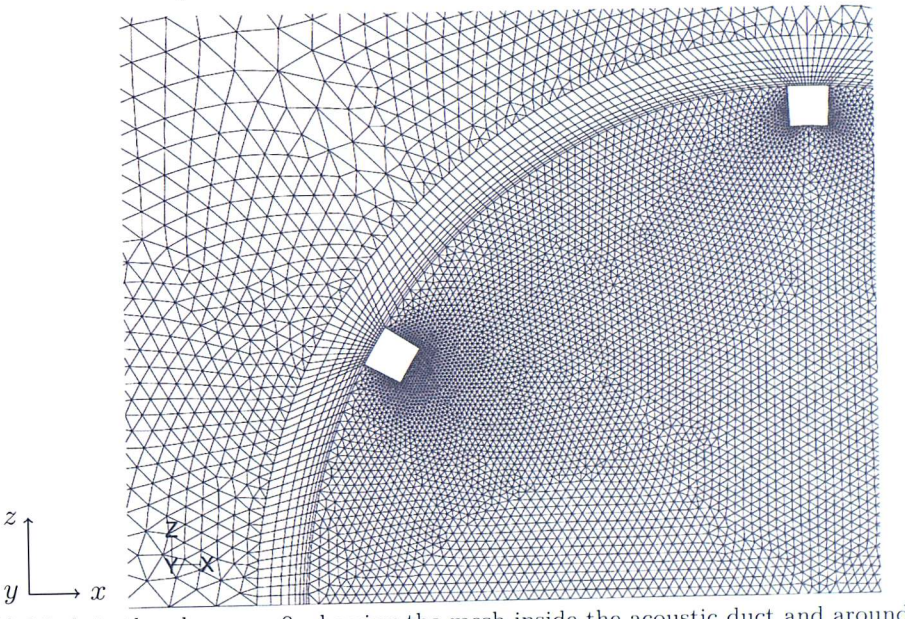
Different aspects of the mesh of the quarter space, open acoustic duct case are illustrated in Figure 4.14 and Figure 4.15. The fine mesh in the acoustic duct that was required to support shedding from the support pillars is indicated. The cell graduation close to the surfaces of the anemometer, required to resolve the flow velocity profile through the boundary layer, is illustrated in Figure 4.15.

Cell thickness normal to the anemometer body (including inside the acoustic duct) was $1.5E-5\,m$, $d/667$ where $d$ was the separation between the major faces of the acoustic duct. $d = 0.01\,m$ in these simulations. Moving away from the hard surfaces, the cells showed a geometric thickness increase per cell of 1.1 out to 1/4 the duct thickness, as illustrated in Figure 4.15. Cell thickness in the centre half of the duct was a constant $d/8$.

It is convenient at this point to define the axes that will be used during discussion. The streamwise direction is in the positive $x$ direction; the axis of rotation is considered the $y$; and the remaining direction is $z$. These are indicated in Figure 4.14 and Figure 4.15, and match the axes defined previously.

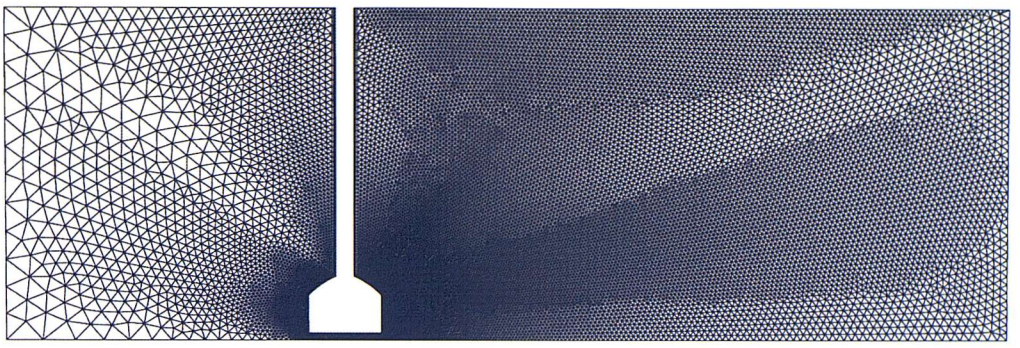



(a) Surface mesh around the anemometer body and support rod, showing cell refinement near the support pillars.

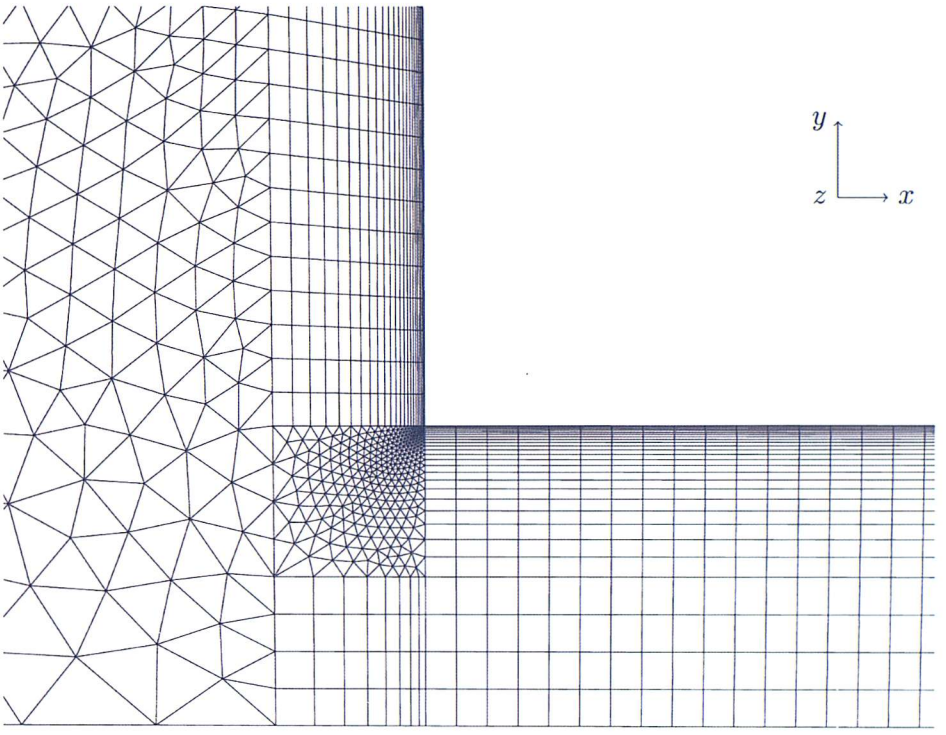



(b) Mesh in the plane $y = 0$, showing the mesh inside the acoustic duct and around the $2\,mm$ wide support pillars. The refined mesh near the support pillars (required to generate vortex shedding in the duct) is illustrated.

Figure 4.14: The quarter mesh used as the basis of the three-dimensional simulations. The full mesh simulation used this mesh reflected across symmetry planes. Flow is in the positive $x$ direction.



(a) Mesh in the plane $z = 0$, showing the support rod, anemometer body and acoustic duct.




(b) Mesh in the plane $z = 0$, zoomed to show the mesh becoming progressively finer, as it approached the outer wall of the anemometer, and the surface of the acoustic duct.

Figure 4.15: Aspects of the quarter mesh used for three-dimensional simulations. The full mesh used this mesh, reflected across symmetry planes. The flow direction matches the positive x direction; in these images from left to right.

### 4.4.1 Steady simulations

The steady simulations used a mesh similar to the quarter mesh illustrated above. Two cases were simulated: the closed duct; and the open duct.

#### No acoustic duct

The steady $C_p$ around the anemometer body is plotted in Figure 4.16, for $Re = 33 \times 10^3$. This result can be compared with the $C_p$ results plotted previously in Figure 3.9. The simulation showed the stagnation region on the upstream face extending along the length of the cylindrical part of the anemometer. It is noted that the measurements showed an interpolated value on the front face, stretched along the anemometer length due to the fouling of one of the pressure taps. The simulations did not show this effect.

The simulation shows a region of reduced $C_p$ close to the intersection between the end cap and the cylinder body, not found in the measurement. This may be due to the measurements having a lower spatial resolution than the simulations. Examination of the simulated flow in this region showed that it did not follow the profile of the body as it passed from the stagnation region to the cap region, but separated from the cap in the interface region, re-attaching as it passed further over the cap.

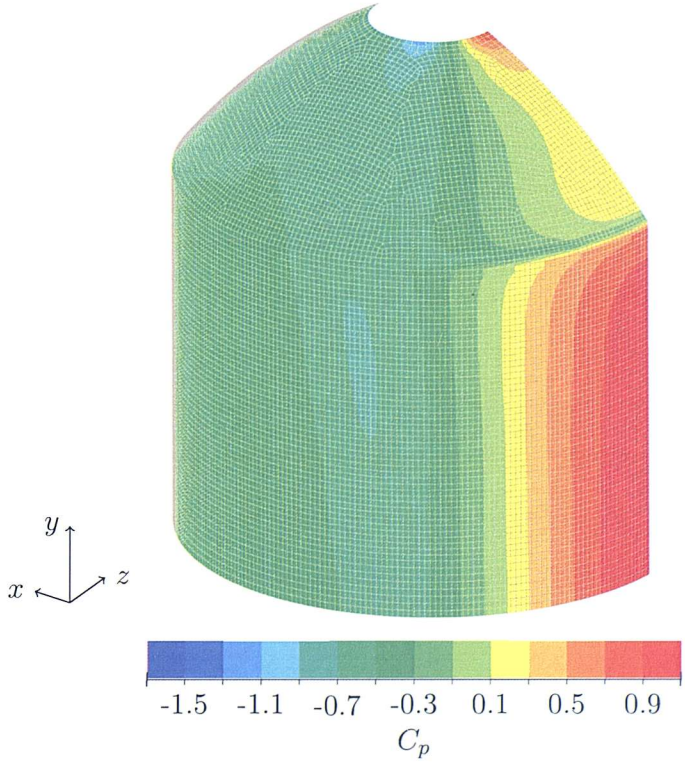



Figure 4.16: Simulated steady $C_p$ around the body without an acoustic duct, for $Re = 33 \times 10^3$.

The $C_p$ around the body, 11.5 $mm$ above the centre of the cylinder is plotted in Figure 4.17, and compared with measurements from Figure 3.4 and Figure 3.7.

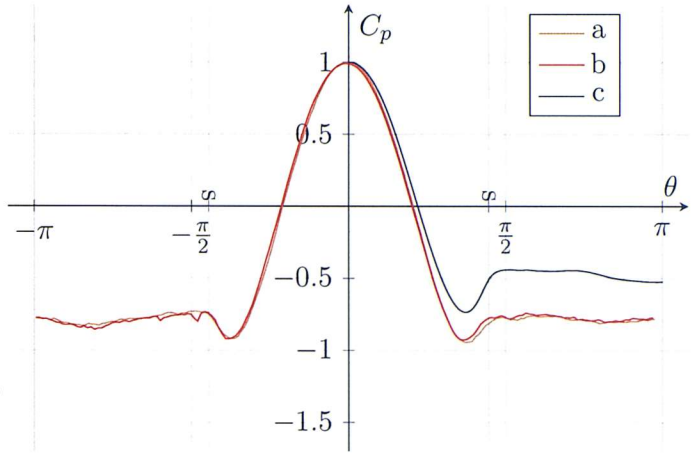



Figure 4.17: Measurement versus steady simulation results for the $C_p$ around the anemometer body without an acoustic duct. $y = 11.5\,mm$ above the centre plane. Labels indicate: a) $Re = 33 \times 10^3$ measurement; b) $Re = 66 \times 10^3$ measurement; and c) $Re = 33 \times 10^3$ simulation.

Separation appears to occur slightly late in the simulation, and the base pressure is higher than measured. This is expected, as the steady wake in the simulation extends further downstream than for the mean, unsteady case presented below: the pressure at the cylinder base is of a lower magnitude than it would be for the shorter wake. Nonetheless, simulation and measurement show good agreement in general character.

The ratio of the streamwise to the input velocity on the $y = 0$ plane is presented in Figure 4.18. This result gives an indication of the behaviour in the wake, and can be compared with results later in this chapter.

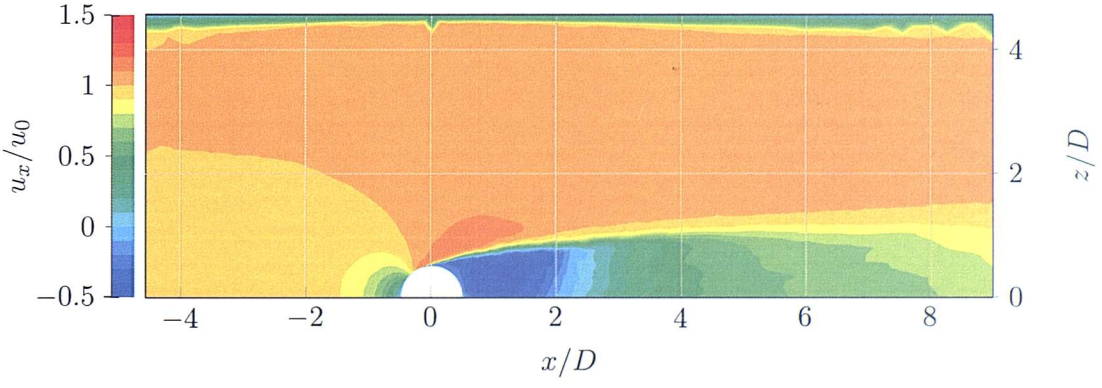
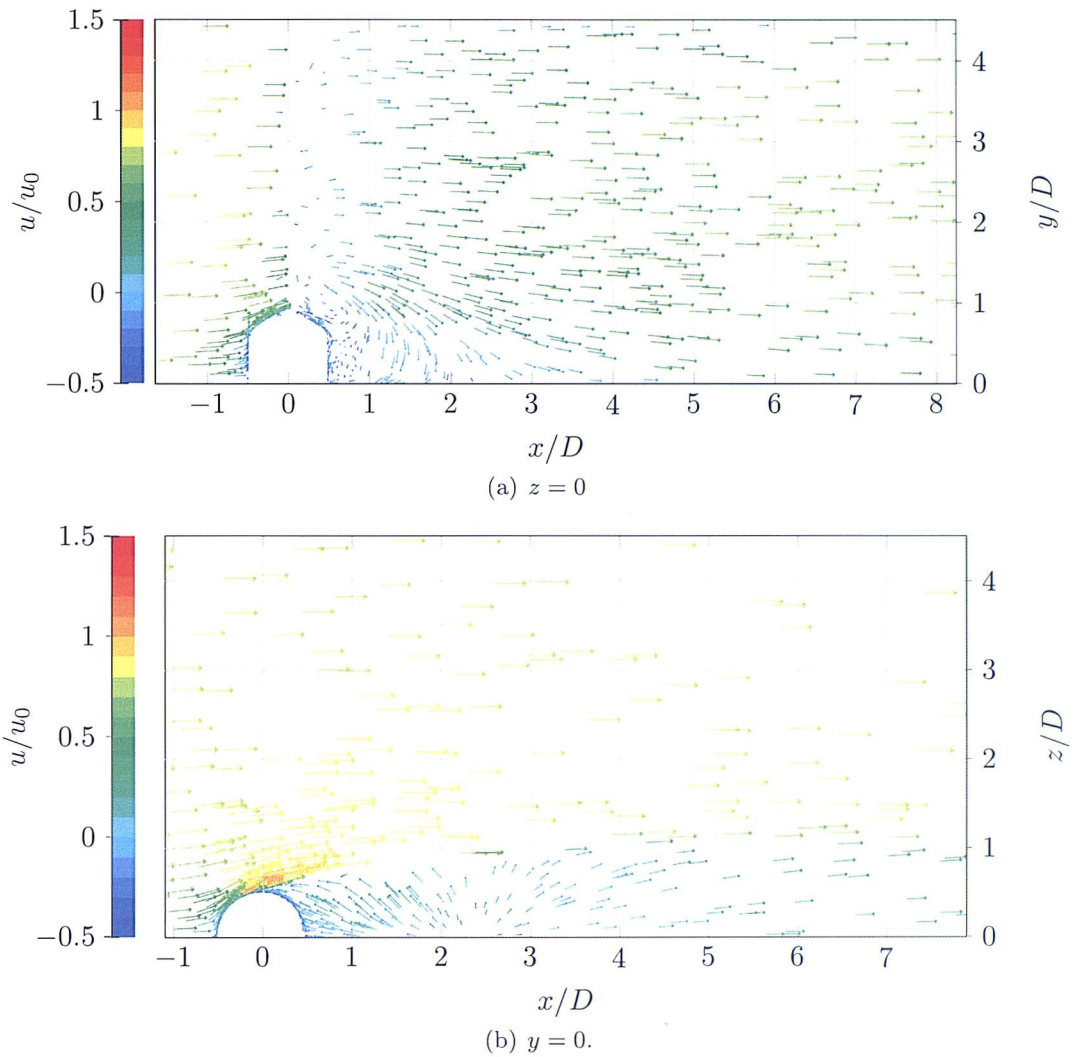



Figure 4.18: Steady $x$ velocity ratio for the quarter mesh simulation without an acoustic duct, in the plane $y = 0$. Comparison with the mean unsteady case shows increased negative x-velocity in the stagnation region for the steady case, and a longer wake. The mean x-velocity becomes positive for $x > 2.3D$.

The velocity field around the anemometer is presented in Figure 4.19. The velocity in the $z = 0$ plane shows the flow to run over the end of the body to form a recirculation region just behind the cap. Behind the body of the cylinder in the 'near wake' region, the $z = 0$

plane shows a low velocity region with no obvious flow direction. Moving downstream in this plane and behind the cylinder, the flow changes from moving upstream to downstream, the transition occurring approximately $1.5\,D$ from the rear of the cylinder.




(a) $z = 0$

(b) $y = 0$.

Figure 4.19: Steady velocity around the anemometer without an acoustic duct. Vectors are coloured by velocity ratio.

The steady flow velocity in the $y = 0$ plane shows the flow to move outward from this transition region.

These topological results compare favourably with those discussed by Zdravkovich et al. [117] in which the flow around a short cylinder with two free ends is discussed.

Zdravkovich et al. [117] considers a sphere to be equivalent to a circular cylinder with curved ends, and an $L/D$ aspect ratio of one. Accordingly, the anemometer displays an $L/D$ ratio close to two. Drag coefficients in this range have been presented by Zdravkovich et al. [117] with $Re = 88 \times 10^3$, showing a trend for a reduction of $C_D$ as the $L/D$ ratio decreases. It appears this aspect ratio and Reynolds number, with plane ends, should display $C_D \approx 0.73$. Two-dimensional cylinders displayed $C_D \approx 1.2$. The reported effect of curved ends is to reduce $C_D$ by 19% for $L/D = 2$, dropping the expected $C_D$ to 0.59. Also

reported, were random, asymmetric, localised pressure distributions over the cylinder: it appears this system does not have flow symmetry in spite of its physical symmetry. This could have implications for convergence rates during simulation, as the simulation forces quarter symmetry.

**Open duct without support pillars.**

The steady $C_p$ over the anemometer surface is plotted in Figure 4.20 for $Re = 33 \times 10^3$. This distribution can be compared with the measured $C_p$ distribution plotted in Figure 3.13.

The simulation shows a similar reduced $C_p$ region, close to the intersection region of the end cap and body, as was displayed by the closed duct simulation. The effect of opening the duct is to generate a low $C_p$ region, near the opened region in the $y = 0$ plane. This is due to stagnation no longer occurring near this plane, as the flow runs into the duct.

The measurement does not show the region of low pressure coefficient near the entrance to the acoustic duct (on the lower edge of Figure 4.20) as the region is small, and the closest tap (measurement tap six, in Figure 3.1) is in the high pressure coefficient region.

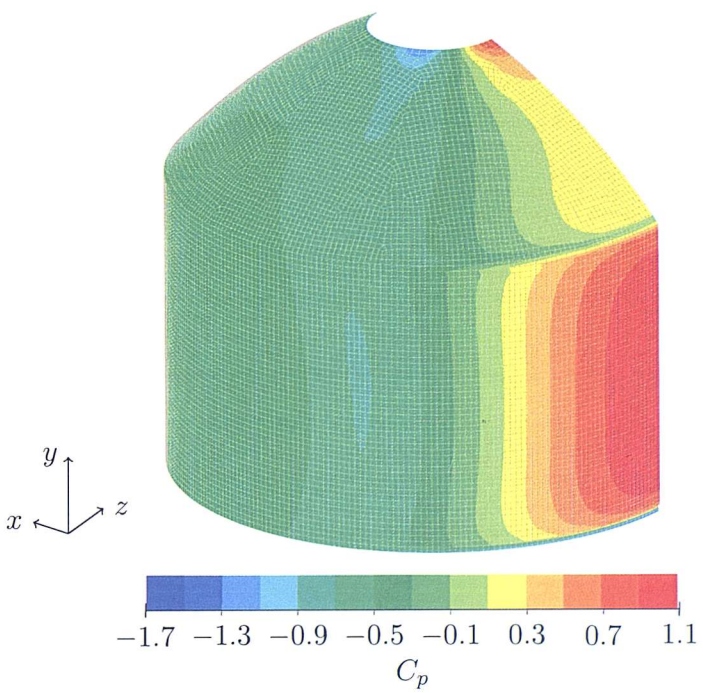



Figure 4.20: Simulated steady $C_p$ around the body with the acoustic duct present. $Re = 33 \times 10^3$.

As the flow runs into the duct, a small separation bubble occurs at the entrance lip. This is illustrated in Figure 4.21, which shows the static velocity vectors in the plane $z = 0$, and contours for $y = 0$ and $z = 0$. These results can be compared with those in Figure 4.19, illustrating the effect of opening the duct.

It appears that the zero streamwise velocity region occurring downstream of the body in the $z = 0$ plane, occurs just over one diameter downstream from the rear face: this position

has moved upstream when compared with the $1.5D$, closed duct case. There are no longer two clear vortices in the near wake: rather, a single vortex close to the interface between the end cap and the anemometer wall, on the rear face.

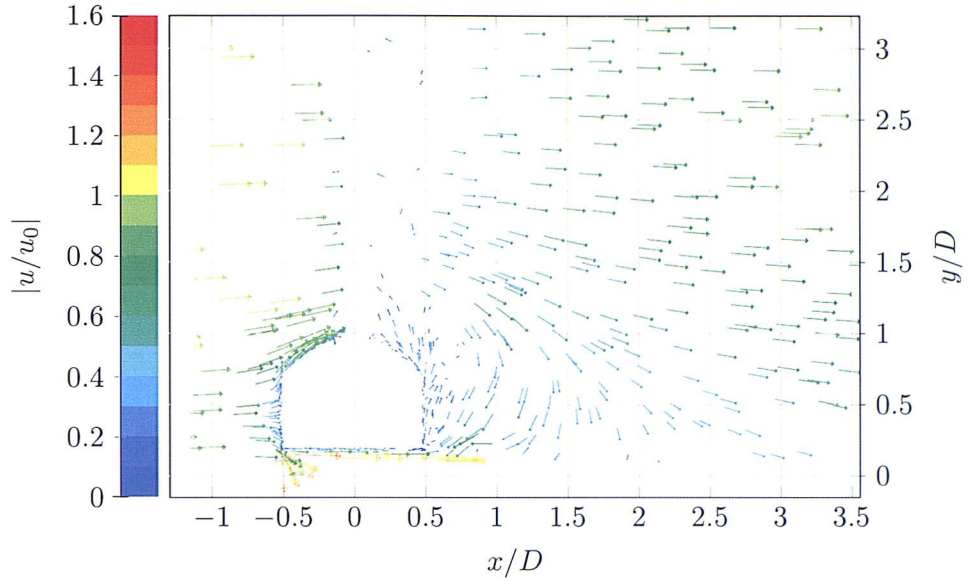
The $y = 0$ plane no longer shows a region downstream from the body, showing flow radiating outwards. The flow through the duct appears to be affecting this region. Opening the duct appears to reduce the wake width, possibly due to reduction of the radiating flow region previously mentioned.

As the flow within the duct is of particular interest, this region is also presented in Figure 4.21.

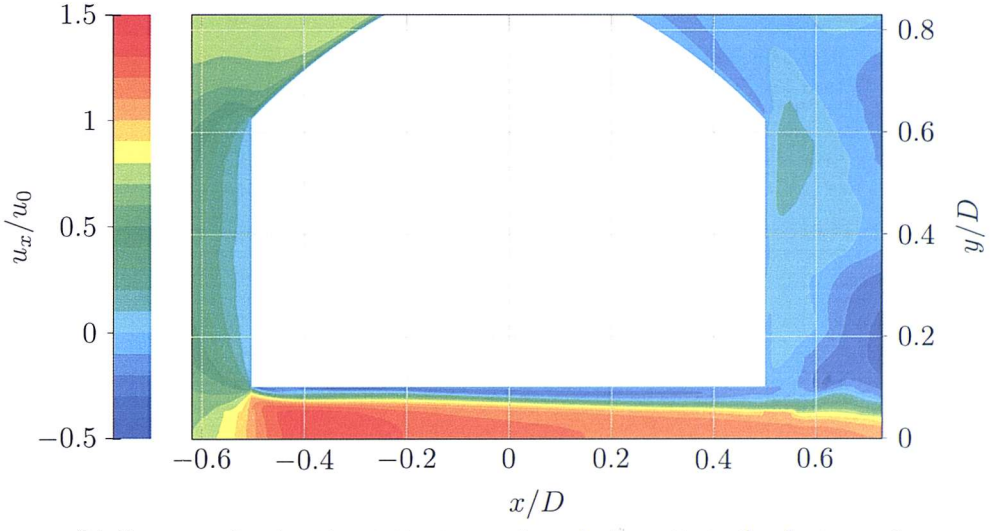
The $C_p$ around the body, $11.5\,mm$ above the centre plane of the duct is plotted in Figure 4.22 and compared with the time-mean measurements from Figure 3.10.

Similar to the 'no duct' case, the agreement between measured and simulated $C_p$ is good up to approximately 80°. Separation occurs in a similar region, but the simulated base pressure is of a smaller magnitude than that measured. This was expected for the steady simulation due to the extended wake that it produces. The measurement showed an irregular $C_p$ variation with position after separation that is not present in this simulation.

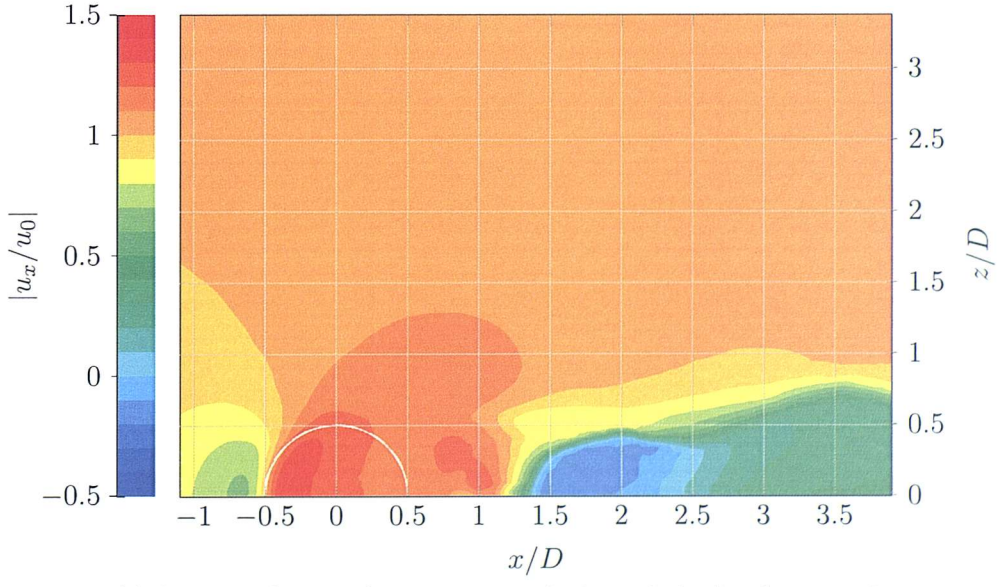
The simulated ratio of the steady duct velocity to the free stream velocity, at positions along the duct centre line is compared with measurements in Figure 4.23. It shows generally good agreement, except the measurement shows a linear change with position near the duct centre, whereas the simulation does not. Also, the measurement shows a velocity ratio increase at the duct exit, not present in the simulation.




(a) Static velocity vectors coloured by velocity magnitude ratio. $z = 0$




(b) Contours showing the static streamwise velocity ratio in the duct. $z = 0$.




(c) Contours showing the streamwise velocity ratio in the plane, $y = 0$

Figure 4.21: Steady streamwise velocity results for the low frequency viscous flow field.

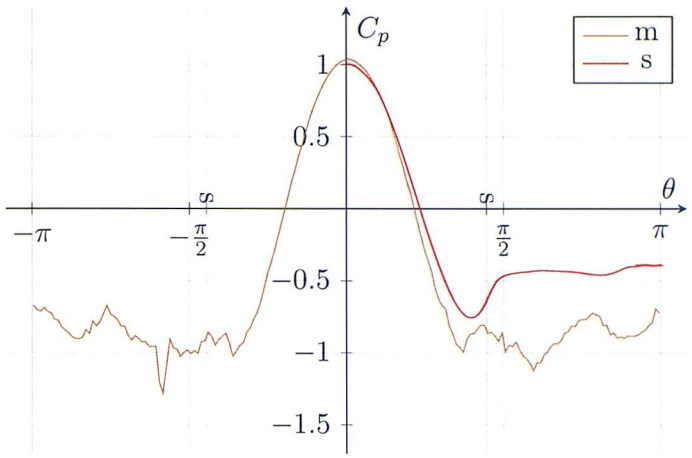



Figure 4.22: Measurement versus steady simulation, for the $C_p$ around the body, 11.5 $mm$ above the centre plane. The duct is open. Labels indicate: m) $Re = 33 \times 10^3$ measurement. s) $Re = 33 \times 10^3$ simulation.

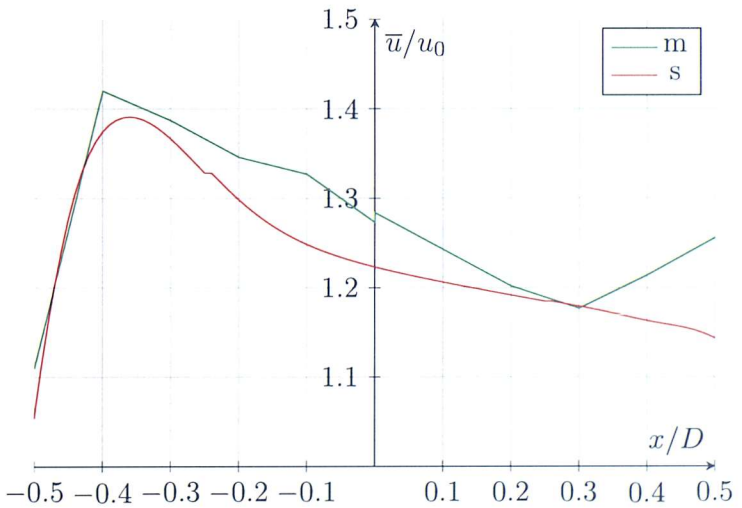



Figure 4.23: Velocity along the duct centre line, averaged over the hot-wire length of $l = 1.25\,mm$ for simulation (s) and measurement (m). Generally good agreement is demonstrated.

**Open duct with support pillars.**

The quarter mesh, steady simulations that included the support pillars demonstrated well behaved convergence for $Re = 33 \times 10^3$, $u = 10\,ms^{-1}$; suggesting the mesh and model were working well. 4500 iteration steps were enough to cause all residuals to drop more than four orders of magnitude.

Increasing the velocity at the input boundary by a factor of five resulted in worse convergence behaviour. Residuals did not improve after 1000 steps: a drop of two magnitude orders for most values.

The low frequency velocity field in the plane $z = 0$ is plotted in Figure 4.24. The flow appears to run over the top of the anemometer body, forming a single vortical region just downstream of the support rod. A region of zero streamwise velocity appears to occur $\sim 1.6D$ downstream on the plane of symmetry in the duct plane.

The low frequency velocity inside the duct, in the $z = 0$ plane, shows a separation bubble at the entrance lip of the duct of length $\sim 3/2h$, where $h$ is the duct separation. This is unlike the previous case, which showed small separation region at the duct entrance that extended into an elongated negative velocity region moving away from the duct wall.

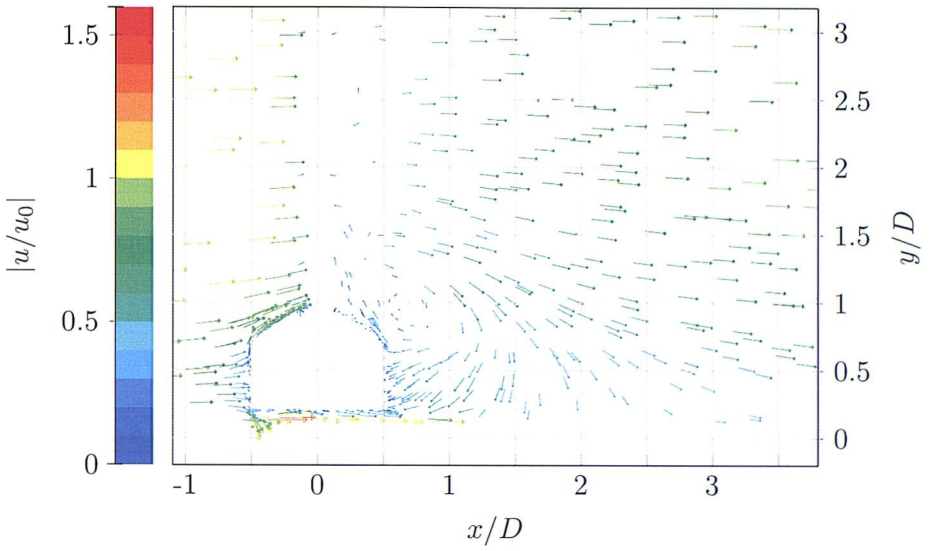
Further downstream of the bubble, the velocity near the duct wall becomes positive again, suggesting boundary layer reattachment.

The low frequency velocity ratio in the $y = 0$ plane shows regions downstream of the pillars that are negative, becoming positive as they move downstream. These are steady wakes behind the pillars: a result of the flow rotating as it passes around them. The pillars appear to influence the mean flow in the duct.

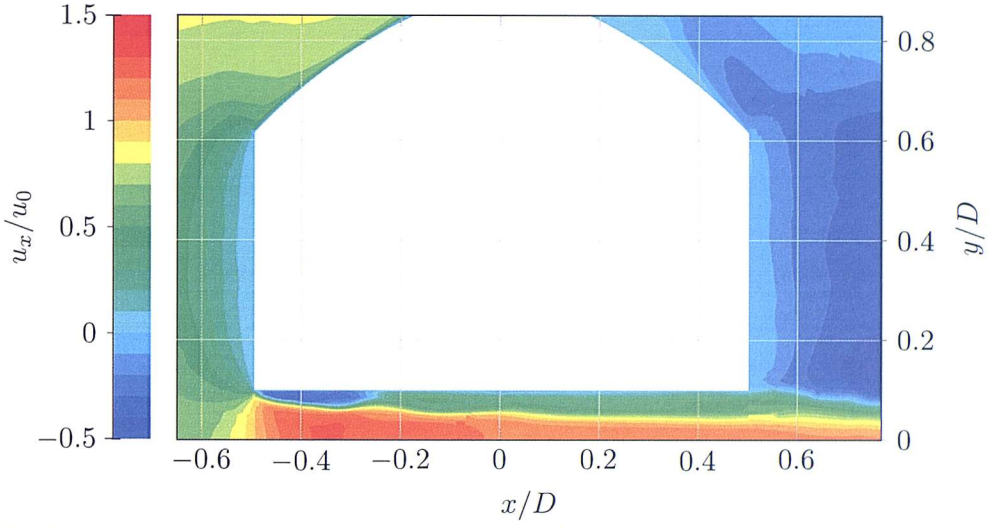
The $C_p$ around the body at $11.5\,mm$ above its centre and the low frequency velocity along the duct centre line is presented in Figure 4.25. Addition of the pillars has resulted in a modulation of the $C_p$ after separation, although the modulation does not result in an appreciably improved match to the measurement. The base pressure has lifted slightly.

The low frequency velocity along the line $z = y = 0$ is presented in Figure 4.26. The simulation without support pillars shows good agreement with measurements at the entrance and near the exit of the duct, but does not show the nearly linear reduction of velocity ratio with position, that is demonstrated by the measurement. Also, the measurement shows a velocity ratio increase at the exit of the duct that is not present for the no pillar simulation. Adding the support pillars to the simulation reduced the velocity at the entrance to the duct, but increased the velocity ratio in the region of $x/D = -0.1$ relative to the velocity ratio at the duct entrance, improving the match of character between measurement and simulation. Also, the velocity ratio shows an increase as the flow leaves the duct, in agreement with the measurement. While it appears that adding the pillars has generally reduced the velocity ratio throughout the duct, the general trend of the ratio is closer to that of the measurement.

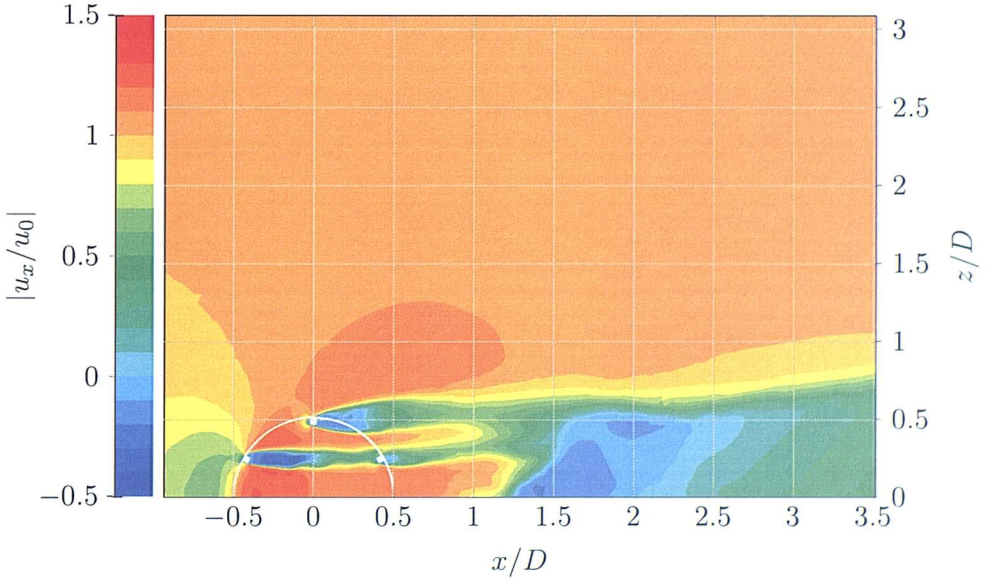
Agreement for the centre-line, low frequency velocity ratio, between measurement and simulation is to within 9 % for an external $Re = 33 \times 10^3$.




(a) Low frequency velocity vectors coloured by velocity magnitude ratio for $z = 0$




(b) Contours showing streamwise, low frequency velocity ratio in the acoustic duct. $z = 0$.




(c) Low frequency velocity contours in the plane $y = 0$

Figure 4.24: Steady simulation of the open acoustic duct case with support pillars. $u_0 = 10\,ms^{-1}$.

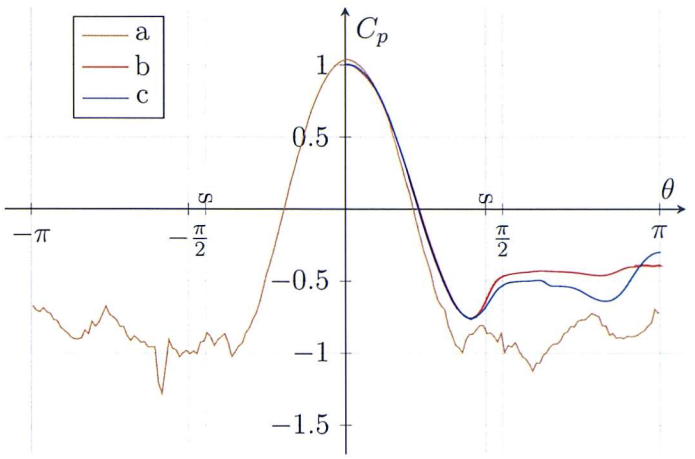



Figure 4.25: Time-mean measurement versus steady simulation results for the $C_p$ around the body, 11.5 $mm$ above the centre plane. The acoustic duct is open. Labels indicate: a) Measurement; b) Simulation, no pillars. c) Simulation, with pillars.

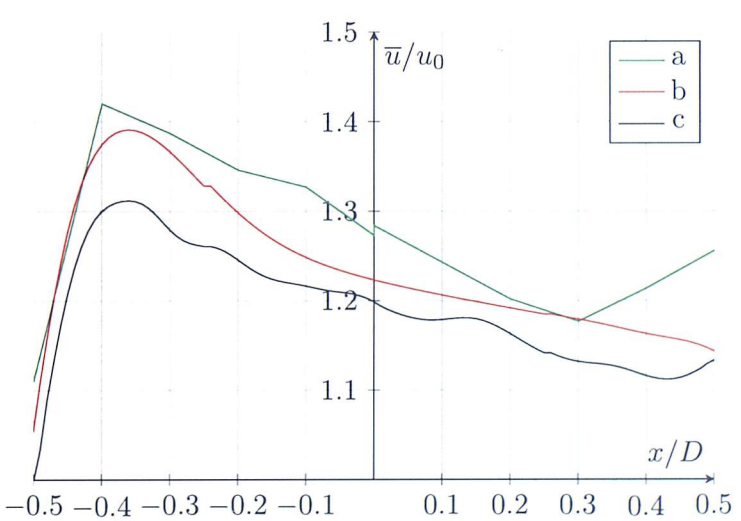



Figure 4.26: Velocity along the duct centre line, averaged over the hot-wire length of $l = 1.25\,mm$ for: a) measurement; b) simulation without support pillars; c) simulation with pillars. Adding the pillars has increased the velocity near the duct centre and increased the exit velocity, but has reduced the velocity near the entrance.

The simulated steady streamwise velocity ratio along the duct centre line is plotted for a range of input velocities in Figure 4.27. Comparison is made with the single velocity result gained using hot-wire measurements, using a free-stream velocity of $10\,ms^{-1}$. These results suggest the spatial oscillation along the centre line is changing significantly with free-stream velocity. Since these simulations used a time-steady analysis, these fluctuations are indicative of time-mean flow fluctuations.

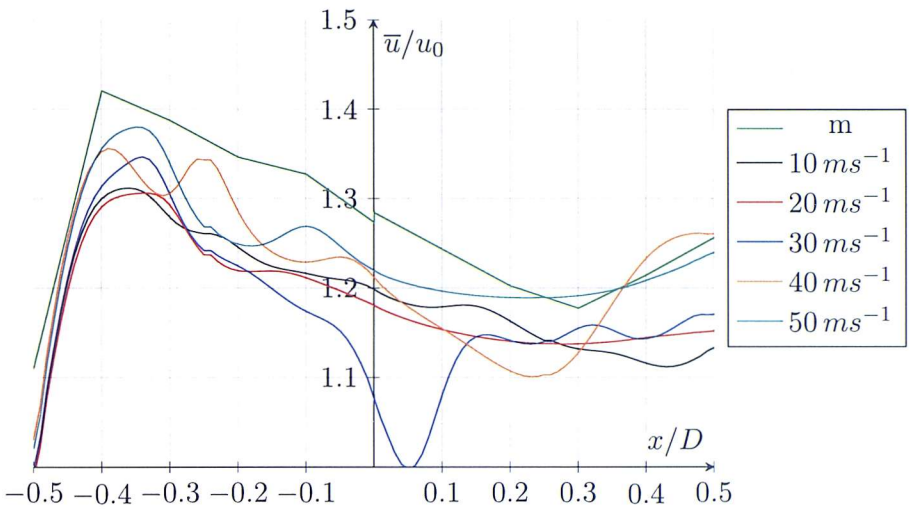



Figure 4.27: Velocity along the duct centre line, averaged over the hot-wire length of $l = 1.25\,mm$ for simulations at different free-stream velocities as indicated. The $10\,ms^{-1}$ measurement is marked as $m$.

### 4.4.2 Unsteady simulations

Unsteady simulations of the flow around and through the anemometer are relevant, as the object is known to generate an unsteady wake. The full mesh is required (as opposed to the quarter mesh for the steady simulations) as symmetry in the slowly changing velocity field does not occur as vortices are shed downstream from the anemometer. Furthermore, published results for time-mean values of $C_p$ over the surface of curved end circular cylinders do not show symmetric distributions according to Zdravkovich et al. [117].

The mesh used was formed by reflecting the mesh of Figure 4.15 across the planes, $y = 0$ and $z = 0$. The onset of shedding was accelerated by causing an artificial asymmetry in the low frequency velocity field, by forcing one side of the domain to behave laminarly. After a duration of $t^* \sim 10$, this condition was removed.

#### Closed duct simulation

Larger time-steps of $dt = 0.1 \times 10^{-3}\ s$ were used for the closed duct case to reduce solution cost. This was equivalent to $t^* = 0.02$, comparable to the time-step used by Iaccarino et al. [57].

The closed duct simulation was performed to $t^* > 300$, to check for duration of experiment effects. The open duct simulations were too expensive for this long an experiment, due to the large cell count around the support pillars and throughout the duct, and the smaller time-steps used. The open duct case without pillars ran to $t^* \approx 55$ from an initial flow field from the closed duct case. The case including the support pillars ran to $t^* \approx 30$.

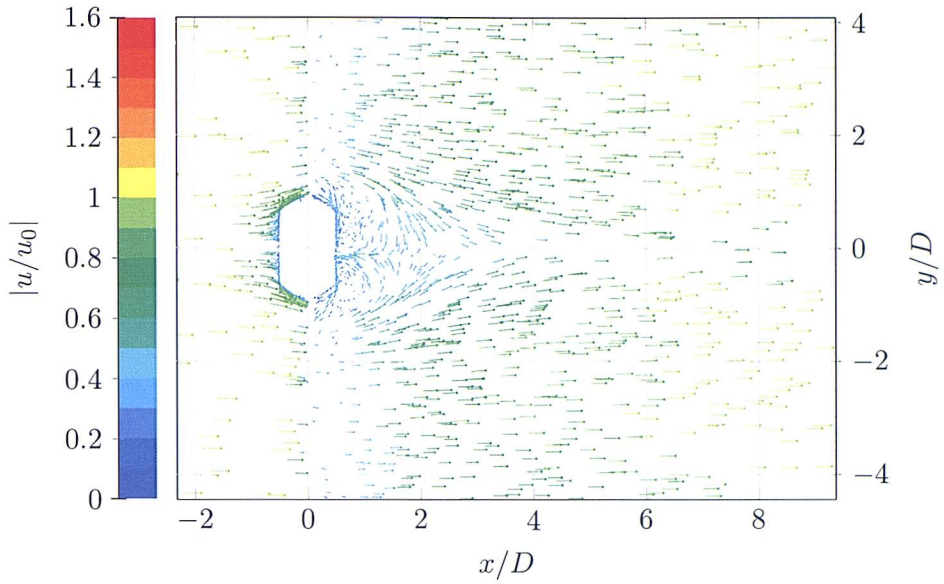
The instantaneous, low frequency velocity field around the closed duct anemometer at $t* = 317$ is presented in Figure 4.28.

The vortex shedding displayed by the anemometer differs significantly from the circular cylinder case. The latter shows clearly defined vortices shed from alternate sides of the cylinder, which run downstream. The three-dimensional case, when viewed in the same plane, shows the shedding of structures with weaker $y$ vorticity, and the shedding is not as regular. The $y$ vorticity of these structures reduces comparatively rapidly. This difference is illustrated by comparing Figure 4.29 with Figure 4.6.

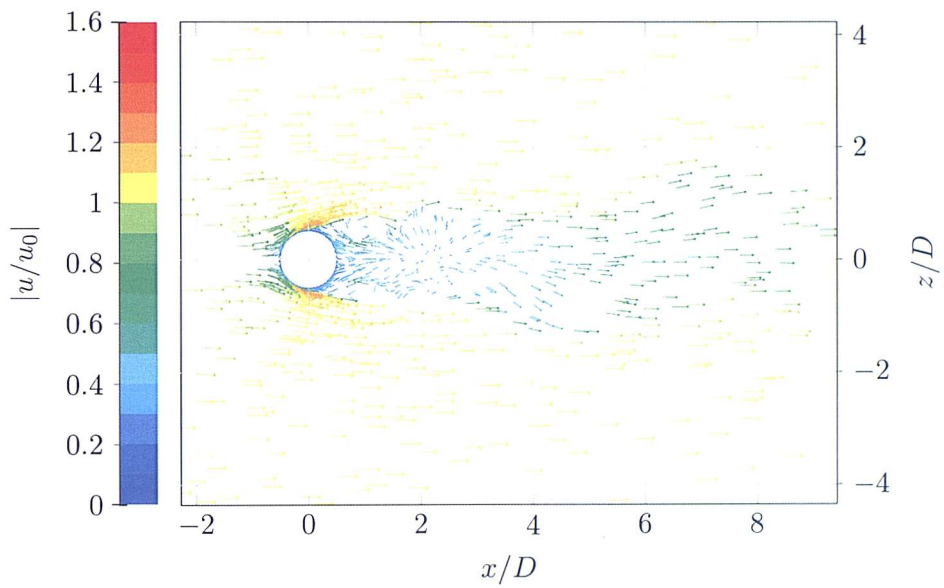
The time-mean $C_p$ around the cylinder at $y = 11.5\,mm$ was calculated from $t^* = 140 \sim 300$. It is compared with measurements and the steady simulation results in Figure 4.30.

The graph shows good agreement between the two simulations. The stagnation $C_p$ for the mean, unsteady case is a little low, possibly a result of the unsteady stagnation $C_p$ displaying a fluctuating result, always below one. The mean, unsteady base $C_p$ is not significantly closer to the measurement than the steady quarter mesh result.

The time-mean $x$ - velocity field for the unsteady simulation using the full mesh is plotted in Figure 4.31. It can be compared with the steady $x$ - velocity field generated with the quarter mesh in Figure 4.18. The differences are partly due to the symmetry enforced by the quarter mesh, which prevented asymmetry in the wake; and partly due to the slowly

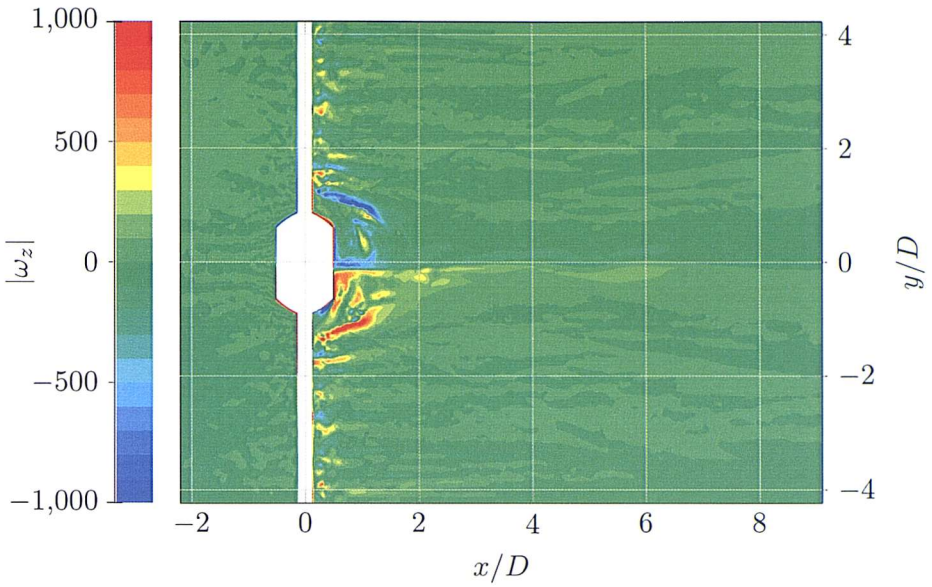



(a) $z = 0$

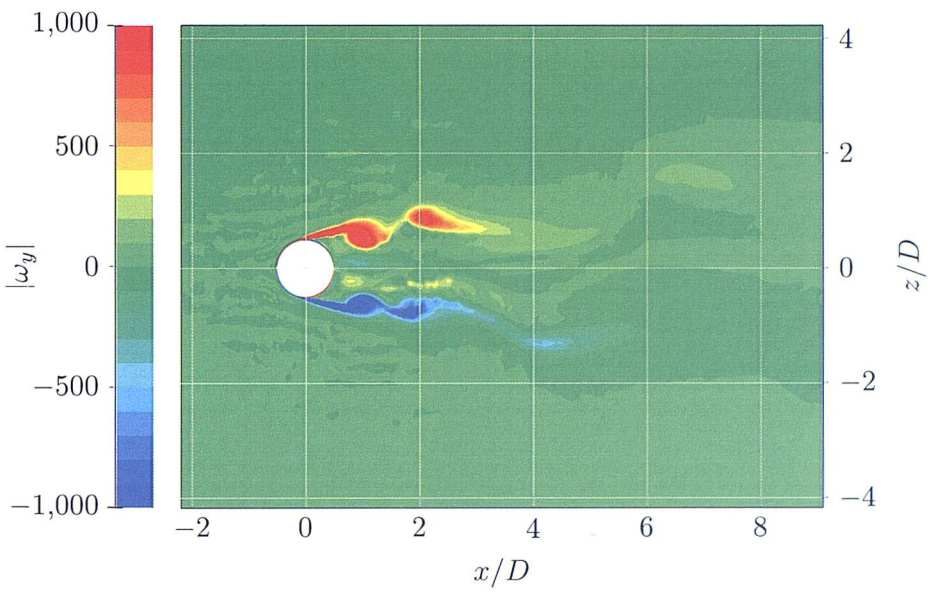



(b) $y = 0$

Figure 4.28: Instantaneous, unsteady, low frequency velocity around the anemometer without an acoustic duct, at $t^* = 317$. Vectors are coloured by velocity magnitude ratio. Asymmetry in the wake is demonstrated, although it is not as strong as for the two-dimensional circular cylinder simulations, shown previously.




(a) $z = 0$




(b) $y = 0$

Figure 4.29: Instantaneous unsteady vorticity around the anemometer without an acoustic duct, at $t^* = 317$. Vortical structures being shed are not as clear as those shed during the two-dimensional circular cylinder simulations.

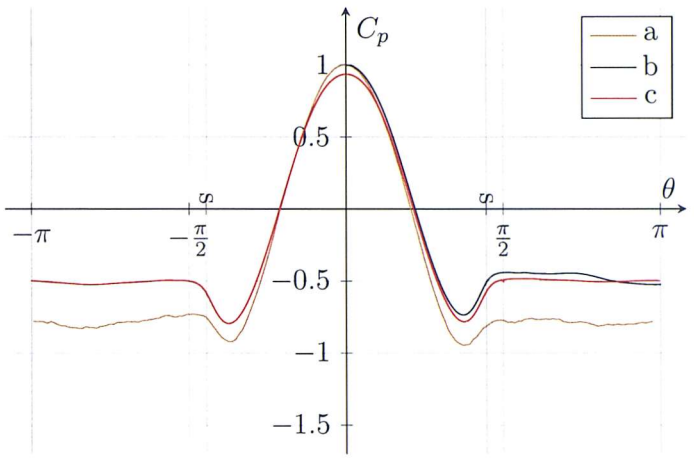



Figure 4.30: Measurement versus steady simulation results, for the $C_p$ around the body, 11.5 $mm$ above the centre plane at $Re = 33 \times 10^3$. The anemometer acoustic duct is not present. Labels indicate: a) Measurement; b) Quarter mesh, steady simulation; and c) Full mesh, mean over unsteady results. The simulation results appear similar.

varying velocity field being partly resolved by the unsteady computation. In particular, the mean $x$-velocity in the wake becomes positive closer to the body, in the unsteady computation. A more negative pressure coefficient over the downstream half of the body might be expected with this effect, and this is demonstrated in Figure 4.30, though not to a large degree.

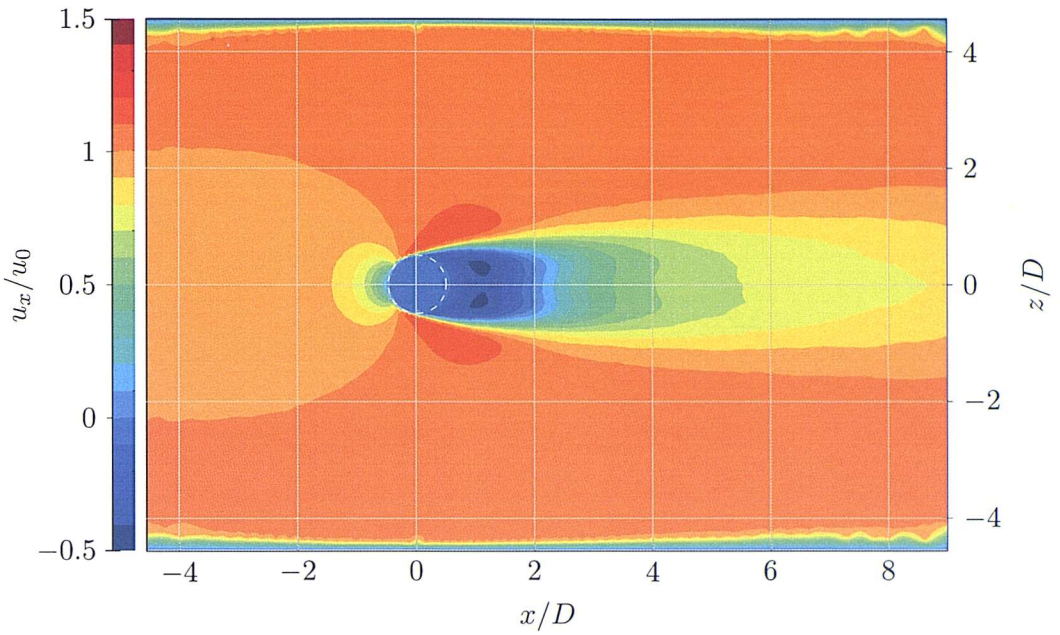



Figure 4.31: Time-mean, x-velocity ratio in the $y = 0$ plane. The mean was taken from $t^* = 140 \sim 300$: thirty two shedding cycles for a circular cylinder of the same diameter as the anemometer, assuming $St = 0.2$. The position of the anemometer body is marked. Comparison with the steady, quarter mesh results in Figure 4.18 shows the near wake shape is different, possibly due to better solution convergence for the unsteady case. The mean x-velocity becomes positive in the wake, with $x > 2.0D$.

### Open acoustic duct without pillars

The time-steps used for the unsteady simulations including the low frequency flow through the acoustic duct were smaller than those used for the simulations without the duct, as the fluctuations inside the duct were expected to be of a higher frequency. In particular, comparison of the velocity spectra outside the duct (Figure 3.26) with the spectra inside the duct (Figure 3.27) suggests an order of magnitude increase in the frequencies of interest. The time-step used in these simulations was $dt = 2.5 \times 10^{-5}\, s$.

The time-mean $C_p$ around the open-duct device in the plane, $y = 11.5\, mm$ is plotted in Figure 4.32, and compared with measurement data and results from the steady, quarter mesh computation. The results for the time-mean, unsteady $C_p$ and the steady, quarter mesh are very similar.

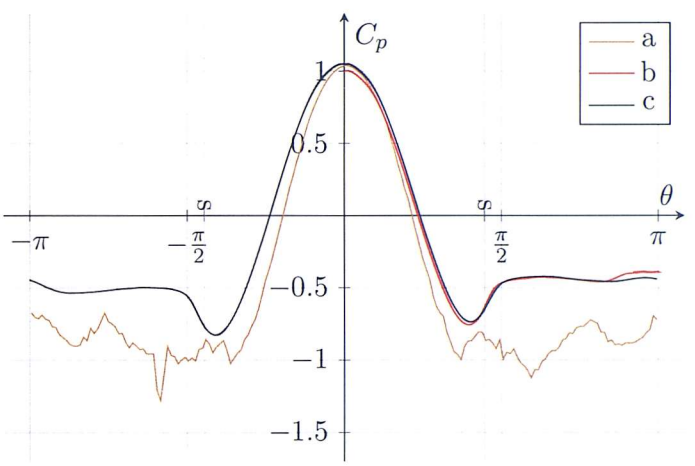
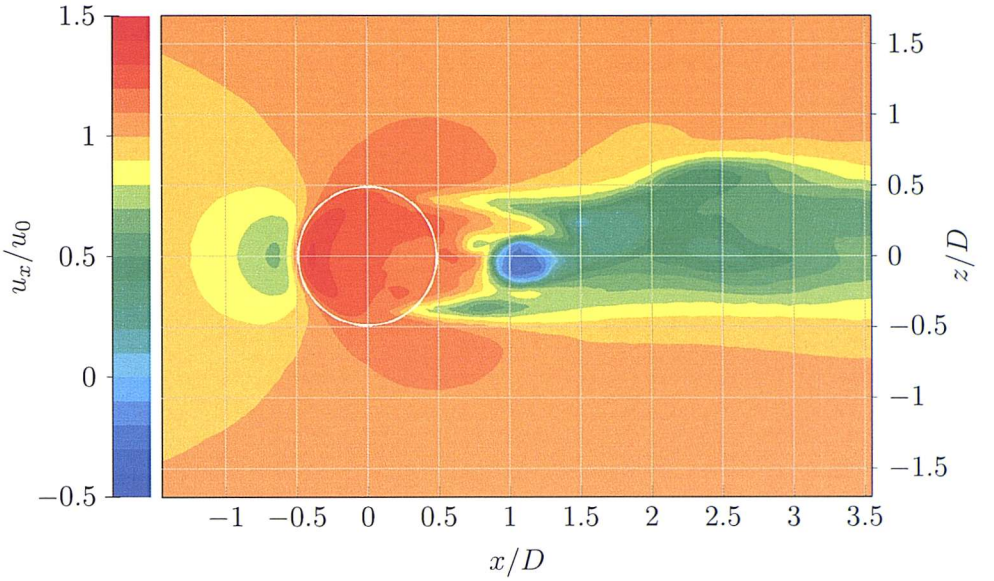



Figure 4.32: Measurement versus steady simulation results for the $C_p$ around the body, $11.5\, mm$ above the centre plane. The acoustic duct is present. Labels indicate: a) Measurement; b) Steady simulation without pillars. c) Mean, unsteady simulation without pillars. Good agreement between the steady, and time-mean unsteady $C_p$ is demonstrated.

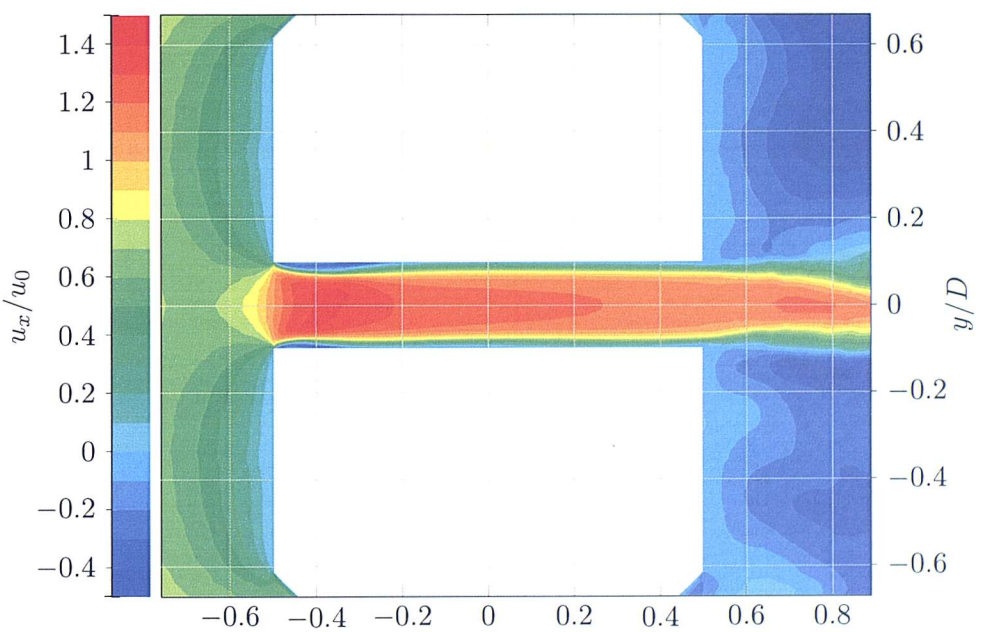
Figure 4.33 gives some insight into the instantaneous flow behaviour occurring through the duct. The high velocity flow passing through the acoustic duct has a similar topology to that generated by the steady case without the support pillars illustrated in Figure 4.21, except its size in the $y$ direction appears to remain largely constant: the steady case showed a contraction. This unsteady simulation showed this region to fluctuate in position rapidly once it had left the duct, compared with the movement of the vortices shed by the relatively large body. The flow through the duct is generally similar to that generated for the steady case (Figure 4.21), except a separation bubble is now clearly defined at the front of the duct in the plane, $z = 0$. The unsteady case also shows asymmetry in the wake. In the near wake, the unsteady case showed the high velocity region leaving the acoustic duct was expanding in the $y$ direction, whereas the steady case did not.

Comparison of the $x$ velocities in the $y = 0$ plane for the two cases shows that the unsteady solution generated a smaller region of negative velocity in the near wake.

It has been demonstrated that the unsteady, full mesh simulation produced results that differed from those generated by the quarter mesh, steady simulation.




(a) $y = 0$.




(b) $z = 0$

Figure 4.33: Instantaneous, unsteady, low frequency streamwise velocity ratio at $t^* = 52$, including flow through the acoustic duct. Support pillars were not included. Asymmetry in the flow is clear.

The time-mean x-velocity in the $y = 0$ plane is plotted in Figure 4.34. This can be compared with the time-mean result for the case without the acoustic duct, in Figure 4.31. Opening the duct has increased the x-velocity in the near wake, in the $y = 0$ plane, as the flow passes through the duct and into this region. The downstream field has changed from a square profile, to pinched and appears to be slightly longer. Some asymmetry in the wake in Figure 4.34 is visible, possibly due to the short time window of $dt^* = 15$ used for

calculation. It is possible that an incomplete shedding cycle was captured, removing the symmetry.

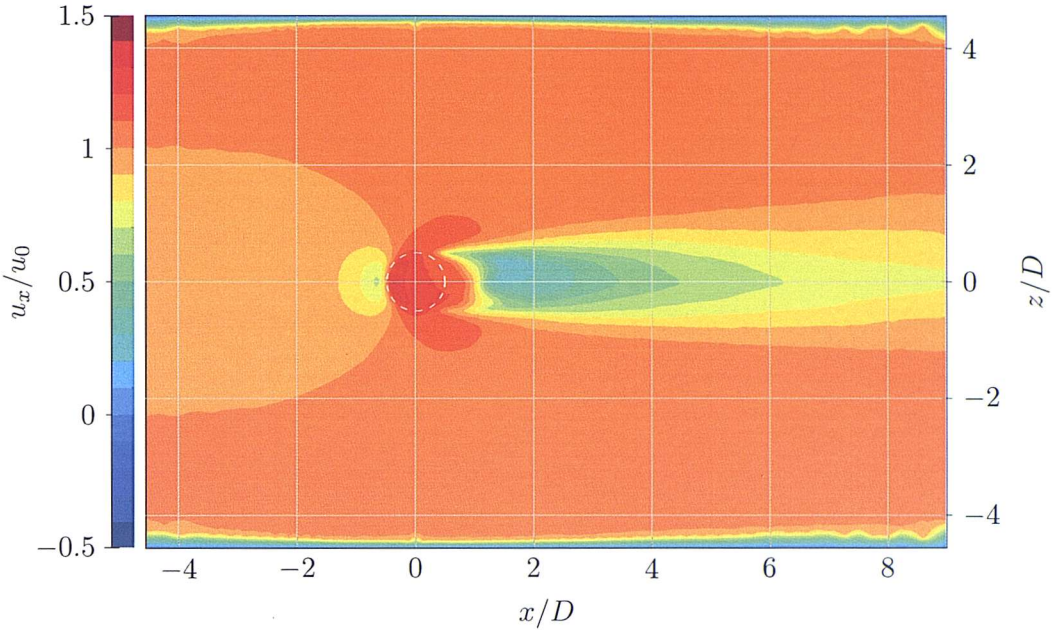



Figure 4.34: Time-mean, low frequency x-velocity ratio in the $y = 0$ plane. The mean was taken from $t^* = 37 \sim 52$: three shedding cycles for a circular cylinder of the same diameter as the anemometer, assuming $St = 0.2$. The position of the anemometer body is marked.

For brevity, the time-mean low frequency velocity along the duct centre line is compared with the results from other analyses and measurements, in Figure 4.36 in the next section.

### Open duct including support pillars

This simulation was particularly expensive as the mesh inside the duct needed to be fine not only to resolve the low frequency velocity up to the duct walls, but also to resolve the unsteady wake shed by the pillars. The total number of cells exceeded six million. Inspection of the wake from the support pillars showed it was fluctuating faster than the external wake, implying a shorter time-step was required. The time step was $dt = 2.5E-5\,s$, $dt^* = 0.005$. The last solution of the open duct case without the support pillars was used to initialise the simulation and 3000 simulation time-steps were generated, before the results were used. This was in order to give the solution time to settle towards a physically realistic result.

The time-mean $C_p$ at $y = 11.5\,mm$ is plotted in Figure 4.35, and compared with measurements and previous simulation results. This mean was over $t^* \approx 14$: a relatively short time. Relatively little change from the other simulations was demonstrated. The addition of pillars did not result in better agreement between measurement and simulation.

It should be noted that the simulated object differs from the measurement slightly, as the rotation of the device during the measurement results in the support pillars changing position relative to the flow direction as the measured point rotates around the axis of rotation. The simulation results are of the $C_p$ around the body, with the support pillars in a constant position with respect to the incident flow. This would result in the wakes cast from the support pillars around the acoustic duct changing position during the measurement, but being static during the simulation.

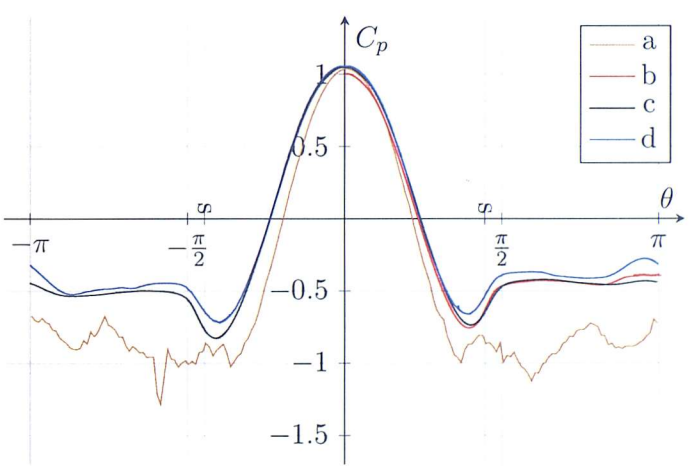



Figure 4.35: Measurement versus simulated $C_p$ around the body, $11.5\,mm$ above the centre plane. Labels indicate: a) Measurement; b) Steady simulation without pillars. c) Mean, unsteady simulation without pillars. d) Mean, unsteady simulation with pillars. The effect of adding the pillars is slight, and does not result in the simulation getting closer to the measured results.

Results for the time-mean, unsteady, low frequency velocity along the duct centre line, in the streamwise direction, are presented in Figure 4.36. Results are for a case without support pillars; a case with support pillars with shedding suppressed due to the use of a

coarse mesh; and a case with support pillars and a fine mesh, which demonstrated shedding.

These simulation results suggest the support pillars reduce the flow velocity at the entrance, cause a relative increase of velocity just upstream of the centre of the duct, and cause a local velocity increase as the flow leaves the duct. The shedding from the pillars resulted in an increase in velocity, just ahead of the duct centre.

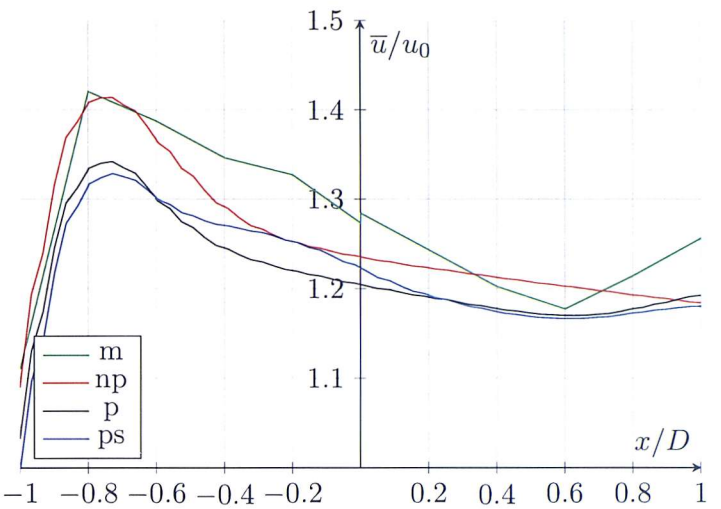
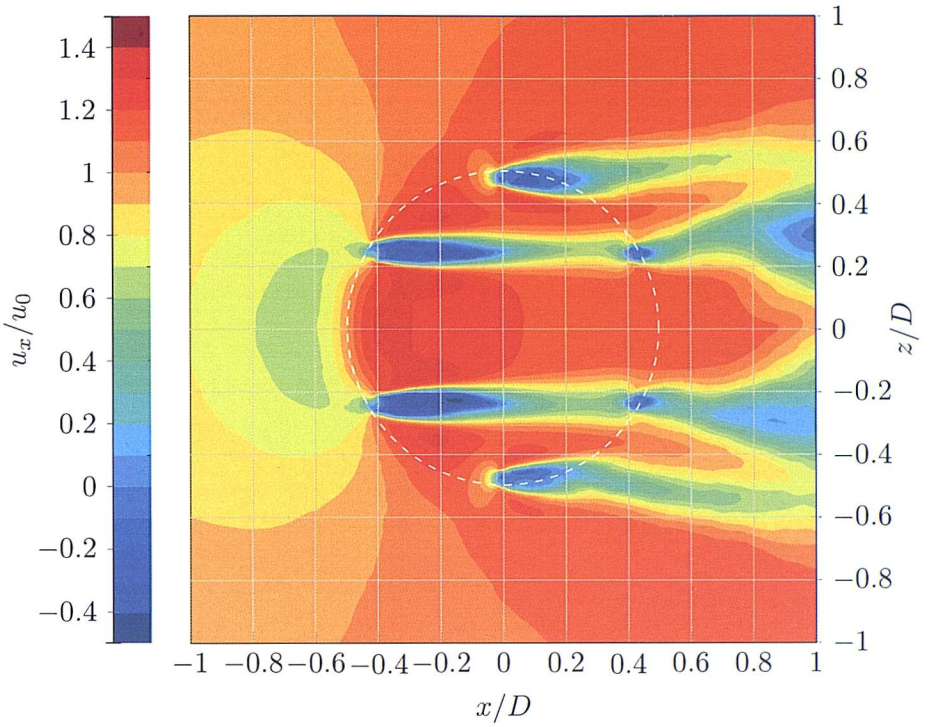
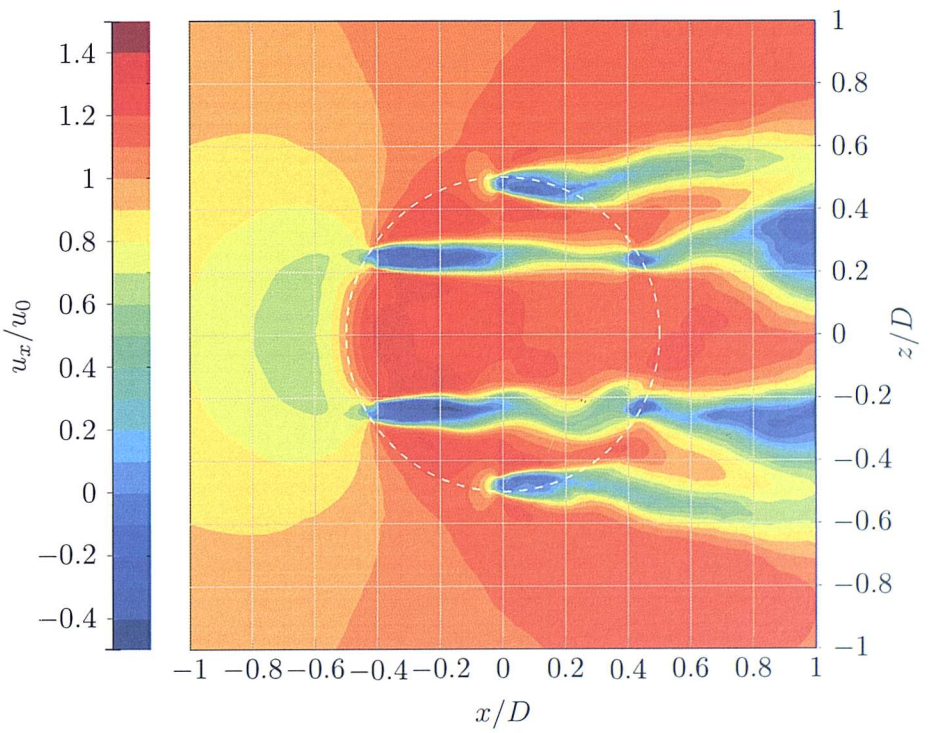



Figure 4.36: Time-mean, unsteady, low frequency velocity along the duct centre line, averaged over $dt^* = 5$. The labels indicate: m) measurement; np) no pillars, time-mean unsteady; p) pillars, time-mean unsteady, coarse mesh; and ps) pillars with a mesh supporting shedding, time-mean unsteady. Including the pillars reduced the velocity at the entrance and increased the exit velocity. A mesh which resolved the shedding from the pillars generated an increase of velocity near the centre of the duct, in agreement with measured data.

Instantaneous and time-mean flow behaviour through the duct in the $y = 0$ plane is illustrated in Figure 4.37. Shedding from the support pillars is visible in the instantaneous case, the separation between vortices on the same side of the wake was estimated to be $D/4 \sim D/3$, referencing the cylinder diameter: this can be considered the wake wavelength. In relation to the diameter of the pillar, $D_p$, the estimation is $6.5D_p \sim 9.5D_p$. This suggests a pillar Strouhal number around $0.1 \sim 0.15$. The simulation ran for $t^* = 25$ from the end of the no pillars simulation before the mean was calculated. While this non-dimensionalised time-mean is short in terms of the length-scales associated with the flow around the cylinder, it is longer in the scales defined by the support pillars, as the pillars have a diameter twenty-five times less than that of the anemometer. The time-mean was long enough for the mean flow to appear substantially symmetric in the duct, as illustrated in Figure 4.37(a).




(a) Mean velocity ratio.




(b) Instantaneous velocity ratio.

Figure 4.37: Low frequency x-velocity ratio in the $y = 0$ plane. The time-mean was taken from $t^* = 25 \sim 32$: $1\frac{1}{2}$ shedding cycles for a circular cylinder of the same diameter as the anemometer, assuming $St = 0.2$. The instantaneous velocity ratio was at $t^* = 32$ and shows shedding to be occurring from the support pillars. The position of the anemometer body is marked.

## 4.5 Conclusions

The viscous, slowly changing flow around and through the anemometer has been simulated using a commercial solver, FLUENT. Analysis was split into four sections, consisting of two and three-dimensional simulation of steady and unsteady flow. Simulation fidelity was judged on topological detail of the flow field; time-mean $C_p$ around the body in question; unsteady base $C_p$. and the slowly changing velocity through the acoustic duct. Simulation results were compared to other simulation results in the literature, and the measurement results detailed in Chapter 3.

The two-dimensional analysis of the circular cylinder was essential, for reasons of cost minimisation. It was established with steady simulations, that for reasonable agreement for boundary layer separation angle, the Reynolds Stress model was required with resolution through the boundary layer. Steady simulations were difficult to converge, often showing asymmetric wakes. The steady simulation showed two, elongated, counter-rotating vortices downstream from the cylinder.

To resolve the unsteady shedding from the cylinder, an unsteady simulation was required. Changing to an unsteady simulation resulted in worse agreement with published measurements for three-dimensional circular cylinders, while demonstrating a good match to published simulation data. It appears that these two-dimensional simulations do not represent the inherently three-dimensional shedding displayed by a circular cylinder in the sub-critical Reynolds number regime.

The unsteady base $C_p$ of the two-dimensional cylinder oscillated around a constant value: the mean of this value was in agreement with published simulation results. The oscillating base pressure was modulated by a second signal, shown to be related to the width of the test section, while the width had little effect on the mean $C_p$. The distance to the downstream boundary was found to have little effect on the cylinder shedding frequency, the $C_p$, and the modulating frequency. Doubling the time-step from $t^* = 0.01$ was shown to mask the modulation, while having little effect on the mean $C_p$.

Refining the mesh in the region close to the cylinder body largely removed the regularity of modulation of the base $C_p$ and reduced the shedding frequency significantly. Its effect on the mean $C_p$ was less pronounced, causing an increase of $C_p$ near separation, and a reduction in the base region. Refining the mesh in the downstream region appeared to cause little further change.

The anemometer simulations were three-dimensional. For the case without the acoustic duct, the simulation generated time-mean $C_p$ results showing the boundary layer had separated at a similar angle to that observed during measurements, but persistently generated a lower than measured $C_p$ after separation. Like the two-dimensional cylinder simulations, the steady simulations were difficult to converge. Velocity vectors showed the flow to separate while running around the side of the cylinder, with a resulting low velocity region in the wake. The flow passed over the cylinder ends, flowing into the low velocity region.

When the acoustic duct was present, the low frequency flow passed through it and moved into the low velocity region in the near wake of the anemometer: a region of high x-velocity is observed in this area. The flow accelerated as it moved into the acoustic duct, slowing as it traveled through it.

The sharp entrance lip of the acoustic duct results in the boundary layer separating and reattaching further into the duct. This region showed increased instability in $C_p$ in Chapter 3 compared to the region further into the duct, an effect expected with separation. Smoothing the entrance lip may result in the boundary layer no longer becoming detached, and may reduce turbulence downstream as a result of the shear layers no longer being free. The presence of the support pillars may result in changes to the lip having minimal effect, however.

Adding the support pillars around the duct caused a region of circulatory flow to occur at the front of the duct: this region affected the downstream flow in the $z = 0$ plane significantly, reducing the thickness of the high velocity region. Downstream of the pillars, wakes occurred.

The unsteady, three-dimensional anemometer simulations showed the vortex shedding of the two-dimensional circular cylinder simulations to be strongly affected by the low aspect ratio of the cylinder. Changing to an unsteady simulation caused the position the mean x-velocity ratio became positive to move upstream: towards the cylinder.

Adding the support pillars was shown to: cause acceleration of the flow near the centre of the duct, in agreement with measurement; cause the entrance velocity to be simulated lower than measured; increase the flow exit velocity; and generally improve the match between measurement and simulation.

# 5 Convected acoustics

## 5.1 Introduction

The convected wave equation derived in Chapter 2 has been solved using a finite element solver written for the project. This chapter presents and discusses some of the results generated. The solver was tested against an established commercial code, PAFEC, for zero, low frequency viscous flow conditions. PAFEC is described in Henshell [49].

To replicate the operation of an acoustic resonance anemometer, the low frequency velocity fields generated in Chapter 4 were used as the convective velocity component in the acoustic duct. Acoustic excitation was achieved by setting the pressure gradient in regions on the surface of the major faces of the acoustic duct. This was to represent the operation of the transducers used to excite the acoustic duct in the working anemometer. Discussion of the boundary conditions used to represent the infinite region is made, along with consideration of solution convergence based on element and domain size.

It is convenient to define $f_0$ as the frequency associated with the maximum pressure magnitude, occurring when a half wavelength occurs between the major faces of the anemometer duct. Likewise, $f_1$ is the frequency for the full wavelength case.

The modified resonance frequencies, dependent on the flow speed through the duct, are $f_0'$ and $f_1'$.

Throughout this chapter the term, 'convective flow' is used instead of 'low frequency viscous flow', for brevity. Simulation of the convective flow was the subject of Chapter 4.

## 5.2 Program description

The program used to solve the convected acoustic equation used an object oriented approach, as described by Mackie [70]. This approach resulted in a list of element objects being created at the start of an analysis. Each object was updated with the positions of its nodes, at which point the element transformation to the unit element was calculated. Each element was updated with the current flow field, and the solution frequency. Each element then calculated its stiffness matrix, before all elements made their contribution to the system stiffness matrix.

The object orientation resulted in each element possessing the functions required to perform calculations using the data it possessed. A single element could be passed to separate computer processors, enabling the element list to be created, and then updated in parallel.

The programming language used was Python: an object oriented, 'high level' language that can be used interactively, as discussed by Beazley [9]. Matrix manipulation was performed by the `Numpy` library, with routines optimised for the computer being used: this resulted in solution speeds associated with compiled languages, with the interactivity of an interpreted language. The result was that the time taken to solve the system equations was very short, but the time to update the elements and build the system matrix was longer.

The program evolved to run in two modes: interactive, and non-interactive. The former allowed dynamic interaction with the element objects, boundary conditions and system matrix and vector. This was useful for development purposes, but could not be run in parallel. An example of the code used to control the solver running in interactive mode can be found in Section A.0.5 and an example of a non-interactive analysis file is given in Section A.0.6

Two files were created during every analysis: A `.vec` file, illustrating the normal vectors describing the faces with damping applied; and a `.res` file, containing the pressure at each node in the mesh, updated after every solution. The pre and post-processor 'GMsh' as described by Geuzaine and Remacle [42], was used to view the contents of the `.vec` and `.res` files during and after solution, and was used to generate the element meshes.

The non-interactive form was called from the command line, as:

```
mpiexec -n 8 fe2.py m92acou2a.pyFE
```

In this case, the 'message parsing interface' (MPI) was used to coordinate parallel processing. The implementation was not fine grained: it consisted of each processor core being used to create a (complete) list of elements, and updating the list for a different frequency on each processor core that was available. While not efficient in memory terms due to the system matrices being built separately on each core, the speed up observed was nearly linear with the number of cores available.

## 5.3 Code validation

**Two-dimensional elements.**

First order elements were validated against PAFEC for the zero flow case using the mesh of Figure 5.1. This test shape nominally represented a small acoustic monopole source, close to a reflecting surface.

$\partial p/\partial n$ along the bottom, and left edge, is zero: a result of the elements being at the edge of the mesh. This boundary condition is equivalent to a hard wall. The left 'wall' will generate a reflection of the source, as the source is not coincident with it. The wall on the lower edge is coincident with the source, resulting in an 'infinite baffle' condition, whereby the acoustic wave will travel along the boundary without refraction.

A non-reflecting boundary is applied along the top edge and the right edge. This approximated the loading that the infinite region presents to the edges: approximated, as the impedance presented to the acoustic wave will depend on the angle of incidence. Waves travelling normally to this boundary will be presented with an impedance of $\rho_0 c$, passing the wave without reflection. Grazing waves will show some reflection, however. This was not a test of the boundary, but a test of agreement between the two solvers, using a simulation offering many calculation pitfalls.

Pressure was set at the excitation node, as marked with an arrow. The results for the pressure at different positions in the mesh show very good agreement, as indicated in Figure 5.2. The boundary conditions and element formulation are behaving similarly for the two solvers.

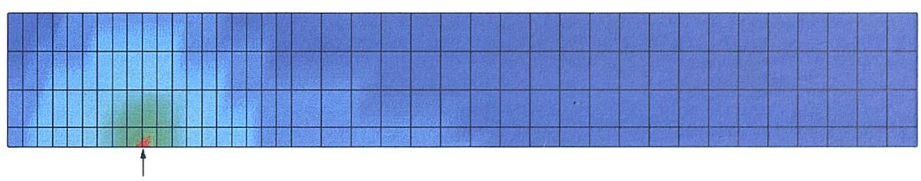


Figure 5.1: The two-dimensional test mesh used to compare results from PAFEC, with results from the convected acoustic solver. Acoustic pressure was set at the node marked with an arrow.

Second order, two-dimensional elements were tested using a two element mesh with damping around the upper and right side, $\partial p/\partial n = 0$ along the bottom and left side, and pressure excitation at a single node on the lower surface. This test is a coarse mesh version of the earlier test. Excellent agreement between the solvers was shown, as illustrated in Figure 5.3.

### 5.3.1 Three-dimensional elements

The mesh illustrated in Figure 5.4 was used to test the first order, three-dimensional elements and the non-reflecting boundary condition. Pressure was set to unity in the obscured corner and the non-reflective boundary was applied to the upper surface. All

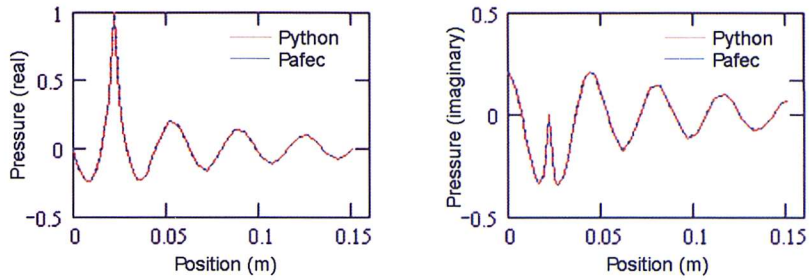



Figure 5.2: First order, two-dimensional element validation results. Pressure along the bottom edge is displayed, showing very good agreement between the convected acoustic equation solver implemented in Python, and PAFEC.

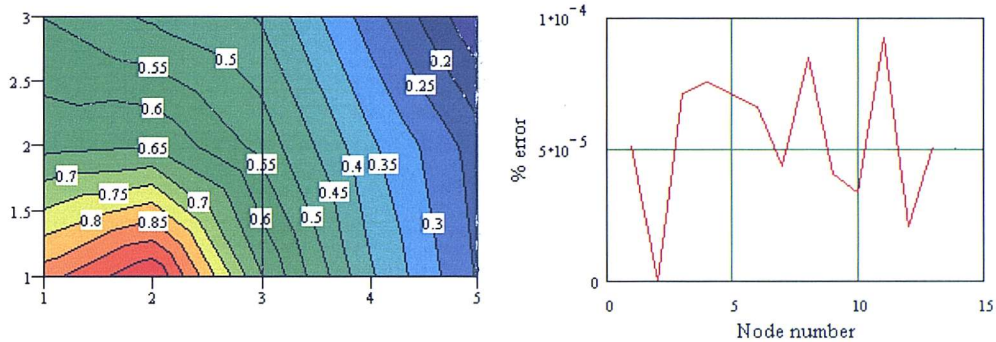
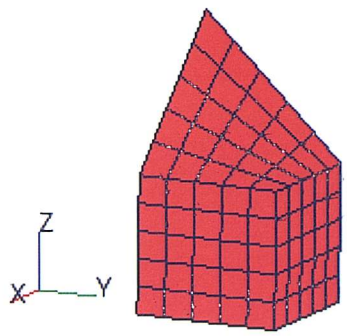



Figure 5.3: The two element mesh used for the validation of the two-dimensional, second order elements is illustrated. The acoustic pressure distribution throughout the two elements is shown, alongside the percentage difference between the two solvers. Good agreement is demonstrated.

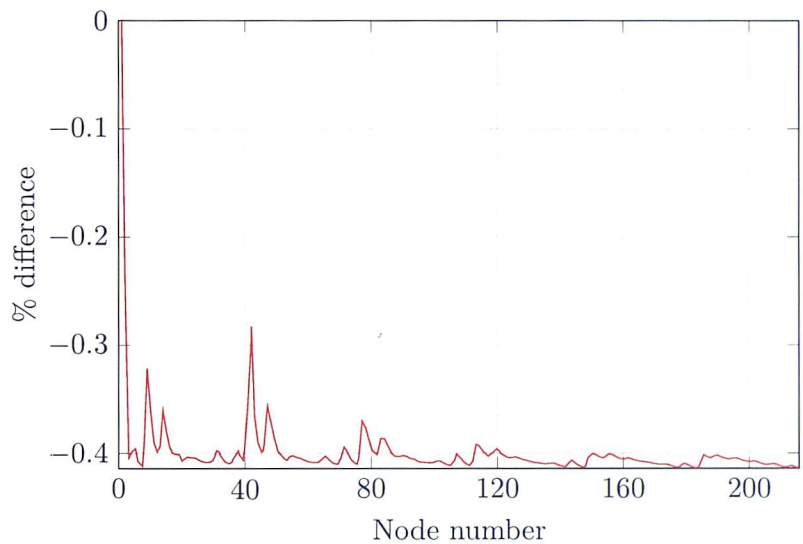
other surfaces have the natural, $\partial p/\partial n = 0$ boundary condition applied, as they are at the edge of the simulated region. Results show good agreement between the convected acoustics solver and PAFEC.

### 5.3.2 Boundary condition validation

A boundary condition was required to load the outer boundaries of elements that were on the interface between the finite region and the external, infinite region. Different approaches for generating this loading have been discussed in Chapter 1. The loading should be such that acoustic waves passing through it are not reflected. The 'quiet' boundary was used, as the field in the infinite region is not of interest and the approach preserves the sparsity of the system matrices. The formulation is described by Henwood and Bonet [50], and has been detailed in Chapter 2. The characteristic acoustic impedance of the medium, defined by Morse and Ingard [75] as $Z = \rho c$ for plane waves, is applied to the edge acting as the interface to the infinite region. In this case, $\rho$ is the density of the medium, and $c$ is the acoustic wave speed.




(a) Three-dimensional test mesh.




(b) Error at each node

Figure 5.4: The mesh used for testing first order, three-dimensional elements is illustrated, with the difference in acoustic pressure at each node between PAFEC and the convected acoustic equation solver. Good agreement is demonstrated.

The boundary was tested by applying it across one end of a square tube. All nodes at the opposite end were driven with a pressure gradient, to generate the plane wave. The acoustic pressure at the excited nodes was inspected. A reflective boundary would result in pressure variations as the frequency changes, as the phase relationship of the reflected component varies with the source. A non-reflective boundary will show no reflections, and the pressure at the excited end of the tube should show no fluctuations as the frequency is changed.

A mesh forty elements long, one element wide and one element thick is illustrated in Figure 5.5. The dimensions of the mesh are, $l = 2\,cm, h = 1\,cm, t = 1\,mm$. Three cases were tested. First, acoustics with no convective flow: 'static acoustics'. Second, acoustics with a convective flow velocity of $u$ was tested. This case used a 'quiet' boundary using an impedance, $Z = \rho c$. Finally, a case of acoustics with convective flow, with a 'quiet'

boundary using a celerity that was dependent on the convected flow velocity was tested. For this case, the value of $c$ used to calculate the applied impedance was modified by the convective velocity: $c' = c + u$. $u = 0.1\,c$ for these experiments.

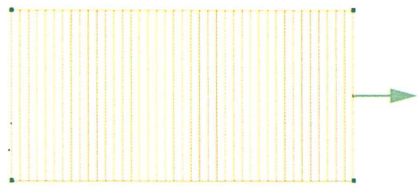


Figure 5.5: The mesh that was used to test the action of the 'quiet' boundary condition is illustrated. $\partial p/\partial n$ was set on the left side and the 'quiet' boundary was set on the right, as indicated by the arrow.

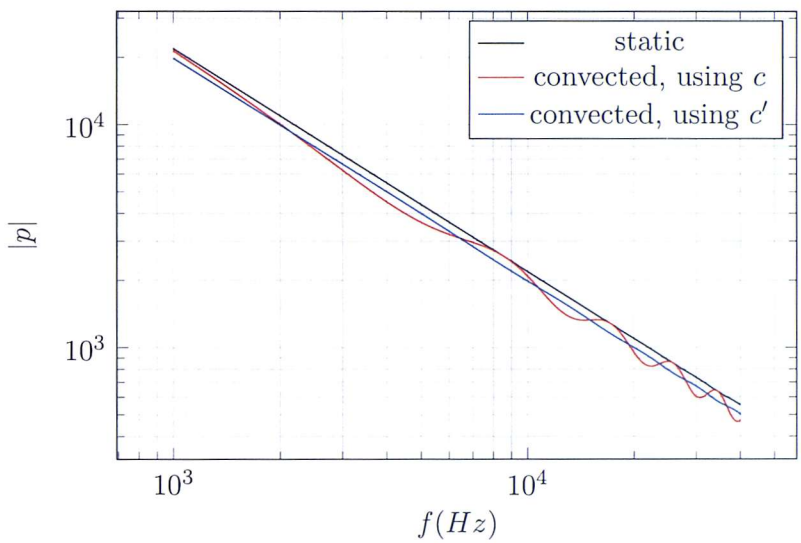


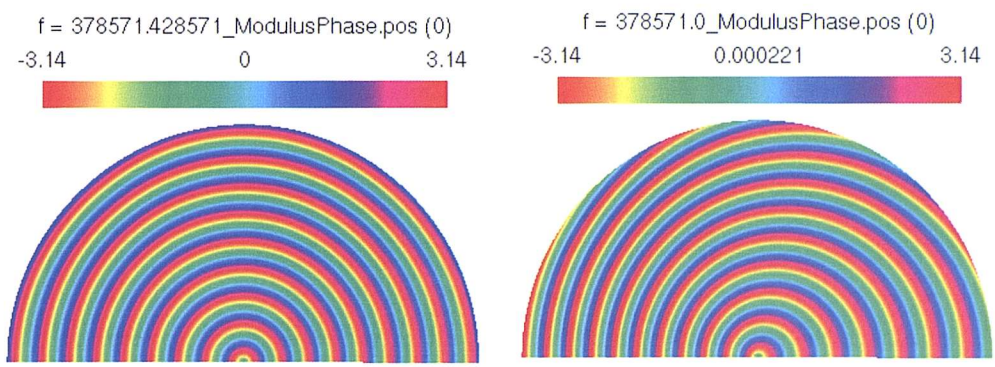

Figure 5.6: Effect on the acoustic pressure at the driven nodes, of adding convective flow and changing the boundary condition applied at the opposite end. The convected case with a boundary condition using $c' = c$ shows reflections are occurring, indicated by a frequency dependent pressure fluctuation.

Figure 5.6 shows the damping layer worked as expected. No ripples were present when the value of $c$ used by the boundary to calculate $Z$ was modified to include the convective velocity normal to the element.

### 5.3.3 Point source in an infinite baffle

Examination of the phase distribution around a point source in uniform flow is included here, as an interesting feature is revealed.

A nominally two-dimensional simulation of a point source radiating into a static medium was performed, using a semi-circle of finite elements terminated over its curved edge, with the 'quiet' boundary previously described. One hundred first order elements were used across the radius, resulting in approximately sixteen elements per acoustic wavelength. One element was used through the thickness. The centre nodes were excited with a pressure gradient boundary condition and the phase of the pressure was inspected over the space. Then, flow was added from left to right, at $u = c/5$. The effect on the phase is plotted in Figure 5.7.




(a) $u = 0$. (b) $u_x = c/5$.

Figure 5.7: The effect on the phase distribution of adding a flow velocity of $c/5$ from left to right is illustrated. The plots show the high frequency acoustic wave velocity normal to the convective flow, is unaffected by the flow.

As indicated by Figure 5.7, the phase normal to the flow direction is unaffected by the flow. This is a result of the approximation performed in moving from Equation 2.23 to Equation 2.24: the terms involving multiplication of two low frequency velocity components were much smaller than the linear velocity terms, and were removed. It is these terms that would be responsible for maintaining the celerity in the frame of reference of the wave. This approximation has resulted in the celerity increasing as the Pythagorean sum of the velocity components. The error is small at low flow velocities and it is in this low-velocity region that this analysis is accurate.

### 5.3.4 Concluding remarks

This section summarised the code development and presented results from validation exercises. The results show good agreement between the commercial, static acoustics solver and the convected Helmholtz equation solver for the zero flow case. The boundary condition used to simulate the infinite space has been tested for reflections and found to perform well.

Limits of applicability of the convected acoustic solver have been established, by considering the phase distribution occurring around a point source on an infinite baffle. The acoustic wave speed was shown not to account for flow velocity normal to the acoustic wave. The errors generated by the approximations used will be small when the convecting field velocities are a small fraction of the speed of sound.

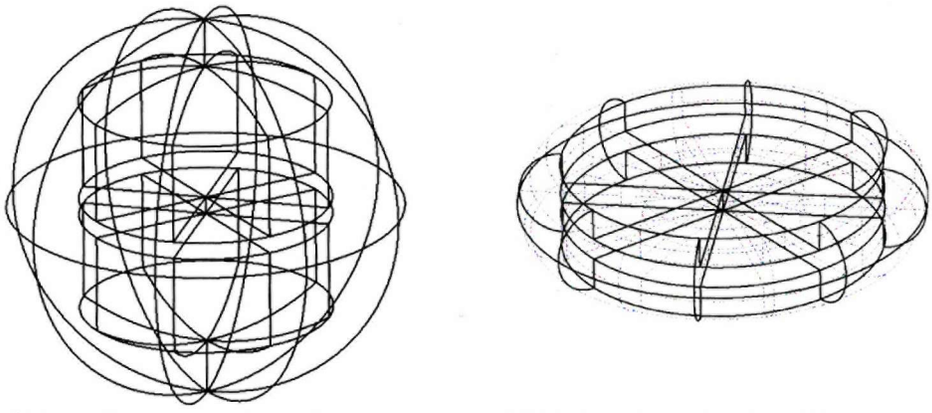
## 5.4 Simulation domain

The two-dimensional simulations were fast because the number of degrees of freedom being solved was low. In these cases it was possible to simulate not only the region inside the acoustic duct, but also the region extending a significant distance beyond the ends of the acoustic duct.

The move to a three-dimensional mesh proved difficult both in solution time and memory requirements due to the regular mesh density required in all regions.

To reduce the problem size, fewer elements were used. This was achieved by reducing the size of the region being resolved, and by testing the effect of increasing the size of the elements. The process of reducing the size of the resolved region is illustrated in the change from Figure 5.8a to Figure5.8b. In the former case, the region to be meshed extends beyond the acoustic duct and around the body of the anemometer to a curved surface which interfaces with the infinite region. The latter case shows a truncated simulation region: just the acoustic duct region, with a curved outer edge which interfaces with the infinite region.

Both approaches were investigated using nominally two-dimensional meshes.



(a) Large domain, descibing the region inside the duct and around the body of the anemometer.

(b) Reduced domain, describing the region inside the duct and immediately outside.

Figure 5.8: Comparison of the regions to be meshed, for the full and reduced domain cases.

### Mesh density

A tube of first order elements was created, $5\,cm$ long. At one end, $\partial p/\partial n$ was set. All other surfaces were left as hard surfaces. The tube was one element tall and deep, and the number of elements along the tube was varied. Inspection of the pressure at the driven end indicated the natural frequencies as peaks in the response, as illustrated in Figure 5.9, for the case of one hundred elements along the length.

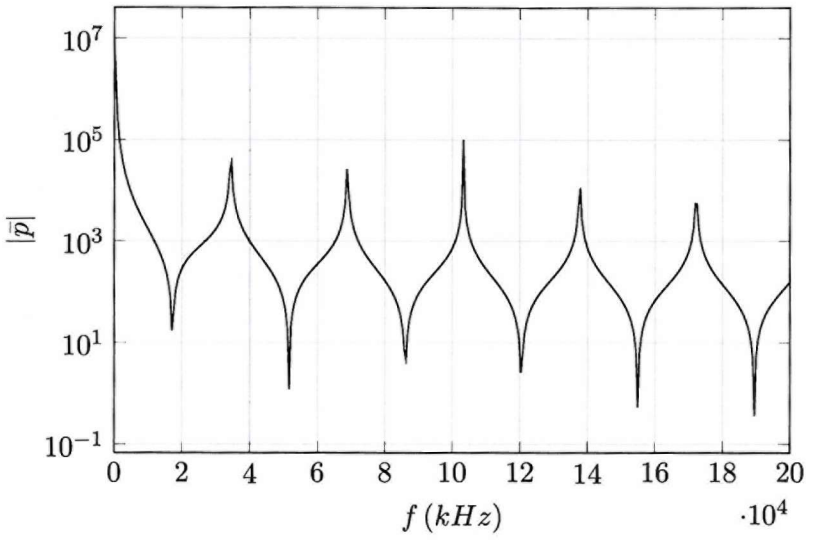



Figure 5.9: Acoustic pressure at the excited end of a closed tube, $5\,cm$ long with one hundred, first order elements along its length. The expected resonance frequencies are: $\lambda = l/n; n = 0.5, 1, 1.5....$ Frequencies include $f_0 = 3440\,Hz$ and $f_1 = 6880\,Hz$.

The frequency of the second peak was extracted using the bisection method, for different numbers of elements along the tube. The results for the frequency error for a given number of elements per wavelength are tabulated in Table 5.1.

| ele/$\lambda$ | $f\,(Hz)$ | Fraction of expected $f_0$ |
|---|---|---|
| 3 | 8046.47 | 1.170 |
| 4 | 7586.29 | 1.103 |
| 5 | 7336.25 | 1.066 |
| 10 | 6993.66 | 1.017 |
| 15 | 6930.40 | 1.007 |
| 20 | 6908.33 | 1.004 |
| 40 | 6887.07 | 1.001 |

Table 5.1: Frequency error associated with the mesh density. Ten elements per acoustic wavelength resulted in a frequency error of 1.7%.

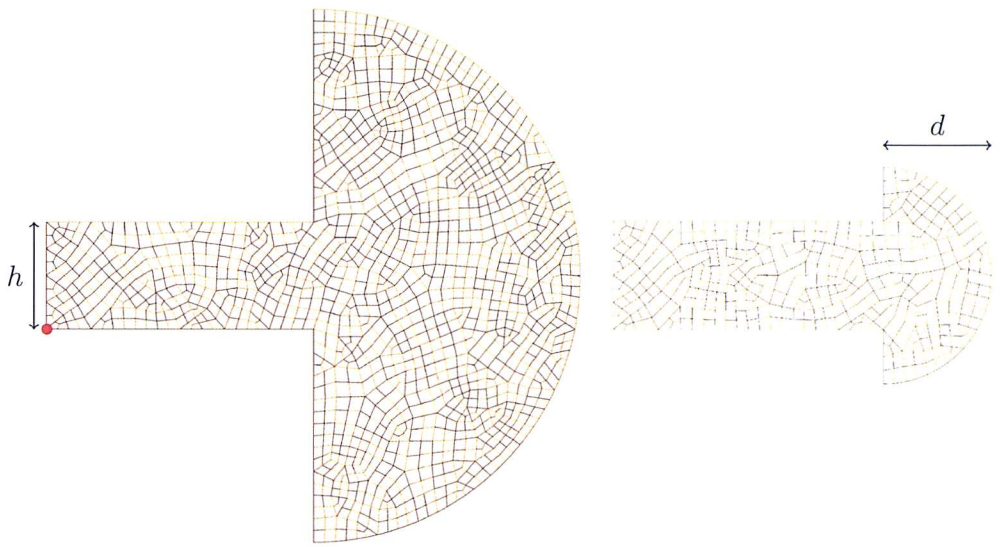
As indicated in Table 5.1, the frequency error caused by using ten first order elements per wavelength is 1.7%. This mesh density has been used to define the largest elements during the convected acoustic analyses.

Although the mesh density was considered acceptable for static acoustics, work by Gabard

et al. [38] has shown that upstream and downstream mesh densities should differ for the same accuracy, due to the differing wavelengths involved. The regular mesh used may therefore be introducing errors, growing with flow velocity.

### Distance to the boundary

The boundary conditions were tested to see if the meshed region could be reduced in size - reducing the number of required elements. A nominally two-dimensional mesh describing one half of the duct was used, and the distance from the outer edge of the duct end to the curved edge of the interface to the infinite region was varied, as illustrated in Figure 5.10.




(a) $d = 5h$ (b) $d = 1h$

Figure 5.10: Mesh used to test the effect of varying the distance, $d$ to the curved boundary, in terms of the duct height, $h$. The excited node is marked.

For simplicity, the centre node was excited. $\frac{\partial p}{\partial n}$ was set, and the acoustic pressure at the node was examined. The requirement of ten elements per wavelength when the duct was resonating with a full wavelength between the duct major faces set the mesh density as illustrated in Figure 5.10: wavelengths shorter than this will show errors that increase as the wavelength decreases.

Elements that had the 'quiet' boundary applied to them were selected automatically by detecting which nodes were on the surface to be affected, this surface being defined geometrically.

The effect of the damping layer over a wide frequency range is illustrated in Figure 5.11, by comparing it to the effect of changing the curved surface to a hard wall.

Figure 5.11 indicates a resonant system with low damping for the undamped case; and a damped system for the 'quiet' case. The low frequency modes displayed by the undamped case have nearly vanished with the quiet boundary. The peaks at $f = 6\,kHz$ and $f = 11.8\,kHz$ showed amplitude distributions varying along the length of the duct, verifying that the peaks were due to lengthwise oscillation that was largely removed by the 'quiet' boundary. Some residual lengthwise resonance occurs for the 'quiet' case, as the boundary does not simulate an infinite pipe due to the curvature on the damped surface, and a change of impedance will occur as the acoustic pressure wave moves beyond the end of the duct.

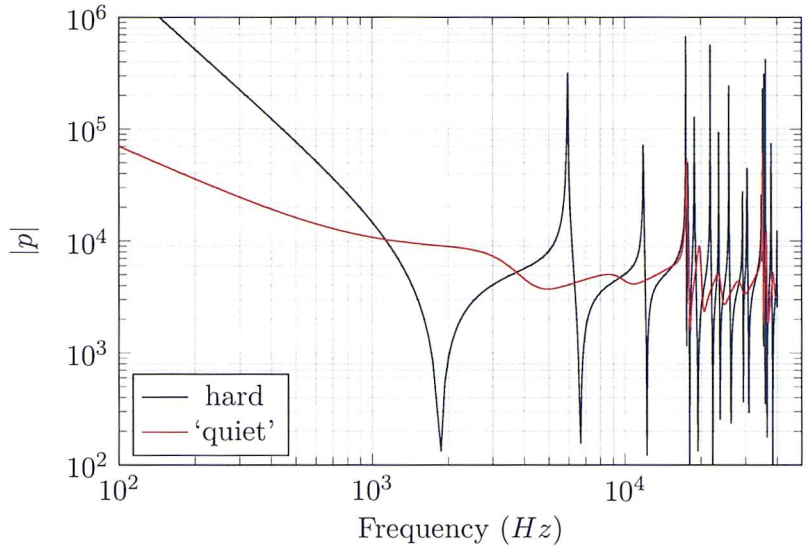
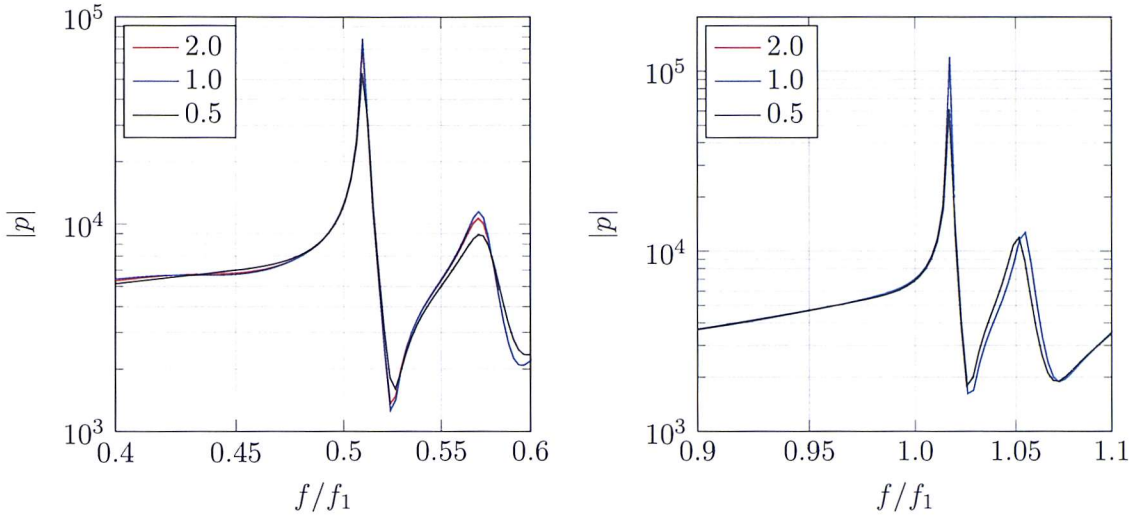



Figure 5.11: Effect of changing from a hard boundary at the curved exit to a 'quiet' boundary, on the pressure at the excitation node. With reference to Figure 5.10, this case used $d = \frac{h}{2}$.

Inspection of the acoustic pressure response closer to the frequencies associated with the vertical modes in the duct was performed to check the effect of reducing the distance to the 'quiet' surface. Figure 5.12 shows the effect is to increase the damping slightly: the acoustic pressure magnitude at resonance is slightly reduced. The effect is more pronounced for the full wavelength resonance. The resonance frequency, and the response slightly away from resonance does not appear to be affected greatly.

These results suggest the 'quiet' boundary can be applied close to the duct for both the half and full wavelength cases. In changing from from $d = 2h$ to $d = 0.5h$, the element count reduced to approximately one quarter of its original value.




(a) Half wavelength across the duct height.

(b) Full wavelength across the duct height.

Figure 5.12: Effect of changing the distance to the 'quiet' boundary, as a function of the separation $h$, between the major faces of the acoustic duct.

## 5.5 Anemometer simulation

The simulation of the anemometer behaviour was split into several sections. In all cases, the same mesh was used (as described in a later section), an excitation was applied over a region approximating a transducer, and the pressure was inspected in another region.

First, a uniform velocity field was used. This simple case required no separate simulation of the low frequency flow, and the flow velocity used was constant at all positions. Second, a steady flow field was assumed. The steady flow fields calculated in Chapter 4 for the quarter mesh, steady case were interpolated over the finite element mesh and duplicated to generate a full mesh. The steady velocity differed at different positions, but was not changing with time. Finally the unsteady, low frequency velocity fields were used step by step, to provide a slowly varying field. Each step was used to convect the steady state acoustic field. The simulated, low frequency velocity field was stored every five time-steps, corresponding to a time step of $dt = 1.25 \times 10^{-4}$: this time-step resulting in a resolvable limit for the velocity fluctuations of $4\,kHz$ according to the Nyquist criterion. This frequency is greater than the frequencies shown to have the greatest spectral content in the acoustic duct with a free field velocity of $u = 10\,ms^{-1}$, as indicated in Figure 3.27. It is an order of magnitude lower than the operating frequency for the acoustics.

All of the simulations in this section used a celerity of $c = 345\,ms^{-1}$, and a density of $\rho = 1.19\,kgm^{-3}$: a result of applying $c = \sqrt{\gamma R_s T}$, and $p = \rho R_s T$, at $T = 20\,C$ with moist air. Here, $\gamma$ is the ratio of specific heats; $R_s$ is the specific gas constant; $T$ is the absolute temperature; and $p$ is the absolute pressure.

### 5.5.1 Mesh and boundary conditions

The mesh used for the simulations in this section is illustrated in Figure 5.14 and Figure 5.15. It has approximately $10,000$ first order hexahedra, and $83,000$ nodes. It is illustrated again in Figure 5.13, showing a more three-dimensional view. The axis set is the same as that defined in the measurements chapter, in Figure 3.1.

The transducers used to excite and sense the acoustic field were located on one side of the duct and were $18\,mm$ in diameter. There were three transducers at a constant radius from the duct axis of rotation. Figure 5.13 shows the region identified to fall within the area of one of them, marked in red.

The effect of sampling and exciting over this finite area was included by applying $\partial p/\partial n$ over the nodes the excitation transducer would be in contact with. The nodes in contact with the observation transducer were used to calculate the mean acoustic pressure.

The 'quiet' boundary previously described was applied around the curved surface at the ends of the duct. The surface was detected automatically: the arrows in Figure 5.13 indicate the surfaces affected, and the normal to each surface. The component of the low frequency flow acting in this direction was used to modify the celerity used by each patch, during the calculation of the impedance to be applied.

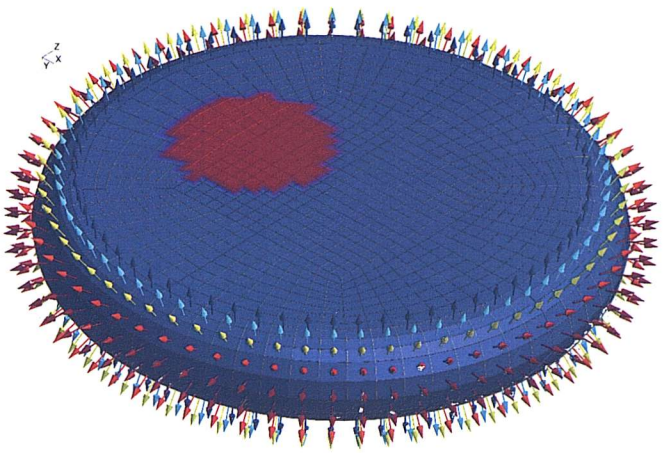


Figure 5.13: The mesh used for acoustic analyses. The drive region is indicated in red; the observation region (not indicated) matches the drive region, but is rotated 120° around the axis of rotational symmetry. The arrows indicate the normal directions to each of the damped surfaces.

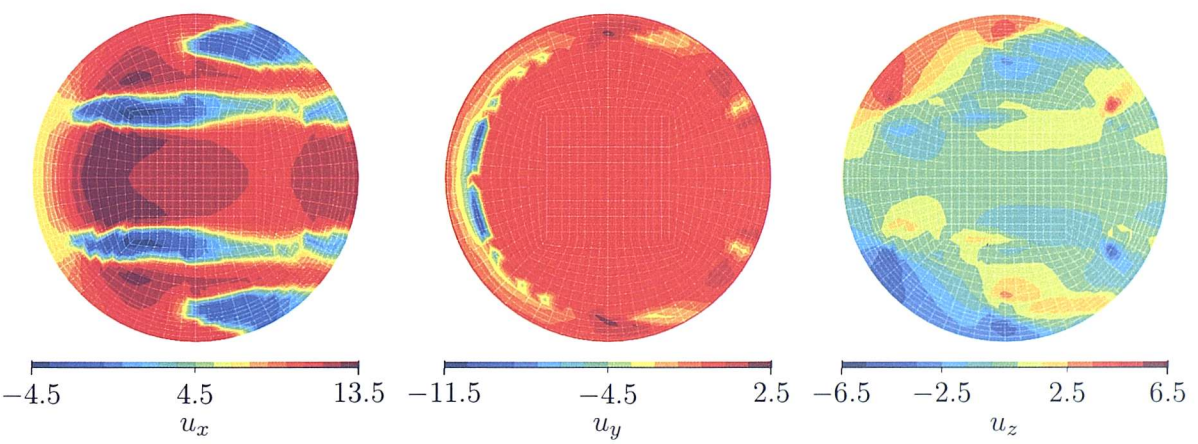
### 5.5.2 Low frequency velocity field interpolation

The convected acoustic solver calculated the mean, low frequency flow through each element as the mean, low frequency velocity at the element nodes. For a non-uniform velocity field, the low frequency velocity at each node was estimated from the velocity at the nearest point in the low frequency, viscous flow mesh. This approach was used as the mesh used during the viscous flow simulation used cells that were much smaller than those used by the convected acoustic solver. The errors caused by this approach would have been larger if a coarse mesh had been used to generate the viscous flow field. The largest position errors noted were $0.8\,mm$, occurring in the region outside the duct where the viscous flow field cells became larger.

During mirroring of the velocity field, care was taken to ensure the low frequency velocity components were treated correctly. Applying a mirror in the $y = 0$ plane for example, would not affect the sign of the x-velocity, but would change the sign of the y-velocity in the new section.

Flow inversion was also catered for, to simulate the effect of reversing the direction of the external low frequency, viscous flow field, without resorting to re-solving it.

A set of results from the interpolation routines are presented in Figure 5.14, and Figure 5.15; generated from a steady, quarter mesh, viscous flow field simulation. These results show the interpolation and duplication routines were working as expected.

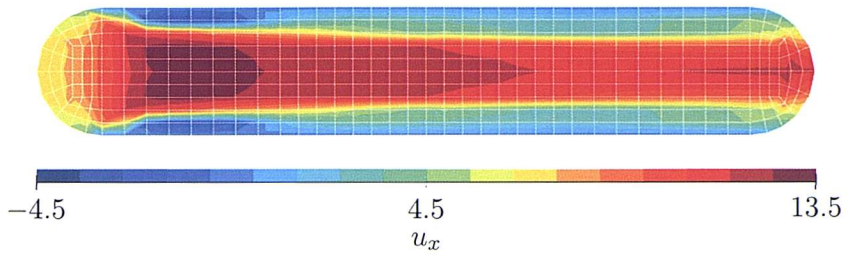



(a) $x$ velocity in the plane, $y = 0$ (b) $y$ velocity on the upper surface of the mesh. (c) $z$ velocity in the plane, $y = 0$

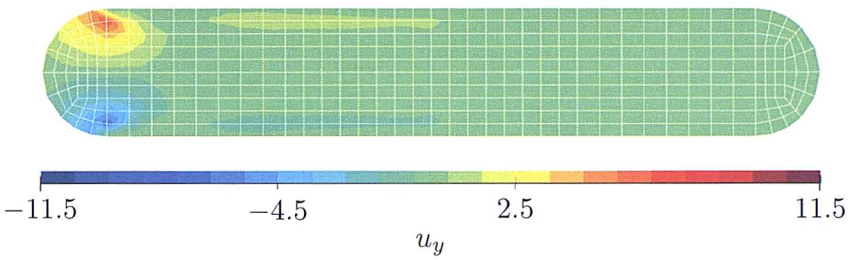
Figure 5.14: Interpolated low frequency velocity results, generated from a quarter mesh viscous flow field simulation. The normal to the mirror plane is pointing up the page. It is noted that the upper surface in subfigure (b) curves into the page, at the outer edge. It is not in a single plane.

### 5.5.3 Resonance hunting

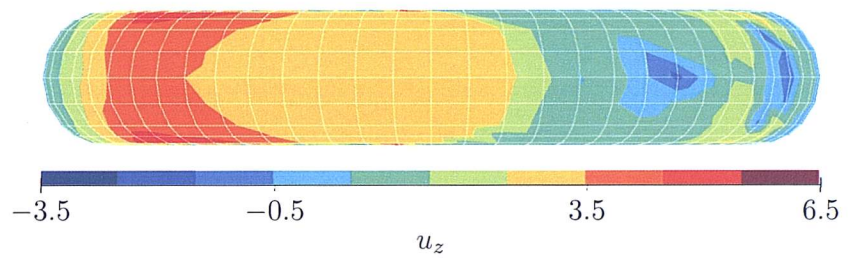
Part of the anemometer measurement process involved inspecting the phase at resonance. This function was duplicated in the solver by performing a search for the frequency resulting




(a) $x$ velocity in the plane, $z = 0$




(b) $y$ velocity in the plane $z = 0$.




(c) $z$ velocity on the surface of the mesh.

Figure 5.15: Interpolated low frequency velocity results, generated from a quarter mesh viscous flow field simulation. The normal to the mirror plane is pointing up the page. It is noted that subfigure (c) is not in a single plane, but curves out of the page.

in the largest pressure magnitude, and inspecting the phase at this frequency. A bisection method was adopted: the routine performed a first pass frequency sweep on the specified limits. The frequency giving the largest value of pressure amplitude was found and at least two new points were placed either side of this frequency. Figure 5.16 shows this process in operation.

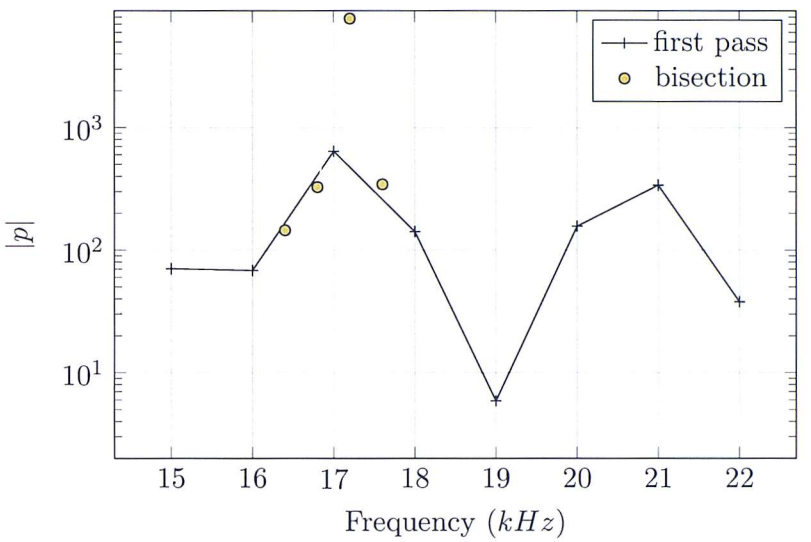



Figure 5.16: Illustration of the frequencies picked by the bisection algorithm during a search for the maximum acoustic pressure magnitude in a frequency range. Two frequencies were selected either side of the frequency showing the largest pressure magnitude. The number of new frequencies equalled four, or the number of processing cores available: whichever was the larger.

With parallel operation, the number of extra points used was increased, in order to accelerate the process.

The plots generated from this point on were generated using an initial 96 points across the indicated frequency range, followed by a search for the peak acoustic pressure amplitude to within $0.1\,Hz$, unless otherwise indicated.

### 5.5.4 Steady, uniform flow

The steady, uniform flow case used a constant flow velocity value at all positions on the acoustic mesh. This value did not change over time.

This case was appealing as it required no separate solution for the flow field: the flow velocity was set equal in all elements. It was therefore the cheapest of the convected acoustic solutions but the least accurate. It is also the simplest case and so provided insight into the behaviour of the system without the added complexity of a slowly changing velocity field. For this reason, this case was used to explore the general operation of an acoustic resonance anemometer before examining in detail its operation at resonance.

### General behaviour with zero convective flow

The mean acoustic pressure across the observation transducer is plotted in Figure 5.17, in response to a constant $\partial p/\partial n$ over the excitation region. The simulation mesh described the entire acoustic duct, but only half of the simulated region is displayed here, so the pressure distribution through the thickness of the duct can be examined. Although symmetry could have been exploited in this case, it was not.

Frequencies of interest have been marked and the pressure distributions at these frequencies plotted in Figure 5.18.

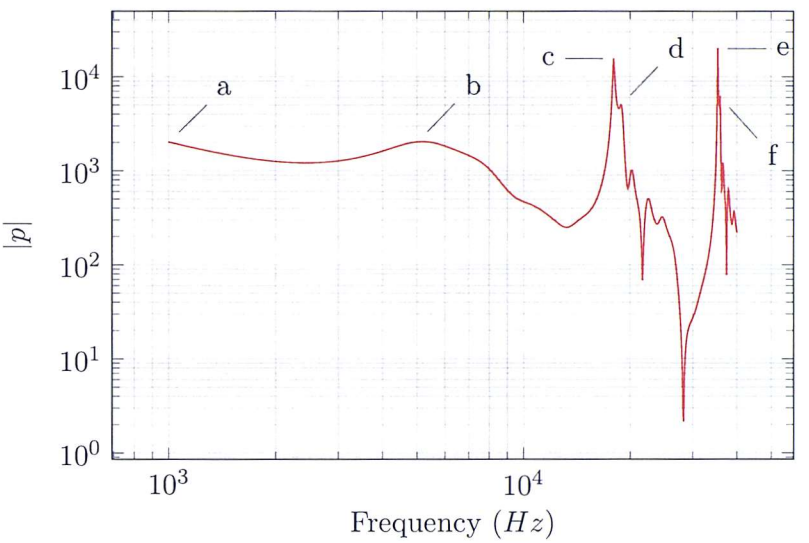
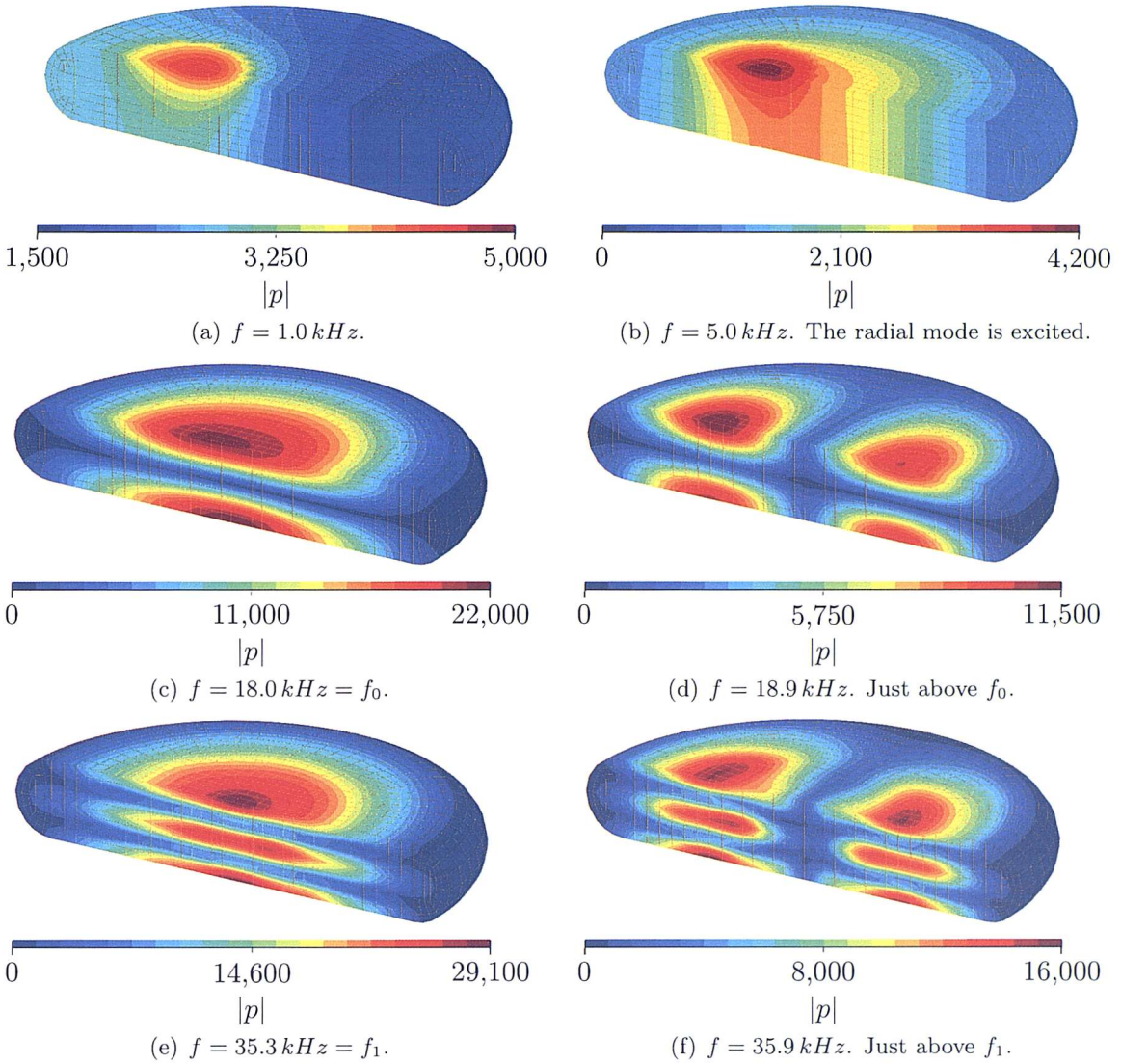



Figure 5.17: Acoustic pressure variation in the observation region versus frequency, for zero convective flow. The frequencies of interest have been marked. 360 frequency points were used.

Figure 5.18 shows the rise in region 'b' to be due to a radial mode of the system. This mode is due to the partial reflection that occurs as the acoustic wave leaves the duct. The partial reflection is a result of the acoustic wave passing into a region with a different acoustic impedance. The excitation region is visible, the pressure distribution adopting the natural mode shape as the distance from the excitation region increases. Below this frequency (region 'a'), no clear modal activity is present, and the excitation region is clearly indicated as a region of increased acoustic pressure.

Region 'c' shows the first mode occurring between the major faces of the duct at the frequency referred to as '$f_0$'. This shows the pressure to be greatest at the walls near the centre of the duct, away from the open ends. The excitation region is not clear as the mode has been strongly excited over successive excitation cycles. Region 'd' is just above this frequency, where a different mode has been excited. The pressure distribution in this case is a result of the excitation position. If the excitation had been applied at a different angle to the axis of rotation, this modal pressure distribution would have rotated also.

Case 'e' shows the resonance caused by a full wavelength occurring between the duct walls. This frequency is referred to as '$f_1$'. This is the region the anemometer operates in. Like




(a) $f = 1.0\,kHz$.

(b) $f = 5.0\,kHz$. The radial mode is excited.

(c) $f = 18.0\,kHz = f_0$.

(d) $f = 18.9\,kHz$. Just above $f_0$.

(e) $f = 35.3\,kHz = f_1$.

(f) $f = 35.9\,kHz$. Just above $f_1$.

Figure 5.18: Pressure magnitude at frequencies of interest, with zero flow. The simulation used the full duct mesh; these results are cut through the centre plane to indicate the pressure distribution through the duct.

the distribution at $f_0$, the excitation region is not visible. Close in frequency is the next pressure peak, case 'f' which, like case 'd' is dependent on the excitation position.

### Response near $f_1$ with zero convective flow

The pressure magnitude response over a range of frequencies close to $f_1$ is plotted in Figure 5.19, with the same markers as Figure 5.17. The frequency scale is now plotted as a function of the expected resonance frequency for the case of an infinite duct, $f_{1\infty}$. There is another interesting frequency present that was previously obscured. It is marked as 'g', and its pressure distribution is plotted in Figure 5.20.

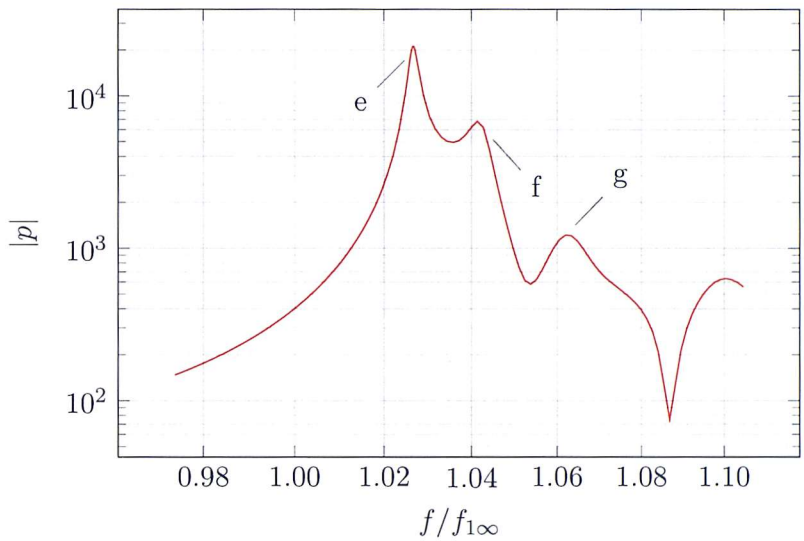



Figure 5.19: Acoustic pressure variation in the observation region versus frequency for zero convective flow. Frequencies of interest have been marked for comparison with previous results.

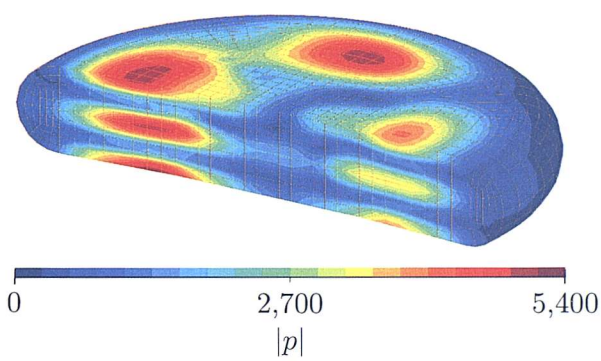



Figure 5.20: Pressure magnitude distribution at the frequency marked, 'g' in Figure 5.19.

The amplitude of the pressure response at the point marked 'g' in Figure 5.19 is more than an order of magnitude lower than the pressure response peak marked 'e'. Inspection of Figure 5.20 shows that this peak may not solely be a result of a natural frequency of the system, but also a result of the choice of observation position relative to the excitation position. The pressure distribution is suggestive of a circumferential mode.

Measured results are compared with simulation results, in Figure 5.21, with arbitrary scaling of the transfer function to facilitate comparison. The simulation shows the first

peak to be of an amplitude approximately three times that of the second peak, whereas the measurement shows only a slight increase. This might be expected, as the simulation has no damping present other than that provided by the 'quiet' boundary. The measurement system would have increased damping due to mechanical and electrical losses, reducing the peak to trough ratios observed. It appears that the errors introduced by the truncated acoustic region are less than those resulting from assumptions made about the mechanical system.

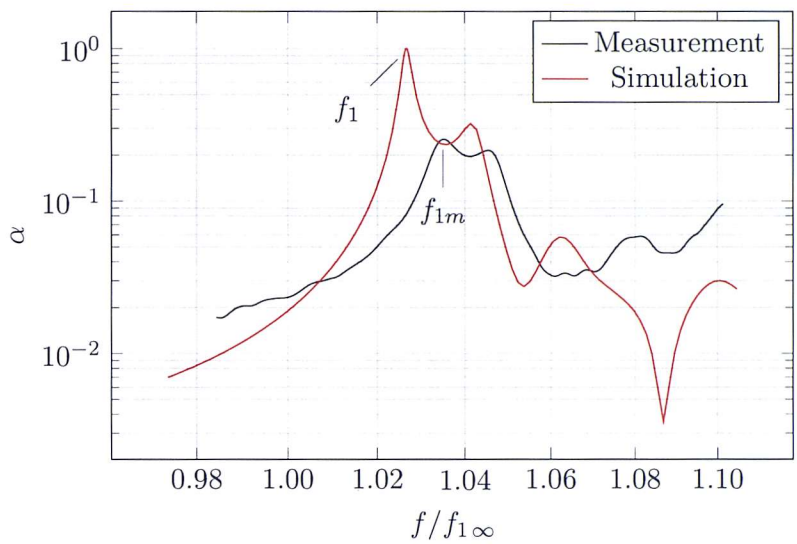



Figure 5.21: Comparison of the simulated and measured transfer function $\alpha$, between two transducers, with one of them acting to excite the acoustic duct. The amplitude scaling is arbitrary. The frequency scale is relative to the expected resonance from an infinite duct. $f_1$ indicates the first peak from simulated data. $f_{1m}$ marks the first peak of the measured data.

The frequency $f_1$ in the simulation is 2.7% higher than that expected for an infinite duct. An error of approximately two percent was expected from the mesh, according to Table 5.1. The remaining 0.7% may be due to end effects of the finite duct.

The difference between $f_1$ and $f_{1m}$ is 0.8%. This value increases to approximately three percent once the errors due to the mesh are accounted for. This difference between measured and simulated $f_1$ could be due to errors in the acoustic duct dimensions and the calculated celerity. The difference in frequency between measurement and simulation for the second peak is 0.4%. A celerity error would scale the frequency error for the two peaks by the same amount, so the difference in error is likely due to dimensioning errors. The approximate three percent error in frequency for $f_1$ corresponds to a physical error of $0.3\,mm$ in the separation between the major faces.

The difference in gradient of the response below $f_1$ between measurement and simulation is possibly a result of the transducer acoustic pressure response. The transducer is electrically filtered during measurements, and no attempt to replicate its response during the simulation was made.

Considering the expected errors, and the lack of simulation of transducer effects, the agreement between measurement and simulation appears good.

The phase over the surface including the transducer at $f = f_1$ is plotted in Figure 5.22. There appears to be a slight variation of phase over the surface.

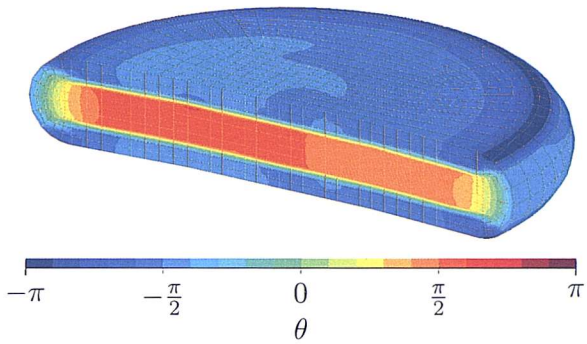



Figure 5.22: Phase distribution over the surface including the transducers at $f_1$. A slight variation of phase is present.

The phase variation along the edge of the cut plane of Figure 5.22, on the side featuring the transducers, is illustrated in Figure 5.23. It shows a small spatial fluctuation and a small step in the region of the transducer, possibly an effect of exciting the duct over a finite area close to the duct edge.

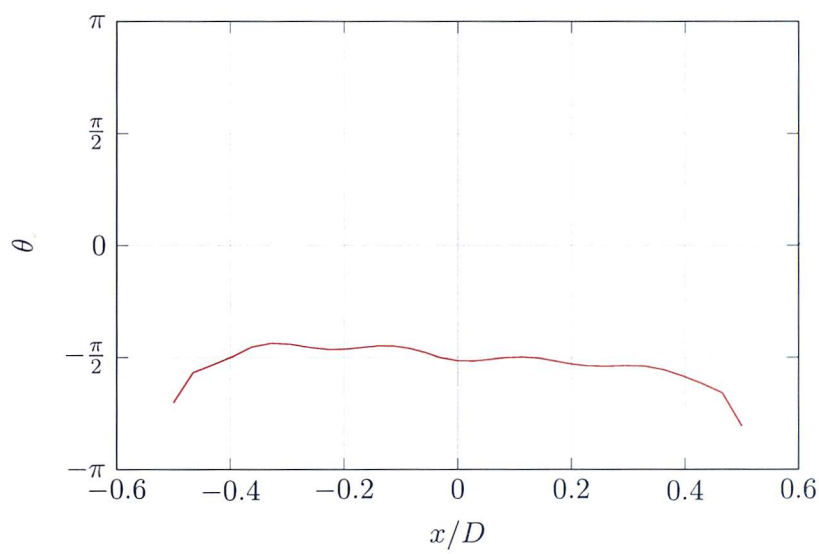



Figure 5.23: Phase along the x-axis of the acoustic duct at $f = f_1$, with the transducer at $-0.4 \lesssim x/D \lesssim -0.1$.

### Effect of uniform flow

The effect of adding a uniform convective flow on the acoustic pressure response over the observation transducer is illustrated in Figure 5.24, for different flow rates.

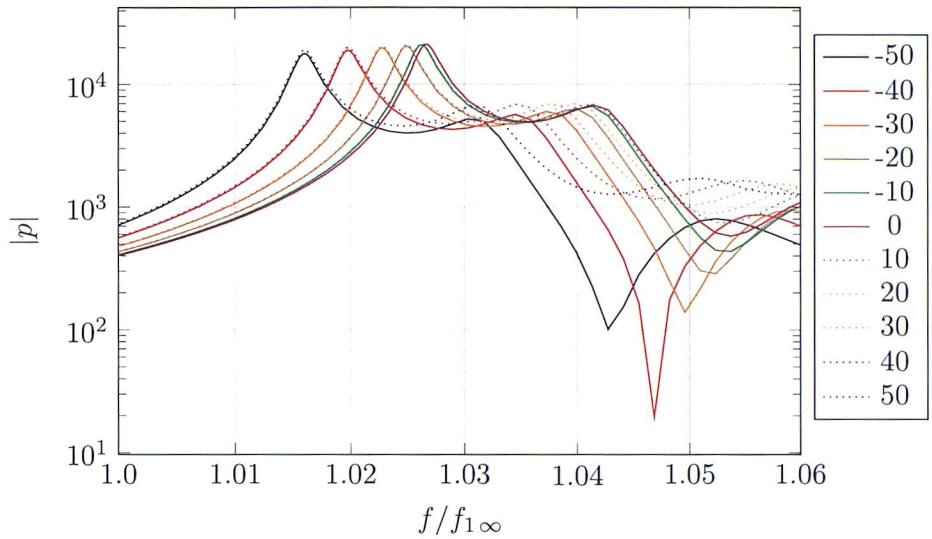



Figure 5.24: Mean acoustic pressure over the observation region, with a constant uniform convective flow velocity of magnitude as indicated. Near $f = f_1'$, the acoustic pressure magnitude for the positive and negative flow velocities of the same magnitude look very similar. Away from $f_1'$, they differ.

The convective flow results in the frequency of the first acoustic pressure peak in this frequency range decreasing as the magnitude of the convective velocity increases: this modified resonance frequency is called $f_1'$. This is in agreement with findings by Morse and Ingard [75].

$f_1'$ is shown to decrease by approximately 1.2%, with $|u_x| = 50\,ms^{-1}$.

Measured data for a case with a matching transducer position relative to the flow was available from an experiment in Chapter 3. With reference to Figure 3.29, 'Case 1' with the transducer pair 'ab' matches the transducer orientation in the simulation. The change of $f_1'$ caused by the change of the external, convective flow velocity is plotted in Figure 5.25. The result shows the measured change of $f_1'$ is greater than that simulated. This could be partly due to the velocity in the duct being greater than the free-stream velocity during measurement, and partly due to the celerity not being preserved during the convected acoustic analysis, as mentioned in Chapter 2, and illustrated in Figure 5.7.

The amplitude and phase distributions for the case $u_x = 30\,ms^{-1}$ at $f_1'$ are presented in Figure 5.26.

The mean phase over the observation region at $f_1'$ for each convective velocity was extracted and plotted in Figure 5.27. A line of best fit through the points generates a gradient of $m = 2.70 \times 10^{-2}/(ms^{-1})$, and an intercept of $c = -1.64$. Indicated on the same figure is the effect of measuring at the half-wavelength resonance.

These simulation results are compared with the measured result from Figure 3.35. The measured gradient of $1.7 \times 10^{-2}/(ms^{-1})$ appears surprisingly low.

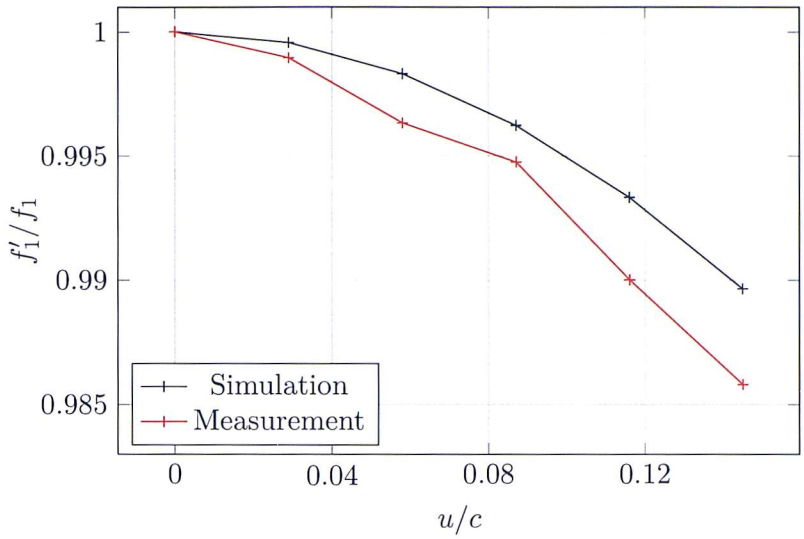
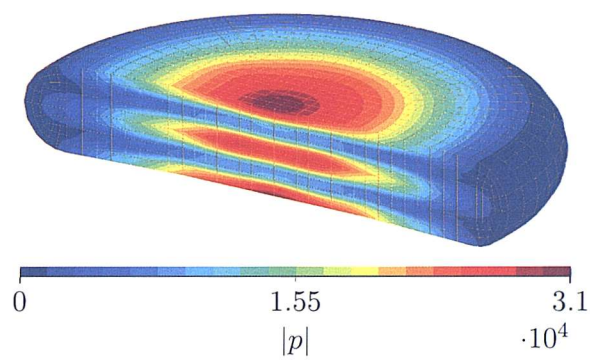
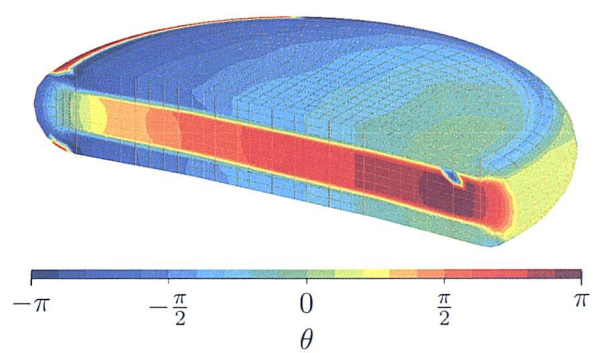



Figure 5.25: Relative change of $f_1'$ versus the steady convective velocity magnitude for a measurement, and a simulation using a uniform and constant convective velocity field.




(a) Acoustic pressure




(b) Acoustic phase

Figure 5.26: Pressure magnitude and phase distribution at $f_1'$, for the convective velocity $u_x = 30\,ms^{-1}$. The acoustic pressure magnitude shows a mode-like distribution as for the zero flow case, but the phase now shows a clear gradient in the direction of the flow. Phase 'wrapping' is evident as sudden changes of colour with position in the phase plot.

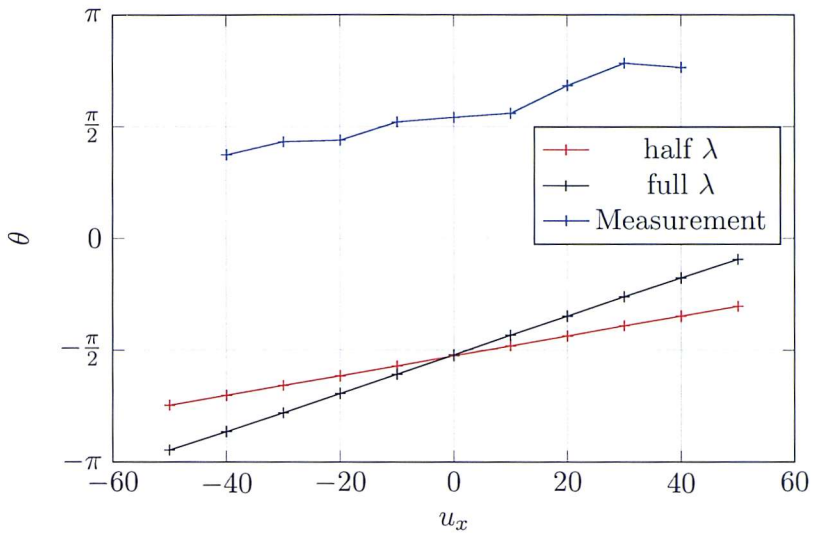



Figure 5.27: The average phase over the observation region at resonance for different convective velocities is indicated for the half-wavelength, and full-wavelength cases. A linear relationship is indicated. The phase gradient changes from $1.4 \times 10^{-2}\,/(ms^{-1})$ to $2.7 \times 10^{-2}\,/(ms^{-1})$: an approximate doubling for the doubling of operating frequency. A measured result is included, from Figure 3.35 for comparison.

### Effect of observing away from resonance

The effect of observing the phase at a constant frequency was tested using the full wavelength across the duct simulation with uniform flow.

The phase was inspected at $f_1$, where $f_1$ is the resonance frequency with zero convective flow. The effect of measuring the acoustic phase at this constant frequency is presented in Figure 5.28.

Measuring the acoustic phase at a constant frequency does not result in a linear relationship between phase and velocity, whereas tracking the resonance does. This result demonstrates the importance of tracking the resonance frequency during operation.

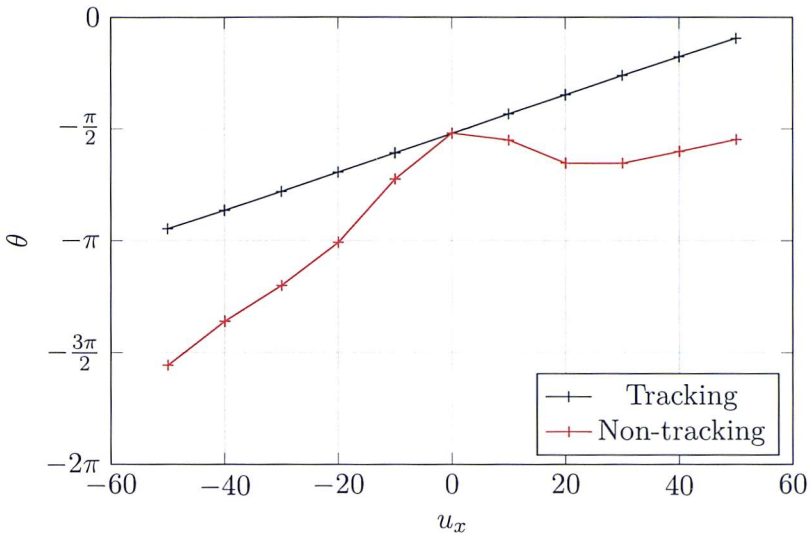



Figure 5.28: The effect of observing the acoustic phase at $f_1$ rather than $f_1'$ is indicated. Measuring the phase at $f_1'$ appears to linearise the relationship between the phase and the uniform convection velocity. The non-tracking phase has been unwrapped, for clarity.

### 5.5.5 Steady, non-uniform viscous flow

The steady, non-uniform flow case uses the low frequency viscous flow field results that were generated assuming a steady solution to convect the acoustic field. While more representative of the flow field around a real device than using a uniform flow field, these fields are assumed to be constant with time: an approximation discussed in Chapter 4.

The steady flow fields were interpolated over the acoustic mesh, and reflected through mirror planes to generate a complete low frequency velocity field. This field was then used to convect the acoustic field.

The acoustic pressure variation over the observation transducer, as the frequency is varied, is plotted in Figure 5.29 for frequencies close to $f_1$.

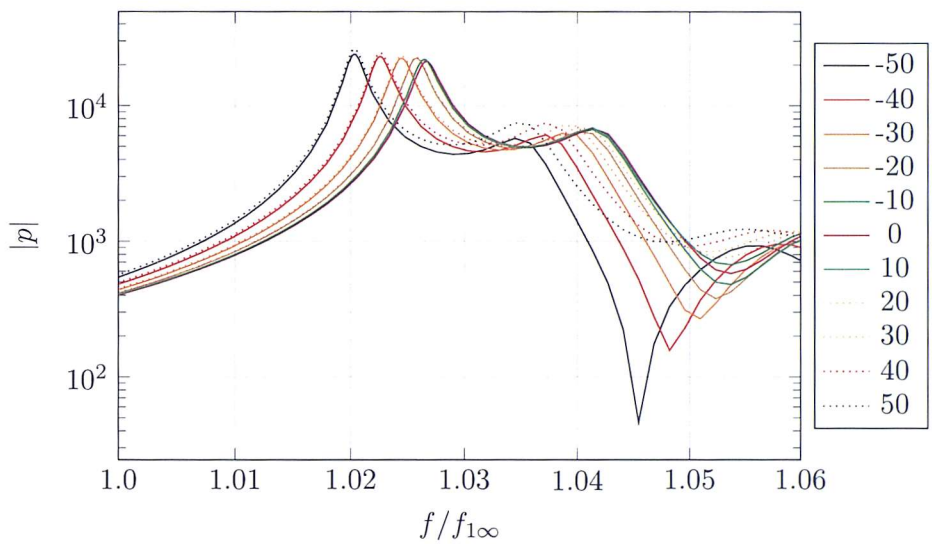



Figure 5.29: Mean acoustic pressure over the observation region using non-uniform, steady viscous flow fields calculated in Chapter 4. The free stream velocities are indicated. The change of $f_1'$ is less than for the uniform velocity case of Figure 5.24.

Comparison of Figure 5.24 with Figure 5.29 shows $f_1'$ to drop less for the viscous flow field solutions than for the uniform flow fields. This implies the mean convective velocity in the duct is higher for the uniform flow field. Calculation of the mean velocity in the duct shows this to be the case, as illustrated in Table 5.2.

| $u_x\,(ms^{-1})$ | $u_{mean_{x,y,z}}\,(ms^{-1})$ | $\frac{u_{mean_x}}{u_x}$ |
|---|---|---|
| 10 | 7.4, 6E-5, 1E-4 | 0.74 |
| 20 | 14.9, 1E-4, 5E-4 | 0.75 |
| 30 | 23.5, 9E-5, 8E-4 | 0.78 |
| 40 | 32.3, 2E-4, 1E-3 | 0.81 |
| 50 | 40.0, 3E-4, 2E-2 | 0.80 |

Table 5.2: Effect of changing from uniform to steady, non-uniform flow, on the mean velocity in the duct.

The phase at $f_1'$ was extracted for each result in Figure 5.29. The result is presented in Figure 5.30. Changing to the non-uniform, steady convective velocity field has resulted in the phase gradient at $f_1'$ reducing, as expected from the tabulated results in Table 5.2. The gradient difference is a factor of 0.77, which is very similar to the mean x-velocity ratio indicated in Table 5.2, of 0.78.

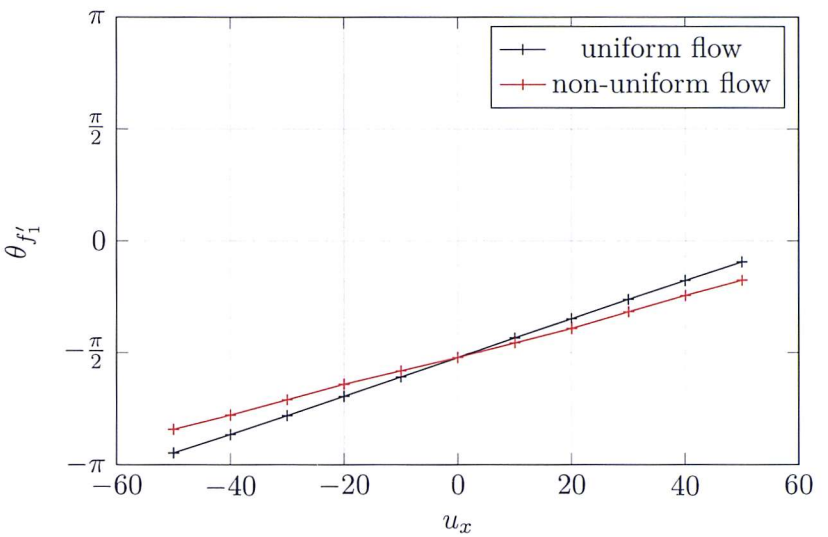



Figure 5.30: Phase at $f_1'$, averaged over the observation region. The new gradient and intercept are $2.07 \times 10^{-2}\,/(ms^{-1})$ and $-1.62$ respectively. These results can be compared with the measured results in Figure 3.35 which show a gradient of $1.7 \times 10^{-2}/ms^{-1}$ for a similar experiment.

### 5.5.6 Unsteady, non-uniform viscous flow

The simulation of the unsteady, slowly changing velocity field with a $10\,ms^{-1}$ free stream flow was used to provide the instantaneous velocity fields in the duct. For each field, the pressure versus frequency response was generated, $f_1'$ detected, and the phase at this frequency extracted. This result gives an indication of the effect the slowly changing convective velocity field has, during an acoustic sample.

The phase for 230 results sets is plotted in Figure 5.31 against the non-dimensionalised time, based on the anemometer diameter. The variation is small: equivalent to a maximum low frequency velocity error of $\pm 0.67\,ms^{-1}$. Performing smoothing over the measurement would reduce this error.

The unsteady phase result is compared to the steady phase results generated previously, in Figure 5.32. It appears that the steady flow simulation generates results in between the expensive, unsteady simulation and the relatively cheap, uniform flow simulation.

Comparing this result with that of Figure 5.30 illustrates how small these unsteady phase fluctuations are compared with the changes caused by $10\,ms^{-1}$ changes to the free-stream velocity.

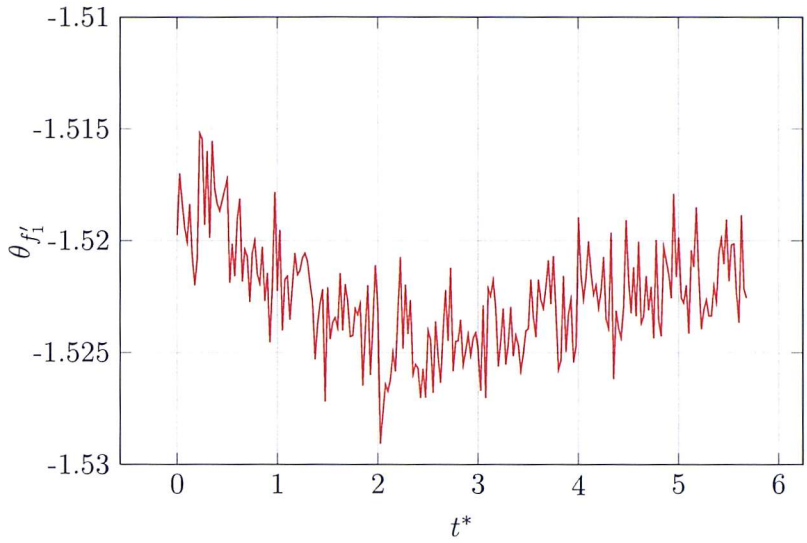



Figure 5.31: Acoustic phase at $f_1'$, using the unsteady, slowly changing viscous flow field generated in Chapter 4 to convect the acoustic field. $t^*$ is based on $d = 5\,cm$, $u = 10\,ms^{-1}$. The phase variation is $-1.529 \sim -1.515$, equivalent to a derived, low frequency velocity of $\pm 0.67\,ms^{-1}$, using a gradient of $2.07 \times 10^{-2}\,/(ms^{-1})$.

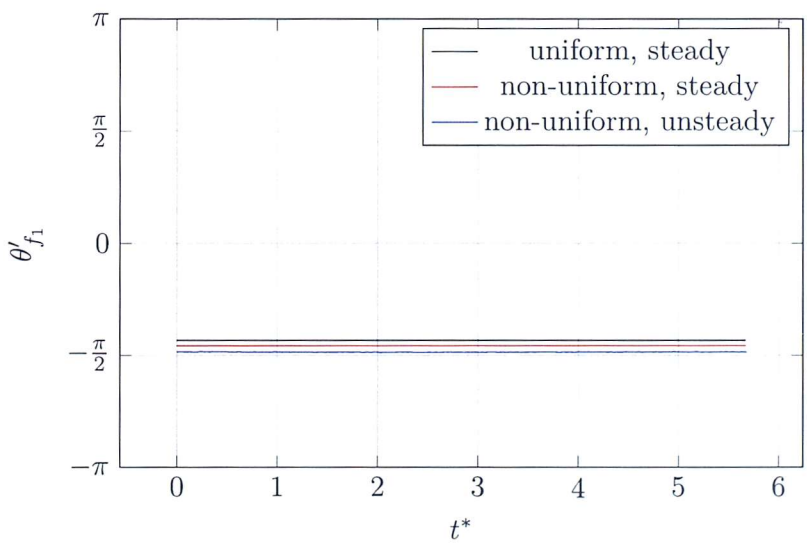



Figure 5.32: Comparison of the phase results generated with three different representations of the slowly changing, viscous convective flow field. The phase fluctuations illustrated in Figure 5.31 appear small on this scale.

### 5.5.7 Summation of point sources

A three-dimensional point source on an infinite baffle with an infinite reflecting surface parallel to the baffle, separated from the baffle by distance $h$, was used to explore a simple case, without the use of the finite element solver. This approach is beneficial for exploring some general principles. It cannot accurately represent aspects of a real anemometer, unlike the finite element and finite volume methods used previously.

Reflections from the duct walls were simulated by using extra 'ghost' sources behind the reflectors; the number of reflections were controlled by the number of these extra sources. The first reflective source was positioned a distance, $h$ behind the upper reflector; the second reflective source a distance, $2h$ behind the lower reflector, and so on.

An expression for the pressure around a periodic, simple point source, is given by Morse and Ingard [75] as,

$$p = -ik\rho cAge^{-i\omega t} \tag{5.1}$$

where,

$$g = \frac{1}{4\pi r}e^{ikr} \tag{5.2}$$

is the Green's function for an infinite medium; $k$ is the wavenumber; $A$ is the excitation strength; $\omega$ is the angular frequency; $t$ is the time; and $r$ is the separation between the source and the observation point. The calculation here was for a half space, so $g$ was multiplied by two.

The effect of successive reflections is illustrated in Figure 5.33, by displaying the acoustic pressure amplitude and phase over a region the same size as the acoustic resonant duct discussed previously for two, twenty, and two hundred sources. The pressure contribution from the first point source is large in the region close to the source, so the plots of pressure amplitude use a saturated value scale. This scale is arbitrarily scaled to unity.

The amplitude and phase along the upper reflector for the three cases is plotted in Figure 5.34. The upper reflector was used as it was less affected by the overwhelming pressure contribution from the point source than the lower reflector.

It appears that when twenty sources are used, a pressure amplitude distribution similar to that calculated by the finite element solver is established. The phase changed from displaying large changes with position with two sources, to small changes with position with twenty sources; this effect was more pronounced with two hundred sources. There is a match in phase between the first source and the region opposite it. This could be expected, as the phase of the signal from each source matches that of the original source at this position, at resonance.

The celerity was modified to be direction dependent and affected by the flow. For a given position in the duct, the line joining the position to each 'ghost' source will have a slightly different angle to the flow; and a different celerity.

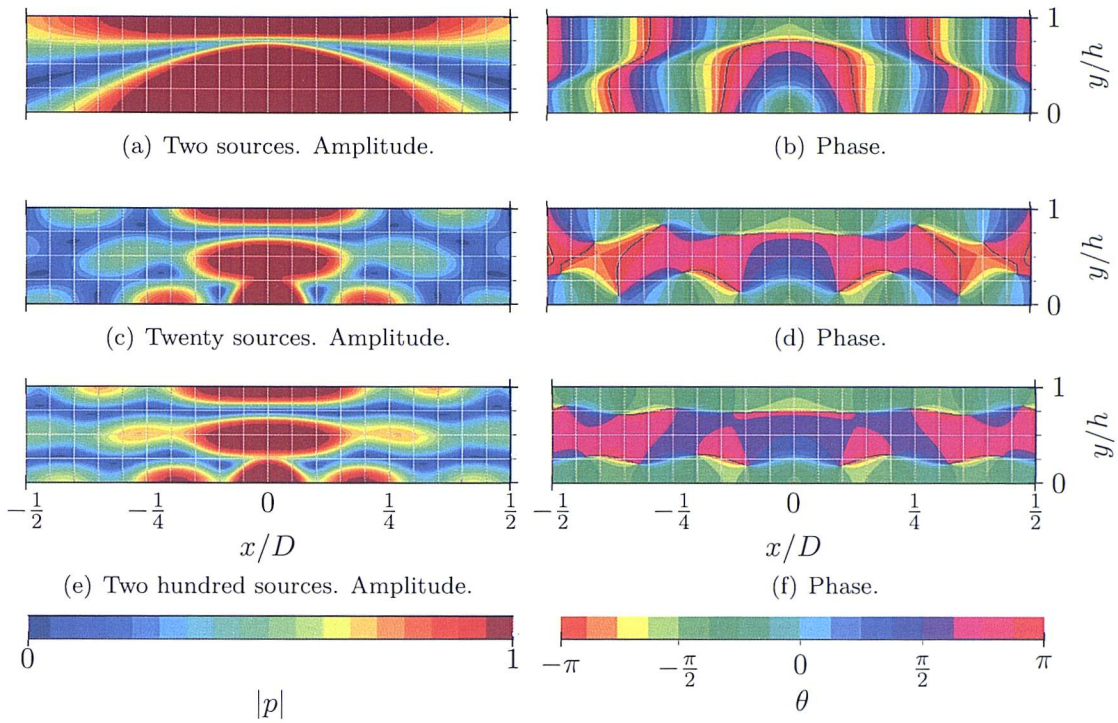



Figure 5.33: The effect of changing the number of reflections included during summation for a point source in the centre of the lower reflector, radiating at the resonance frequency. There is zero convective flow. It is shown that after several reflections, the pressure and phase distributions are similar to those generated using the finite element method. The pressure scaling is arbitrary.

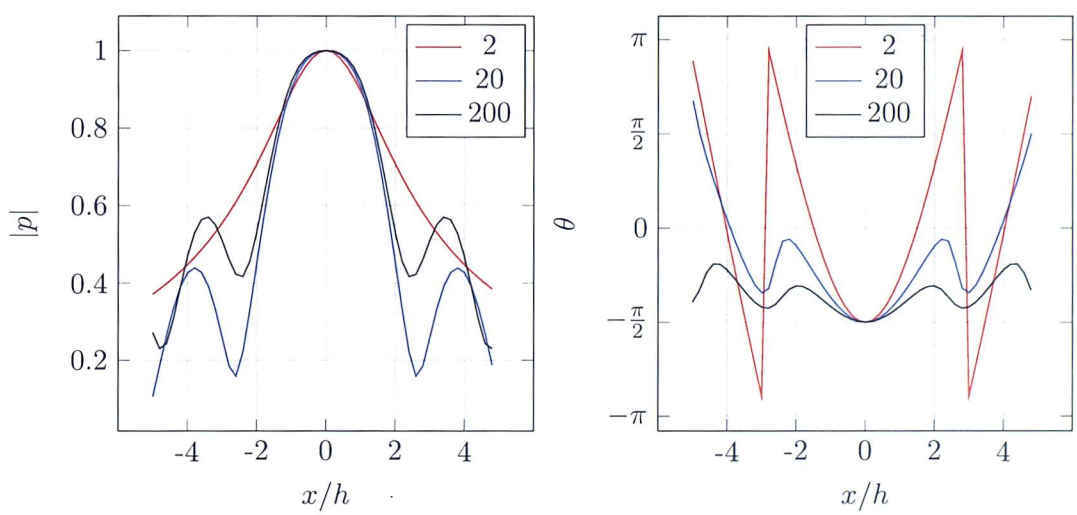



Figure 5.34: Acoustic pressure amplitude and phase along the upper edge of of the distributions illustrated in Figure 5.33 for different numbers of sources, as indicated. Amplitude has been scaled to unity in each case. The variation of phase with position decreases as the number of sources increases.

The paths involved in the calculation of the modified celerity are illustrated in Figure 5.35. The acoustic signal is considered to expand around the source position with velocity, $c$. During the expansion, it is convected by the flow, with velocity $|\boldsymbol{u}|$. If the time taken is $t$, the signal will have expanded to a radius of $c\,t$ around the source, and will have been convected a distance $|\boldsymbol{u}\,t|$ by the flow. If these actions are considered in isolation of each other, the signal can be considered to move from the destination coordinate $b$, along $-\boldsymbol{u}t$ to $a$. The signal will intersect the expanding circle around $o$ at time $t$.

The resultant expression can be solved for the time for the signal to reach the target. A quadratic equation results which when solved, generates two roots. Since the convection coordinate is subtracted from the finish point and multiplied by $t$, the positive time is the one of interest. The negative time is a result of the circle expanding and hitting the convection signal as it moves in the direction of the convection; the opposite direction from that used during the problem description above.

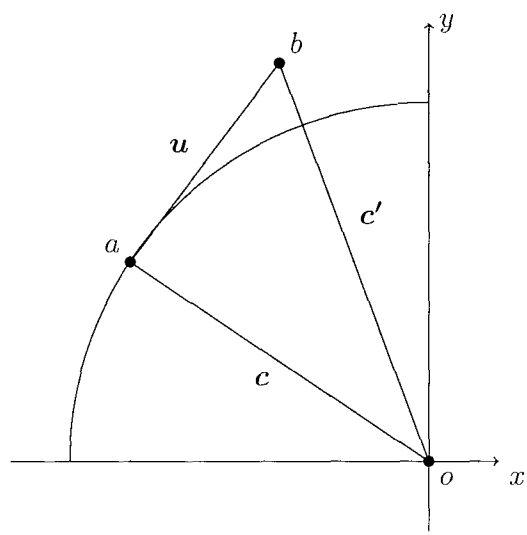



Figure 5.35: Diagram illustrating the calculation of the convected celerity, $c'$. The non-convected signal expands around $o$ with speed $c$, reaching $a$ in time, $t$. The signal is simultaneously convected along $\boldsymbol{u}$ to position $b$. The time taken for the convected signal to get to $b$ can be calculated by considering the time at which the circular expansion intersects with the path along $-\boldsymbol{u}$, starting from $b$.

Referring to Figure 5.35, the time taken for the convected signal to pass from the origin $o$, to position $b$ can be calculated as follows.

An equation describing a circular wavefront expanding in two dimensions around an origin, $o$ is,

$$x^2 + y^2 = (ct)^2 \tag{5.3}$$

where $x$ and $y$ are coordinates; $c$ is the acoustic celerity; and $t$ is time. While the expansion occurs, the signal is simultaneously convected by the convection velocity, $\boldsymbol{u}$. The portion of the wavefront originally heading towards $a$ is convected to position $b$ over the same time

period, $t$.

The two signal paths are considered in isolation. Since the position $b$ is known, the path backwards along $\boldsymbol{u}$ can be considered: at time $t$, this path will intersect with the expanding circle. If the coordinates of $b$ are $b_x$ and $b_y$, and the components of $\boldsymbol{u}$ are $u_x$ and $u_y$, the following can be written:

$$x = b_x - u_x t \quad y = b_y - u_y t \tag{5.4}$$

This expression for $x$ and $y$ can be substituted into Equation 5.3 and solved for $t$.

$$\begin{aligned}(ct)^2 &= x^2 + y^2 \\ &= (b_x - u_x t)^2 + (b_y - u_y t)^2 \\ &= (b_x^2 - 2b_x u_x t + u_x^2 t^2) + (b_y^2 - 2b_y u_y t + u_y^2 t^2)\end{aligned} \tag{5.5}$$

Factorising Equation 5.5 into $t$ yields,

$$t^2(u_x^2 + u_y^2 - c^2) + t(-2b_x u_x - 2b_y u_y) + (b_x^2 + b_y^2) = 0 \tag{5.6}$$

The roots of this quadratic equation are,

$$\frac{-(-2b_x u_x - 2b_y u_y) \pm \sqrt{(-2b_x u_x - 2b_y u_y)^2 - 4(u_x^2 + u_y^2 - c^2)(b_x^2 + b_y^2)}}{2(u_x^2 + u_y^2 - c^2)} \tag{5.7}$$

As mentioned previously, a positive and negative root occur: the positive root corresponds to the time required for the acoustic signal to move from $o$ to $b$, this equalling the time taken for the signal to move from $b$ along $-\boldsymbol{u}$ to $a$. The negative root is the time taken for the signal to move from $b$ in the direction of $\boldsymbol{u}$, and intersect the expanding circle around $o$. The positive root is the result of interest in this case.

Once the propogation time is known, the distance from $o$ to $b$ can be used with $t$, to calculate the convected celerity.

The direction dependent celerity was calculated for the case, $c = 344\,ms^{-1}$, $u_x = 44\,ms^{-1}$ usig this algorithm. These values were chosen for ease of confirmation that the upstream convected celerity equaled the sum of the convective velocity and the non-convected celerity. Figure 5.36 shows that the celerity was behaving as expected.

In order to examine the phase distribution at resonance, the new frequency giving the greatest pressure magnitude at the position opposite the source, on the second reflector was simulated when flow was present. The distribution of phase and amplitude at this frequency for different numbers of sources is presented in Figure 5.37 for the case, $u_x = 1\,ms^{-1}$.

The amplitude and phase along the upper reflector for the three cases is plotted in Figure 5.38.

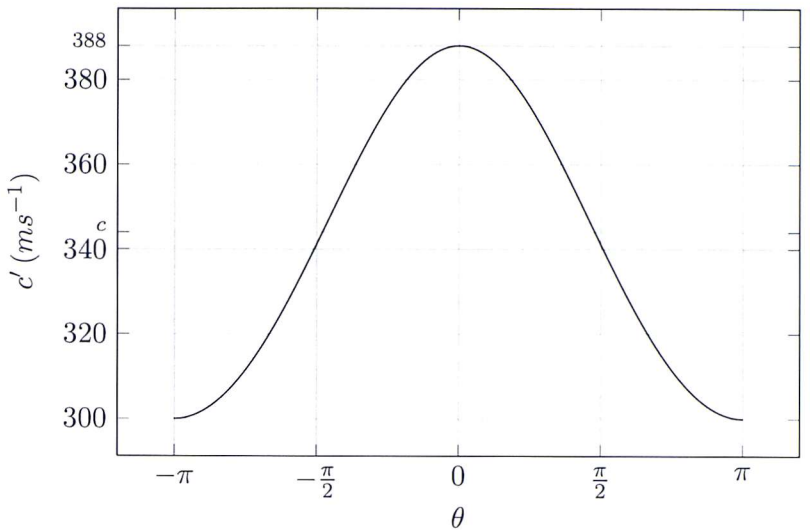
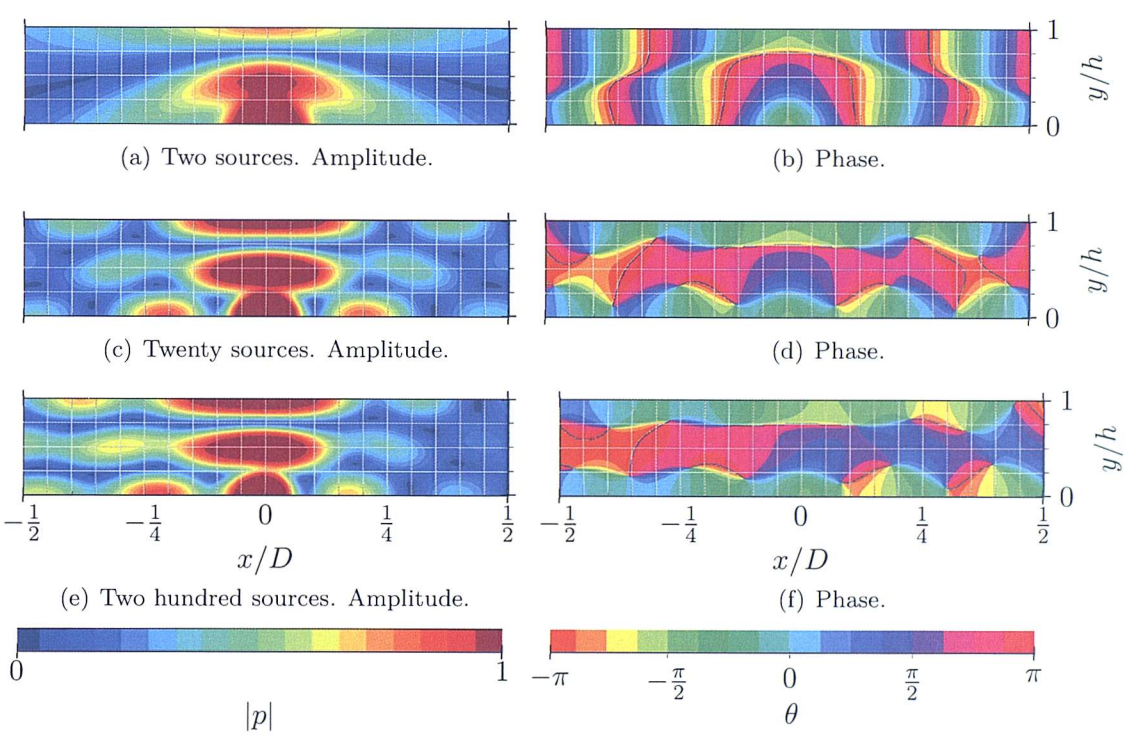



Figure 5.36: Direction dependent celerity calculated for the case, $c = 344\,ms^{-1}$, $u_x = 44\,ms^1$. Upstream and downstream celerity shows the static celerity is adding to the flow velocity.




(a) Two sources. Amplitude.
(b) Phase.
(c) Twenty sources. Amplitude.
(d) Phase.
(e) Two hundred sources. Amplitude.
(f) Phase.

Figure 5.37: The effect of changing the number of 'ghost' sources included during summation, for a point source in the centre of the lower reflector with convective flow moving from left to right at $1\,ms^{-1}$. The excitation frequency is slightly lower than the static acoustic case and was selected to cause the largest acoustic pressure amplitude opposite the source. The amplitude scaling is arbitrary.

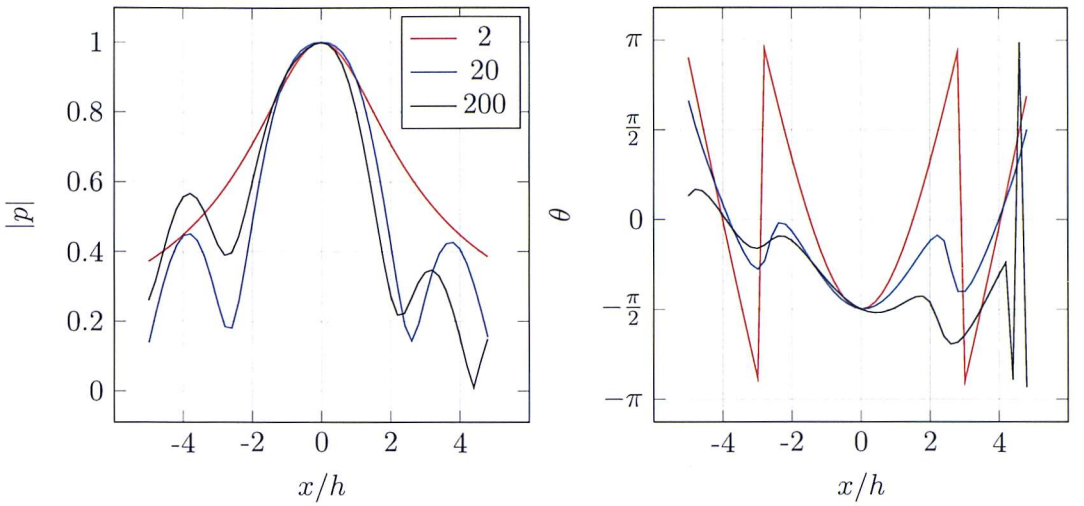



Figure 5.38: Acoustic pressure amplitude and phase along the upper edge of the distributions illustrated in Figure 5.37 for different numbers of sources, as indicated. Amplitude has been scaled to unity in each case.

It appears that the pressure amplitude has been affected by the flow: the distribution is no longer symmetric around the source, but increases slightly on the upsteam side.

The phase shows a clear change: a gradient is now present along the duct length that was not present for the static case.

Phase results along the surface for the case of two sources look similar to the zero flow case. With twenty sources a phase gradient along the length is indicated but with two hundered sources, the gradient has clearly changed from the static case. It appears that summing the pressure contributions of the reflections inside the duct while accounting for the flow induced direction dependent celerity, generates a phase gradient along the duct at resonance. This effect may play a major role in the operation of the acoustic resonance anemometer.

## 5.6 Performance limits

Measurements are made at the walls of a duct consisting of two circular, parallel plates. The length to separation ratio varies from five at the centre plane to zero at the edges. Experiments using plane Couette flow have been performed by Tillmark and Alfredsson [105], showing that below $Re = 360$ turbulence is not maintained in duct flow. $Re$ was calculated using half the duct width. The anemometer duct shows this Reynolds number at an approximate $u = 0.1\,ms^{-1}$. Velocities lower than this may result in turbulence no longer being supported inside the duct, with a resulting change in behaviour.

Fully developed pipe flow is turbulent when $Re > 2300$ according to Hinze [53] but it is likely that this system will be strongly affected by effects caused at the edge of the duct: reducing the applicability of analyses assuming fully developed flow. The duct length in question ($5\,cm$) may also render the consideration of whether turbulence can be supported over a significant distance irrelevant. The sharp edge at the entrance of the duct will encourage boundary layer separation, reducing the critical Reynolds number for the duct, but the acceleration of the flow in this region will act to damp the turbulence as described by Hinze [53]. $Re = 2300$ for this duct at approximately $6\,ms^{-1}$, so there may be a change of flow behaviour below this velocity. The geometry of the duct analysed during this project makes Reynolds number based predictions of the velocities that its behaviour will change at, uncertain.

Rounding the entrance may increase the critical Reynolds number, as it will reduce the magnitude of the adverse pressure gradient occurring as the flow passes over the lip. This could have the effect of extending the operating velocity range.

The plate separation is maintained by support pillars around the duct. The Reynolds number associated with support pillars of $2\,mm$ width is approximately $Re = 1300$ with $10\,ms^{-1}$ flow. This suggests the pillars will shed into the duct during measurements of moderate flow rates, adding a fluctuating component to the duct velocity not present in the external field. The effect of this has been discussed previously. This behaviour will change at low velocities: below $Re = 300$, the shedding will become irregular. The effect of the finite aspect ratio of the pillars and the proximity of the duct faces will modify the shedding behaviour, making simulation of the flow necessary for prediction of behaviour. Nevertheless, it is suggested that velocities in the region of $1\,ms^{-1}$ will demonstrate a change of duct flow.

The flow around the body will change, depending on the Reynolds number. The velocity extremes displaying sub-critical flow around a circular cylinder of $D = 5\,cm$ occur in the region $0.1\,ms^{-1} < u < 60\,ms^{-1}$. The aspect ratio of the anemometer and the curved ends will increase this range slightly: measurements by Wieselsberger [114] have shown an increase in critical Reynolds number from $Re_{crit} \approx 3.2 \times 10^5$ for the infinite aspect ratio circular cylinder, to $Re_{crit} \approx 3.9 \times 10^5$ for a circular cylinder with $L/D = 5$. This $D = 5\,cm$ body will enter the supercritical flow regime around $u = 73\,ms^{-1}$.

The phase measurements made by the anemometer are limited to values between $-\pi$ and $\pi$. A signal resulting in a phase value close to $\pi$, which then increases in angle will 'wrap' back

around to $-\pi$. This behaviour is difficult to compensate for. The relationship between the free stream low frequency flow velocity and the acoustic phase at resonance inside the duct, given by Figure 5.27, suggests that the largest velocity range measurable is $\pm 116\, ms^{-1}$ with a full wavelength across the duct. Use of a half wavelength approximately doubles this range, at the cost of velocity resolution due to quantisation limits.

Accuracy of the anemometer may be affected by shedding from the support pillars around the acoustic duct illustrated in Figure 3.1. These pillars shed vortices into the acoustic duct as illustrated in Figure 4.37, generating noise in the acoustic phase response as illustrated in Figure 5.31. The velocity error calculated using the phase-velocity relationship previously mentioned, was $\pm 0.7\, ms^{-1}$.

The simulated ratio between the free stream velocity magnitude and the steady, spatially mean velocity magnitude through the acoustic duct, has been tabulated in Table 5.2 as varying from $0.74 < u_{duct}/u_{stream} < 0.8$ between $u_{stream} = 10\, ms^{-1}$ to $u_{stream} = 50\, ms^{-1}$. As the free-stream velocity increases, the velocity in the duct becomes proportionally higher, indicating a progressive change of flow behaviour. This effect would be compensated for during calibration but may affect the maximum velocity range for the device.

## 5.7 Concluding remarks

The finite element solver of the convected acoustic equation written for this project, has been used in this chapter to study the acoustic behaviour inside a duct passing a slowly changing, viscous flow field. Validation of the code has been discussed in Section 5.3, with good results. The effect of truncating the resolved acoustic region has been quantified in Section 5.4, with the findings that the resolved region needs to extend only a small distance from the duct. This helped to reduce the cost of the analyses. The effect of mesh density on the resonant frequencies of a tube was used to quantify the errors caused by mesh resolution. The method of finding the resonance frequency of interest was discussed in Section 5.5.3, including an approach to maximise the use of parallel processing computers.

The acoustic behaviour of the duct was examined across a wide range of frequencies, and then in more detail across a narrow band in Section 5.5.4, The acoustic pressure distributions at frequencies of interest were examined. Measurements of the acoustic transfer function generated by a working anemometer were compared with simulation results, showing the frequency of interest to be simulated to within 3% for zero convective flow. The effect of uniform convective flow on the acoustic pressure response in the duct was examined and the change of resonant frequency of the duct was found to agree with measurement to within 1.5%. The phase at resonance was inspected for a range of uniform flow velocities for both full and half wavelength resonance of the acoustic duct. The phase versus velocity gradient for the simulation was close to double that of the measurement. The simulation showed the phase versus velocity gradient was linearly related to the operating frequency of the anemometer. It was demonstrated that operating at resonance linearises the phase versus velocity relationship.

Steady viscous velocity field solutions were used to convect the high frequency acoustic field in Section 5.5.5 and the mean velocity through the duct being lower than the free stream velocity resulted in a reduction of gradient in the relationship between phase and free stream velocity.

The slowly changing viscous flow fields calculated in Chapter 4 were used to convect the high frequency acoustic field in Section 5.5.6, showing that fluctuations in the viscous velocity field through the duct caused a maximum phase error amounting to $\pm 0.67\, ms^{-1}$.

Finally, a simulation of repeated reflections of a point source in a duct was used to demonstrate that the phase difference occurring along the duct in the presence of a convective flow, at resonance, is partly due to the change in celerity that occurs for different propagation directions.

# 6 Conclusions and Further Work

This chapter is split into two sections: in the first part, some of the conclusions drawn throughout this thesis are discussed with reference to the research contribution they made. The second part lists possible future work.

### 6.0.1 Research contribution

In Chapter 2 a treatment of the Navier-Stokes equations was specified to enable the modelling of a convected acoustic field. An expression suitable for modelling the effect of a slowly changing, low-speed viscous velocity field on a high frequency, inviscid acoustic field was derived. The approach adopted was specifically suited to the analysis of the effect of a low-velocity convective field.

Chapter 3 presented measurements of quantities describing aspects of the slowly changing viscous velocity field around an anemometer similar in shape to a circular cylinder of low aspect ratio, with domed ends. The quantities included time-mean pressure coefficient on the anemometer body, and velocity spectra downstream. Splitting the cylinder by adding an acoustic duct through which the slowly changing flow field could pass, resulted in an object that had not been previously measured in this way. Measurements included the time-mean pressure coefficient over the anemometer outer surface and the surface of the duct and the slowly changing velocity through the acoustic duct. Previously unavailable data regarding the amplitude and phase of the acoustic signal in the duct were presented, at and close to the acoustic resonance, for different convective flow velocities. A bistable flow state was demonstrated, in which the flow showed sudden changes of direction around the anemometer.

In Chapter 4 the requirements for the simulation of a bluff body in the sub-critical Reynolds number region were established, including selection of appropriate turbulence model and mesh density for steady Reynolds-averaged Navier-Stokes treatment. For unsteady Reynolds-averaged Navier-Stokes treatment, the time-step selection was also assessed. Simulation results were compared with previously available data for two-dimensional circular cylinders, and the newly acquired measured data for the new device. The slowly changing, viscous flow field was generated, showing that a separation region exists at the leading edge of the duct, and that vortex shedding occurs from the support pillars: both effects contributing to unsteadiness of measurement results.

In Chapter 5 the finite element solver created for the project was used to solve the equation derived in Chapter 2. Simulations involving steady uniform convective flow, steady non-uniform convective flow and slowly changing, non-uniform convective flow were used to gain

an understanding of the errors caused by using these different approaches for representing the slowly changing, viscous velocity field. The finite element solver was used to replicate the operation of an acoustic resonance anemometer with success: a linear phase variation with velocity was demonstrated, as long as the phase at resonance was used. It was demonstrated that measurement at resonance linearises the phase response to changes in the free stream viscous flow velocity. Understanding of the operation of the device was extended with a simple summation of point sources model. It was demonstrated that for the case of an infinite duct, acoustically excited at resonance with the acoustic wave travelling nominally perpendicularly to the flow, a phase gradient exists along the duct walls that is affected by the flow. This phase gradient was a result of the different path taken for the signal from each source to reach a point in the duct, each path being at a different angle to the convective flow and therefore having a different celerity.

### 6.0.2 Future work

As discussed in Chapter 2, the expression used to model the convected acoustic field is limited to low convective velocities. In order to extend the analysis to cope with higher convective flow velocities, extra Mach terms need to be included. This approach has been used by Tsuji et al. [108] to examine the effect of convective flow in automotive exhausts. This would enable the design of the anemometer to be optimised for an increased velocity range.

Extending the measurements of the slowly changing flow field to higher free stream velocities would provide extra validation data for the viscous flow field simulations. This would be of particular interest if the convected acoustic field expression was modified to include higher order Mach terms. The bistable state discovered during Chapter 3 is particularly interesting and may be related to the configuration of the support pillars. The unsteady viscous flow field simulation could be used to investigate the effect further.

The instabilities in the slowly changing flow through the duct related to separation of the flow at the entrance to the acoustic duct and to the vortex shedding from the support pillars, contributes to errors in the measured results of the anemometer. This is an area that would benefit from future study: the methods described in this thesis could be used to examine the effect of rounding the entrance to the duct and changing the number and configuration of the support pillars.

Measurement of the third velocity component remains an area of interest. The methods described in this thesis could be used to examine different duct configurations to this end.

# A Appendix

This chapter is included to present content that was considered relevant, but detracted from the body of the work.

### A.0.3 Magnitude of acoustic velocity

From a sound pressure level estimated in the gap at resonance, the acoustic velocity can be calculated from first principles as,

$$y = A\sin(\omega t - kx) \tag{A.1}$$

with acoustic displacement $y$, amplitude $A$, angular frequency $\omega$, time $t$, wave number $k$ and position $x$. The relationship between pressure and Equation A.1 is

$$\begin{aligned} p &= -B\frac{\partial y}{\partial x} \\ &= BkA\cos(\omega t - kx) \end{aligned} \tag{A.2}$$

where $B$ is the bulk modulus. The acoustic velocity is the time differential of the displacement,

$$\begin{aligned} v &= \frac{\partial y}{\partial t} \\ &= \omega A\cos(\omega t - kx) \end{aligned} \tag{A.3}$$

If intensity is the average power per unit area, it is calculated as,

$$P = pv \tag{A.4}$$

$$= BA^2k\omega\cos^2(\omega t - kx) \tag{A.5}$$

$$I = \frac{1}{2}BA^2k\omega \tag{A.6}$$

with power $P$ and intensity $I$. If the Decibel scale is defined as,

$$\beta = (10dB)\log(\frac{I}{I_0}) \tag{A.7}$$

where $\beta$ is the sound level in decibels (dB) and $I_0$ is the reference intensity, in this case $10^{-12}W/m^2$, these expressions can be combined to yield the relationship between acoustic velocity and intensity level as

$$v = \omega * \sqrt{\frac{2(I_0 10^{\frac{\beta}{10dB}})}{Bk\omega}} \tag{A.8}$$

For the case $f = 40000Hz$, $\beta = 120dB$, the acoustic velocity is $0.07ms^{-1}$ and the acoustic displacement is $2.77 * 10^{-7}m$. This *maximum* velocity is can be compared to the lowest low frequency velocities used of $1ms^{-1}$.

### A.0.4 Magnitude of terms in the convected acoustic equation

This section examines the relative contribution from the terms in the convected acoustic equation in greater detail than the main text.

$$\frac{D}{Dt}(2.11) - \frac{\partial}{\partial x_i}(2.21) = 0 \tag{A.9}$$

becomes,

$$\frac{D}{Dt}\left(\frac{D\rho'}{Dt} + \tilde{\rho}\frac{\partial u_i'}{\partial x_i}\right) - \frac{\partial}{\partial x_i}\left(\tilde{\rho}\frac{Du_i'}{Dt} + \rho'\frac{D\tilde{u}_i}{Dt} + \tilde{\rho}u_j'\frac{\partial \tilde{u}_i}{\partial x_j} + \frac{\partial p'}{\partial x_i}\right) \tag{A.10}$$

Expanding the convective derivative in Equation A.9,

$$\begin{aligned}
\frac{D}{Dt}(2.11) &= \frac{D}{Dt}\left(\frac{D\rho'}{Dt} + \tilde{\rho}\frac{\partial u_i'}{\partial x_i}\right) \\
&= \frac{D^2\rho'}{Dt^2} + \frac{D}{Dt}\left(\tilde{\rho}\frac{\partial u_i'}{\partial x_i}\right) \\
&= \frac{D^2\rho'}{Dt^2} + \frac{D\tilde{\rho}}{Dt}\frac{\partial u_i'}{\partial x_i} + \tilde{\rho}\frac{D}{Dt}\left(\frac{\partial u_i'}{\partial x_i}\right) \\
&= \frac{D^2\rho'}{Dt^2} + \left(\frac{\partial \tilde{\rho}}{\partial t} + u_k\frac{\partial \tilde{\rho}}{\partial x_k}\right)\frac{\partial u_i'}{\partial x_i} + \tilde{\rho}\left(\frac{\partial}{\partial t}\left(\frac{\partial u_i'}{\partial x_i}\right) + \tilde{u_k}\frac{\partial}{\partial x_k}\left(\frac{\partial u_i'}{\partial x_i}\right)\right) \\
&= \frac{D^2\rho'}{Dt^2} + \frac{\partial \tilde{\rho}}{\partial t}\frac{\partial u_i'}{\partial x_i} + u_k\frac{\partial \tilde{\rho}}{\partial x_k}\frac{\partial u_i'}{\partial x_i} + \tilde{\rho}\frac{\partial^2 u_i'}{\partial t \partial x_i} + \tilde{\rho}\tilde{u_k}\frac{\partial^2 u_i'}{\partial x_k \partial x_i}
\end{aligned} \tag{A.11}$$

The spatial differential term is calculated using the suffix, $i$. Total derivatives will use the suffix $k$ as $j$ is already in use in some terms.

$$
\begin{aligned}
\frac{\partial}{\partial x_i}(2.21) &= \frac{\partial}{\partial x_i}\left(\tilde{\rho}\frac{Du_i'}{Dt} + \rho'\frac{D\tilde{u}_i}{Dt} + \tilde{\rho}u_j'\frac{\partial \tilde{u}_i}{\partial x_j} + \frac{\partial p'}{\partial x_i}\right) \\
&= \frac{\partial}{\partial x_i}\left(\tilde{\rho}\left(\frac{\partial u_i'}{\partial t} + \tilde{u_k}\frac{\partial u_i'}{\partial x_k}\right) + \rho'\left(\frac{\partial \tilde{u}_i}{\partial t} + \tilde{u_k}\frac{\partial \tilde{u}_i}{\partial x_k}\right) + \tilde{\rho}u_j'\frac{\partial \tilde{u}_i}{\partial x_j} + \frac{\partial p'}{\partial x_i}\right) \\
&= \frac{\partial}{\partial x_i}\left(\tilde{\rho}\frac{\partial u_i'}{\partial t} + \tilde{\rho}\tilde{u_k}\frac{\partial u_i'}{\partial x_k} + \rho'\frac{\partial \tilde{u}_i}{\partial t} + \rho'\tilde{u_k}\frac{\partial \tilde{u}_i}{\partial x_k} + \tilde{\rho}u_j'\frac{\partial \tilde{u}_i}{\partial x_j} + \frac{\partial p'}{\partial x_i}\right) \\
&= \left(\frac{\partial \tilde{\rho}}{\partial x_i}\frac{\partial u_i'}{\partial t} + \tilde{\rho}\frac{\partial^2 u_i'}{\partial x_i \partial t}\right) + \left(\frac{\partial \tilde{\rho}}{\partial x_i}\tilde{u_k}\frac{\partial u_i'}{\partial x_k} + \tilde{\rho}\frac{\partial \tilde{u_k}}{\partial x_i}\frac{\partial u_i'}{\partial x_k} + \tilde{\rho}\tilde{u_k}\frac{\partial^2 u_i'}{\partial x_i \partial x_k}\right) \\
&\quad + \left(\frac{\partial \rho'}{\partial x_i}\frac{\partial \tilde{u}_i}{\partial t} + \rho'\frac{\partial^2 \tilde{u}_i}{\partial x_i \partial t}\right) \\
&\quad + \left(\frac{\partial \rho'}{\partial x_i}\tilde{u_k}\frac{\partial \tilde{u}_i}{\partial x_k} + \rho'\frac{\partial \tilde{u_k}}{\partial x_i}\frac{\partial \tilde{u}_i}{\partial x_k} + \rho'\tilde{u_k}\frac{\partial^2 \tilde{u}_i}{\partial x_i \partial x_k}\right) \\
&\quad + \left(\frac{\partial \tilde{\rho}}{\partial x_i}u_j'\frac{\partial \tilde{u}_i}{\partial x_j} + \tilde{\rho}\frac{\partial u_j'}{\partial x_i}\frac{\partial \tilde{u}_i}{\partial x_j} + \tilde{\rho}u_j'\frac{\partial^2 \tilde{u}_i}{\partial x_i \partial x_j}\right) + \frac{\partial^2 p'}{\partial x_i \partial x_i}
\end{aligned}
\tag{A.12}
$$

The subtraction is performed with labelled terms, to ease discussion.

$$
\begin{aligned}
&\left(\overbrace{\frac{D^2\rho'}{Dt^2}}^{1} + \overbrace{\frac{\partial \tilde{\rho}}{\partial t}\frac{\partial u_i'}{\partial x_i}}^{2} + \overbrace{u_k\frac{\partial \tilde{\rho}}{\partial x_k}\frac{\partial u_i'}{\partial x_i}}^{3} + \overbrace{\tilde{\rho}\frac{\partial^2 u_i'}{\partial t \partial x_i}}^{4} + \overbrace{\tilde{\rho}\tilde{u_k}\frac{\partial^2 u_i'}{\partial x_k \partial x_i}}^{5}\right) \\
&- \left(\overbrace{\frac{\partial \tilde{\rho}}{\partial x_i}\frac{\partial u_i'}{\partial t}}^{6} + \overbrace{\tilde{\rho}\frac{\partial^2 u_i'}{\partial x_i \partial t}}^{7}\right) \\
&- \left(\overbrace{\frac{\partial \tilde{\rho}}{\partial x_i}\tilde{u_k}\frac{\partial u_i'}{\partial x_k}}^{8} + \overbrace{\tilde{\rho}\frac{\partial \tilde{u_k}}{\partial x_i}\frac{\partial u_i'}{\partial x_k}}^{9} + \overbrace{\tilde{\rho}\tilde{u_k}\frac{\partial^2 u_i'}{\partial x_i \partial x_k}}^{10}\right) \\
&- \left(\overbrace{\frac{\partial \rho'}{\partial x_i}\frac{\partial \tilde{u}_i}{\partial t}}^{11} + \overbrace{\rho'\frac{\partial^2 \tilde{u}_i}{\partial x_i \partial t}}^{12}\right) \\
&- \left(\overbrace{\frac{\partial \rho'}{\partial x_i}\tilde{u_k}\frac{\partial \tilde{u}_i}{\partial x_k}}^{13} + \overbrace{\rho'\frac{\partial \tilde{u_k}}{\partial x_i}\frac{\partial \tilde{u}_i}{\partial x_k}}^{14} + \overbrace{\rho'\tilde{u_k}\frac{\partial^2 \tilde{u}_i}{\partial x_i \partial x_k}}^{15}\right) \\
&- \left(\overbrace{\frac{\partial \tilde{\rho}}{\partial x_i}u_j'\frac{\partial \tilde{u}_i}{\partial x_j}}^{16} + \overbrace{\tilde{\rho}\frac{\partial u_j'}{\partial x_i}\frac{\partial \tilde{u}_i}{\partial x_j}}^{17} + \overbrace{\tilde{\rho}u_j'\frac{\partial^2 \tilde{u}_i}{\partial x_i \partial x_j}}^{18}\right) - \overbrace{\frac{\partial^2 p'}{\partial x_i \partial x_i}}^{19}
\end{aligned}
\tag{A.13}
$$

Terms four and seven cancel, as do terms five and ten.

For incompressible flow, $\tilde{\rho}$ is constant: derivatives of $\tilde{\rho}$ are therefore zero. Terms two, three, six, eight and sixteen become zero.

Incompressible flow also results in $\partial\tilde{u}_i/\partial x_i = 0$, from Equation 2.6. This causes terms twelve, fifteen and eighteen to become zero. The terms remaining are gathered:

$$\overbrace{\frac{D^2\rho'}{Dt^2}}^{1} - \overbrace{\tilde{\rho}\frac{\partial\tilde{u}_k}{\partial x_i}\frac{\partial u_i'}{\partial x_k}}^{9} - \overbrace{\frac{\partial\rho'}{\partial x_i}\frac{\partial\tilde{u}_i}{\partial t}}^{11} - \overbrace{\frac{\partial\rho'}{\partial x_i}\tilde{u}_k\frac{\partial\tilde{u}_i}{\partial x_k}}^{13} - \overbrace{\rho'\frac{\partial\tilde{u}_k}{\partial x_i}\frac{\partial\tilde{u}_i}{\partial x_k}}^{14} - \overbrace{\tilde{\rho}\frac{\partial u_j'}{\partial x_i}\frac{\partial\tilde{u}_i}{\partial x_j}}^{17} - \overbrace{\frac{\partial^2 p'}{\partial x_i\partial x_i}}^{19} \tag{A.14}$$

Term 1 is expanded in Equation A.15 in order to determine its magnitude:

$$\frac{D^2\rho'}{Dt^2} = \overbrace{\frac{\partial^2\rho'}{\partial t^2}}^{1.1} + \overbrace{\frac{\partial\tilde{u}_i}{\partial t}\frac{\partial\rho'}{\partial x_i}}^{1.2} + \overbrace{\tilde{u}_i\frac{\partial^2\rho'}{\partial t\partial x_i}}^{1.3} + \overbrace{\tilde{u}_j\frac{\partial^2\rho'}{\partial x_j\partial t}}^{1.4} + \overbrace{\tilde{u}_j\frac{\partial\tilde{u}_i}{\partial x_j}\frac{\partial\rho'}{\partial x_i}}^{1.5} + \overbrace{\tilde{u}_j\tilde{u}_i\frac{\partial^2\rho'}{\partial x_j\partial x_i}}^{1.6} \tag{A.15}$$

The acoustic time scale can be expressed in terms of the acoustic length scale and acoustic celerity, as $t = l/c$ with the time scale, $t$; the acoustic length scale, $l$; and the acoustic celerity, $c$.

The time scale for the acoustic density fluctuation is therefore $l/c$. The approximate magnitude of the first term can be calculated as,

$$\frac{\partial^2\rho'}{\partial t^2} = \frac{\partial}{\partial t}\left(\frac{\partial\rho'}{\partial t}\right) \approx \frac{1}{l/c}\left(\frac{\rho'}{l/c}\right) \approx \rho'/(l/c)^2 \tag{A.16}$$

The approximate magnitude of each term is listed in Table A.1.

| Term | Approximate magnitude | |
|---|---|---|
| 1.1 | $\rho'/(l/c)^2$ | $= cc\rho'/l^2$ |
| 1.2 | $\tilde{u}/(L/\tilde{u}) \times \rho'/l$ | $= \tilde{u}\tilde{u}\rho'/(Ll)$ |
| 1.3 | $\tilde{u}\rho'/((l/c)l)$ | $= \tilde{u}c\rho'/l^2$ |
| 1.4 | $\tilde{u}\rho'/(ll/c)$ | $= \tilde{u}c\rho'/l^2$ |
| 1.5 | $\tilde{u}\tilde{u}/L \times \rho'/l$ | $= \tilde{u}\tilde{u}\rho'/(Ll)$ |
| 1.6 | | $\tilde{u}\tilde{u}\rho'/l^2$ |

Table A.1: The approximate magnitudes of the terms in the first term of Equation A.14. If the flow length scale, $L \approx l$, the acoustic length scale and the flow velocity $\tilde{u} < c$, the acoustic celerity, term 1.1 is related to terms 1.3 and 1.4 by a factor, $M$. The remaining terms are related to term 1.1 by a factor, $M^2$. Terms other than 1.1 can therefore be ignored at low Mach numbers.

As illustrated in Table A.1, $D^2\rho'/Dt^2 \approx \partial^2\rho'/\partial t^2$ in this analysis. Its magnitude is therefore approximately $c^2\rho'/l^2$.

The approximate magnitudes of the terms of Equation A.14 are presented in Table A.2. In this case, the flow time scale is replaced with $L/\tilde{u}$, similar to the replacement for the

acoustic time scale described above. The acoustic pressure fluctuation is replaced using, $p' \approx c^2\rho'$.

| Term | Approximate magnitude | |
|---|---|---|
| 1 | $\rho'/(l/c)^2$ | $= cc\rho'/l^2$ |
| 9 | $\tilde{\rho}\tilde{u}u'/Ll$ | $= \tilde{u}u'\tilde{\rho}/(Ll)$ |
| 11 | $\rho'\tilde{u}/(lL/\tilde{u})$ | $= \tilde{u}\tilde{u}\rho'/(lL)$ |
| 13 | $\rho'\tilde{u}\tilde{u}/(lL)$ | $= \tilde{u}\tilde{u}\rho'/(lL)$ |
| 14 | $\rho'\tilde{u}\tilde{u}/(LL)$ | $= \tilde{u}\tilde{u}\rho'/(lL)$ |
| 17 | $\tilde{\rho}u'\tilde{u}/(lL)$ | $= \tilde{u}u'\tilde{\rho}/(lL)$ |
| 19 | $c^2\rho'/(ll)$ | $= cc\rho'/(ll)$ |

Table A.2: The approximate magnitudes of the terms in Equation A.14. If the flow length scale, $L \approx l$, terms 11, 13 and 14 are of order $M^2$ compared to terms 1 and 19. Terms 9 and 17 have a dependency on $u'\tilde{\rho}$ which can be shown to be of a similar magnitude to $c\rho'$ inside the anemometer duct. Terms 9 and 17 are therefore of factor $M$, compared to terms 1 and 19. In the low flow speed case, terms other than 1 and 19 contribute relatively little, and can be ignored.

Table A.2 shows that terms 9 and 17 contribute a magnitude of factor $M$ compared to terms 1 and 19; and that the remaining terms are of magnitude $M^2$. For low speed flows with $M < 0.1$ terms other than terms 1 and 19 contribute a relatively small amount and can be ignored.

### A.0.5 Use of the interactive convected acoustic solver

The following text is typical of an interactive convected acoustics analysis.

```
import fe2
a = fe2.Solver()
a.load('m92acou2a.pyFE')
a.setup()
a.analyse()
a.addFreq(1000)
```

where, `fe2` is the main program. `Solver` is the main solver object, containing references to all the functions but devoid of data: it is assigned to the object, `a`.

`load`, `setup` and `analyse` are functions which interrogate an analysis file; create and initialise the list of element objects; and perform the analysis, respectively. `addFreq()` is included here to illustrate how to add another frequency to the analysis.

### A.0.6 An analysis file for the convected acoustic solver

The text in Figure A.1 was a working file, used to solve the convected acoustic field in a previously generated mesh.

```
# PyFe file.
cores: max
# import nodes and elements from gmsh saved file:
nodes, elements: 'm92acou2a.msh'

# preprocess
strip_unused_nodes

# Interpolate velocities using those nodes and elements:
# velocities: interpolate from file 'm.dat', symmetry=yz, invert=x

# Save the interpolation results if desired:
# velocities: save to file 'm90acou1.interpolate'

# If interpolated velocities are available, load:
# velocities: load from file 'm90acou2.interpolate'

# Define uniform flow:
velocities:  ux: 0, uy: 0, uz:0

# Specify drive regions or nodes.  Specify drive type (p or dp/dn)
drive:  dp/dn @ node list; 14, 7

# Observation regions / nodes used during search for peak pressure.
# observe: circle, centre, 0.05, -0.05, -0.01, edge, 0.06, -0.05, -0.01

# Damping.  With side view: 'h', plate separation; 'R',
# anemometer radius; 'h2', diameter of the damping semicircle.
damping: Curved shell: R=0.025, h=0.01, h2=0.05 . No flow compensation.

# Add analysis frequencies
frequencies:  start:1000, stop:40000,  number:400

# or perform a pressure peak search.
# peak search:  fmin: 15000, fmax:22000, splits:2, dfmin:0.1
```

Figure A.1: Example .pyFE file, controlling the solution of a convected acoustic simulation.

# Bibliography


[1] M. A. Ardekani. Hot-wire calibration using vortex shedding. *Measurement*, 42, 2009.

[2] R. J. Astley. Infinite elements for wave problems: a review of current formulations and an assessment of accuracy. *International Journal for Numerical Methods in Engineering*, 49:951–976, 2000.

[3] M. Bailey. Personal communication., November 2006.

[4] P. Balachandran. *Fundamentals of Compressible Fluid Dynamics.* PHI Learning Pvt. Ltd, 2006.

[5] Hyochoong Bang. *The Finite Element Method using Matlab.* CRC Press, 1 edition, 1997.

[6] J. Barlow, Jr W. Rae, and A.Pope. *Low-speed wind tunnel testing.* Wiley-interscience, 3 edition, 1999.

[7] Isaac Barona. Uspp (universal serial port python library). 2001.

[8] J S Barton and M Saoudi. A fiber optic vortex flowmeter. *Journal of Physics E: Scientific Instruments*, 19(1):64–66, 1986. URL `http://stacks.iop.org/0022-3735/19/64`.

[9] David Beazley. *Python Essential Reference.* New riders publishing, 1999.

[10] Peter Bettess. *Infinite Elements.* Penshaw Press, 1992.

[11] L. Bradbury and I. Castro. A pulsed-wire technique for velocity measurements in highly turbulent flows. *Journal of Fluid Mechanics*, 49, 1971.

[12] P. Bradshaw. *An introduction to turbulence and its measurement.* Robert Maxwell, M.C., 2nd edition, 1975.

[13] R. R. Brook. Effective dynamic response of paired gill anemometers. *Boundary-Layer Meteorology*, 11, 1977.

[14] Paul Browne, Agnès Ramuzat, Rahul Saxena, and Ajit Yoganathan. Experimental investigation of the steady flow downstream of the st. jude blieaflet heart valve: A comparison between laser doppler velocimetry and particle image velocimetry techniques. *Annals of Biomedical Engineering*, 28, 2000.

[15] *Technical Review No. 3.* Bruel Kjaer, 1987.

[16] H. Bruun. *Hot-wire anemometry.* Oxford University Press, 1 edition, 1995.

[17] G. Byrne, S. James, and R. Tatam. A bragg grating based fibre optic reference beam laser doppler anemometer. *Measurement Science and Technology*, 12, 2001.

[18] Brian Cantwell and Donald Coles. An experimental study of entrainment and transport in the turbulent near wake of a circular cylinder. *Journal of Fluid Mechanics*, 136:321–374, 1983.

[19] S. H. Chue. Pressure probes for fluid measurement. *Progress in Aerospace Sciences*, 16:147 – 223, 1975.

[20] P. A. Coppin and K. J. Taylor. A three-component sonic anemometer/thermometer system for general micrometeorological research. *Boundary Layer Meteorology*, 27, 1983.

[21] Jared S. Cox. Computation of vortex shedding and radiated sound for a circular cylinder: Subcritical to transcritical reynolds numbers. *Theoretical and Computational Fluid Dynamics*, 12:233 – 253, 1998.

[22] Timothy L. Crawford and Ronald J. Dobosy. A sensitive fast-response probe to measure the turbulence and heat flux from any airplane. *Boundary-Layer Meteorology*, 1992.

[23] J. Å. Dahlberg, T. F. Pederson, and Peter Busche. Accuwind - methods for classification of cup anemometers. Technical report, Risø National Laboratory, 2006.

[24] Sang Joon Lee Daichin. Evaluation of recursive piv algorithm with correlation based correction method using various flow images. *KSME International Journal*, 17(3), 2003.

[25] FrankUlrish Dentler. The effect of rainfall on measurements of mean wind speed with cup anemometers in the surface layer at sea. *Boundary-Layer Meteorology*, 14 (1), 1978.

[26] R L Desjardins, W S Reid, D J Buckley, and W Fagan. Description and performance testing of a low friction, twin-propeller anemometer with wind vane. *Journal of Physics E: Scientific Instruments*, 19(8):632–637, 1986. URL `http://stacks.iop.org/0022-3735/19/632`.

[27] R. J. Dobosy, T. L. Crawford, D. L. Auble, G. H. Crescenti, and R. C. Johnson. The extreme turbulence (et) probe for measuring boundary-layer turbulence during hurricane-force winds. In *11th Symposium on Meteorological Observations and Instrumentation*, 2001.

[28] W. J. Duncan, A. S. Thom, and A. D. Young. *Mechanics of Fluids.* Arnold, second edition, 1975.

[29] Dantec Dynamics. Minicta anemometer package. how to get started., 2004.

[30] Andreas Fischer, Lars Büttner, Jügen Czarske, Mechael Eggert, Gesine Grosche, and Harold Müller. Investigation of time-resolved single detector doppler global velocimetry using sinusoidal laser frequency modulation. *Measurement Science and Technology*, 18, 2007.

[31] C. A. J. Fletcher. *Computational Techniques for Fluid Dynamics. Volume I.* Springer-Verlag, 2 edition, 2006.

[32] C. A. J. Fletcher. *Computational Techniques for Fluid Dynamics. Volume II.* Springer-Verlag, 2 edition, 2006.

[33] *Fluent 6.2 User's Guide.* Fluent Inc., Centerra Resource Park, 10 Cavendish Court, Lebanon, NH 03766, 2005.

[34] J. F. Foss, J. K. Schwannecke, A. R. Lawrenze, M. W. Mets, S. C. Treat, and M. D. Dusel. The thermal transient anemometer. *Measurement Science and Technology*, 15, 2004.

[35] J. F. Foss, J. A. Peabody, M. J. Norconk, and A. R. Lawrenze. Ambient temperature and free stream turbulence effects on the thermal transient anemometer. *Measurement Science and technology*, 17, 2006.

[36] J. Franke and W. Frank. Large eddy simulation of the flow past a circular cylinder at red=3900. *Journal of Wind Engineering and Industrial Aerodynamics*, 2002.

[37] *FCO510 User Guide.* Furness Controls Limited, Beeching Road, Bexhill, East Sussex, TN39 3LJ, England, 2009.

[38] G. Gabard, R. J. Astley, and M. Ben Tahar. Stability and accuracy of finite element methods for flow acoustics. i: general theory and application to one-dimensional propagation. *International Journal for Numerical Methods in Engineering.*, 63, 2005.

[39] *Flotek 1440.* GDJ Inc., 7585 Tyler Boulevard, Mentor, Ohio, 44060, USA., 2007.

[40] *PTX/PMP 1400 Series.* GE industrial sensing, 2009.

[41] J. H. Gerrard. A disturbance-sensitive reynolds number range of the flow past a circular cylinder. *Journal of Fluid Mechanics*, 22, 1965.

[42] C. Geuzaine and J. F. Remacle. Gmsh: a three-dimensional finite element mesh generator with built-in pre- and post-processing facilities. *International Journal for Numerical Methods in Engineering*, 79, 2009.

[43] Gerald C. Gill. Development and use of the gill uvw anemometer. *Boundary-Layer Meteorology*, 8, 1975.

[44] *Extreme Weather WindObserver.* Gill Instruments Ltd, Saltmarsh Park, 67 Gosport Street, Lymington, Hampshire, SO41 9EG, UK, 2009.

[45] *WE550 wind sensor.* Global Water, 11390 Amalgam Way, Feb 2007.

[46] A. E. Green, M. J. Judd, J. K. McAneney, M. S. Astill, and P. T. Prendergast. A rapid-response 2-d drag anemometer for atmospheric turbulence measurements. *Boundary-Layer Meteorology*, 57, 1991.

[47] P. M. Gresho and R. L. Sani. *Incompressible flow and the finite element method. Volume One.* John Wiley and Sons, 2000.

[48] Steen Hanson. Broadening of the measured frequency spectrum in a differential laser anemometer due to interference plane gradients. *Journal of Physics D: Applied Physics*, 6(2):164–171, 1973. URL `http://stacks.iop.org/0022-3727/6/164`.

[49] R. D. Henshell. *Pafec. Theory.* Pafec Ltd, 1984.

[50] David Henwood and Javier Bonet. *Finite Elements. A gentle introduction.* Macmillan, 1996.

[51] W. H. Herschel. The pitot-tube and other anemometers for aeroplanes. Technical Report 546, The United States Bureau of Standards, 1935. Year wasn't mentioned on the document, but Barlow claims it is 1935.

[52] B. B. Hicks. Propeller anemometers as sensors of atmospheric turbulence. *Boundary-layer Meteorology*, 3, 1972.

[53] J. O. Hinze. *Turbulence.* McGraw-Hill, second edition, 1975.

[54] M. Hölling, B. Schulte, S. Barth, and J. Peinke. Sphere anemometer - a faster alternative solution to cup anemometry. *Journal of Physics*, 75, 2007.

[55] T. W. Horst and S. P. Oncley. Corrections to inertial-range power spectra measured by csat3 and solent sonic anemometers, 1. path averaging errors. *Boundary Layer Meteorology*, 119, 2006.

[56] Tihomir S. Hristov, Scott D. Miller, and Carl A. Friehe. Linear time-invarient compensation of cup and vane intertia. *Boundary-Layer Meteorology*, 97(2), 2000.

[57] G. Iaccarino, A. Ooi, P. A. Durbin, and M. Behnia. Reynolds averaged simulation of unsteady separated flow. *International Journal of Heat and Fluid Flow*, 24:147–156, 2003. Square cylinder. Discussion of RANS and URANS and when to use unsteady. Steady state found to be poor for square cylinder, unsteady good. Coherent vortex shedding demands URANS as the flow is not 'statistically stationary'. 50 steps per shedding cycle.

[58] Gianluca Iaccarino. Predictions of a turbulent separated flow using commercial cfd codes. *Journal of Fluid Engineering*, 123(4):819–828, 2001.

[59] Y. Kagawa, T. Tsuchiya, T. Hara, and T. Tsuji. Discrete huygens' modelling simulation of sound wave propagation in velocity varying environments. *Journal of Sound and Vibration*, 246, 2001.

[60] J. Kaimal and J. Businger. A continuous wave sonic anemometer. *Journal of applied Meteorology*, 2, 1963.

[61] Savvas Kapartis. *Acoustic resonance research program definition and objectives.* FT Technologies, Church Lane, Teddington, Middlesex, 2005.

[62] M. A. Kegarise and E. F. Spina. A comparative study of constant-voltage and constant-temperature hot-wire anemometers: Part ii - the dynamic response. *Experiments in Fluids*, 29, 2000.

[63] G. Kiel. Total-head meter with small sensitivity to yaw. Technical Report 775, National Advisory Committee for Aeronautics, 1935. Claims genuine total head at low Re, upto 40 degrees.

[64] L. Kristensen. The perennial cup anemometer. *Wind Energy*, 2, 1999.

[65] Leif Kristensen. Cups, props and vanes. Technical Report Risø-R-766(EN), Risø National Laboratory, 1996.

[66] B. E. Launder, G. J. Reece, and W. Rodi. Progress in the development of a reynolds-stress turbulence closure. *Journal of Fluid Mechanics*, 1975.

[67] I. V. Lebedev, B. S. Rinkevichyus, and E. V. Yastrebova. Measuring local velocities of small scale flows using a laser. *Zhurnal Prikladnoi Mekhaniki i Tekhnicheskoi Fiziki*, 10(5), 1969.

[68] W. Linke. New measurements on aerodynamics of cylinders particularly their friction resistance. *Physikalische Zeitschrift*, 32, 1931.

[69] Y. S. K. Liow, B. T. Tan, M. C. Thompson, and K. Hourigan. Sound generated in laminar flow past a two-dimensional rectangular cylinder. *Journal of Sound and Vibration*, 295:407–427, 2006.

[70] R. I. Mackie. *Object-oriented methods and Finite Element analysis*. Saxe-Coburg, 2001.

[71] M. Manshadi, P. Tamadonfar, M. Soltani, K. Ghorbanian, and M. Masdari. Power spectrum and fft-based signal analysis in turbulence measurements. *PROCEEDINGS OF WORLD ACADEMY OF SCIENCE, ENGINEERING AND TECHNOLOGY*, 30, 2008.

[72] Kenneth G. Merriam and Ellis R Spaulding. Comparative tests of pitot-static tubes. Technical Report 546, NACA, 1935. Year wasn't mentioned on the document, but Barlow claims it is 1935.

[73] Y. Mitsuata and H. Asai. A sonic anemometer for the measurement of vorticity and its transport in the surface layer. *Experiments in fluids*, 2(3), 1984.

[74] Gerald L. Morrison and Charles A. Gaharan. Uncertainty estimates in dgv systems due to pixel location and velocity gradients. *Measurement science and technology*, 12, 2001.

[75] Phillip M. Morse and K. Uno Ingard. *Theoretical acoustics*. McGraw-Hill, 1 edition, 1968.

[76] Harald Müller, Mechael Eggert, Jügen Czarske, Lars Büttner, and Andreas Fischer. Single-camera doppler global velocimetry based on frequency modulation techniques. *Experiments in Fluids*, 43(2 - 3), 2007.

[77] K. Okamoto, S. Nishio, T. Saga, and T. Kobayashi. Standard images for particle-image velocimetry. *Measurement Science and Technology*, (11), 2000.

[78] K. Okamoto, S. Nishio, T. Saga, T. Kobayashi, and K. Takehara. Evaluation of the 3d-piv standard images (piv-std project). *Journal of visualization*, (3), 2000.

[79] K. H. Papadopoulos, N. C. Stefantos, U. S. Paulsen, and E. Morfiadakis. Effects of turbulence and flow inclination on the performance of cup anemometers in the field. *Boundary-Layer Meteorology*, 101(1), 2001.

[80] J. Patterson. The cup anemometer. *Transactions of the Royal Society of Canada, III*, 20, 1926.

[81] K. S. Peat and K. L. Rathi. A finite element analysis of the convected acoustic wave motion in dissipative silencers. *Journal of Sound and Vibration*, 184:529–545, 1995.

[82] Kieth S. Peat and Ray Kirby. Acoustic wave motion along a narrow cylindrical duct in the presence of an axial mean flow and temperature gradient. *Journal of the Acoustic Society of America*, 107(4):1859–1867, 1999.

[83] H. J. Pfeifer, H. D. vom Stein, and B. Koch. Investigation of a supersonic free jet by means of a laser anemometer. *Applied Physics*, 4, 1974.

[84] M. J. F. P. Pluijm, G. J. A. Sars, and C. H. Massen. Calibration unit for micro-anemometers at very low air velocities. *Applied Scientific Research*, 43, 1986.

[85] A. K. Prasad. Stereoscopic particle image velocimetry. *Experiments in Fluids*, 29, 2000.

[86] *Wind monitor 05103.* R. M. Young Company, 2801 Aero Park Drive, Traverse City, Michigan, 49686, USA, 2009. URL `www.youngusa.com`.

[87] E. J. Richards and D. J. Mead. *Noise and Acoustic fatigue in Aeronautics.* Wiley, 1968.

[88] Risø. P2546adatasheet. 2009.

[89] *Gill UVX Anemometer.* R.M.Young Company, 2801 Aero Park Drive, Traverse City, Michigan, 49686, USA, 2009. URL `www.youngusa.com`.

[90] *Young USA price list.* R.M.Young Company, 2801 Aero Park Drive, Traverse City, Michigan, 49686, USA, 2009. URL `www.youngusa.com/PRICELIST.pdf`.

[91] M J Rudd. A new theoretical model for the laser dopplermeter. *Journal of Physics E: Scientific Instruments*, 2(1):55–58, 1969. URL `http://stacks.iop.org/0022-3735/2/55`.

[92] Fulvio Scarano. *Particle Image Velocimetry.* Springer-Verlag Berlin / Heidelberg, 2008.

[93] P. Schotanus, F. T. M. Nieuwstadt, and H. A. R. De Bruin. Temperature measurement with a sonic anemometer and its application to heat and moisture fluxes. *Boundary Layer Meteorology*, 26, 1983.

[94] C. Y. She and R. F. Kelly. Photon-burst correlation techniques for atmospheric crosswind measurements. *Applied Physics B*, 33, 1984.

[95] W. J. Shuttleworth, D. D. McNeil, and C. J. Moore. A switched continuous-wave sonic anemometer for measuring surface heat fluxes. *Boundary Layer Meteorology*, 23, 82.

[96] B. A. Singer, D. P. Lockard, and G. M. Lilley. Hybrid acoustic predictions. *Computers and Mathematics with Applications*, 46, 2003.

[97] S. P. Singh and S. Mittal. Flow past a cylinder: shear layer instability and drag crisis. *International Journal for Numerical Methods in Fluids*, 47(1):75–98, 2005.

[98] Yu. P. Solov'ev, A. I. Korovushkin, and Yu. N. Toloknov. Characteristics of a cup anemometer and a procedure of measuring the wind velocity. *Physical Oceanography*, 14(3), 2004.

[99] K. Squires. Detached-eddy simulation: current status and perspectives. *Proceedings of Direct and Large-Eddy simulations*, 2004.

[100] C. J. Stewart. Measurement of air speed in aeroplanes. *Journal of Scientific Instruments*, 1:43–50, 1923. doi: 10.1088/0950-7671/1/2/302.

[101] Z. Sun, H. Zhang, and J. Zhou. Evaluation of uncertainty in a vortex flowmeter measurement. *Measurement*, 41, 2008.

[102] S. Szepessy. On the spanwise correlation of vortex shedding from a circular cylinder at high subcritical reynolds number. *Phys. Fluids*, 6 (7):2406–2416, 1994.

[103] D H Thompson. A tracer-particle fluid velocity meter incorporating a laser. *Journal of Physics E: Scientific Instruments*, 1(9):929–932, 1968. URL `http://stacks.iop.org/0022-3735/1/929`.

[104] Lonny L. Thompson. A review of finite-element methods for time-harmonic acoustics. *Journal of the Acoustical Society of America*, 119(3):1315–1330, March 2006.

[105] Nils Tillmark and P. Henrik Alfredsson. Experiments on transition in plane couette flow. *Journal of Fluid Mechanics*, 235, 1992.

[106] A. Travin, M. Shur, M. Strelets, and P. Spalart. Detached-eddy simulations past a circular cylinder. *Flow, Turbulence and Combustion*, 63:293–313, 1999.

[107] C. Tropea, J. Foss, and A. Yarin, editors. *Springer Handbook of Experimental Fluid Mechanics*. Springer, 2007.

[108] T. Tsuji, T.Tsuchiya, and Y. Kagawa. Finite element and boundary element modelling for the acoustic wave transmission in mean flow medium. *Journal of Sound and Vibration*, 255:849–866, 2002.

[109] H. D. vom Stein and H. J. Pfeifer. A doppler difference method for velocity measurements. *Metrologia*, 5(2), 1969.

[110] M. Wang and D. Kassoy. Standing acoustic waves in a low mach number shear flow. *American Institute of Aeronautics and Astronautics*, 30, 1992.

[111] M. Wang and D. R. Kassoy. Transient acoustic processes in a low-mach-number shear flow. *Journal of Fluid Mechanics*, 238, 1990.

[112] M. L. Wesely, C. B. Tanner, and G. W. Thurtell. An improved pressure-sphere anemometer. *Boundary-Layer Meteorology*, 2:275 - 2283, 1972.

[113] J Westerweel. Fundamentals of digital particle image velocimetry. *Measurement Science and Technology*, 8(12):1379–1392, 1997. URL `http://stacks.iop.org/0957-0233/8/1379`.

[114] C. Wieselsberger. Further information on the laws of fluid resistance. *Physikalische Zeitschrift*, 23, 1922.

[115] Y. Yeh and H. Z. Cummins. Localised flow measurements with an he-ne laser spectrometer. *Applied Physics Letters*, 4:176, 1964.

[116] M. M. Zdravkovich. *Flow Around Circular Cylinders Volume 1: Fundamentals*. Oxford Science Publications, 2007.

[117] M. M. Zdravkovich, V. P. Brand, G. Mathew, and A. Weston. Flow past circular cylinders with two free ends. *Journal of Fluid Mechanics*, 203:557 – 575, 1989.

[118] P. Zhang, T. W. Wu, and L. Lee. A coupled fem / bem formulation for acoustic radiation in subsonic non-uniform flow. *Journal of Sound and Vibration*, 192:333–347, 1995.

[119] O. C. Zienkiewicz and R. L. Taylor. *The Finite Element Method.* Mc Graw Hill, 1989.

[120] O. C. Zienkiewicz and R. L. Taylor. *The Finite Element Method volume 3. Fluid Dynamics.* Butterworth-Heinemann, 2000.